Stanford Geothermal Program
Interdisciplinary Research
in Engineering and Earth Sciences
Stanford University
Stanford, California

A STUDY OF NON-ISOTHERMAL SINGLE AND TWO-PHASE FLOW THROUGH CONSOLIDATED SANDSTONES

by
Norio Arihara

November 1974

This research was carried out
under Research Grant GI-34925
by the National Science Foundation

This report was prepared originally as a dissertation submitted to the Department of Petroleum Engineering and the Committee on the Graduate Division of Stanford University in partial fulfillment of the requirements for the degree of Doctor of Philosophy.

ACKNOWLEDGEMENTS

The author would like to express his sincere appreciation to his adviser, Dr. Henry J. Ramey, Jr., for his instruction and guidance throughout this investigation. Dr. Ramey's encouragement will not be forgotten.

The author is deeply grateful to his friends, particularly Francis Cassé and Paul Atkinson, for their helpful. comments and timely help through the days of experimental work.

The construction of the equipment was aided by many persons. Stanford staff included Peter Gordon, Luke Meisenback, Frank Peters, and Alice Mansourian. Special thanks are due to Dr. Paul Baker and the Chevron Oil Field Research Company for advice concerning the liquid saturation probe design, and Dr. Stan Jones and the Marathon Oil Company for advice and help concerning the large Hassler-Sleeve core holder with pressure taps.

The author wishes to express his deepest gratitude to his wife, Michiko, for encouragement, devotion, and perseverance all through the graduate study years.

This research was carried out under Research Grant GI-34925 by the National Science Foundation. Financial aid from the National Science Foundation is hereby gratefully acknowledged.

ABSTRACT

The main purpose of this study was to investigate non-isothermal single and two-phase flow of a single component fluid (water) in consolidated porous media. Thus the two-phase flow was boiling water flow. To our knowledge, there has been only one study of non-isothermal boiling flow in an unconsolidated sand pack, although previous work on thermal oil recovery by hot fluid injection presents information useful for the present study.

Equipment was constructed to perform linear flow experiments through cylindrical consolidated cores. Both natural (Berea) and synthetic cement consolidated sand cores were used..

Successful fabrication of the synthetic sandstones was important to permit reproducible fabrication of high porosity, low permeability sandstones with thermowells, pressure ports, and glass tube capacitance probe guides cast in place.

Hot fluid injection and cold water injection experiments were carried out in both natural and synthetic sandstones. The overall heat transfer coefficient for the core holder was measured and compared with design calculations with good results. The steady-state overall heat

transfer coefficient was measured and found to depend on mass flow rate to a minor degree. The thermal efficiency of hot water and cold water injection was found to depend on heat injection rate: the higher the heat injection rate, the higher the thermal efficiency. This trend was also found by previous investigators for unconsolidated sands. One major result of this study is that much of the previous works with non-isothermal single phase flow in unconsolidated sands may be extended to consolidated sandstones despite significant differences in isothermal flow characteristics of these systems.

One unique system considered in this study was injection of cold fluid into an initially hot porous medium. This is analogous to heat scavenging on condensate reinjection in geothermal fluid production. It was discovered that the overall heat transfer coefficient depended on the process (hot or cold injection), and the novel concept of thermal efficiency of cold fluid injection was introduced. Results for cold water injection indicate that lower injection rate, or smaller temperature difference between the surroundings and injected water is advantageous for heat scavenging from the surroundings by cold water injection into the geothermal reservoir.

In two-phase boiling flow experiments, hot, compressed liquid water steadily entered the upstream end of the core, moved downstream a certain distance, started vaporizing, and

flowed through the remainder of the core as a mixture of steam and liquid water. Although beyond. the original objective for this phase of the project, boiling flow experimental data show that significant decreases in both temperature and pressure can occur within the two-phase region. Even when flow is very non-isothermal, two-phase flow can be isenthalpic and steady state, if heat transfer between the core and the surroundings is of a low level.

Finally, preliminary experiments were conducted with a capacitance probe liquid saturation detector, and liquid saturation calculations were performed for the boiling flow experiments.

TABLE OF CONTENTS

TABLE OF CONTENTS. CONTINUED

LIST OF FIGURES

LIST OF FIGURES, CONTINUED

LIST OF **FIGURES,** CONTINUED

LIST OF FIGURES, CONTINUED

LIST OF FIGURES, CONTINUED

LIST OF TABLES

INTRODUCTION

The public has begun to pay much attention to Geothermal Energy as a potential major new source of energy to be developed in the future. Prime considerations in geothermal energy extraction from underground sources would appear to be: 1) how much energy can be recovered; and 2) how fast can it be extracted? In order to find useful answers to these questions, the basic characteristics and behavior of the reservoir rocks and fluids in geothermal systems require investigation.

The present research was started with an objective to study the thermodynamic and fluidmechanic behavior of non-isothermal flow of single and two-phase, single-component fluids through consolidated porous media.

Published information on oil recovery by hot fluid injection and Underground combustion present some of the important features of non-isothermal, two-phase flow which appear pertinent to geothermal reservoirs. But there has been no specific study of the flow of single component (water) two-phase (thus non-isothermal) boiling flow in porous media. In view of the fact that all heat effects (sensible heat, latent heat of vaporization, etc.) are much greater for water than for hydrocarbons, it was expected that some severe anomalies might be found.

A bench-scale model was designed and constructed to permit a thorough examination of thermodynamic and fluid-mechanic aspects of the two-phase flow regime. In addition to this experiment, a variety of important peripheral experiments were accomplished with the same experimental apparatus. For example, cold water injection into a system initially containing hot water is a potentially practical operation for geothermal. heat scavenging from the rock matrix by condensate injection. Hot water injection into a system containing water at a lower temperature is also a useful peripheral experiment to aid comparison of the present studies with previous oil recovery work.

Much time was spent learning to create synthetic consolidated sandstones of specific desirable properties (high porosity, low permeability). Pertinent work in this area was reviewed as a subject of great importance to this field of study. Another major problem was determination of a reliable method of measurement of liquid saturation (pore volume fraction containing liquid phase) in the porous media over a range of temperature and pressure.

Finally, in order to aid understanding of mass and heat transfer through porous media, published theoretical and experimental results were reviewed, and a comprehensive survey was published.[43]

LITERATURE SURVEY

Although the study of application of reservoir engineering principles to geothermal energy is recent, there are many publications aimed at oil recovery by addition of heat to a reservoir which are useful in the present study. It should be clear that much of the following literature had a different objective for application than recovery of Geothermal Energy.

Hot Fluid Injection

The first significant study of heat transport in a formation caused by hot fluid injection was presented by Lauwerier[1] in 1955. Lauwerier assumed that injection rate, V_w, and temperature, T_i, would remain constant, the flow system was linear, thermal conductivity in the direction of flow was zero, and that the thermal conductivity in the flooded layer perpendicular to the direction of flow was infinite so that the temperature in the flooded layer was always uniform at a given location in the flooded zone. Sometimes this is called the "zero dimension" assumption in pipe flow. The conductivity in the overburden and underburden, λ_2, was assumed to be finite and constant. Thus loss of heat from the injected fluid to the adjacent strata would result in a decrease in temperature in the direction of flow.

With these assumptions, the problem to be solved was expressed by the following set of equations:

$$\text{for } |\eta| > 1 \qquad \theta \frac{\partial^2 T_2}{\partial \eta^2} = \frac{\partial T_2}{\partial \tau}$$

$$\text{for } |\eta| = 1 \qquad \begin{cases} \dfrac{\partial T_2}{\partial \tau} + \dfrac{\partial T_2}{\partial \xi} - \dfrac{\partial T_2}{\partial \eta} = 0 \\ T_1 = T_2 \end{cases} \tag{1}$$

$$\text{for } \tau = 0 \qquad T_1 = T_2 \begin{cases} T_i & \text{if } \xi < 0 \\ 0 & \text{if } \xi > 0 \end{cases}$$

where the different quantities are defined as follows:

$$\xi = \frac{\lambda_2}{b^2 \rho_w C_w V_w} x \qquad \tau = \frac{\lambda_2}{b^2 \rho_1 C_1} t$$

$$\theta = \frac{\rho_1 C_1}{\rho_2 C_2} \qquad \eta = \frac{y}{b}$$

x = distance in flow-direction

b = half the formation thickness.

Other symbols are defined in the nomenclature.

Applying sequential Laplace transformation with respect to the distance and the time variables, Lauwerier obtained the result:

$$T = T_i \operatorname{erfc} \left(\frac{\xi + |\eta| - 1}{2\sqrt{\theta(\tau - \xi)}} \right) \alpha(\tau - \xi) \tag{2}$$

where

$$\eta = \begin{cases} \frac{y}{b} \text{ for } |y| > b \\ 1 \text{ for } |y| < b \end{cases}$$

$$\alpha(\tau - \xi) = \begin{cases} 1 \text{ for } \tau \geq \xi \\ 0 \text{ for } \tau < \xi. \end{cases}$$

In 1959, Marx and Langenheim[2] presented a solution for a heat loss problem similar to the one considered by Lauwerier. Their report described a method for estimating thermal invasion rates, cumulative heated area and theoretical economic limits for sustained heat injection at a constant rate into a radial flow system. They assumed that heat injected at a constant rate H_o raised the temperature of the flooded zone to T_1 and maintained this temperature. Their heat balance led to the following:

$$H_o = 2\int_o^t \left[\frac{\lambda_2 \Delta T}{\sqrt{\pi D(t-\tau)}}\right]\left(\frac{dA}{d\tau}\right)d\tau + 2\rho_1 C_1 b \Delta T \frac{dA}{dt} \qquad (3)$$

where $\Delta T = T_1 - T_o$.

This equation is an application of an earlier equation for estimating the extent of the fractured area in hydraulic fracturing derived by Carter.' In the growing hydraulic fracture problem, the fracture was assumed to be of uniform width, and the pressure in the fracture was assumed to be constant and equal to the sand face injection pressure. Because the fracture had no flow resistance, the assumption of a constant pressure in the

fracture was reasonable in spite of the fact that fluid leaks from the fracture into the formation. On the other hand, Ramey[4] pointed out that the constant elevated temperature in the flooded region assumed by Marx and Langenheim should be realistic only in the case that the heat injection medium is steam or other condensible gases near the boiling point at the injection pressure. In order to have a temperature maintained at the same level in the flooded zone, a small pressure gradient in the direction of flow is also required. Steam at the boiling point tends to follow the saturation curve requiring that temperature decreases as pressure decreases.

In Eq. 3, the first term on the right represents the flux of the heat **loss** from the injected fluid into the overburden and underburden, and the second term represents the rate at which the amount of heat remaining in the pay zone is increased. The flux **of** the heat **loss** can be derived easily in the same way as Churchill[5] described. Eq. 3 can be solved for the heated area A(t) (as Carter solved the same type of equation) by utilizing the Laplace transform method. The result of Marx and Langenheim **is:**

$$A(t) = \frac{H_o \rho_1 C_1 b D}{2\lambda_2^2 \Delta T} \left[e^{\tau^2} \operatorname{erfc} \tau + \frac{2\tau}{\sqrt{\pi}} - 1 \right] \qquad (4)$$

where $\tau = \frac{\lambda_2}{\rho_1 C_1 b} \sqrt{\frac{t}{D}}$.

Ramey[4] indicated several important points with regard to the mathematical model of Marx and Langenheim:

1. No restriction is placed on the direction of development of the heated area (may be linear, radial, or any two-dimensional geometry);

2. It is not necessary that the heat injection rate be constant;

3. The solution could provide useful information for heat injection in any type of well pattern with any specified swept area data.

Ramey presented results for a heat injection rate, H, as a function of time:

$$A(t) = \left(\frac{H(t)}{2\rho_1 C_1 b \Delta T}\right) * (e^{\tau^2} \operatorname{erfc} \tau). \tag{5}$$

The symbol, *, represents the convolution of two functions, or:

$$F_1(t) * F_2(t) = \int_0^t F_1(\tau) F_2(t - \tau) d\tau \tag{6}$$

$$= \int_0^t F_1(t - \tau) F_2(\tau) d\tau$$

Another expression of A(t) presented by Ramey is useful when the heat injection rate has constant values for increments of time such that

$$H = H_1 \text{ for } 0 \leq t < t_1$$

$$H_2 \text{ for } t_1 \leq t < t_2$$

H_n for $t_{n-1} \leq t < t_n$

Then, the heated area at time t results in:

$$A(t) = \frac{\rho_1 C_1 b D}{2\lambda_2 \Delta T} \left[H_n \left(e^{\tau_n^2} \operatorname{erfc} \tau_n + \frac{2\tau_n}{\sqrt{\pi}} - 1 \right) + \sum_{m=1}^{n-1} (H_m - H_{m+1}) \left(e^{\tau_m^2} \operatorname{erfc} \tau_m + \frac{2\tau_m}{\sqrt{\pi}} - 1 \right) \right] \tag{7}$$

Heat stored in the flooded formation, H_s, at time t can be calculated by the volume integral:

$$H_s = \int_V \rho_1 C_1 [T_1 - T_o] dV \tag{8}$$

where T_o is initial temperature of the formation. Heat injected to time t is:

$$H_i = \int_o^t q \rho_w C_w (T_i - T_o) dt \tag{9}$$

The thermal efficiency, E, is defined as the fraction of the cumulative heat injected remaining in the injection interval:

$$E = \frac{H_s}{H_i} \tag{10}$$

Rubinshtein' introduced the idea of the fraction of the total heat injected lost to adjacent strata, $W_o^* = 1 - E$. It is remarkable that Ramey[6] found the identical heat loss results for the Lauwerier model and the Marx-Langenheim models as follows:

$$1 - W_o^* = E = \frac{\theta}{\tau} \left[e^{\tau/\theta} \operatorname{erfc} \sqrt{\frac{\tau}{\theta}} - 1 + 2\sqrt{\frac{\tau}{\theta \pi}} \right] \tag{11}$$

The equal thermal efficiency results apparently because the Lauwerier heat model yields a larger heated area at a lower average temperature, while the Marx-Langenheim heat model yields a smaller heated area at a higher temperature.

In the 1959 study, Rubinshtein also presented the thermal efficiency for a radial flow model of hot water injection with fewer assumptions than used previously by Lauwerier. Rubinshtein assumed constant isotropic thermal conductivities in the flow layer and in the impermeable strata surrounding the reservoir, and obtained:

$$E = 1 - (1 - \beta)\left\{\frac{2}{3}\sqrt{\frac{\gamma\tau}{\pi}}\left[1 - (1 - \beta)\sum_{n=1}^{m}\beta^{n-1}\left(1 + \frac{n^2}{\gamma\tau}\right)e^{-n^2/\gamma\tau}\right]\right.$$

$$\left. + (1 - \beta)\sum_{n-1}^{\infty} n\beta^{n-1}\left(1 + \frac{2n^2}{3\gamma\tau}\right)\operatorname{erfc}\frac{n}{\sqrt{\gamma\tau}}\right\} \qquad (12)$$

where

$$\beta = \frac{\gamma a - 1}{\gamma a + 1}$$

$$\gamma = \frac{\lambda_1}{\lambda_2}$$

$$a^2 = \frac{\lambda_2\rho_1 C_1}{\lambda_1\rho_2 C_2}$$

In the case $\gamma = a = 1$, Ramey showed the following expression:

$$E = 1 - \left\{\frac{2}{3}\sqrt{\frac{\tau}{\pi}}\left[1 - \left(1 + \frac{1}{\tau}\right)e^{-1/\tau}\right] + \left(1 + \frac{2}{3\tau}\right)\operatorname{erfc}\frac{1}{\sqrt{\tau}}\right\} \qquad (13)$$

Although Rubinshtein did not solve for temperature distributions, Spillette[8] solved numerically the energy balance equation with the same assumptions as Rubinshtein. According to Spillette's calculation, the primary effects of including horizontal heat conduction in the analysis are the lowering of the calculated sand temperatures near the point of injection and the propagation of injected energy further into the reservoir.

Baker[9,10,11] accomplished a series of experimental studies of heat transfer in hot fluid injection with a radial flow model. Initially, he studied displacement of cold water by hot water. First, he carried out hot water injection, and obtained radial temperature distributions which were in good agreement with theoretical results given by Lauwerier, Ramey, and Spillette. Thermal efficiency was calculated numerically with experimentally measured values of temperature. Baker observed that higher thermal efficiencies were obtained at higher rates of heat injection. For steam injection, Baker found that thermal efficiency decreased with cumulative injected heat, and that the heating process was more efficient at higher heat injection rates. But surprisingly, he obtained the result that thermal efficiency was a function of dimensionless time, $\alpha t/h^2$, alone. This contradicted his previous hot water injection studies.

Crichlow[12] also found rate sensitivity of thermal efficiency in hot fluid injection experiments, although results for steam injection were not consistent. He explained thermal efficiency dependence on flow rate by the presence of a film coefficient at the boundary between the pay zone and the surroundings.

According to Crichlow, this effect was significant at flow rates much higher than those normally encountered in oil reservoirs.

In 1969, Prats[13] analyzed the thermal efficiency for thermal recovery processes. He employed the same analytical method as Marx and Langenheim, but introduced far greater generality. His heat balance equation is:

$$Q(t) = \frac{dH(t)}{dt} + 2 \int_{-\infty}^{\infty} \int_{-\infty}^{\infty} U_{hz}(x, y, o, t)dxdy \qquad (14)$$

where

$Q(t)$ = net rate of heat injected

$H(t)$ = heat stored in the pay zone

$U_{hz}(x, y, z, t)$ = heat flux in the vertical direction and $z=0$ is the interface plane between the pay zone and the adjacent zone.

Eq. 14 is essentially the same as Eq. 3 of Marx and Langenheim. Prats divided the heat storage in the formation into two parts: heat in the pay zone near to and far from the injection well:

$$H(t) = H_n(t) + H_f(t).$$

Eq. 14 was solved by the Laplace transform method.

$$H(t) = \int_o^t Q(t')K(\theta_n\sqrt{t - t'})dt' - F \int_o^t H_f(t')\frac{d}{dt} K(\theta_n\sqrt{t - t'})dt' \qquad (15)$$

where

$$K(z) = e^{z^2} \text{ erfc } z$$

$$\theta_n = \frac{\lambda_{h2z}}{b\sqrt{\alpha_2}(\rho C)_n}$$

$$F = \frac{(\rho C)_f - (\rho C)_n}{(\rho C)_f}.$$

For hot water injection at constant heat injection rate and assuming F = 0, Prats obtained a thermal efficiency expression which is identical with Eq. 11 presented by Ramey for the models of Lauwerier, and Marx and Langenheim. An important contribution of Prats lies in the estimate of the thermal efficiency for steam injection. In steam flooding there is a steam zone near the injection well, and hot water zone outside the steam region. Understanding that the parameter F is generally positive, he developed lower and upper bounds for the thermal efficiency. Other interesting studies of thermal efficiency for steam injection may be found in references 44 and 45.

Two-Phase Flow

Although much analytical and experimental work has been done in the study of oil recovery by steam injection and hot water injection, there has been no specific study of non-isothermal boiling two-phase flow of water through porous media to our knowledge. In 1951, Miller[14] presented experimental results and analysis of single-component boiling two-phase flow of propane. His report gives broad information and instruction about in-phase boiling flow experiments, although there are large differences in the thermodynamic and physical properties

of water and propane. Miller performed laboratory experiments with specially designed apparatus to have adiabatic, two-phase, steady flow of propane through a horizontal column of sand. His flow tube was five feet long, and was constructed from six lengths of pipe, connected together by flanges. Between the flanges of the adjoining sections, blind flanges were used to which manometer lines and thermocouple lead wires were connected. In order to have an adiabatic condition, the flow tube as a whole was placed inside a circular, compartmented air duct, which provided means for fixing the temperature distribution in the air along the outside of the flow tube to correspond to the temperature distribution of the flowing propane inside the tube. After adiabatic and steady-flow conditions were attained, no appreciable heat transfer across the walls of the flow tube existed. In all the experiments, the propane entered the column entirely as a liquid, started to vaporize at an appreciable distance downstream from the inlet, and then flowed in two phases throughout the remainder of the column. Temperature and pressure distributions and the total mass rate of flow were measured.

The problem posed by Miller was to calculate the total mass rate of flow and pressure distribution along the column of sand, for a given pressure and temperature of the liquid entering stream, a given pressure or temperature of the discharging gas-liquid mixture, and given sand and fluid characteristics.

According to his method of analysis, he started with the following mass and energy equations for steady, two-phase, adiabatic flow:

$$\dot{m}_g + \dot{m}_\ell = \dot{m} = \text{constant} \tag{16}$$

$$\dot{m}_g h_g + \dot{m}_\ell h_\ell = \dot{m} h = \text{constant} \tag{17}$$

where $\dot{m}$, $\dot{m}_g$, $\dot{m}_\ell$ are total mass rate of flow, mass rates of steam and water respectively, and h, h_g, h_ℓ are the enthalpy of a two-phase mixture of steam and of water, respectively. Introducing the mass fraction of steam as:

$$f = \frac{\dot{m}_g}{\dot{m}} \tag{18}$$

the energy equation becomes:

$$(1 - f)h_\ell + fh_g = h. \tag{19}$$

Hence:

$$f = \frac{h - h_\ell}{h_g - h_\ell}. \tag{20}$$

From Darcy's law, the mass rate of flow of each phase is given as:

$$\dot{m}_g = -\frac{A\rho_g k_g}{\mu_g}\left(\frac{dp_g}{dx}\right), \qquad \dot{m}_\ell = -\frac{A\rho_\ell k_\ell}{\mu_\ell}\left(\frac{dp_\ell}{dx}\right) \tag{21}$$

if capillary pressure between vapor and liquid is neglected, Eqs. 21 become

$$\frac{m_\ell}{\dot{m}_g} = \frac{k_\ell \rho_\ell \mu_g}{k_g \rho_g \mu_\ell} = \frac{1 - f}{f} \tag{22}$$

where k, μ, and ρ are permeability, viscosity and density, respectively, and the subscripts g and ℓ pertain to steam and liquid phases, respectively. Finally

$$\frac{k_\ell}{k_g} = \frac{\mu_\ell \rho_g}{\mu_g \rho_\ell}\left(\frac{1 - f}{f}\right) = \frac{\mu_\ell}{\mu_g}\frac{\rho_g}{\rho_\ell}\left(\frac{h_g - h}{h - h_\ell}\right). \tag{23}$$

Because t mperature is a function of pressure in the two-phase flow region, the permeability ratio given by Eq. 23 may be computed by specifying pressure only. Then, Miller calculated the individual relative permeabilities by assuming that the correlation between k_ℓ/k and k_ℓ/k_g presented by Muskat, et al.,[22] was valid for his case. The total mass rate of flow and the pressure distribution were obtained simply by numerical integration:

$$\dot{m}\, x = Ak \int_p^{p_i} \left(\frac{\rho_\ell k_\ell/k}{\mu_\ell} + \frac{\rho_g k_g/k}{\mu_g}\right) dp \tag{24}$$

where p_i and p are fluid pressures at the upstream and **of** the column, and at a distance x from the inlet face, respectively. Because a remarkable agreement between experimental results and analytical theory was obtained, Miller concluded that phase equilibrium was attained very rapidly under the conditions of his experiment.

Luikov[15] described mathematically the heat and mass transfer phenomenon of vapor-liquid mixtures in capillary-porous bodies. He considered that the transfer of vapor took place by molecular means in the form of diffusion and by molar means by a convective motion due to a pressure drop, and that liquid transfer took place by means of diffusion, capillary absorption and convective motion. In the following description, the properties in vapor form are denoted by suffix g, in liquid form by ℓ, and **of** solid by 0.

The differential equation for mass transfer of steam or liquid is:

$$\frac{\partial \omega_i}{\partial t} = - \text{div } j_i + I_i \qquad i = g, Q \tag{25}$$

where ω_i is the volumetric concentration or mass per unit bulk core volume, j_i is the mass rate of the motor-molecular transfer flow, I_i is the volumetric capacity of the source (or sink) of phase i and $I_g = -I_{\ell}$. The volumetric concentration can be expressed as:

$$\omega_i = \frac{m_i}{V} = \rho_i \phi S_i \tag{26}$$

where m_i, V, ρ_i, ϕ, and S_i are mass, bulk volume of the porous medium, density, porosity, and saturation, respectively. Introducing the relative concentration u_i as:

$$u_i = \frac{m_i}{m_\Theta} = \frac{\omega_i}{\gamma_o} \tag{27}$$

where γ_o is the density of the dry core (mass of sand per unit bulk volume), the mass transfer equation becomes:

$$\frac{\partial (\gamma_o u_i)}{\partial t} = - \text{div } j_i + I_i \tag{28}$$

and

$$\frac{\partial (\gamma_o u)}{\partial t} = - \text{div } (j_g + j_\ell) \tag{28}$$

where $u = u_g + u_\ell$. The differential equation for heat transfer is obtained from th equation for internal energy transfer. At constant pressure, the local derivative of volumetric concentra-

tion of the enthalpy of the system is equal to the divergence of the flow of enthalpy:

$$\frac{\partial}{\partial t}\left(h_o\gamma_o + h_g\gamma_o u_g + h_\ell\gamma_o u_\ell\right) = -\operatorname{div}(j_q + h_g j_g + h_\ell j_\ell) \tag{30}$$

where h_i is the specific enthalpy, and j_q is the density of the molecular flow of energy, or heat flux. j_q contains not only the specific flow of heat caused by the drop in temperature, but also heat transfer by means of diffusion of mass. The isobaric specific heat is denoted by C_i:

$$C_i = \left(\frac{\partial h_i}{\partial T}\right)_p.$$

Then $C\gamma_o \frac{\partial T}{\partial t} = -\operatorname{div} j_q - (h_g I_g + h_\ell I_\ell) - (C_g j_g + C_\ell j_\ell)\nabla T$ (31)

where

$$C\gamma_o = (C_o u_o + C_g u_g + C_\ell u_\ell)\gamma_o$$

$$= C_o\rho_o(1 - \phi) + C_g\rho_g\phi S_g + C_\ell\rho_\ell\phi S_\ell.$$

Since $I_g = -I_\ell$, Eq. 31 becomes

$$C\gamma_o \frac{\partial T}{\partial t} = -\operatorname{div} j_q - h_{fg} I_g - (C_g j_g + C_\ell j_\ell)\nabla T \tag{32}$$

where $h_{fg} = h_g - h_\ell$.

Assuming that vapor is in thermodynamic equilibrium with the bound liquid, the vapor pressure is that of the saturated vapor, p_s, and thus is a single-valued function of temperature:

$$p_g = p_s = f(T). \tag{33}$$

Then, Luikov derived the equations of mass transfer through porous media on the basis of molecular and molar transfer mechanisms.

Steam flow by diffusion can be stated as:

$$j_{mg} = - \varepsilon D \frac{d\rho_{go}}{dT} \nabla T$$

$$= - a_{mg} \gamma_o \delta_g \nabla T \qquad (34)$$

where

$$\frac{d\rho_{go}}{dT} = \frac{M_g}{M_p} \frac{dp_s}{dt} .$$

In Eq. 34, εD is the coefficient of steam diffusion within the porous medium, $\rho_{go} = \rho_g/\rho$, M_g is the molecular weight of steam, M is the mean molecular weight of the mixture, $a_{mg} = \frac{\varepsilon D \rho}{\gamma_o}$, and $\delta_g = \frac{d\rho_{go}}{dT}$.

For liquid transfer by means of diffusion and capillary absorption:

$$j_{m\ell} = -a_{m\ell} \gamma_o [\nabla u + \delta_\ell \nabla T] \qquad (35)$$

where $a_{m\ell}$ is the liquid diffusion coefficient, and δ_ℓ is the thermal gradient coefficient of the liquid. Hence,

$$j_m = j_{mg} + j_{m\ell} = -a_m \gamma_o (\nabla u + \delta \nabla T) \qquad (36)$$

where $a_m = a_{m\ell}$ and

$$\delta = \frac{a_{m\ell} \delta_\ell + a_m \delta_g}{a_{m\ell}}$$

The molar transfer of steam and liquid water due to a gradient of the total pressure, VP, is described by Darcy's law:

$$\frac{\rho_{\sim} k}{} \nabla p = - \lambda_{p\sim} \nabla p$$

$$j_{p\ell} = - \lambda_{p\ell} \nabla p$$

Therefore $$j_p - j_{pg} + j_{p\ell} = \lambda_p \nabla p \qquad (37)$$

where λ_p ($= \lambda_{pg} + \lambda_p$) is the coefficient of filtration transfer of the mixture.

The total mixture flow caused by the influence of all the transfer forces is equal to:

$$j = - a_m \gamma_o (\nabla u + \delta \nabla T + \delta_p \nabla p) \qquad (38)$$

where $\delta_p = \frac{\lambda p}{a_m \gamma_o}$

Heat transfer by conduction is described by Fourier's law:

$$j_q = \text{XVT}$$

where is the total coefficient of thermal conductivity of the porous medium and mixture of steam and water. Thus the system of differential equations of mass and heat transfer can be written in the form:

$$\frac{\partial u}{\partial t} = \text{div}[a_m (\nabla u + \delta \nabla T + \delta_p \nabla p)] \qquad (39)$$

$$C\gamma_o \frac{\partial T}{\partial t} = \text{div}(\lambda \nabla T) - h_{fg} I_g + a_{m\ell}\gamma_o C_\ell V u \cdot \nabla T$$

$$+ (\lambda_{pg} C_g + \lambda_{p\ell} C_\ell) \nabla p \cdot \nabla T \qquad (40)$$

$$+ (a_{mg}\gamma_o \delta_g C_g + a_{m\ell}\gamma_o \delta_\ell C_\ell)(\nabla T)^2$$

$$P = P_s = f(T).$$

In most mathematical models, mass and heat transfer due to diffusion and capillary absorption are neglected, thus Eqs. 39 and 40 become simpler, but are still highly nonlinear. Reference [16] reports solution of these mass and heat transfer equations simultaneously in a model study of a transient flow system.

In the Petroleum Engineering literature, there has been a significant amount of work presented on the simulation of thermal oil recovery processes which involve steam injection. Among them, the works of Coats, et al.,[17] and Weinstein, et al.,[18] are comprehensive, and directly applicable to the present study of two-phase boiling flow of water. Although the solution techniques of Coats, et al., and Weinstein, et al., are completely different, both solved the same mass and energy transport equations simultaneously, including interphase mass transfer accounting for steam condensation.

Synthetic Sandstone

Although unconsolidated sand packs have often been used as porous media for laboratory studies, natural sandstone or artificially-cemented sandstone of properties similar to natural sandstone is more desirable to simulate natural reservoir

conditions. Synthetic sandstone is more favorable when sandstone of a special shape, or specific characteristics (porosity, permeability) are needed.

Wygal[19] showed that a process of artificial cementation could be used to change unconsolidated packs into synthetic sandstones having properties similar to those of natural rock, especially in terms of the drainage and imbibition relative permeabilities. A core was made of 5 weight per cent cement and 95 weight per cent of 70-80 mesh sand. Wygal also described in detail a technique for the construction of synthetic rock as follows:

1. Mix the sand with about 0.5 weight per cent of blending water.

2. Coat the dampened sand grains with the dry cement.

3. Pour the mixture into the container continuously through a particle distributor of wire mesh.

4. Inject water at a rate such that imbibition forces are dominant.

5. Allow the cement to hydrate for an appropriate time.

Heath[10] employed Wygal's technique, and presented the results obtained by changing some factors which affect the porosity and permeability of synthetic sandstones. According to Heath, the main factors and their effects are as follows:

1. Sand grain size -- Permeability increases with grain size for a given porosity. To obtain low porosity, it is necessary to c mbine two sizes at a grain-diameter ratio of about 6:1, and at a weight ratio of large grains to small grains of about 3:1.

2. Blending water -- More water increases both porosity and permeability.

3. Cement -- Both porosity and permeability decrease with increasing amount of cement.

Evers, et al.,[21] prepared sandstone of very low permeability to meet the requirements for their scaled model. Their method is different from Wygal's technique. Instead of injecting water into a dry mix of sand and cement in the container, Evers, et al., tamped a wet mortar into mold. The resultant permeabilities (ranging from 0.016 millidarcies to 0.162 millidarcies) and porosities (ranging from 10% to 18%) were obtained from mixtures of sand and cement for water-cement ratios of 0.30 to 0.40: sand.-cement ratios in the range of 1/1 to 2/1; and sand grain size from 100-200 to 12-18 mesh.

Saturation Measurement

The word "saturation" may be used in many ways in non-isothermal boiling flow in porous media. It can refer to steam and liquid water in equilibrium, to saturation of a solvent with a solute, or to the volume fraction of pore space which is filled with a given fluid phase such as oil, water, or gas. It is the latter sense that will be used in the following.

Means of measuring liquid pore space saturation which have received consideration include: electrical conductivity of the fluids; emissions from radioactive tracers dissolved in the fluids: the radioactivity of silver or rhodium caused by reflection of neutrons from hydrogen atoms in the fluids: the attenuation of a microwave beam: the diminution and phase shift of ultrasonic

wave trains; the reduction in intensity of x-ray beams in passing through fluids, and magnetic reluctance.

Musket, et al.,[22] and Botset[23] utilized piezometer rings which served as both electrodes and pressure taps. The piezometer rings were separated by insulating tubes forming portions of the flow tube. Connecting any two adjoining electrodes to an a.c. bridge, the average conductivity and thus liquid saturation between the two electrodes could be measured. They succeeded in measuring the saturation distribution in the flow system of water and CO_2 gas.

Neutrons are particles with no electric charge and with a mass approximately equal to that of a proton, the nucleus of the hydrogen atom, When a fast neutron is scattered by a hydrogen nucleus, it may lose any fraction of its kinetic energy. In the average collision, it loses one half its kinetic energy. All common elements other than hydrogen are so much heavier that a neutron will lose only a small fraction of its energy in a single elastic collision. The number of slow neutrons emerging from an object irradiated by fast neutrons, therefore, yields a rough index of the quantity of hydrogen it contains. Brunner and Mardock[24] used this neutron-scattering method to measure oil saturation in porous media. The neutron source was an intimate mixture of radium and beryllium. In order to measure the flux of slow neutrons, they found rhodium to be the most satisfactory. When slow neutrons strike rhodium, they induce radioactivity (mainly beta) which a Geiger-Mueller counter can detect. Brunner and Mardock presented a calibration curve for an unconsolidated sand pack showing number of counts vs. oil saturation, and also

the saturation distribution along the length of a core. Because this method detects the concentration of hydrogen atoms, it is also applicable to a water-steam flow system, because the mass of the water phase is dominant in the mixture; therefore, slow neutrons should indicate the liquid saturation.

Finnemore and Schaaf[25] reported the design considerations and the procedures for the use of a gamma-ray attenuation system designed to measure the moisture content of a soil in either a transient or a static condition. Their system consisted of a 220 mc cesium 137 source, sodium iodide crystal detector, pulse amplifier and analyzer, and scaler. They found that the following attenuation equation was appropriate:

$$N_w = N_d\, e^{-U_w WL} \quad \text{or} \quad W = \frac{1}{U_w L}\, \ell n\, \frac{N_d}{N_w}$$

where

N_w = count reading for wet soil

N_d = count reading for dry soil

U_w = the total linear attenuation coefficient of water

W = volume fraction of bulk volume occupied by moisture

L = thickness of the soil column.

Schaaf[26] utilized the gamma-ray attenuation system to determine moisture content at various spatial and temporal locations in an unsteady, unsaturated flow from a horizontal cylindrical source into porous media.

Baker[11] developed a capacitance probe which utilized the difference in dielectric constant between steam and hot water in a porous media. The instrument consisted of a probe which could be moved in a glass guide in a sand pack, a driving mechanism for the probe, electronic circuitry, and a recorder. Details of construction of the probe, and two diagrams of the electrical circuit are shown in Appendix C. As can be seen in the figures describing the probe and the probe circuitry, the probe is essentially a capacitor in an oscillator circuit whose resonant frequency changes with the changing capacitance of the probe. The probe is a silver-plated glass tube at the center of which a brass rod with a piece of closed copper tube at the end is held by Teflon spacers. The sensitive part of the probe is a small gap between the silver-coated glass tube and the copper tube. Therefore, most of the capacitance is fixed. When the probe is traversed in the glass guide in the sand pack, an electric field reaches outside the guide, and has different intensity according to the dielectric constant of the medium surrounding the glass guide. The frequency difference between the oscillator including the capacitance probe and a standard oscillator is detected and amplified. For recording, the circuit in Fig. C-3 was used to obtain a d.c. voltage whose magnitude was proportional to the frequency difference. Baker found the probe to work satisfactorily at room temperature with oil and water, gas and water, oil and alcohol, and other two-phase, two-component systems. Baker presented the saturation distributions given by the probe during his steam flooding experiments. Although he did not calibrate his probe at elevated temperatures, the data showed good

agreement with the average water saturation, and the steam front location. This method appeared best suited for the subject study.

The energy in an x-ray beam that has passed through an absorbing material is expressed by the following formula:

$$E = E_o \, e^{-\mu cd}$$

where E_o is the energy in the incident beam, μ is the mass absorption coefficient, c is the density or concentration of absorbing material, and d is the length of path of the beam in the absorber. Because every material has a different power to absorb x-rays, the reduction in intensity of an x-ray beam as it passes through a core depends on the fluids present. The beam emerging from the core can be measured as ionic current flowing across an air-filled ionization chamber. Morgan, et al.,[27] presented water saturation distributions detected by X-ray absorption along the length of cores subjected to gas drives.

EXPERIMENTAL EQUIPMENT

A schematic diagram of the completed apparatus is shown in Fig. 1, and photographs of the apparatus are shown in Fig. 2 (a) and (b). Referring to the flow diagram in Fig. 1, cold feed water is pumped through a tubular furnace and into a core contained in a Hassler sleeve core holder. The core holder is contained within an air bath used to set ambient temperatures as high as 410°F. An accumulator is located immediately downstream of the pump to eliminate flow pulsations. The accumulator is a diaphragm type with nitrogen pressure above the diaphragm. The nitrogen source can also be used to hold pressure on the Viton sleeve in the Hassler core holder.

Flow rate is measured both upstream and downstream of the core. A flowrator is upstream of the core, while the total mass rate can be determined by timed weighing of the cooled water from the outflow of the system. Both regulating and metering valves are used to adjust the back pressure and flow rate. Helicoid pressure gages are installed on each side of the core. Porous metal filters (60 micron elements) are located before the tubular furnace, and before the back-pressure valve. The main flow line is 1/4 inch O.D. stainless steel tubing, and other lines are 1/8 inch O.D. stainless steel tubing. All fittings, valves, filters,

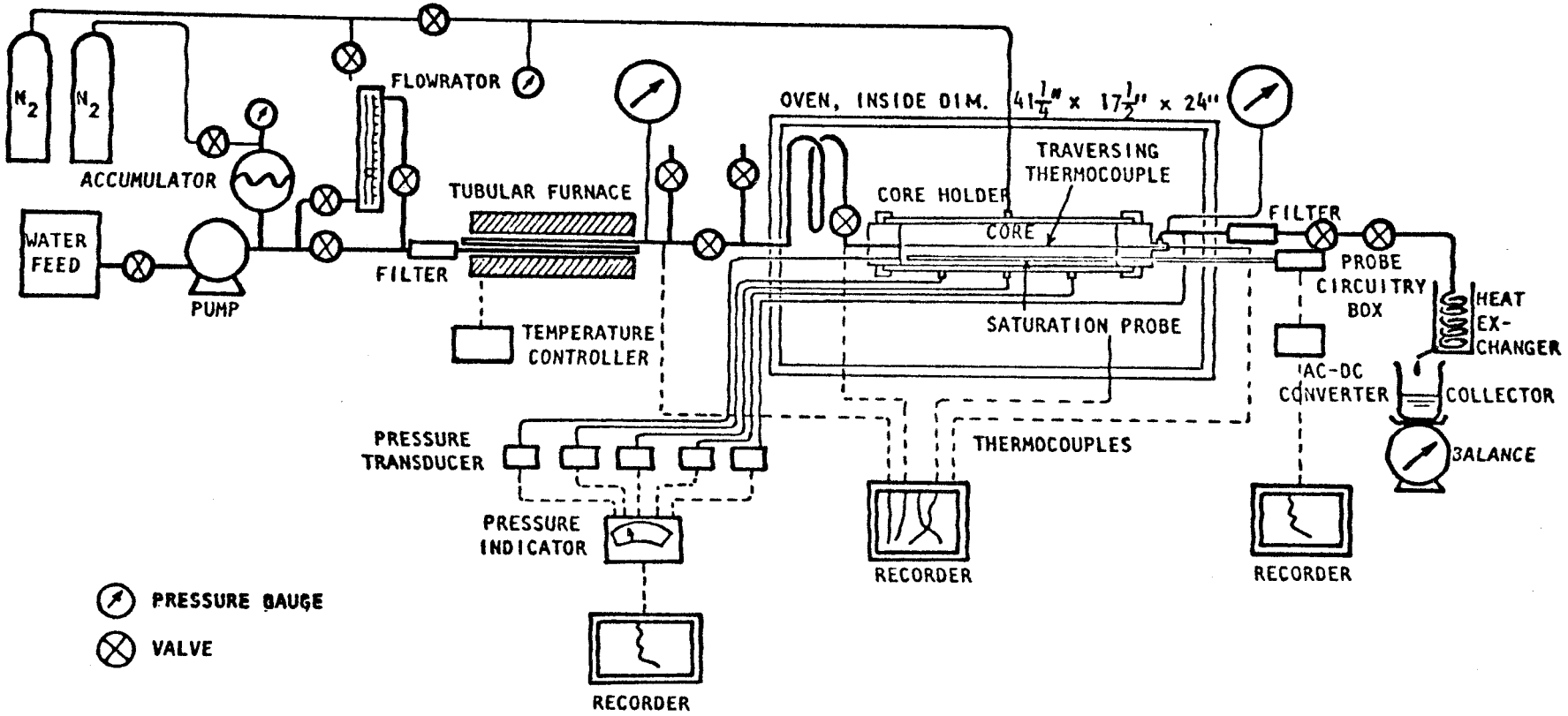

FIGURE 1. SCHEMATIC DIAGRAM OF APPARATUS

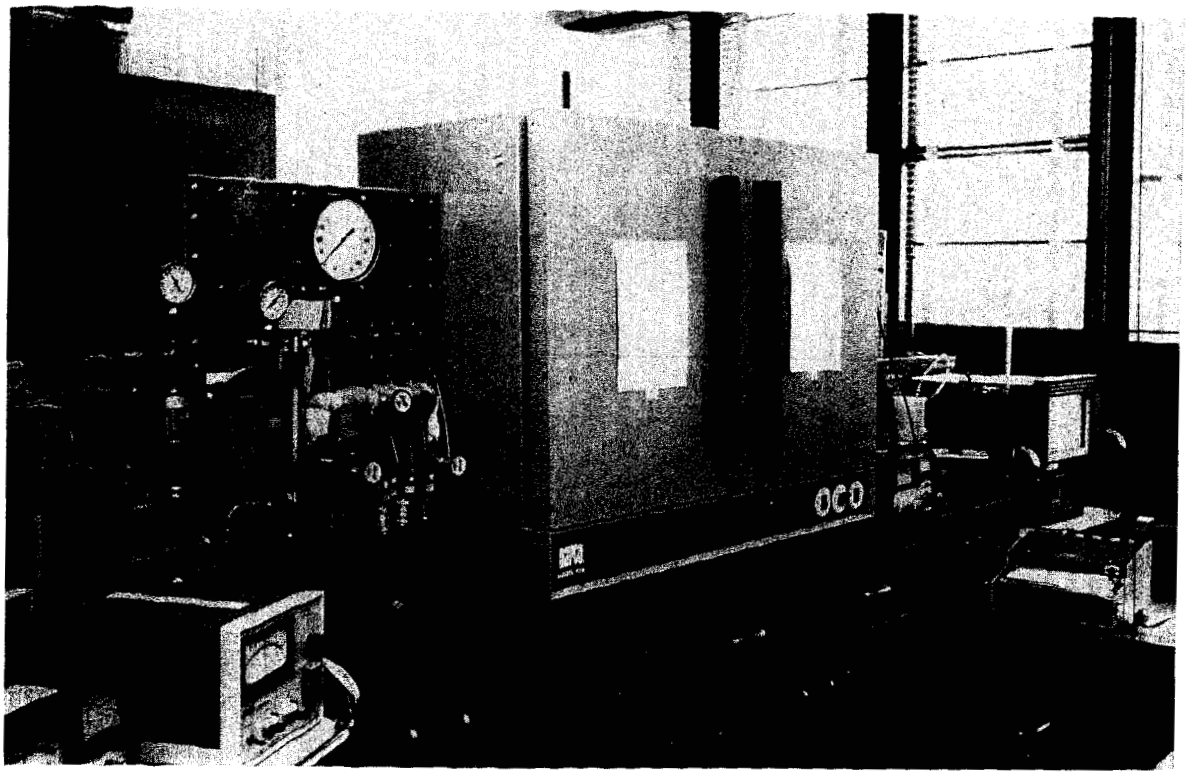

FIGURE 2 (a). PHOTOGRAPH OF APPARATUS.

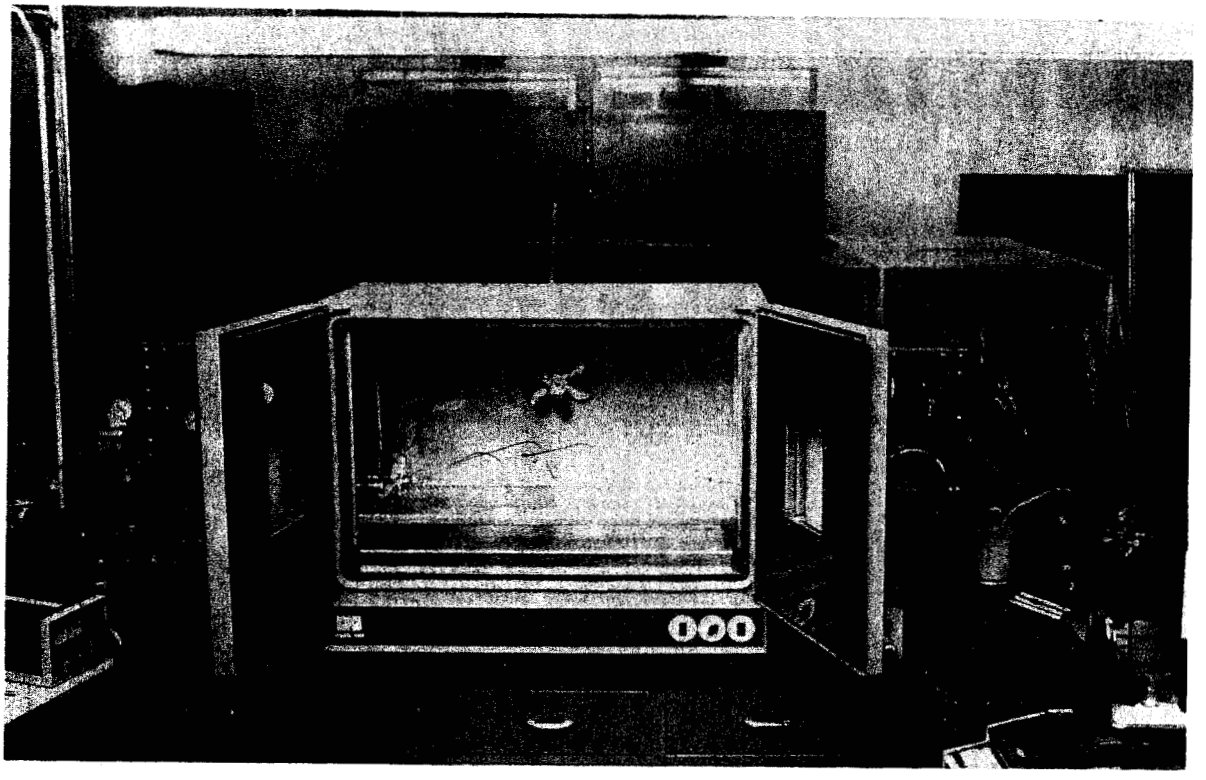

FIGURE 2 (b). PHOTOGRAPH OF APPARATUS.

Stanford Geothermal Program
Interdisciplinary Research
in Engineering and Earth Sciences
Stanford University
Stanford, California

A STUDY OF NON-ISOTHERMAL SINGLE AND TWO-PHASE FLOW THROUGH CONSOLIDATED SANDSTONES

by
Norio Arihara

November 1974

This research was carried out
under Research Grant GI-34925
by the National Science Foundation

This report was prepared originally as a dissertation submitted to the Department of Petroleum Engineering and the Committee on the Graduate Division of Stanford University in partial fulfillment of the requirements for the degree of Doctor of Philosophy.

ACKNOWLEDGEMENTS

The author would like to express his sincere appreciation to his adviser, Dr. Henry J. Ramey, Jr., for his instruction and guidance throughout this investigation. Dr. Ramey's encouragement will not be forgotten.

The author is deeply grateful to his friends, particularly Francis Cassé and Paul Atkinson, for their helpful. comments and timely help through the days of experimental work.

The construction of the equipment was aided by many persons. Stanford staff included Peter Gordon, Luke Meisenback, Frank Peters, and Alice Mansourian. Special thanks are due to Dr. Paul Baker and the Chevron Oil Field Research Company for advice concerning the liquid saturation probe design, and Dr. Stan Jones and the Marathon Oil Company for advice and help concerning the large Hassler-Sleeve core holder with pressure taps.

The author wishes to express his deepest gratitude to his wife, Michiko, for encouragement, devotion, and perseverance all through the graduate study years.

This research was carried out under Research Grant GI-34925 by the National Science Foundation. Financial aid from the National Science Foundation is hereby gratefully acknowledged.

ABSTRACT

The main purpose of this study was to investigate non-isothermal single and two-phase flow of a single component fluid (water) in consolidated porous media. Thus the two-phase flow was boiling water flow. To our knowledge, there has been only one study of non-isothermal boiling flow in an unconsolidated sand pack, although previous work on thermal oil recovery by hot fluid injection presents information useful for the present study.

Equipment was constructed to perform linear flow experiments through cylindrical consolidated cores. Both natural (Berea) and synthetic cement consolidated sand cores were used..

Successful fabrication of the synthetic sandstones was important to permit reproducible fabrication of high porosity, low permeability sandstones with thermowells, pressure ports, and glass tube capacitance probe guides cast in place.

Hot fluid injection and cold water injection experiments were carried out in both natural and synthetic sandstones. The overall heat transfer coefficient for the core holder was measured and compared with design calculations with good results. The steady-state overall heat

transfer coefficient was measured and found to depend on mass flow rate to a minor degree. The thermal efficiency of hot water and cold water injection was found to depend on heat injection rate: the higher the heat injection rate, the higher the thermal efficiency. This trend was also found by previous investigators for unconsolidated sands. One major result of this study is that much of the previous works with non-isothermal single phase flow in unconsolidated sands may be extended to consolidated sandstones despite significant differences in isothermal flow characteristics of these systems.

One unique system considered in this study was injection of cold fluid into an initially hot porous medium. This is analogous to heat scavenging on condensate reinjection in geothermal fluid production. It was discovered that the overall heat transfer coefficient depended on the process (hot or cold injection), and the novel concept of thermal efficiency of cold fluid injection was introduced. Results for cold water injection indicate that lower injection rate, or smaller temperature difference between the surroundings and injected water is advantageous for heat scavenging from the surroundings by cold water injection into the geothermal reservoir.

In two-phase boiling flow experiments, hot, compressed liquid water steadily entered the upstream end of the core, moved downstream a certain distance, started vaporizing, and

flowed through the remainder of the core as a mixture of steam and liquid water. Although beyond. the original objective for this phase of the project, boiling flow experimental data show that significant decreases in both temperature and pressure can occur within the two-phase region. Even when flow is very non-isothermal, two-phase flow can be isenthalpic and steady state, if heat transfer between the core and the surroundings is of a low level.

Finally, preliminary experiments were conducted with a capacitance probe liquid saturation detector, and liquid saturation calculations were performed for the boiling flow experiments.

TABLE OF CONTENTS

TABLE OF CONTENTS. CONTINUED

LIST OF FIGURES

LIST OF FIGURES, CONTINUED

LIST OF **FIGURES,** CONTINUED

LIST OF FIGURES, CONTINUED

LIST OF FIGURES, CONTINUED

LIST OF TABLES

INTRODUCTION

The public has begun to pay much attention to Geothermal Energy as a potential major new source of energy to be developed in the future. Prime considerations in geothermal energy extraction from underground sources would appear to be: 1) how much energy can be recovered; and 2) how fast can it be extracted? In order to find useful answers to these questions, the basic characteristics and behavior of the reservoir rocks and fluids in geothermal systems require investigation.

The present research was started with an objective to study the thermodynamic and fluidmechanic behavior of non-isothermal flow of single and two-phase, single-component fluids through consolidated porous media.

Published information on oil recovery by hot fluid injection and Underground combustion present some of the important features of non-isothermal, two-phase flow which appear pertinent to geothermal reservoirs. But there has been no specific study of the flow of single component (water) two-phase (thus non-isothermal) boiling flow in porous media. In view of the fact that all heat effects (sensible heat, latent heat of vaporization, etc.) are much greater for water than for hydrocarbons, it was expected that some severe anomalies might be found.

A bench-scale model was designed and constructed to permit a thorough examination of thermodynamic and fluid-mechanic aspects of the two-phase flow regime. In addition to this experiment, a variety of important peripheral experiments were accomplished with the same experimental apparatus. For example, cold water injection into a system initially containing hot water is a potentially practical operation for geothermal. heat scavenging from the rock matrix by condensate injection. Hot water injection into a system containing water at a lower temperature is also a useful peripheral experiment to aid comparison of the present studies with previous oil recovery work.

Much time was spent learning to create synthetic consolidated sandstones of specific desirable properties (high porosity, low permeability). Pertinent work in this area was reviewed as a subject of great importance to this field of study. Another major problem was determination of a reliable method of measurement of liquid saturation (pore volume fraction containing liquid phase) in the porous media over a range of temperature and pressure.

Finally, in order to aid understanding of mass and heat transfer through porous media, published theoretical and experimental results were reviewed, and a comprehensive survey was published.[43]

LITERATURE SURVEY

Although the study of application of reservoir engineering principles to geothermal energy is recent, there are many publications aimed at oil recovery by addition of heat to a reservoir which are useful in the present study. It should be clear that much of the following literature had a different objective for application than recovery of Geothermal Energy.

Hot Fluid Injection

The first significant study of heat transport in a formation caused by hot fluid injection was presented by Lauwerier[1] in 1955. Lauwerier assumed that injection rate, V_w, and temperature, T_i, would remain constant, the flow system was linear, thermal conductivity in the direction of flow was zero, and that the thermal conductivity in the flooded layer perpendicular to the direction of flow was infinite so that the temperature in the flooded layer was always uniform at a given location in the flooded zone. Sometimes this is called the "zero dimension" assumption in pipe flow. The conductivity in the overburden and underburden, λ_2, was assumed to be finite and constant. Thus loss of heat from the injected fluid to the adjacent strata would result in a decrease in temperature in the direction of flow.

With these assumptions, the problem to be solved was expressed by the following set of equations:

$$\text{for } |\eta| > 1 \qquad \theta \frac{\partial^2 T_2}{\partial \eta^2} = \frac{\partial T_2}{\partial \tau}$$

$$\text{for } |\eta| = 1 \qquad \begin{cases} \dfrac{\partial T_2}{\partial \tau} + \dfrac{\partial T_2}{\partial \xi} - \dfrac{\partial T_2}{\partial \eta} = 0 \\ T_1 = T_2 \end{cases} \tag{1}$$

$$\text{for } \tau = 0 \qquad T_1 = T_2 \begin{cases} T_i & \text{if } \xi < 0 \\ 0 & \text{if } \xi > 0 \end{cases}$$

where the different quantities are defined as follows:

$$\xi = \frac{\lambda_2}{b^2 \rho_w C_w V_w} x \qquad \tau = \frac{\lambda_2}{b^2 \rho_1 C_1} t$$

$$\theta = \frac{\rho_1 C_1}{\rho_2 C_2} \qquad \eta = \frac{y}{b}$$

x = distance in flow-direction

b = half the formation thickness.

Other symbols are defined in the nomenclature.

Applying sequential Laplace transformation with respect to the distance and the time variables, Lauwerier obtained the result:

$$T = T_i \operatorname{erfc} \left(\frac{\xi + |\eta| - 1}{2\sqrt{\theta(\tau - \xi)}} \right) \alpha(\tau - \xi) \tag{2}$$

where

$$\eta = \begin{cases} \frac{y}{b} \text{ for } |y| > b \\ 1 \text{ for } |y| < b \end{cases}$$

$$\alpha(\tau - \xi) = \begin{cases} 1 \text{ for } \tau \geq \xi \\ 0 \text{ for } \tau < \xi. \end{cases}$$

In 1959, Marx and Langenheim[2] presented a solution for a heat loss problem similar to the one considered by Lauwerier. Their report described a method for estimating thermal invasion rates, cumulative heated area and theoretical economic limits for sustained heat injection at a constant rate into a radial flow system. They assumed that heat injected at a constant rate H_o raised the temperature of the flooded zone to T_1 and maintained this temperature. Their heat balance led to the following:

$$H_o = 2\int_o^t \left[\frac{\lambda_2 \Delta T}{\sqrt{\pi D(t-\tau)}}\right]\left(\frac{dA}{d\tau}\right)d\tau + 2\rho_1 C_1 b \Delta T \frac{dA}{dt} \qquad (3)$$

where $\Delta T = T_1 - T_o$.

This equation is an application of an earlier equation for estimating the extent of the fractured area in hydraulic fracturing derived by Carter.' In the growing hydraulic fracture problem, the fracture was assumed to be of uniform width, and the pressure in the fracture was assumed to be constant and equal to the sand face injection pressure. Because the fracture had no flow resistance, the assumption of a constant pressure in the

fracture was reasonable in spite of the fact that fluid leaks from the fracture into the formation. On the other hand, Ramey[4] pointed out that the constant elevated temperature in the flooded region assumed by Marx and Langenheim should be realistic only in the case that the heat injection medium is steam or other condensible gases near the boiling point at the injection pressure. In order to have a temperature maintained at the same level in the flooded zone, a small pressure gradient in the direction of flow is also required. Steam at the boiling point tends to follow the saturation curve requiring that temperature decreases as pressure decreases.

In Eq. 3, the first term on the right represents the flux of the heat **loss** from the injected fluid into the overburden and underburden, and the second term represents the rate at which the amount of heat remaining in the pay zone is increased. The flux **of** the heat **loss** can be derived easily in the same way as Churchill[5] described. Eq. 3 can be solved for the heated area A(t) (as Carter solved the same type of equation) by utilizing the Laplace transform method. The result of Marx and Langenheim **is:**

$$A(t) = \frac{H_o \rho_1 C_1 b D}{2\lambda_2^2 \Delta T} \left[e^{\tau^2} \operatorname{erfc} \tau + \frac{2\tau}{\sqrt{\pi}} - 1 \right] \qquad (4)$$

where $\tau = \frac{\lambda_2}{\rho_1 C_1 b} \sqrt{\frac{t}{D}}$.

Ramey[4] indicated several important points with regard to the mathematical model of Marx and Langenheim:

1. No restriction is placed on the direction of development of the heated area (may be linear, radial, or any two-dimensional geometry);

2. It is not necessary that the heat injection rate be constant;

3. The solution could provide useful information for heat injection in any type of well pattern with any specified swept area data.

Ramey presented results for a heat injection rate, H, as a function of time:

$$A(t) = \left(\frac{H(t)}{2\rho_1 C_1 b \Delta T}\right) * (e^{\tau^2} \operatorname{erfc} \tau). \tag{5}$$

The symbol, *, represents the convolution of two functions, or:

$$F_1(t) * F_2(t) = \int_0^t F_1(\tau) F_2(t - \tau) d\tau \tag{6}$$

$$= \int_0^t F_1(t - \tau) F_2(\tau) d\tau$$

Another expression of A(t) presented by Ramey is useful when the heat injection rate has constant values for increments of time such that

$$H = H_1 \text{ for } 0 \leq t < t_1$$

$$H_2 \text{ for } t_1 \leq t < t_2$$

H_n for $t_{n-1} \leq t < t_n$

Then, the heated area at time t results in:

$$A(t) = \frac{\rho_1 C_1 b D}{2\lambda_2 \Delta T} \left[H_n \left(e^{\tau_n^2} \operatorname{erfc} \tau_n + \frac{2\tau_n}{\sqrt{\pi}} - 1 \right) + \sum_{m=1}^{n-1} (H_m - H_{m+1}) \left(e^{\tau_m^2} \operatorname{erfc} \tau_m + \frac{2\tau_m}{\sqrt{\pi}} - 1 \right) \right] \tag{7}$$

Heat stored in the flooded formation, H_s, at time t can be calculated by the volume integral:

$$H_s = \int_V \rho_1 C_1 [T_1 - T_o] dV \tag{8}$$

where T_o is initial temperature of the formation. Heat injected to time t is:

$$H_i = \int_o^t q \rho_w C_w (T_i - T_o) dt \tag{9}$$

The thermal efficiency, E, is defined as the fraction of the cumulative heat injected remaining in the injection interval:

$$E = \frac{H_s}{H_i} \tag{10}$$

Rubinshtein' introduced the idea of the fraction of the total heat injected lost to adjacent strata, $W_o^* = 1 - E$. It is remarkable that Ramey[6] found the identical heat loss results for the Lauwerier model and the Marx-Langenheim models as follows:

$$1 - W_o^* = E = \frac{\theta}{\tau} \left[e^{\tau/\theta} \operatorname{erfc} \sqrt{\frac{\tau}{\theta}} - 1 + 2\sqrt{\frac{\tau}{\theta \pi}} \right] \tag{11}$$

The equal thermal efficiency results apparently because the Lauwerier heat model yields a larger heated area at a lower average temperature, while the Marx-Langenheim heat model yields a smaller heated area at a higher temperature.

In the 1959 study, Rubinshtein also presented the thermal efficiency for a radial flow model of hot water injection with fewer assumptions than used previously by Lauwerier. Rubinshtein assumed constant isotropic thermal conductivities in the flow layer and in the impermeable strata surrounding the reservoir, and obtained:

$$E = 1 - (1 - \beta)\left\{\frac{2}{3}\sqrt{\frac{\gamma\tau}{\pi}}\left[1 - (1 - \beta)\sum_{n=1}^{m}\beta^{n-1}\left(1 + \frac{n^2}{\gamma\tau}\right)e^{-n^2/\gamma\tau}\right]\right.$$

$$\left. + (1 - \beta)\sum_{n-1}^{\infty} n\beta^{n-1}\left(1 + \frac{2n^2}{3\gamma\tau}\right)\operatorname{erfc}\frac{n}{\sqrt{\gamma\tau}}\right\} \qquad (12)$$

where

$$\beta = \frac{\gamma a - 1}{\gamma a + 1}$$

$$\gamma = \frac{\lambda_1}{\lambda_2}$$

$$a^2 = \frac{\lambda_2\rho_1 C_1}{\lambda_1\rho_2 C_2}$$

In the case $\gamma = a = 1$, Ramey showed the following expression:

$$E = 1 - \left\{\frac{2}{3}\sqrt{\frac{\tau}{\pi}}\left[1 - \left(1 + \frac{1}{\tau}\right)e^{-1/\tau}\right] + \left(1 + \frac{2}{3\tau}\right)\operatorname{erfc}\frac{1}{\sqrt{\tau}}\right\} \qquad (13)$$

Although Rubinshtein did not solve for temperature distributions, Spillette[8] solved numerically the energy balance equation with the same assumptions as Rubinshtein. According to Spillette's calculation, the primary effects of including horizontal heat conduction in the analysis are the lowering of the calculated sand temperatures near the point of injection and the propagation of injected energy further into the reservoir.

Baker[9,10,11] accomplished a series of experimental studies of heat transfer in hot fluid injection with a radial flow model. Initially, he studied displacement of cold water by hot water. First, he carried out hot water injection, and obtained radial temperature distributions which were in good agreement with theoretical results given by Lauwerier, Ramey, and Spillette. Thermal efficiency was calculated numerically with experimentally measured values of temperature. Baker observed that higher thermal efficiencies were obtained at higher rates of heat injection. For steam injection, Baker found that thermal efficiency decreased with cumulative injected heat, and that the heating process was more efficient at higher heat injection rates. But surprisingly, he obtained the result that thermal efficiency was a function of dimensionless time, $\alpha t/h^2$, alone. This contradicted his previous hot water injection studies.

Crichlow[12] also found rate sensitivity of thermal efficiency in hot fluid injection experiments, although results for steam injection were not consistent. He explained thermal efficiency dependence on flow rate by the presence of a film coefficient at the boundary between the pay zone and the surroundings.

According to Crichlow, this effect was significant at flow rates much higher than those normally encountered in oil reservoirs.

In 1969, Prats[13] analyzed the thermal efficiency for thermal recovery processes. He employed the same analytical method as Marx and Langenheim, but introduced far greater generality. His heat balance equation is:

$$Q(t) = \frac{dH(t)}{dt} + 2 \int_{-\infty}^{\infty} \int_{-\infty}^{\infty} U_{hz}(x, y, o, t)dxdy \qquad (14)$$

where

$Q(t)$ = net rate of heat injected

$H(t)$ = heat stored in the pay zone

$U_{hz}(x, y, z, t)$ = heat flux in the vertical direction and $z=0$ is the interface plane between the pay zone and the adjacent zone.

Eq. 14 is essentially the same as Eq. 3 of Marx and Langenheim. Prats divided the heat storage in the formation into two parts: heat in the pay zone near to and far from the injection well:

$$H(t) = H_n(t) + H_f(t).$$

Eq. 14 was solved by the Laplace transform method.

$$H(t) = \int_o^t Q(t')K(\theta_n\sqrt{t - t'})dt' - F \int_o^t H_f(t')\frac{d}{dt} K(\theta_n\sqrt{t - t'})dt' \qquad (15)$$

where

$$K(z) = e^{z^2} \text{ erfc } z$$

$$\theta_n = \frac{\lambda_{h2z}}{b\sqrt{\alpha_2}(\rho C)_n}$$

$$F = \frac{(\rho C)_f - (\rho C)_n}{(\rho C)_f}.$$

For hot water injection at constant heat injection rate and assuming F = 0, Prats obtained a thermal efficiency expression which is identical with Eq. 11 presented by Ramey for the models of Lauwerier, and Marx and Langenheim. An important contribution of Prats lies in the estimate of the thermal efficiency for steam injection. In steam flooding there is a steam zone near the injection well, and hot water zone outside the steam region. Understanding that the parameter F is generally positive, he developed lower and upper bounds for the thermal efficiency. Other interesting studies of thermal efficiency for steam injection may be found in references 44 and 45.

Two-Phase Flow

Although much analytical and experimental work has been done in the study of oil recovery by steam injection and hot water injection, there has been no specific study of non-isothermal boiling two-phase flow of water through porous media to our knowledge. In 1951, Miller[14] presented experimental results and analysis of single-component boiling two-phase flow of propane. His report gives broad information and instruction about in-phase boiling flow experiments, although there are large differences in the thermodynamic and physical properties

of water and propane. Miller performed laboratory experiments with specially designed apparatus to have adiabatic, two-phase, steady flow of propane through a horizontal column of sand. His flow tube was five feet long, and was constructed from six lengths of pipe, connected together by flanges. Between the flanges of the adjoining sections, blind flanges were used to which manometer lines and thermocouple lead wires were connected. In order to have an adiabatic condition, the flow tube as a whole was placed inside a circular, compartmented air duct, which provided means for fixing the temperature distribution in the air along the outside of the flow tube to correspond to the temperature distribution of the flowing propane inside the tube. After adiabatic and steady-flow conditions were attained, no appreciable heat transfer across the walls of the flow tube existed. In all the experiments, the propane entered the column entirely as a liquid, started to vaporize at an appreciable distance downstream from the inlet, and then flowed in two phases throughout the remainder of the column. Temperature and pressure distributions and the total mass rate of flow were measured.

The problem posed by Miller was to calculate the total mass rate of flow and pressure distribution along the column of sand, for a given pressure and temperature of the liquid entering stream, a given pressure or temperature of the discharging gas-liquid mixture, and given sand and fluid characteristics.

According to his method of analysis, he started with the following mass and energy equations for steady, two-phase, adiabatic flow:

$$\dot{m}_g + \dot{m}_\ell = \dot{m} = \text{constant} \tag{16}$$

$$\dot{m}_g h_g + \dot{m}_\ell h_\ell = \dot{m} h = \text{constant} \tag{17}$$

where $\dot{m}$, $\dot{m}_g$, $\dot{m}_\ell$ are total mass rate of flow, mass rates of steam and water respectively, and h, h_g, h_ℓ are the enthalpy of a two-phase mixture of steam and of water, respectively. Introducing the mass fraction of steam as:

$$f = \frac{\dot{m}_g}{\dot{m}} \tag{18}$$

the energy equation becomes:

$$(1 - f)h_\ell + fh_g = h. \tag{19}$$

Hence:

$$f = \frac{h - h_\ell}{h_g - h_\ell}. \tag{20}$$

From Darcy's law, the mass rate of flow of each phase is given as:

$$\dot{m}_g = -\frac{A\rho_g k_g}{\mu_g}\left(\frac{dp_g}{dx}\right), \qquad \dot{m}_\ell = -\frac{A\rho_\ell k_\ell}{\mu_\ell}\left(\frac{dp_\ell}{dx}\right) \tag{21}$$

if capillary pressure between vapor and liquid is neglected, Eqs. 21 become

$$\frac{m_\ell}{\dot{m}_g} = \frac{k_\ell \rho_\ell \mu_g}{k_g \rho_g \mu_\ell} = \frac{1 - f}{f} \tag{22}$$

where k, μ, and ρ are permeability, viscosity and density, respectively, and the subscripts g and ℓ pertain to steam and liquid phases, respectively. Finally

$$\frac{k_\ell}{k_g} = \frac{\mu_\ell \rho_g}{\mu_g \rho_\ell}\left(\frac{1 - f}{f}\right) = \frac{\mu_\ell}{\mu_g}\frac{\rho_g}{\rho_\ell}\left(\frac{h_g - h}{h - h_\ell}\right). \tag{23}$$

Because t mperature is a function of pressure in the two-phase flow region, the permeability ratio given by Eq. 23 may be computed by specifying pressure only. Then, Miller calculated the individual relative permeabilities by assuming that the correlation between k_ℓ/k and k_ℓ/k_g presented by Muskat, et al.,[22] was valid for his case. The total mass rate of flow and the pressure distribution were obtained simply by numerical integration:

$$\dot{m}\, x = Ak \int_p^{p_i} \left(\frac{\rho_\ell k_\ell/k}{\mu_\ell} + \frac{\rho_g k_g/k}{\mu_g}\right) dp \tag{24}$$

where p_i and p are fluid pressures at the upstream and **of** the column, and at a distance x from the inlet face, respectively. Because a remarkable agreement between experimental results and analytical theory was obtained, Miller concluded that phase equilibrium was attained very rapidly under the conditions of his experiment.

Luikov[15] described mathematically the heat and mass transfer phenomenon of vapor-liquid mixtures in capillary-porous bodies. He considered that the transfer of vapor took place by molecular means in the form of diffusion and by molar means by a convective motion due to a pressure drop, and that liquid transfer took place by means of diffusion, capillary absorption and convective motion. In the following description, the properties in vapor form are denoted by suffix g, in liquid form by ℓ, and **of** solid by 0.

The differential equation for mass transfer of steam or liquid is:

$$\frac{\partial \omega_i}{\partial t} = - \text{div } j_i + I_i \qquad i = g, Q \tag{25}$$

where ω_i is the volumetric concentration or mass per unit bulk core volume, j_i is the mass rate of the motor-molecular transfer flow, I_i is the volumetric capacity of the source (or sink) of phase i and $I_g = -I_{\ell}$. The volumetric concentration can be expressed as:

$$\omega_i = \frac{m_i}{V} = \rho_i \phi S_i \tag{26}$$

where m_i, V, ρ_i, ϕ, and S_i are mass, bulk volume of the porous medium, density, porosity, and saturation, respectively. Introducing the relative concentration u_i as:

$$u_i = \frac{m_i}{m_\Theta} = \frac{\omega_i}{\gamma_o} \tag{27}$$

where γ_o is the density of the dry core (mass of sand per unit bulk volume), the mass transfer equation becomes:

$$\frac{\partial (\gamma_o u_i)}{\partial t} = - \text{div } j_i + I_i \tag{28}$$

and

$$\frac{\partial (\gamma_o u)}{\partial t} = - \text{div } (j_g + j_\ell) \tag{28}$$

where $u = u_g + u_\ell$. The differential equation for heat transfer is obtained from th equation for internal energy transfer. At constant pressure, the local derivative of volumetric concentra-

tion of the enthalpy of the system is equal to the divergence of the flow of enthalpy:

$$\frac{\partial}{\partial t}\left(h_o\gamma_o + h_g\gamma_o u_g + h_\ell\gamma_o u_\ell\right) = -\operatorname{div}(j_q + h_g j_g + h_\ell j_\ell) \tag{30}$$

where h_i is the specific enthalpy, and j_q is the density of the molecular flow of energy, or heat flux. j_q contains not only the specific flow of heat caused by the drop in temperature, but also heat transfer by means of diffusion of mass. The isobaric specific heat is denoted by C_i:

$$C_i = \left(\frac{\partial h_i}{\partial T}\right)_p.$$

Then $C\gamma_o \frac{\partial T}{\partial t} = -\operatorname{div} j_q - (h_g I_g + h_\ell I_\ell) - (C_g j_g + C_\ell j_\ell)\nabla T$ (31)

where

$$C\gamma_o = (C_o u_o + C_g u_g + C_\ell u_\ell)\gamma_o$$

$$= C_o\rho_o(1 - \phi) + C_g\rho_g\phi S_g + C_\ell\rho_\ell\phi S_\ell.$$

Since $I_g = -I_\ell$, Eq. 31 becomes

$$C\gamma_o \frac{\partial T}{\partial t} = -\operatorname{div} j_q - h_{fg} I_g - (C_g j_g + C_\ell j_\ell)\nabla T \tag{32}$$

where $h_{fg} = h_g - h_\ell$.

Assuming that vapor is in thermodynamic equilibrium with the bound liquid, the vapor pressure is that of the saturated vapor, p_s, and thus is a single-valued function of temperature:

$$p_g = p_s = f(T). \tag{33}$$

Then, Luikov derived the equations of mass transfer through porous media on the basis of molecular and molar transfer mechanisms.

Steam flow by diffusion can be stated as:

$$j_{mg} = - \varepsilon D \frac{d\rho_{go}}{dT} \nabla T$$

$$= - a_{mg} \gamma_o \delta_g \nabla T \qquad (34)$$

where

$$\frac{d\rho_{go}}{dT} = \frac{M_g}{M_p} \frac{dp_s}{dt} .$$

In Eq. 34, εD is the coefficient of steam diffusion within the porous medium, $\rho_{go} = \rho_g/\rho$, M_g is the molecular weight of steam, M is the mean molecular weight of the mixture, $a_{mg} = \frac{\varepsilon D \rho}{\gamma_o}$, and $\delta_g = \frac{d\rho_{go}}{dT}$.

For liquid transfer by means of diffusion and capillary absorption:

$$j_{m\ell} = -a_{m\ell} \gamma_o [\nabla u + \delta_\ell \nabla T] \qquad (35)$$

where $a_{m\ell}$ is the liquid diffusion coefficient, and δ_ℓ is the thermal gradient coefficient of the liquid. Hence,

$$j_m = j_{mg} + j_{m\ell} = -a_m \gamma_o (\nabla u + \delta \nabla T) \qquad (36)$$

where $a_m = a_{m\ell}$ and

$$\delta = \frac{a_{m\ell} \delta_\ell + a_m \delta_g}{a_{m\ell}}$$

The molar transfer of steam and liquid water due to a gradient of the total pressure, VP, is described by Darcy's law:

$$\frac{\rho_{\sim} k}{} \nabla p = - \lambda_{p\sim} \nabla p$$

$$j_{p\ell} = - \lambda_{p\ell} \nabla p$$

Therefore $$j_p - j_{pg} + j_{p\ell} = \lambda_p \nabla p \qquad (37)$$

where λ_p ($= \lambda_{pg} + \lambda_p$) is the coefficient of filtration transfer of the mixture.

The total mixture flow caused by the influence of all the transfer forces is equal to:

$$j = - a_m \gamma_o (\nabla u + \delta \nabla T + \delta_p \nabla p) \qquad (38)$$

where $\delta_p = \frac{\lambda p}{a_m \gamma_o}$

Heat transfer by conduction is described by Fourier's law:

$$j_q = \text{XVT}$$

where is the total coefficient of thermal conductivity of the porous medium and mixture of steam and water. Thus the system of differential equations of mass and heat transfer can be written in the form:

$$\frac{\partial u}{\partial t} = \text{div}[a_m (\nabla u + \delta \nabla T + \delta_p \nabla p)] \qquad (39)$$

$$C\gamma_o \frac{\partial T}{\partial t} = \text{div}(\lambda \nabla T) - h_{fg} I_g + a_{m\ell}\gamma_o C_\ell V u \cdot \nabla T$$

$$+ (\lambda_{pg} C_g + \lambda_{p\ell} C_\ell) \nabla p \cdot \nabla T \qquad (40)$$

$$+ (a_{mg}\gamma_o \delta_g C_g + a_{m\ell}\gamma_o \delta_\ell C_\ell)(\nabla T)^2$$

$$P = P_s = f(T).$$

In most mathematical models, mass and heat transfer due to diffusion and capillary absorption are neglected, thus Eqs. 39 and 40 become simpler, but are still highly nonlinear. Reference [16] reports solution of these mass and heat transfer equations simultaneously in a model study of a transient flow system.

In the Petroleum Engineering literature, there has been a significant amount of work presented on the simulation of thermal oil recovery processes which involve steam injection. Among them, the works of Coats, et al.,[17] and Weinstein, et al.,[18] are comprehensive, and directly applicable to the present study of two-phase boiling flow of water. Although the solution techniques of Coats, et al., and Weinstein, et al., are completely different, both solved the same mass and energy transport equations simultaneously, including interphase mass transfer accounting for steam condensation.

Synthetic Sandstone

Although unconsolidated sand packs have often been used as porous media for laboratory studies, natural sandstone or artificially-cemented sandstone of properties similar to natural sandstone is more desirable to simulate natural reservoir

conditions. Synthetic sandstone is more favorable when sandstone of a special shape, or specific characteristics (porosity, permeability) are needed.

Wygal[19] showed that a process of artificial cementation could be used to change unconsolidated packs into synthetic sandstones having properties similar to those of natural rock, especially in terms of the drainage and imbibition relative permeabilities. A core was made of 5 weight per cent cement and 95 weight per cent of 70-80 mesh sand. Wygal also described in detail a technique for the construction of synthetic rock as follows:

1. Mix the sand with about 0.5 weight per cent of blending water.

2. Coat the dampened sand grains with the dry cement.

3. Pour the mixture into the container continuously through a particle distributor of wire mesh.

4. Inject water at a rate such that imbibition forces are dominant.

5. Allow the cement to hydrate for an appropriate time.

Heath[10] employed Wygal's technique, and presented the results obtained by changing some factors which affect the porosity and permeability of synthetic sandstones. According to Heath, the main factors and their effects are as follows:

1. Sand grain size -- Permeability increases with grain size for a given porosity. To obtain low porosity, it is necessary to c mbine two sizes at a grain-diameter ratio of about 6:1, and at a weight ratio of large grains to small grains of about 3:1.

2. Blending water -- More water increases both porosity and permeability.

3. Cement -- Both porosity and permeability decrease with increasing amount of cement.

Evers, et al.,[21] prepared sandstone of very low permeability to meet the requirements for their scaled model. Their method is different from Wygal's technique. Instead of injecting water into a dry mix of sand and cement in the container, Evers, et al., tamped a wet mortar into mold. The resultant permeabilities (ranging from 0.016 millidarcies to 0.162 millidarcies) and porosities (ranging from 10% to 18%) were obtained from mixtures of sand and cement for water-cement ratios of 0.30 to 0.40: sand.-cement ratios in the range of 1/1 to 2/1; and sand grain size from 100-200 to 12-18 mesh.

Saturation Measurement

The word "saturation" may be used in many ways in non-isothermal boiling flow in porous media. It can refer to steam and liquid water in equilibrium, to saturation of a solvent with a solute, or to the volume fraction of pore space which is filled with a given fluid phase such as oil, water, or gas. It is the latter sense that will be used in the following.

Means of measuring liquid pore space saturation which have received consideration include: electrical conductivity of the fluids; emissions from radioactive tracers dissolved in the fluids: the radioactivity of silver or rhodium caused by reflection of neutrons from hydrogen atoms in the fluids: the attenuation of a microwave beam: the diminution and phase shift of ultrasonic

wave trains; the reduction in intensity of x-ray beams in passing through fluids, and magnetic reluctance.

Musket, et al.,[22] and Botset[23] utilized piezometer rings which served as both electrodes and pressure taps. The piezometer rings were separated by insulating tubes forming portions of the flow tube. Connecting any two adjoining electrodes to an a.c. bridge, the average conductivity and thus liquid saturation between the two electrodes could be measured. They succeeded in measuring the saturation distribution in the flow system of water and CO_2 gas.

Neutrons are particles with no electric charge and with a mass approximately equal to that of a proton, the nucleus of the hydrogen atom, When a fast neutron is scattered by a hydrogen nucleus, it may lose any fraction of its kinetic energy. In the average collision, it loses one half its kinetic energy. All common elements other than hydrogen are so much heavier that a neutron will lose only a small fraction of its energy in a single elastic collision. The number of slow neutrons emerging from an object irradiated by fast neutrons, therefore, yields a rough index of the quantity of hydrogen it contains. Brunner and Mardock[24] used this neutron-scattering method to measure oil saturation in porous media. The neutron source was an intimate mixture of radium and beryllium. In order to measure the flux of slow neutrons, they found rhodium to be the most satisfactory. When slow neutrons strike rhodium, they induce radioactivity (mainly beta) which a Geiger-Mueller counter can detect. Brunner and Mardock presented a calibration curve for an unconsolidated sand pack showing number of counts vs. oil saturation, and also

the saturation distribution along the length of a core. Because this method detects the concentration of hydrogen atoms, it is also applicable to a water-steam flow system, because the mass of the water phase is dominant in the mixture; therefore, slow neutrons should indicate the liquid saturation.

Finnemore and Schaaf[25] reported the design considerations and the procedures for the use of a gamma-ray attenuation system designed to measure the moisture content of a soil in either a transient or a static condition. Their system consisted of a 220 mc cesium 137 source, sodium iodide crystal detector, pulse amplifier and analyzer, and scaler. They found that the following attenuation equation was appropriate:

$$N_w = N_d\, e^{-U_w WL} \quad \text{or} \quad W = \frac{1}{U_w L}\, \ell n\, \frac{N_d}{N_w}$$

where

N_w = count reading for wet soil

N_d = count reading for dry soil

U_w = the total linear attenuation coefficient of water

W = volume fraction of bulk volume occupied by moisture

L = thickness of the soil column.

Schaaf[26] utilized the gamma-ray attenuation system to determine moisture content at various spatial and temporal locations in an unsteady, unsaturated flow from a horizontal cylindrical source into porous media.

Baker[11] developed a capacitance probe which utilized the difference in dielectric constant between steam and hot water in a porous media. The instrument consisted of a probe which could be moved in a glass guide in a sand pack, a driving mechanism for the probe, electronic circuitry, and a recorder. Details of construction of the probe, and two diagrams of the electrical circuit are shown in Appendix C. As can be seen in the figures describing the probe and the probe circuitry, the probe is essentially a capacitor in an oscillator circuit whose resonant frequency changes with the changing capacitance of the probe. The probe is a silver-plated glass tube at the center of which a brass rod with a piece of closed copper tube at the end is held by Teflon spacers. The sensitive part of the probe is a small gap between the silver-coated glass tube and the copper tube. Therefore, most of the capacitance is fixed. When the probe is traversed in the glass guide in the sand pack, an electric field reaches outside the guide, and has different intensity according to the dielectric constant of the medium surrounding the glass guide. The frequency difference between the oscillator including the capacitance probe and a standard oscillator is detected and amplified. For recording, the circuit in Fig. C-3 was used to obtain a d.c. voltage whose magnitude was proportional to the frequency difference. Baker found the probe to work satisfactorily at room temperature with oil and water, gas and water, oil and alcohol, and other two-phase, two-component systems. Baker presented the saturation distributions given by the probe during his steam flooding experiments. Although he did not calibrate his probe at elevated temperatures, the data showed good

agreement with the average water saturation, and the steam front location. This method appeared best suited for the subject study.

The energy in an x-ray beam that has passed through an absorbing material is expressed by the following formula:

$$E = E_o \, e^{-\mu cd}$$

where E_o is the energy in the incident beam, μ is the mass absorption coefficient, c is the density or concentration of absorbing material, and d is the length of path of the beam in the absorber. Because every material has a different power to absorb x-rays, the reduction in intensity of an x-ray beam as it passes through a core depends on the fluids present. The beam emerging from the core can be measured as ionic current flowing across an air-filled ionization chamber. Morgan, et al.,[27] presented water saturation distributions detected by X-ray absorption along the length of cores subjected to gas drives.

EXPERIMENTAL EQUIPMENT

A schematic diagram of the completed apparatus is shown in Fig. 1, and photographs of the apparatus are shown in Fig. 2 (a) and (b). Referring to the flow diagram in Fig. 1, cold feed water is pumped through a tubular furnace and into a core contained in a Hassler sleeve core holder. The core holder is contained within an air bath used to set ambient temperatures as high as 410°F. An accumulator is located immediately downstream of the pump to eliminate flow pulsations. The accumulator is a diaphragm type with nitrogen pressure above the diaphragm. The nitrogen source can also be used to hold pressure on the Viton sleeve in the Hassler core holder.

Flow rate is measured both upstream and downstream of the core. A flowrator is upstream of the core, while the total mass rate can be determined by timed weighing of the cooled water from the outflow of the system. Both regulating and metering valves are used to adjust the back pressure and flow rate. Helicoid pressure gages are installed on each side of the core. Porous metal filters (60 micron elements) are located before the tubular furnace, and before the back-pressure valve. The main flow line is 1/4 inch O.D. stainless steel tubing, and other lines are 1/8 inch O.D. stainless steel tubing. All fittings, valves, filters,

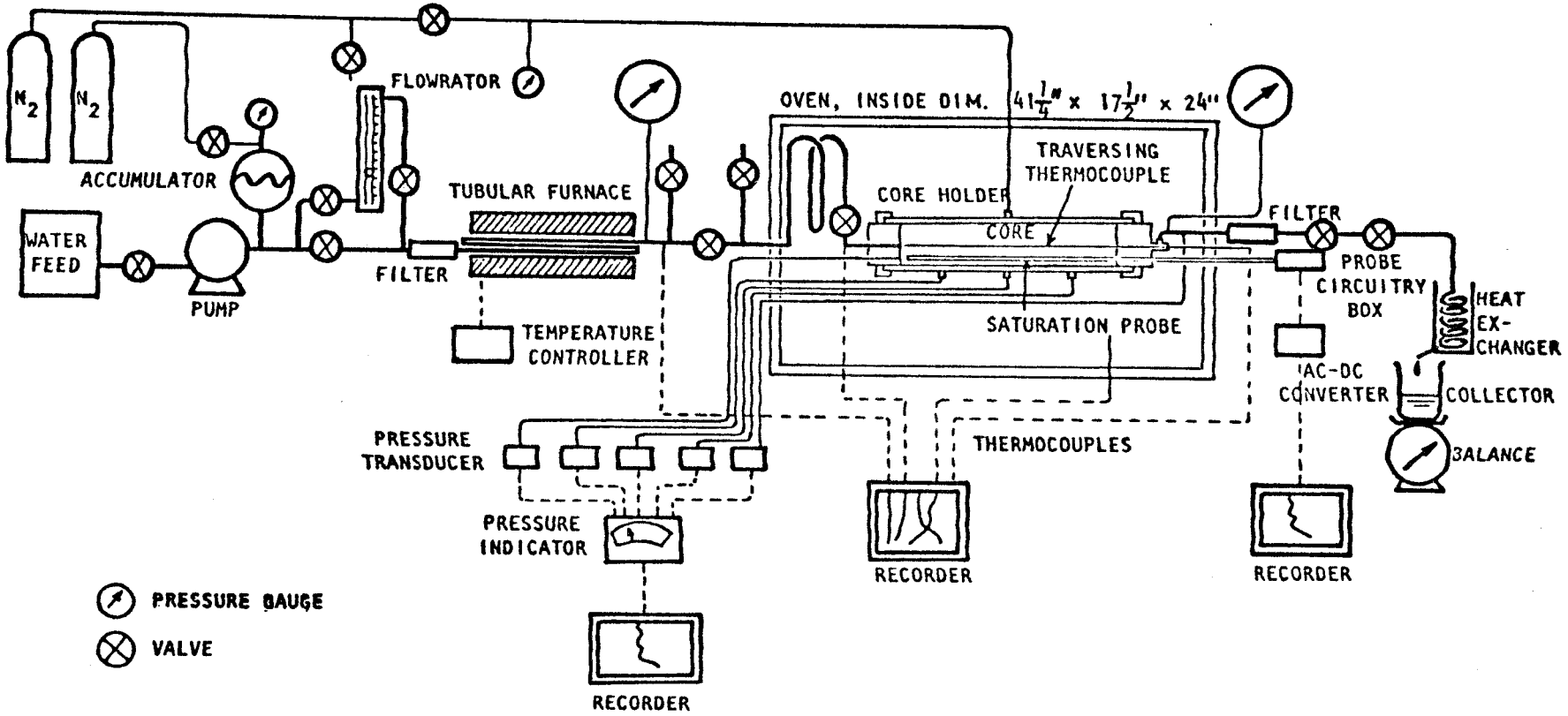

FIGURE 1. SCHEMATIC DIAGRAM OF APPARATUS

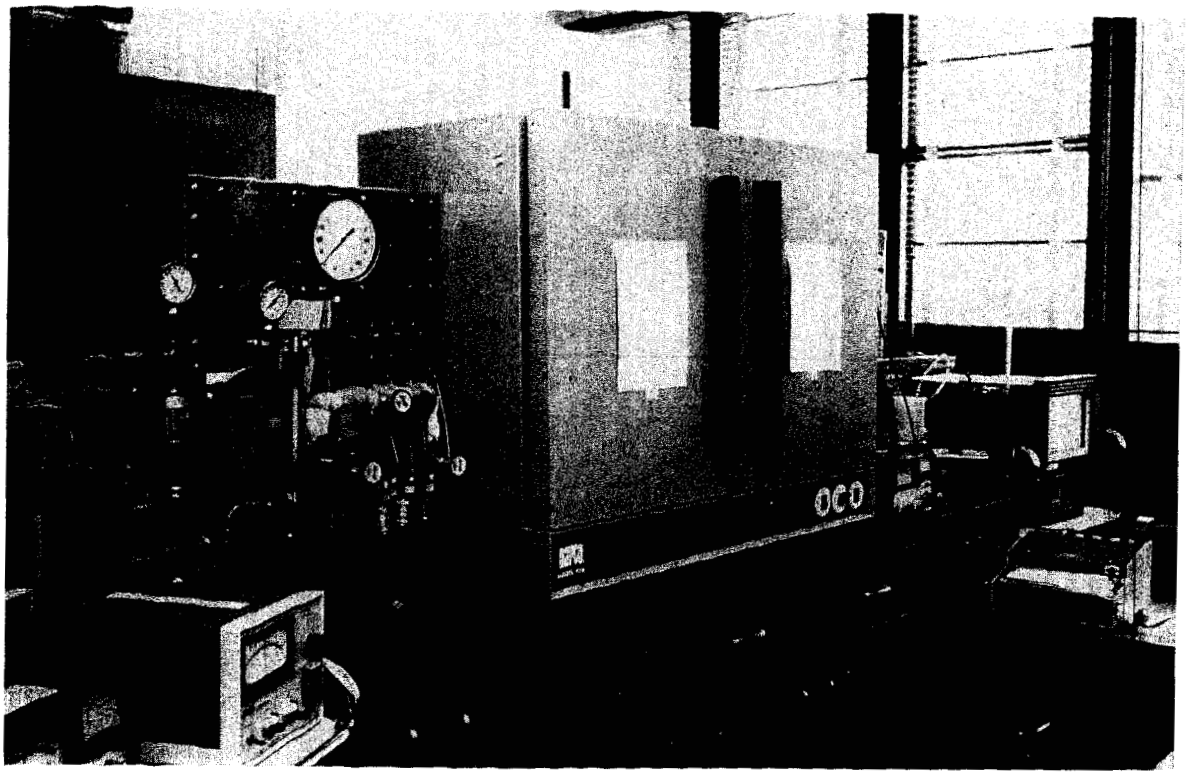

FIGURE 2 (a). PHOTOGRAPH OF APPARATUS.

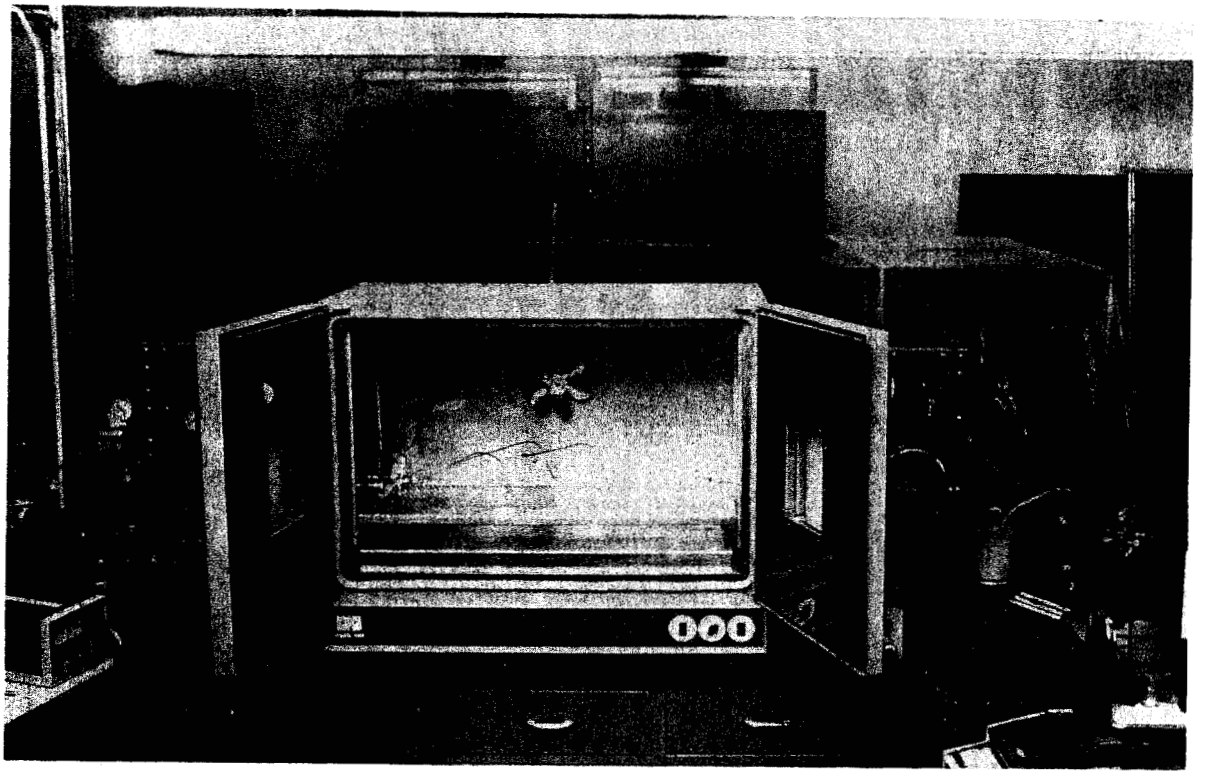

FIGURE 2 (b). PHOTOGRAPH OF APPARATUS.

and gages are stainless steel.

The temperature of the flowing fluid is measured after the tubular furnace, at the core inlet and exit, and throughout the entire length of the core via a traversing thermocouple. The traversing thermocouple is a 1/25 inch diameter sheathed thermocouple inside a 1/16 inch O.D. stainless steel tubing. All temperatures are recorded on a Leeds & Northrup Speedomax W, 24 points recorder. In addition to temperature, pressures are measured at the inlet and outlet of the core, and at three locations along the core by means of pressure transducers.

A detailed description of the major equipment components is as follows.

Core Holder

A modification of a Hassler-type core holder designed by the Marathon Oil Company (Jones[28]) was employed. Fig. 3 shows a detailed drawing of the core holder. The core holder consists of an outer shell, the Viton tubing, and several end pieces. The shell is 26 inches long by 3.5 inches O.D. with a 0.438 inch wall thickness. The shell has four entry ports or taps: one for the overburden pressure, and three for pressure measurements at intervals of 6 inches along the core. Obviously, more pressure taps may be used. The Viton tubing is 26 inches long by 2.5 inches O.D., and 0.25 inch wall thickness. The inlet parts are an inlet plug, a compression ring, and a cap. The cap

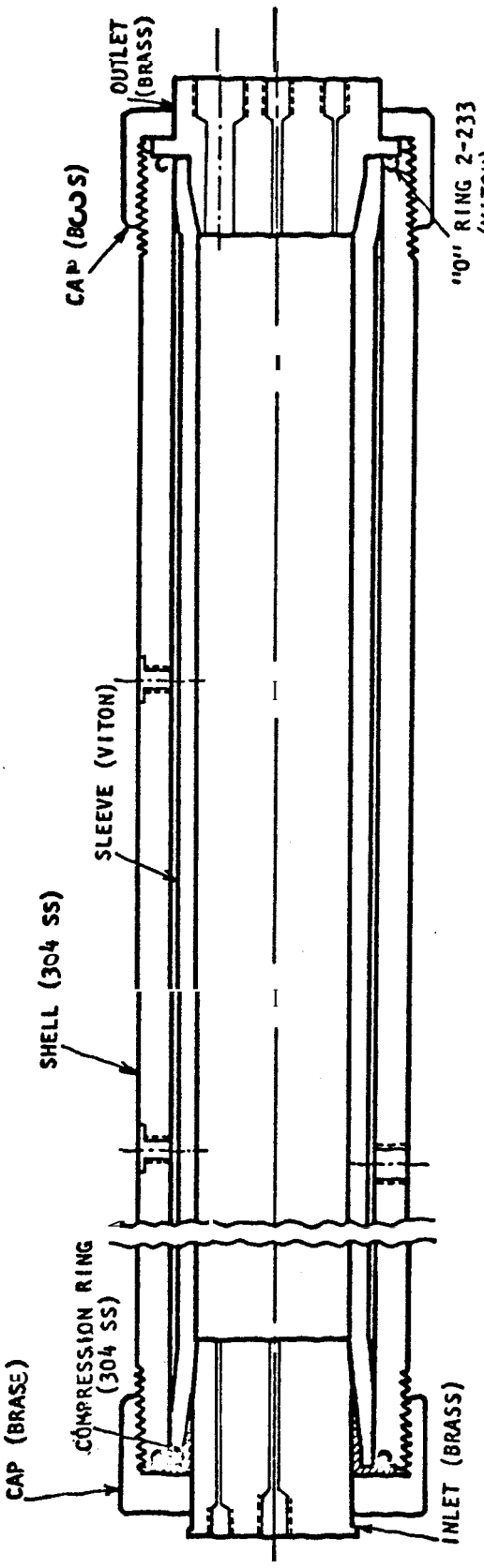

FIGURE 3. CORE HOLDER

holds the compression ring tightly against an O-ring. The inlet plug is adjustable so that the inside face may make good contact with the core. The inlet plug has taps for inlet flow and pressure measurement. The outlet plug has taps for exit flow, a pressure tap, and a hole through which the guide tubing for the saturation probe passes. A thermocouple well for the traversing sheathed thermocouple passes through the tap for exit flow, and through a heat exchanger type Swagelock fitting as shown in Fig. 4. The materials used in the core holder are 304 stainless steel for the outer shell and the compression ring, and brass for the other parts. The core holder and end plugs are secured by end plates and four tie rods. Fig. 5 shows the core holder assembly in the air bath.

Oven

An air bath with a working space of 42 inches by 18 inches with 24 inches height was used to house the 28-inch long core holder. Air circulation is provided by a fan, and the oven is equipped with windows. It takes about two hours to reach a uniform elevated temperature with the core holder and a water-saturated core. Use of the multi-channel recorder allows monitoring several points in the system to assure that an isothermal condition is attained prior to the runs.

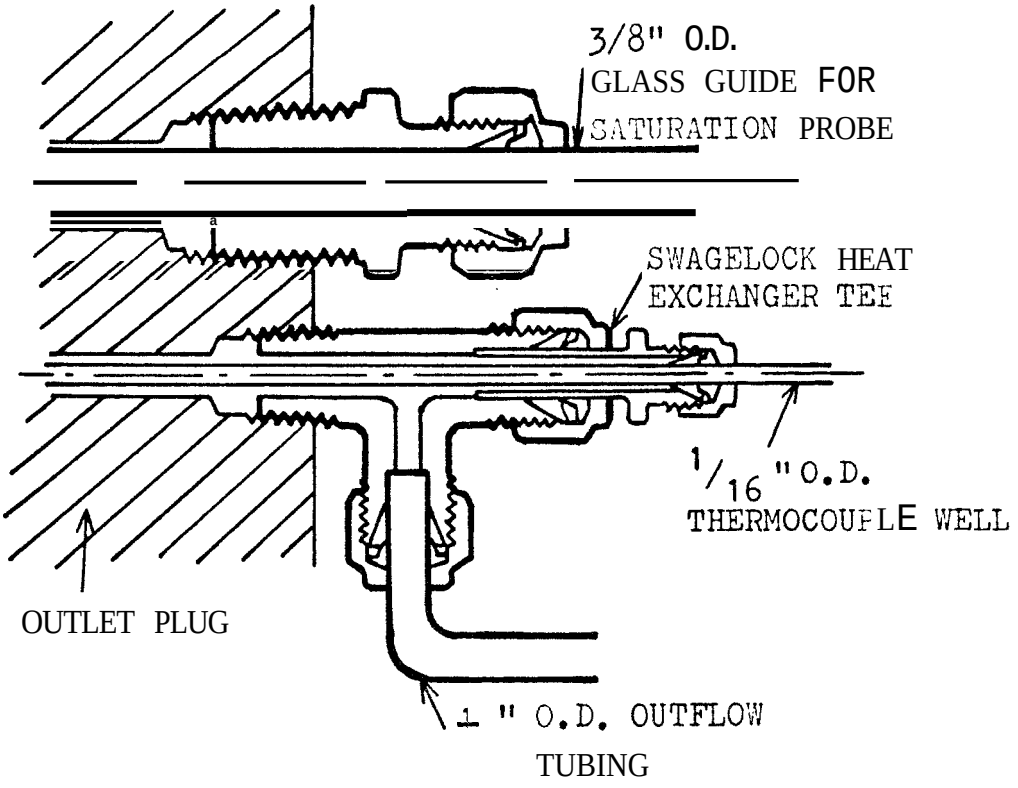

FIGURE 4. DETAILS OF OUTLET FITTINGS

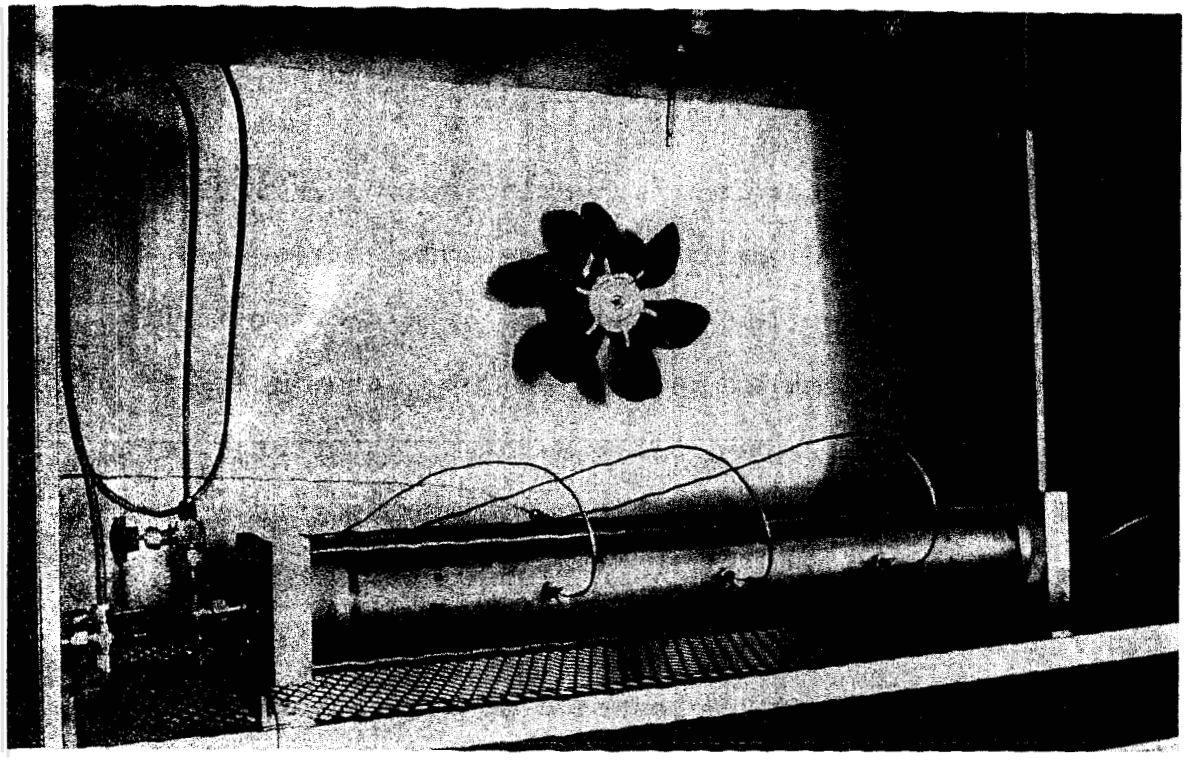

FIGURE 5. THE CORE HOLDER ASSEMBLY IN THE AIR BATH

Several lines exit the oven through ports in the walls. These lines are: the inlet and outlet flow lines; five pressure measurement lines; the confining pressure line; the traversing thermocouple well; and. the guide tube for the saturation probe.

Tubular Furnace

The tubular furnace has a heating space, 24 inches long by 2 inches in diameter. The maximum working temperature is 2000°F. The flow tubing goes back and forth three times through the tubular furnace so that water of room temperature at the furnace inlet becomes hot water or even super-heated steam at the outlet. The temperature of the tubular furnace is adjusted by a temperature controller which regulates input by rhythmically turning the load circuit on and off with the percentage of time on infinitely variable from 5% to 100%.

Porous Media

Two types of porous media have been used: a Berea sandstone core, and several synthetic consolidated sandstone cores. In the case of the Berea sandstone core, a groove was cut on the side surface and a 1/16 inch O.D. stainless steel tubing with one end plugged by silver solder was cemented in the groove. Fondu calcium aluminate cement, silica sand of about 100 Tyler mesh size, and water were used as the materials to make the synthetic cores. The

proportions of sand and cement were 80% sand by weight, and 20% cement by weight. The sand-cement mixture was prepared by thoroughly mixing sand, first with the blending water (0.5% by weight), and second with cement. The mixture was poured into a mold formed with a plastic tubing in which a glass tubing for the liquid saturation probe and a thermocouple tubing were held in place. While pouring the sand, the mold was tapped and vibrated from time to time in order to compact the sand. Water was injected through a fitting on a disc flange connected to the end of the mold. After the breakthrough of the injected water, the mold was disconnected from the water and allowed to hydrate for one day. After 24 hours, the plastic tubing was peeled off, and the core was machined (filed) to a desired size: 2 inches O.D. by 23.5 inches long. This method of making artificial sandstone cores was found to be reproducible and reliable. For the mixture of 80% sand and 20% cement by weight, the permeability and porosity were about 100 millidarcies, and 35% of bulk volume, respectively. This combination of low permeability and high porosity is ideal for the purposes of this study.

In addition to the method mentioned above, several other techniques were tried to prepare synthetic sandstone cores.

1. One test involved a termary pack of large sand grains, small sand grains, and cement, with water addition by im-

bibition. This procedure was found to be inappropriate to make long, homogeneous cores.

2. A wet mixture of 100 mesh sand, cement, and water were packed into the plastic form instead of packing the dry mixture described above. This procedure was found to give unsatisfactory results for homogeneity and low permeability.

3. Cores were made in stainless steel tubes instead of the Hassler type core holder. The core did not adhere to the tube wall and it was not possible to eliminate bypass flow along the inside wall.

Pressure Measurement

The inlet and outlet pressures, and the pressure differences across intervals along the core were measured with Celesco model KP15 differential pressure transducers, and Celesco model CD25 transducer indicators. The range of pressure differences can be varied by use of different metal plates in the transducer. The transducer and indicator provide a signal to a Heathkit servo recorder.

In order to gain pressure data at intervals along the core, taps were made through the sidewall of the shell and the Viton sleeve tubing. Detail of the pressure taps on the sidewall of the shell is shown in Fig. 6. The Viton sleeve penetrators were used with Swagelok SS-200-1-OR fittings. The Viton sleeve was drilled using the Swagelok fitting as a drill guide after the core holder was assembled

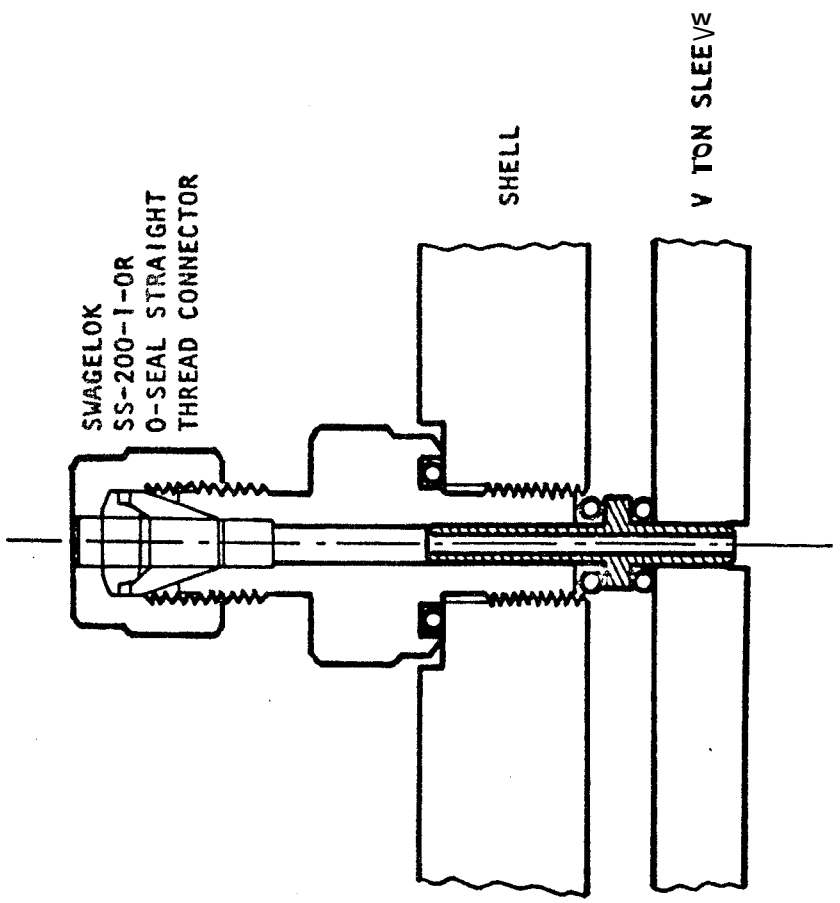

FIGURE 6. PRESSURE TAP

containing the core. One O-ring was used on each side of the flange on the sleeve penetrators to avoid leaks. The design of the pressure tap was also supplied by S. C. Jones, courtesy of the Marathon Oil Company.[28]

Saturation Measurement

For the purposes of this initial study of boiling water flow, the Baker capacitance probe was selected. The Chevron Oil Field Research Company kindly supplied complete details of both the probe and the detector circuit. (See Appendix C.)

EXPERIMENTAL PROCEDURE

Several different kinds of experiments can be accomplished with the apparatus described in the previous section. It was decided to run a series of basic single-phase experiments prior to performing the boiling two-phase, non-isothermal flow experiments. These basic experiments included:

1. Measurement of absolute permeability to gas and liquid water at a range of temperatures.
2. Injection of hot water into a system containing water at a lower temperature.
3. Cold water injection into a system containing hot water initially.
4. Injection of steam into a system containing liquid water at a lower temperature.
5. Two-phase fluid production from a closed system containing compressed hot water initially.

The first step to be taken was to make the core saturated with a test fluid: nitrogen gas or distilled and deaerated water. First, the pore space was evacuated by a vacuum pump via the exit valve. Then, the test fluid was allowed to imbibe into the core through the inlet valve while the exit valve was still connected to the vacuum pump. After breakthrough, the core was flooded with several pore volumes of fluid.

In measurement of absolute permeability, the injected fluid was heated by the tubular furnace to the constant temperature of the core.

The procedure in making a run was similar for injection of either hot water or steam. The pump and the tubular furnace were turned on and set to maintain certain pressure and temperature levels. Until the temperature of the injected fluid reached a desired level, the hot fluid was vented to the atmosphere via a bypass. When the recorded temperature of the injected fluid showed the desired constant value, the bypass valve was closed and the inlet valve to the core was opened, starting the run. The inlet pressure was set by the relief valve in the pump. The flow rate, or outlet pressure, was regulated by adjusting the outlet valves. The temperature of injected fluid, and the pressure drop across the whole length of the core were continuously recorded. The flow rate was measured periodically. Temperatures along the core were measured by traversing the thermocouple. The sensing time per point used was 6 seconds, although a value as low as 1.5 seconds could have been used.

For the cold water injection experiments, the procedure was the same as for the hot fluid injection, except that the core was initially heated and set to maintain a constant temperature instead of heating the injected fluid.

For a run of the depletion type, both the inlet and outlet valves were closed, and the core was heated to a desired initial temperature and pressure at which the water in the core was in the compressed liquid phase. Keeping the inlet valve closed, the outlet valve was suddenly opened to the atmosphere, and the producing pressure was recorded as a function of time. Both pressure and temperature along the axis of the core were recorded as functions of time.

The main experiment considered under the category of "Two-Phase Flow Experiments" was the steady injection of hot, compressed liquid water into the core at a rate such that a boiling front would form somewhere within the core length leading to an obvious two-phase, declining temperature and pressure flow region. The experimental procedure was as follows:

First, the core was saturated with water and heated to an initial temperature and pressure well within the compressed liquid region on a pressure-temperature diagram for flat-surface, water-steam equilibrium. During the heating procedure, hot water was circulated at a low rate through the core with the outlet conditions maintained in the liquid region. After temperatures along the axis of the core were stabilized, two-phase flow was initiated by opening the outlet valve and increasing the pressure drop across the core. A variety of experimental conditions

could be obtained by changing the inlet temperature and the pressure drop across the core. Pressures at the five transducer taps and temperature and liquid saturation in the axial direction were measured. It was possible to achieve approximately steady-state temperature and pressure distributions, although it was anticipated that conditions would never be truly steady state.

EXPERIMENTAL RESULTS AND ANALYSIS

Absolute Permeability

The permeability of a porous medium to a single-phase gas usually exceeds the permeability of the same porous medium to a single-phase liquid. The difference in these permeabilities is caused by the phenomenon known as slip, and reactions between liquids and the solid. The first studies concerned an investigation of the effect of temperature level upon the absolute permeability to both gas and water for the synthetic cores. No such information had been presented previously.

Klinkenberg[29] developed the relation between the permeability of a porous medium to gas and to a nonreactive liquid as follows:

$$k_a = k\left(1 + \frac{4C\bar{\lambda}}{r}\right) \tag{41}$$

where k_a is the apparent or observed permeability to gas, k is the absolute permeability to gas at high pressures which is equal to the absolute permeability to a single liquid phase, $\bar{\lambda}$ is the mean free path of the gas molecules, r is radius of a capillary (assumed to be constant), and C is a proportionality factor. The mean free path can be expressed as:

$$\bar{\lambda} = \frac{1}{\sqrt{2}\pi d^2 n} = \frac{RT}{\sqrt{2}\pi p_m N d^2} \tag{42}$$

where d is a collision diameter, n is the concentration of molecules per unit volume, N is Avogadro's Number, p_m is the mean pressure, T is temperature, and R is the universal gas constant. From Eq. 42, Eq. 41 becomes:

$$k_a = k\left(1 + \frac{4CRT}{\sqrt{2}\pi rNd^2 p_m}\right) = k\left(1 + \frac{b}{p_m}\right) \qquad (43)$$

where b is often referred to as the Klinkenberg factor, which is constant for a given gas and a given porous medium at a constant temperature. From Eq. 43, the Klinkenberg factor is clearly directly proportional to temperature.

Fig. 7 presents the measured permeabilities to nitrogen for a synthetic sandstone core graphed against the reciprocal mean core pressure for a variety of temperatures ranging from 75°F to 342°F. All data can be represented by a single line, indicating no significant effect of temperature level for the range of temperatures studied, although the slope of the line, kb, should change in proportion to temperature in accordance with Eq. 43. A possible explanation about lack of dependence of the slope on temperature is that the proportionality factor, C, may be directly proportional to the reciprocal temperature for the present case. The Klinkenberg factor is 3.77 psi, much higher than would be expected from correlations for natural sandstone cores. Also shown on the ordinate of Fig. 7 is the absolute permeability to water for the same synthetic core, 98 millidarcies at 76 to 340°F. This is a few pes cent I-ower than the absolute permeability to gas, 100 millidarcies.

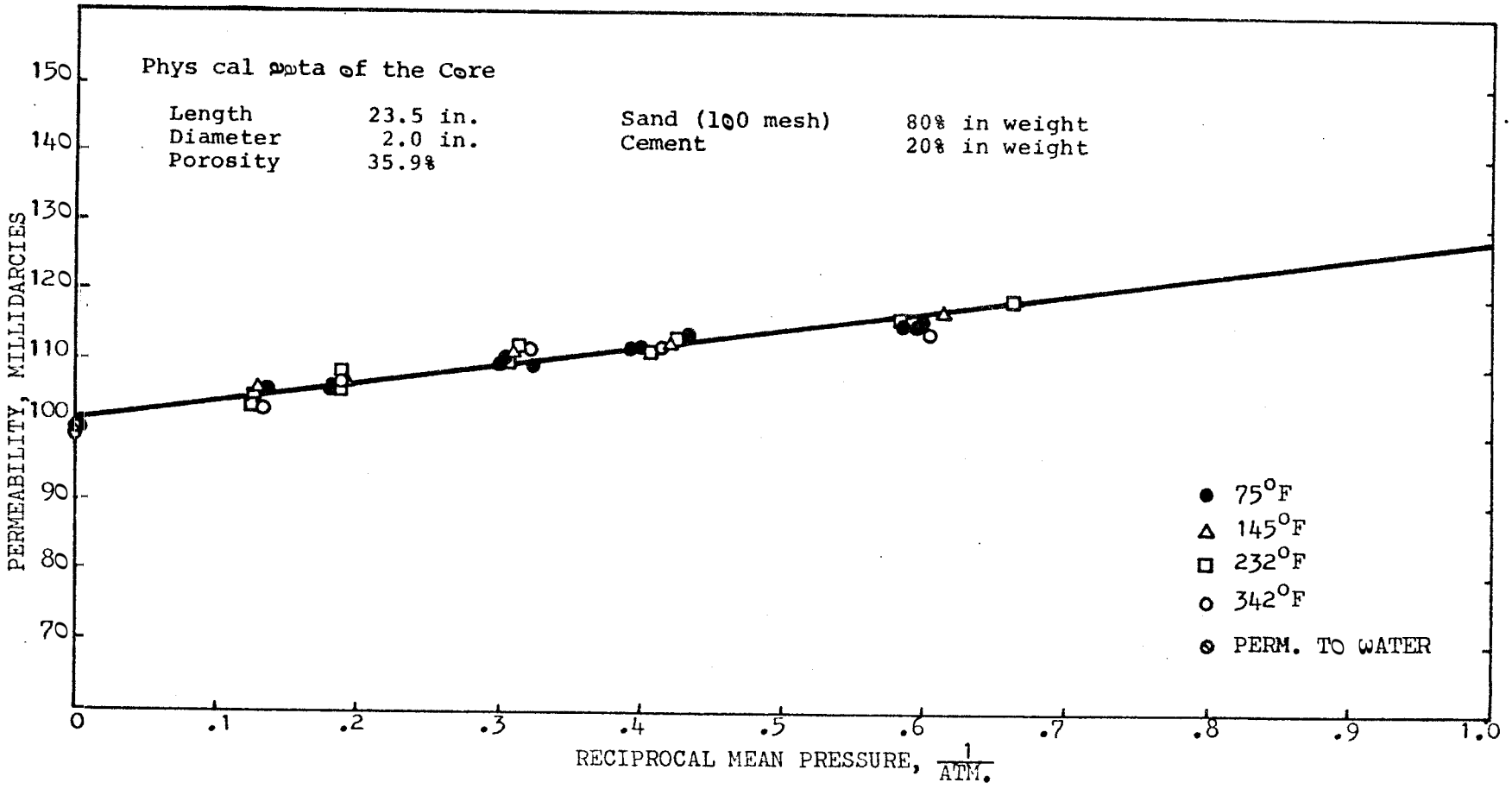

FIGURE 7. PERMEABILITY TO NITROGEN VS. RECIPROCAL MEAN PRESSURE FOR A SYNTHETIC SANDSTONE CORE

Although not evident on Fig. 7, the same permeability to water was measured for a range of temperatures from 76°F to 340°F. Unlike previous findings by Weinbrandt, et al.,[30] for natural sandstones, no effect of temperature was found. One significant difference other than the nature of the core was that the confining pressure was only 400 psi for the present studies as compared to at least several thousand psi for the Weinbrandt, et al., study. This compound effect of the confining pressure and temperature on the permeability to liquid has been investigated carefully by Cassé[31] recently. According to the results of Cassé, the temperature effect on the absolute permeability to water is minor at low confining pressure, which is consistent with the present work. In the case of the Berea sandstone core, which was 2 inches O.D. by 23.5 inches long and of 22% porosity, no temperature effect was found for temperatures varying from 70°F to 320°F with water.

Hot Water Injection

Four runs of hot water injection were made for each core at varying injection rates and injection temperatures. Figs. 8-15 present temperature vs. distance along the core. Figs. 8-11 are for the synthetic sandstone core, and Figs. 12-15 are for the Berea sandstone core. These figures provide basic information on single-phase nonisothermal flow. From these data it is possible to compute effective thermal conductivities in the direction of flow, and heat loss radially from the core. As can be seen in each figure, heat flow changes from an unsteady state at early stages to a nearly steady-state process at long times. The temperature distribution along the core shows transient heating curves for short times. During the intermediate period, there are almost constant incremental changes of temperature with time at any given location. At long times, the incremental changes in point temperatures become smaller, and eventually the temperature profile stabilizes. The heat transfer process is then apparently steady state, and the temperature changes nearly linearly along the axis of the core. At steady-state conditions, the net heat injection rate is exactly balanced by the radial heat loss from the system.

In order to evaluate the experimental results, a mathematical model similar to the one of Lauwerier can be used. In the present work, the core is cylindrical, and the heat transfer from the core to the surroundings can be expressed by forced convection, rather than conduction. In addition to these differences from Lauwerier's model, the injection temperature is a continuous function of time rather than being constant.

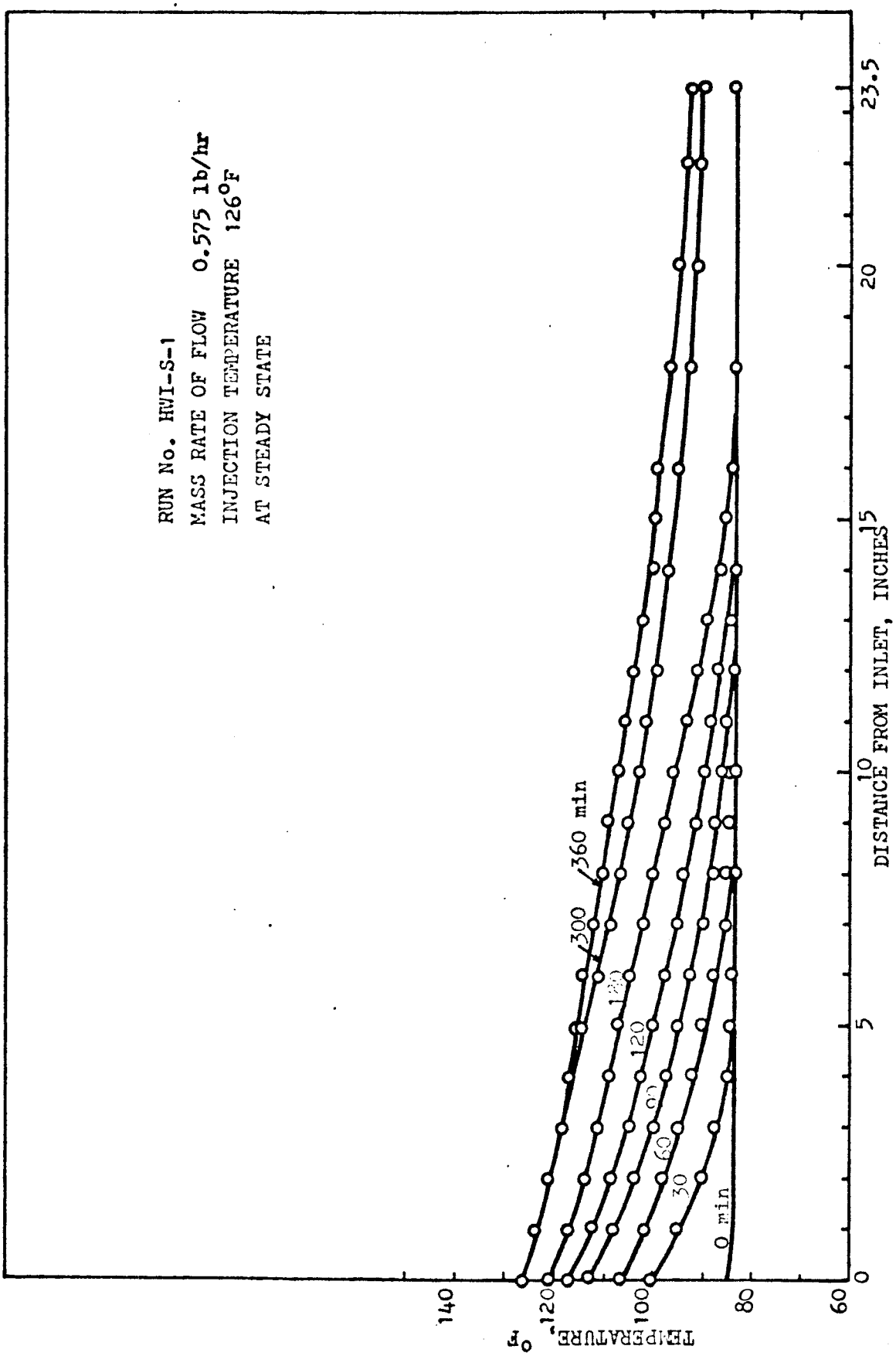

FIGURE 8. TEMPERATURE VS. DISTANCE FOR HOT WATER INJECTION, SYNTHETIC SANDSTONE; RATE = 0.575 lb/hr, TEMP. = 126°F

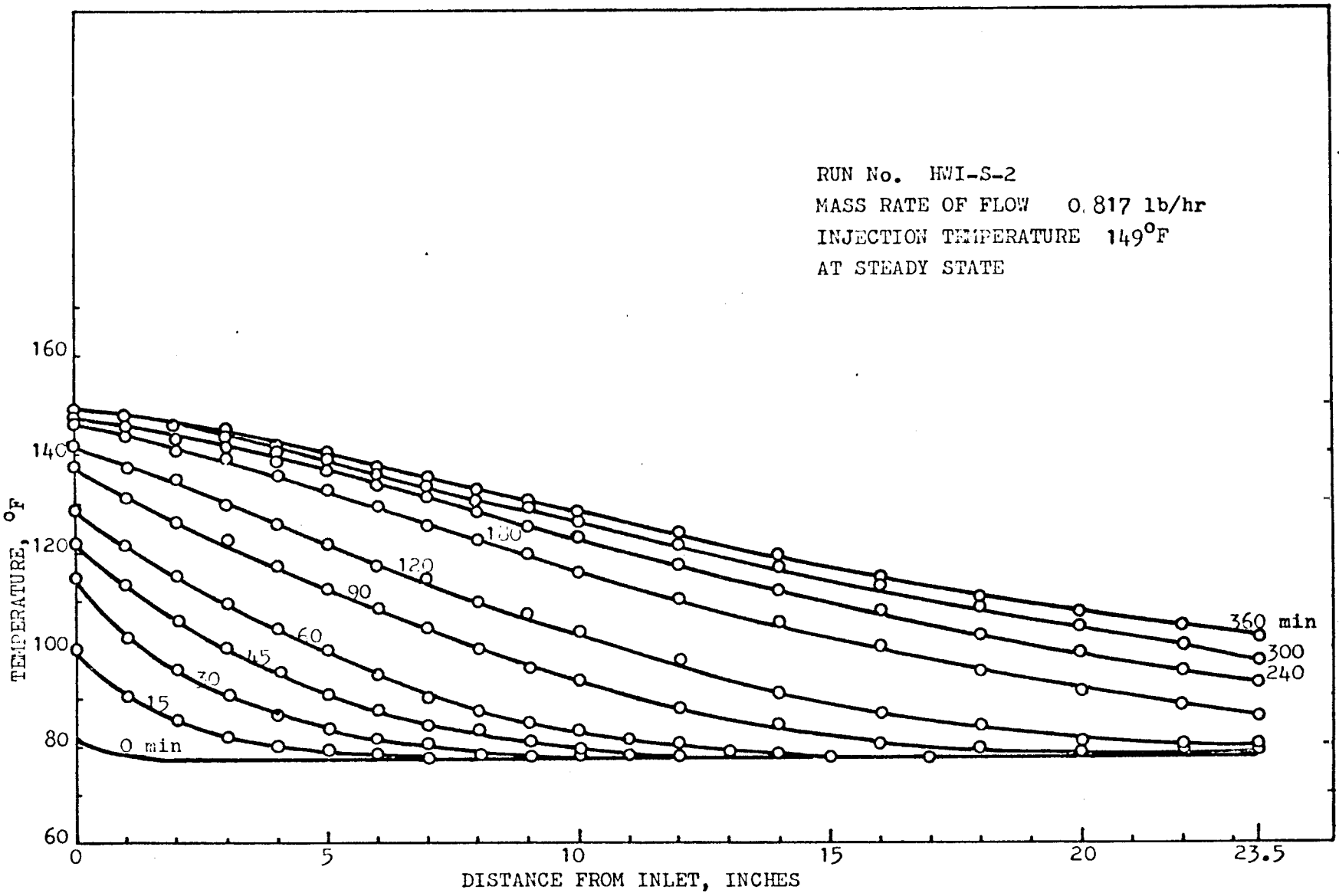

FIGURE 9. TEMPERATURE VS. DISTANCE FOR HOT WATER INJECTION, SYNTHETIC SANDSTONE; RATE = 0.817 lb/hr, TEMP.= 149°F

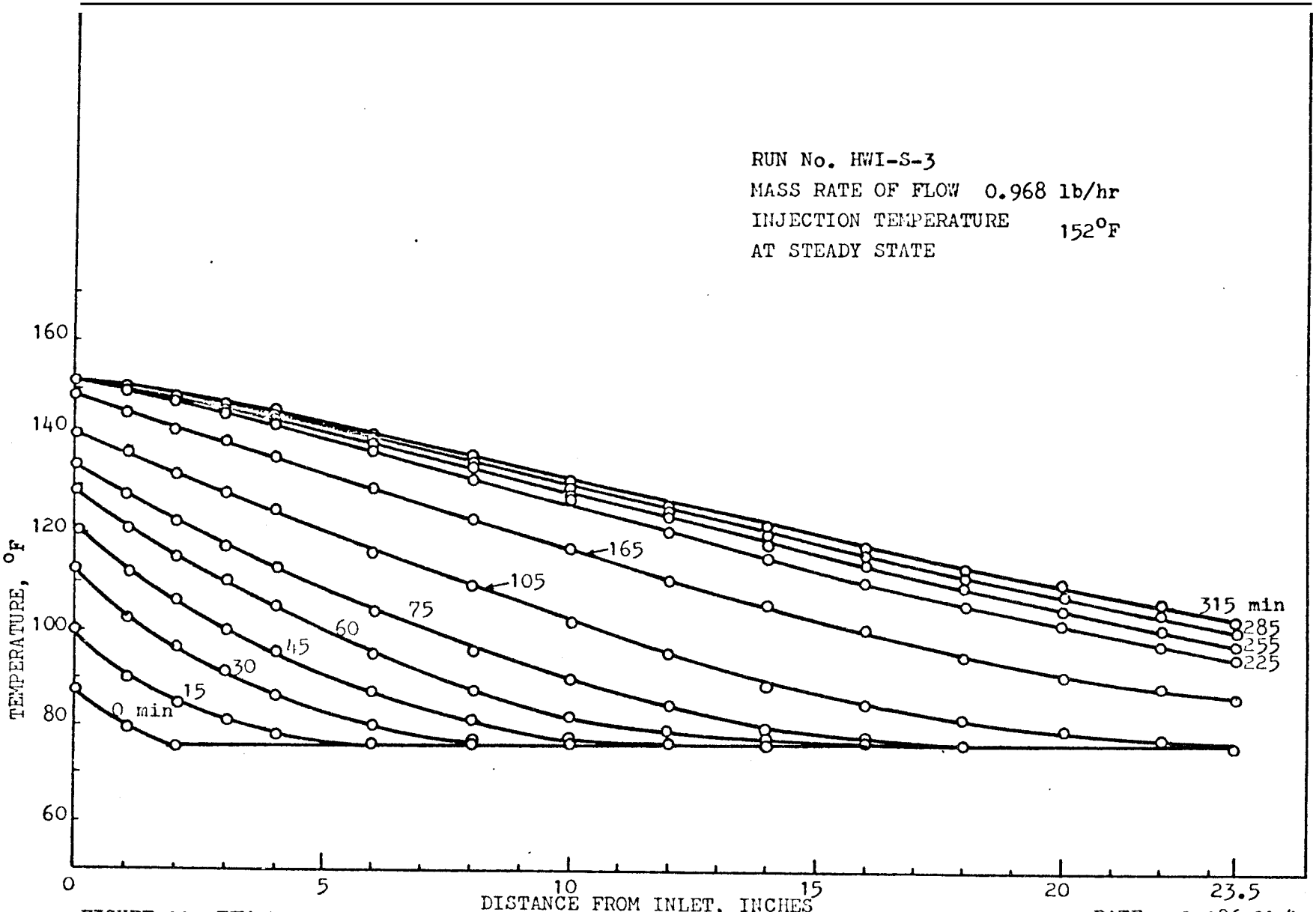

FIGURE 10. TEMPERATURE VS. DISTANCE FOR HOT WATER INJECTION, SYNTHETIC SANDSTONE. RATE = 0.986 lb/hr TEMP. = 152°F

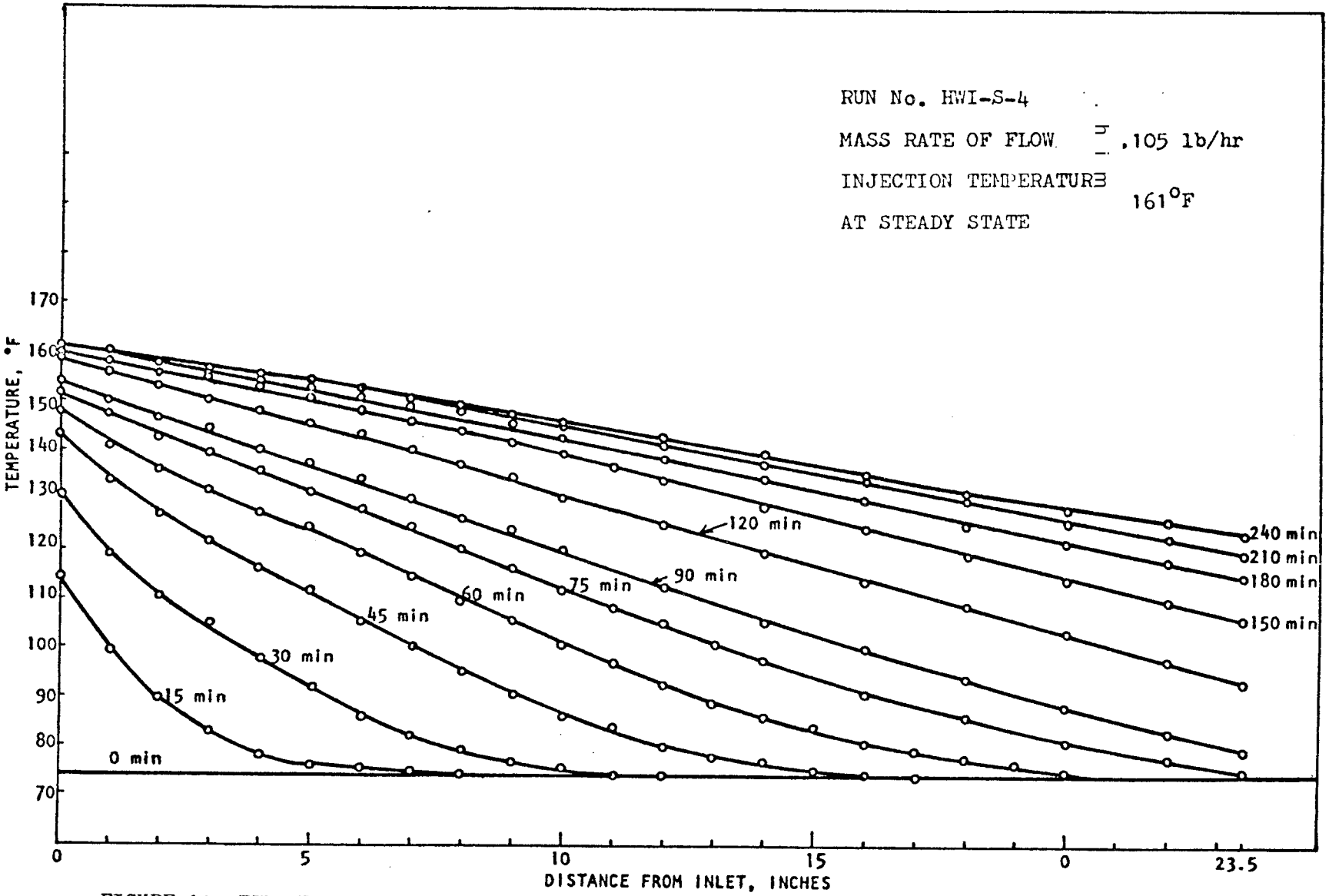

FIGURE 11. TEMPERATURE VS. DISTANCE FOR HOT WATER INJECTION, SYNTHETIC SAND TONE; RATE = 2.105 lb/hr , TEMP. = 161°F

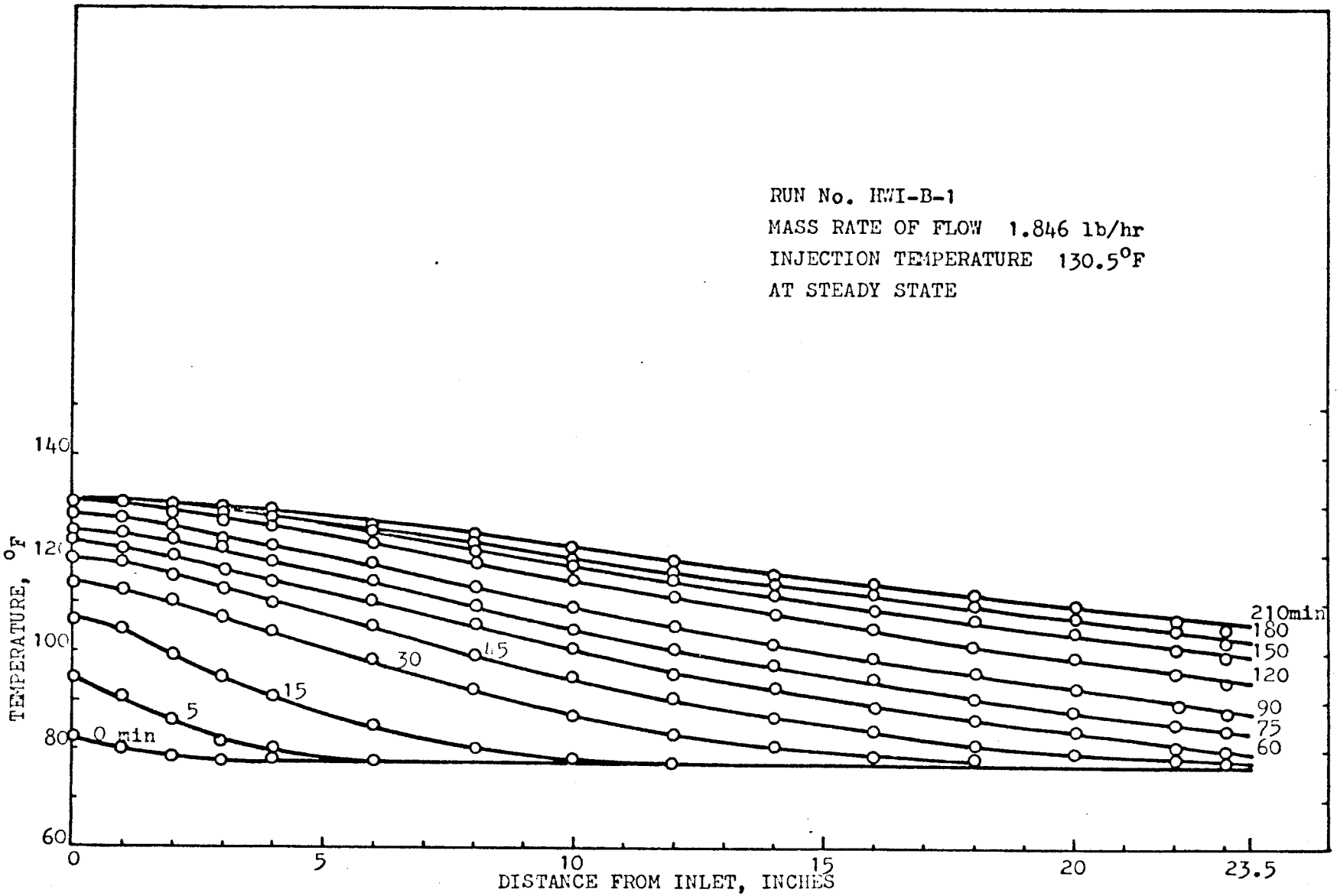

FIGURE 12. TEMPERATURE VS. DISTANCE FOR HOT WATER INJECTION, BEREA SANDSTONE; RATE = 1.846 lb/hr, TEMP. = 130.5°F

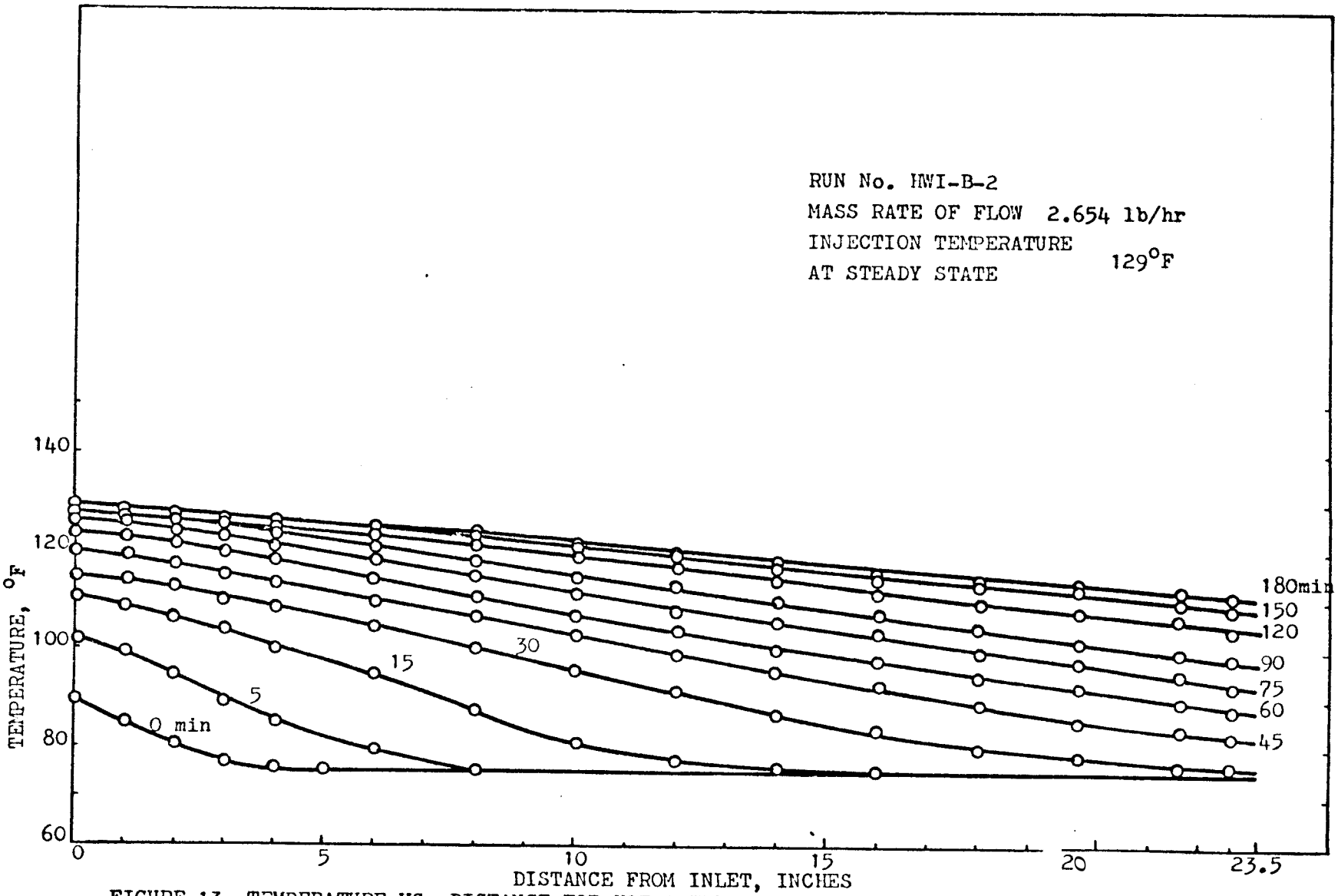

FIGURE 13. TEMPERATURE VS. DISTANCE FOR HOT WATER INJECTION, BEREA SANDSTONE; RATE = 2.654 lb/hr, TEMP. = 129°F

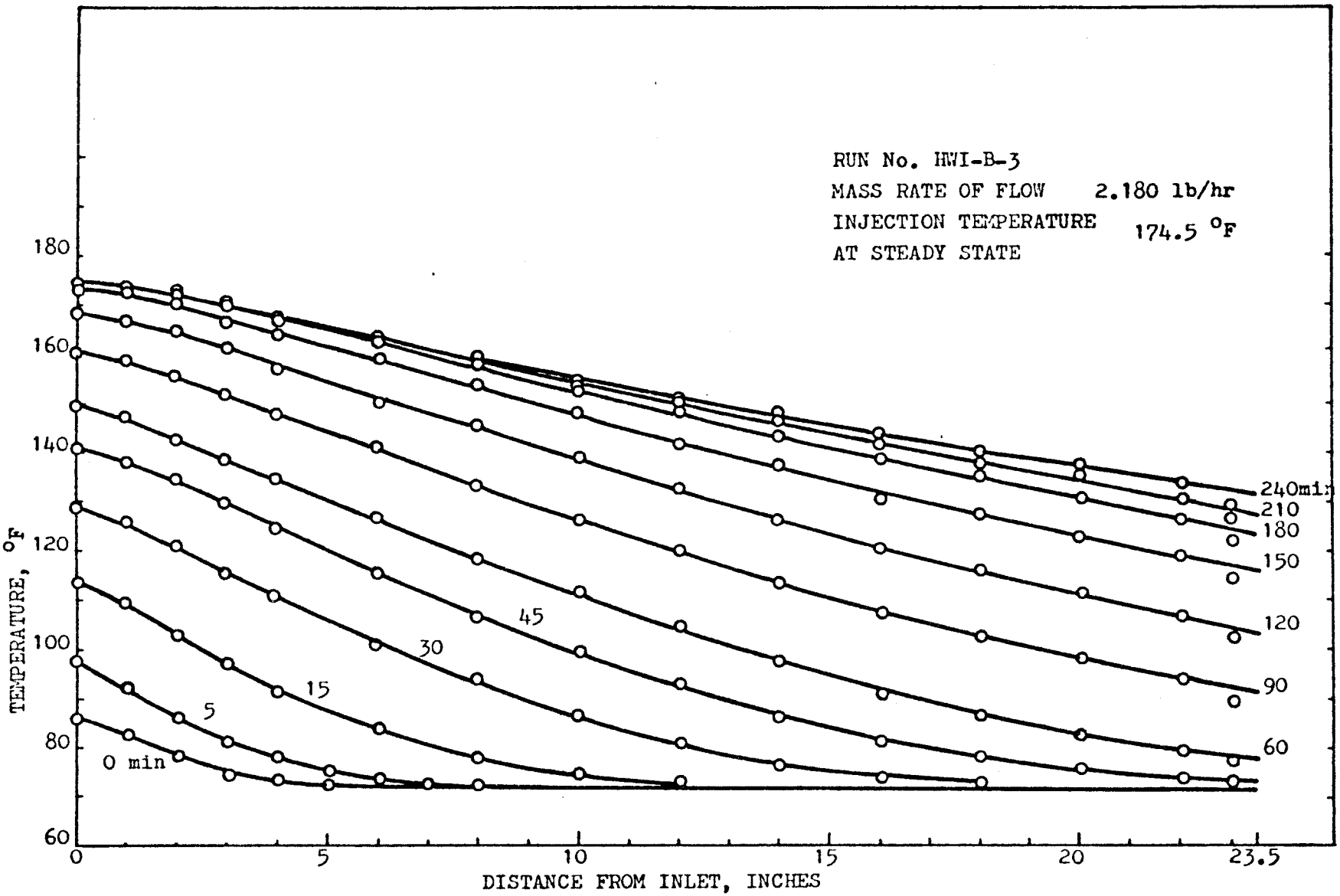

FIGURE 14. TEMPERATURE VS. DISTANCE FOR HOT WATER INJECTION, BEREA SANDSTONE; RATE = 2.180 lb/hr, TEMP. = 174.5°F

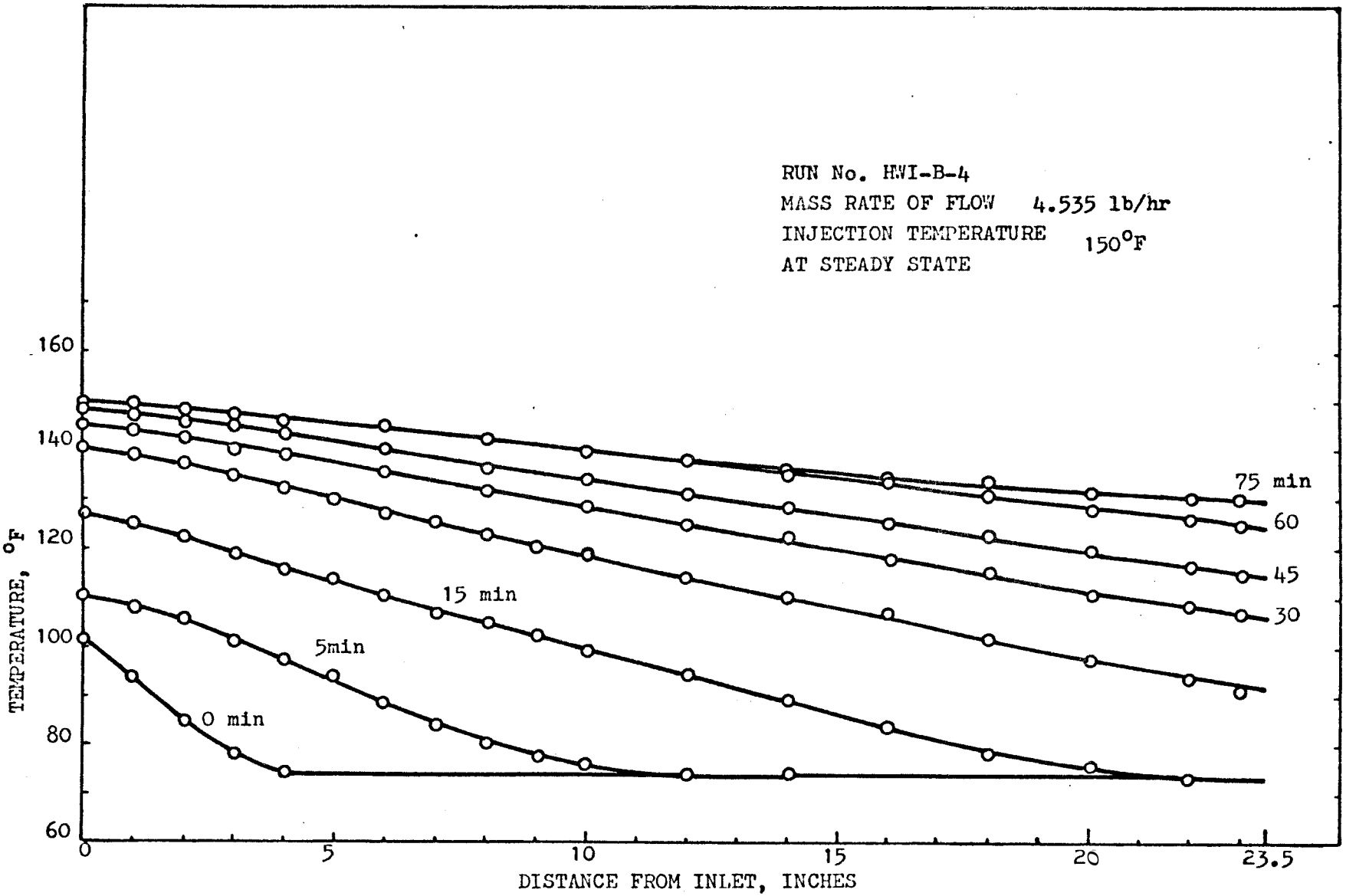

FIGURE 15. TEMPERATURE VS. DISTANCE FOR HOT WATER INJECTION, BEREA SANDSTONE; RATE = 4.535 lb/hr, TEMP. = 150°F

Applying a heat balance to the hatched region of Fig. 16, the following equation is obtained:

$$r_o \rho_1 C_1 \frac{\partial T}{\partial t} + r_o \rho_w V_w C_w \frac{\partial T}{\partial x} + 2UT = 0 \qquad (44)$$

where $T = T_1 - T_\infty$

and

$$\rho_1 C_1 = (1 - \phi)\rho_S C_S + \phi \rho_w C_w.$$

The constants in the previous equation are similar to the ones used by Lauwerier except the following:

T_∞ = the ambient temperature, °F

r_o = the radius of the core, ft

U = the overall heat transfer coefficient, Btu/hr-ft^2-°F, based on the radius of the core.

Introducing the dimensionless variables ξ and τ defined by:

$$x = \frac{r_o \rho_w V_w C_w}{2u} \xi \quad , \qquad t = \frac{r_o \rho_1 C_1}{2u} \tau.$$

The problem to be solved can now be expressed as:

$$\frac{\partial T}{\partial \tau} + \frac{\partial T}{\partial \xi} + T = 0 \qquad \text{for } \xi > 0,\ \tau > 0 \qquad (45)$$

and

$$T = T_i - T_\infty = F(a\tau) \qquad \text{for } \xi = 0,\ \tau > 0$$

$$T = 0 \qquad \text{for } \xi > 0,\ \tau = 0$$

where

$$a = \frac{r_o \rho_1 C_1}{2U}. \qquad (a\tau = t)$$

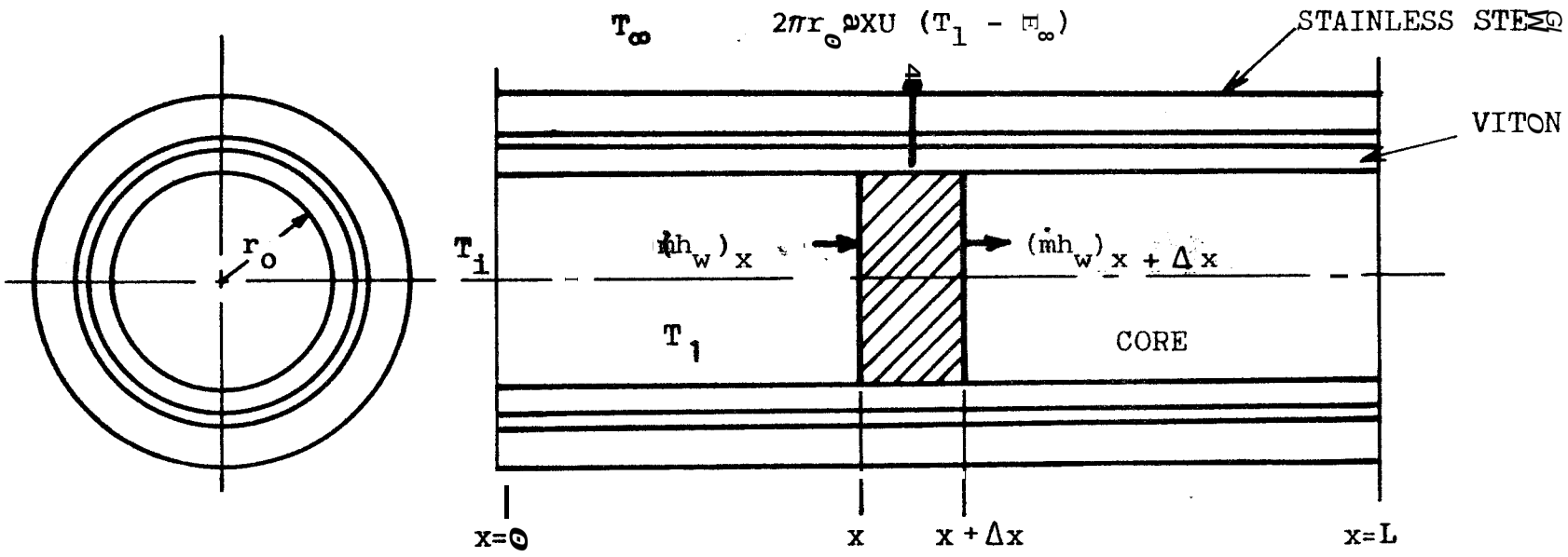

FIGURE 16. HEAT BALANCE ON CORE ELEMENT
TO DERIVE EQ. 44

The solution can be obtained by using the Laplace transformation method, and yields:

$$T_1 = T_\infty + e^{-\xi} F(a\tau - a\xi)\alpha(\tau - \xi), \text{ or} \tag{46}$$

$$T_1 = T_\infty \exp\left(-\frac{2UX}{r_o \rho_w V_w C_w}\right) F\left(t - \frac{\rho_1 C_1 X}{\rho_w C_w V_w}\right)$$

$$\cdot \alpha\left(\frac{2U}{r_o \rho_1 C_1} t - \frac{2UX}{r_o \rho_w V_w C_w}\right) \tag{46}'$$

where

$$\alpha(\tau - \xi) = \begin{cases} 1 & \text{for } \tau \geq \xi \\ 0 & \text{for } \tau < \xi \end{cases}$$

As shown in the experimental results, $F(t)$ is not constant but is a function of time which can be expressed as $F(t) = T_{io}(1 - e^{-\beta t})$, where T_{io} and β are certain constants.

Fig. 17 shows an example of the calculated temperature distributions at various times. Fig. 18 presents the temperature of the core at the inlet end, $[F(t) + T_\infty]$, vs. injection time. For the calculation, the following constants were used:

$$\rho_S = 165.4 \text{ lb/ft}^3$$

$$C_S = 0.21 \text{ Btu/lb-°F}$$

$$\rho_w = 62.0 \text{ lb/ft}^3$$

$$C_w = 1.0 \text{ Btu/lb-°F}$$

$$\phi = 22\%$$

$$U = 1.246 \text{ Btu/hr-ft}^2\text{-°F}$$

Thermal properties of sands and water are shown in Appendix B. The values of ρ_S, C_S, ρ_w, and C_w given above are for the average temperature. U was calculated with the experimental data as shown in the later section.

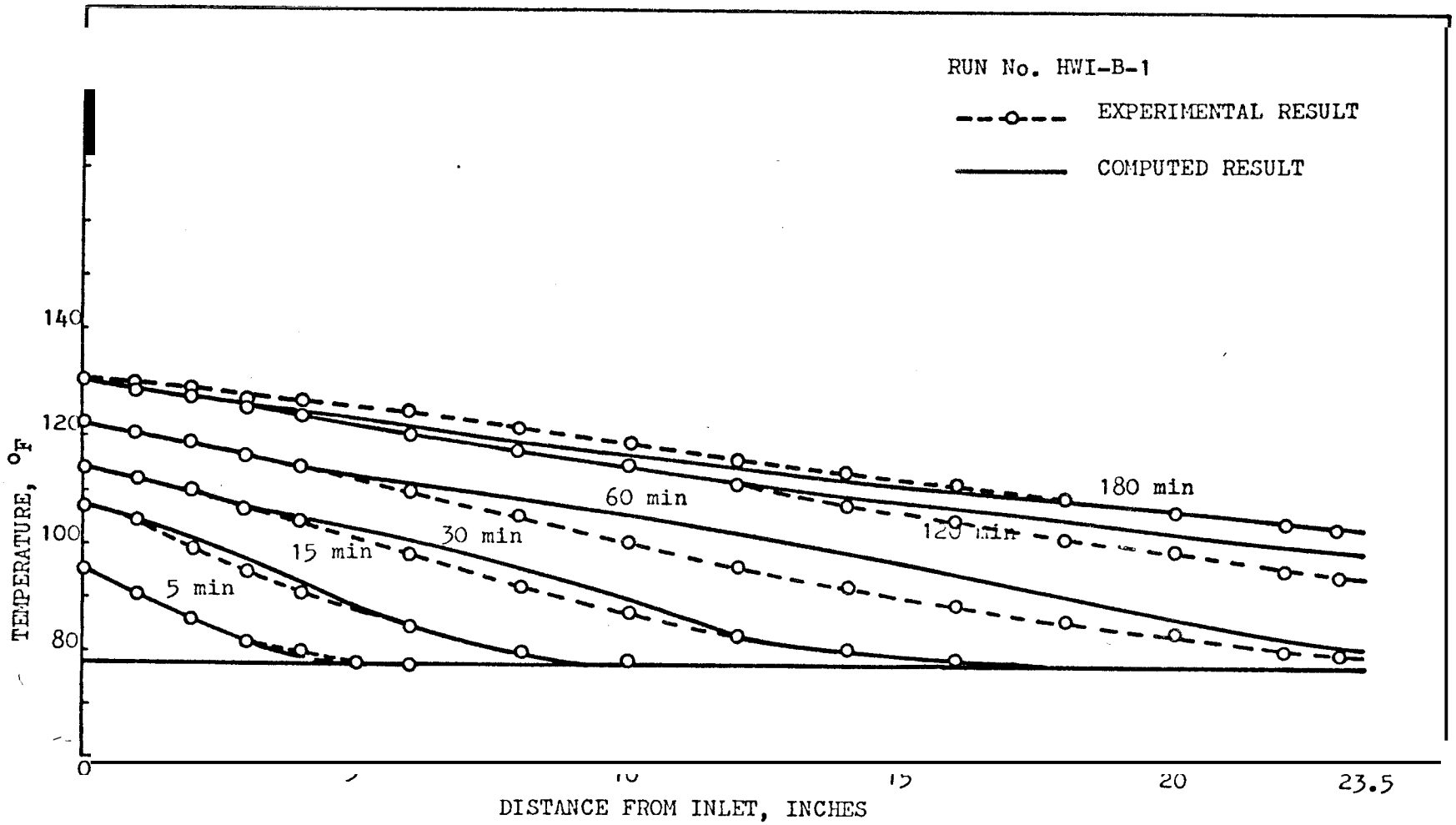

FIGURE 17. COMPARISON OF THEORETICAL AND EXPERIMENTAL TEMPERATURE DISTRIBUTIONS FOR HOT WATER INJECTION, BEREA SANDSTONE

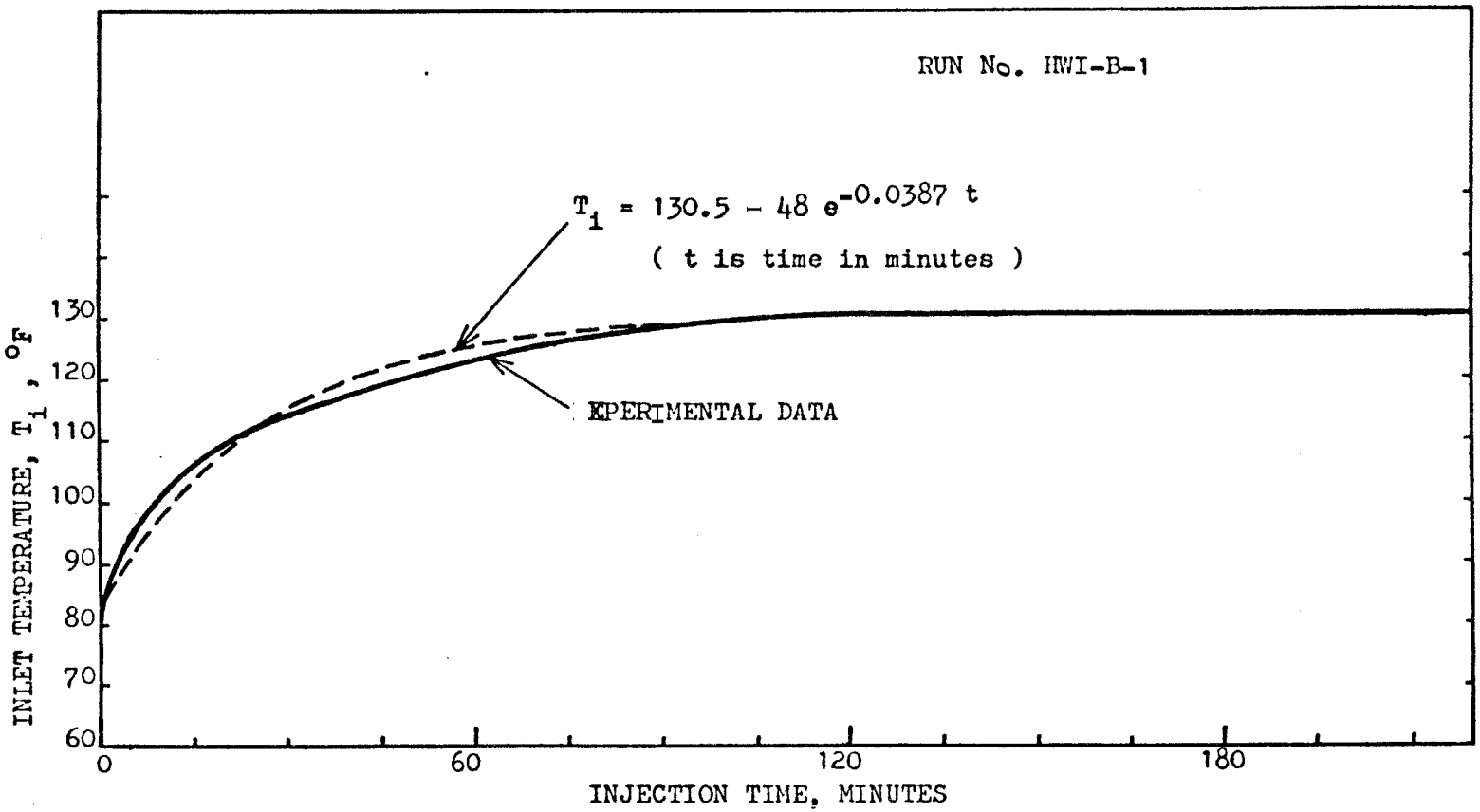

FIGURE 1 . TEMPERATURE HISTORY AT THE INLET OF TXE CORE, BEREA SANDSTONE

The main reason for the differences between the observed and calculated temperature distributions is that the overall heat transfer coefficient was assumed to be constant throughout the run. Actually, the overall coefficient U must have a higher value before the heating process reaches a steady state, than the 1.246 Btu/hr-ft^2-°F value which was estimated for the steady state.

In regard to radial heat loss, two factors are of importance: (1) the thermal efficiency of the hot fluid injection, and (2) the overall heat transfer coefficient between the core within the sleeve and the surroundings.

Thermal Efficiency

"Thermal efficiency" has been defined in oil recovery by hot fluid injection as the fraction of the cumulative heat which is still within the injection interval (the remainder being lost to the overburden and underburden), For varying injection rate and temperature, the thermal efficiency at a total injection time t may be defined as:

$$E(t) = \frac{\int_0^L \pi r_o^2 [\rho_S C_S (1 - \phi) + \rho_w C_w \phi] [T_1(t, x) - T_o] dX}{\int_0^t \dot{m}(t)\, C_w\, [T_i(t) - T_o] dt} \qquad (47)$$

In this formula, the specific heat of sand grains, C_S, the specific heat of water, C_w, and the density of water, ρ_w, are all temperature dependent. These thermal properties are available in the literature and are summarized in Appendix B. Using the temperature distributions presented in Figs. 8-15, thermal efficiencies were computed by numerical integration. Figs. 19 and 20 show the results for the synthetic core and Berea sandstone core, respectively. Thermal efficiency is graphed against cumulative heat injected, with heat injection rate as a parameter, showing heat injection rate dependence of thermal efficiency. The greater the rate of heat injection, $\dot{m}C_w\Delta T$, the higher is the thermal efficiency. This trend was also observed by Baker[9], Ersoy[46] and Crichlow[12]. In the practical application of reservoir heating, the reservoir volume to be heated, and a temperature to be attained must be specified. Generally, high mass and heat injection rates appear to be more advantageous. On the other hand,

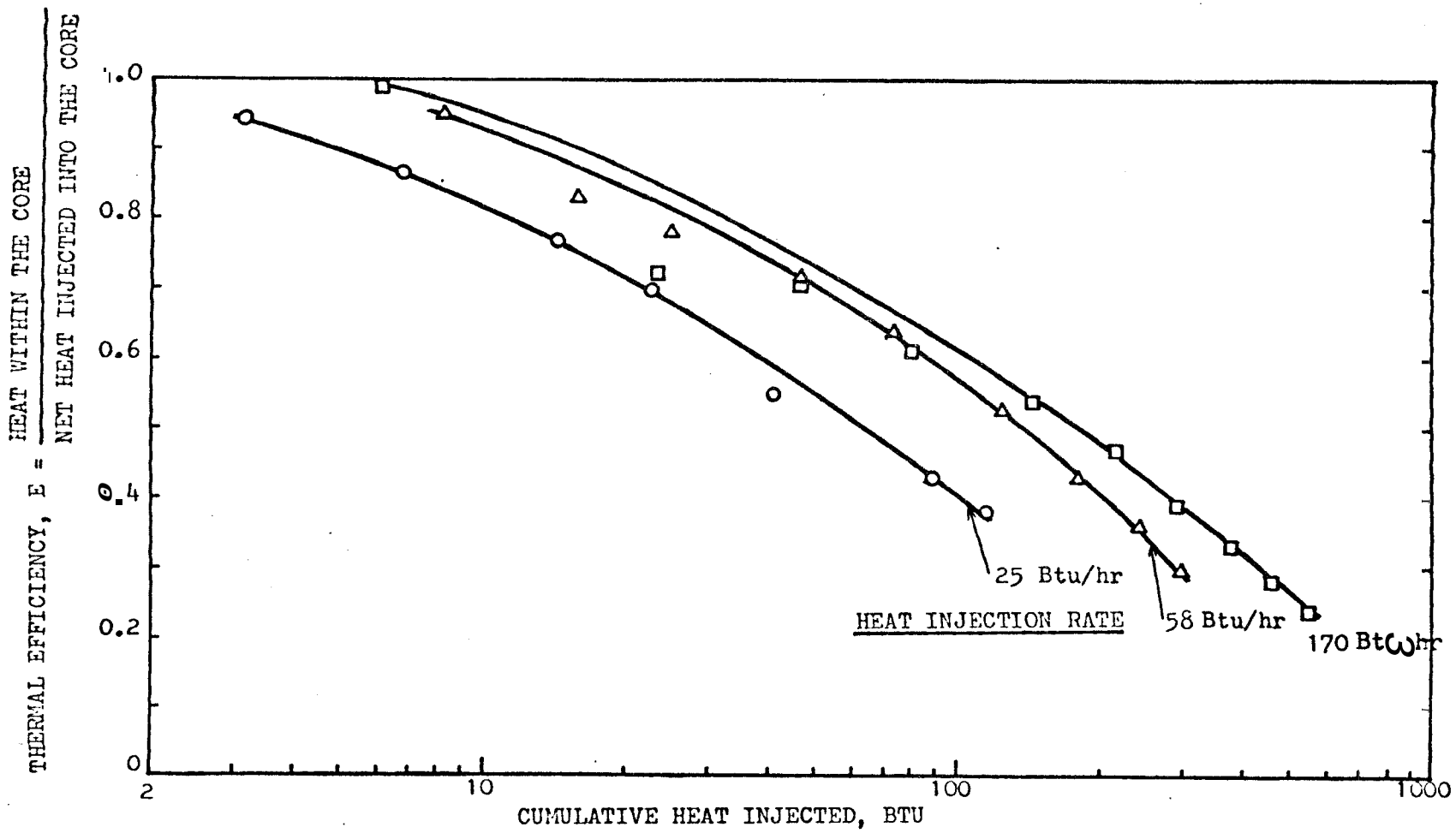

FIGURE 19. THERMAL EFFICIENCY AS A FUNCTION OF CUMULATIVE HEAT INJECTED IN HOT WATER INJECTION, SYNTHETIC SANDSTONE

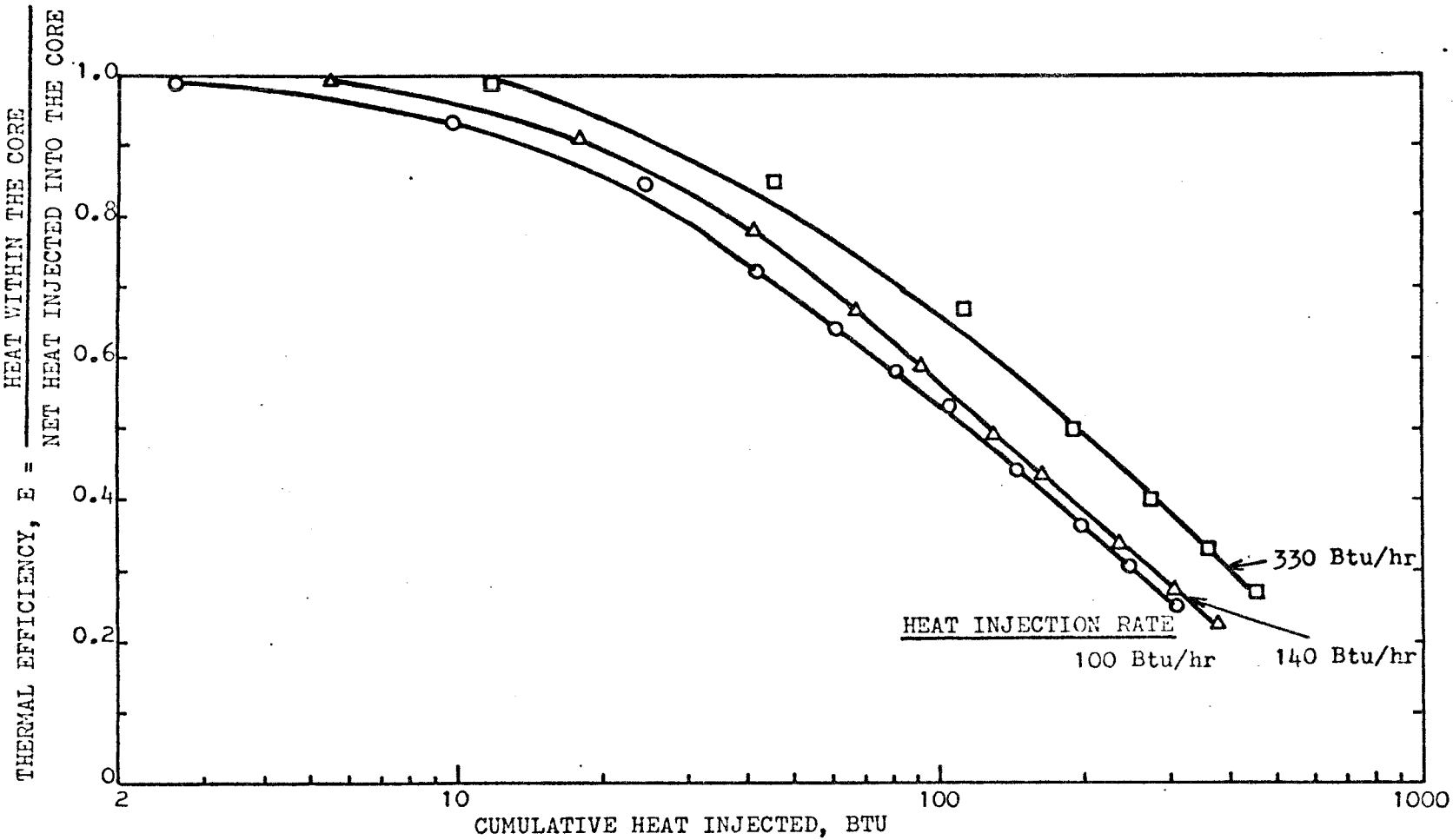

FIGURE 20. THERMAL EFFICIENCY AS A FUNCTION OF CUMULATIVE HEAT INJECTED IN HOT WATER INJECTION, BEREA SANDSTONE

thermal efficiencies can also be graphed against the injection time, as presented on Figs. 21 and 22. On this basis, the dependence on injection rate is reversed, i.e., the lower $(\dot{m}C_w\Delta T)$ is, the higher the efficiency. From Figs. 21 and 22, it is noted that a higher heat injection rate causes a greater heat transfer from the core to the surroundings. This fact can be explained by the observation that the overall heat transfer coefficient of the core holder depends upon mass flow rate. As described in the following section, the higher mass flow rate is, the larger the overall heat transfer coefficient will be (see Fig. 23).

Finally, it should be noted that Eq. 47 defines thermal efficiency as the ratio of the heat contained within the core at any time divided by the cumulative heat injected at that time. The heat flow out the exit of the core has not been subtracted as was done by Crichlow[12]. Results can be placed on the same basis as those of Crichlow easily, because the outflow temperature is known as a function of time. See the temperature profiles in Fig. 15 for example. This correction will have no effect on conclusions reached in the preceeding.

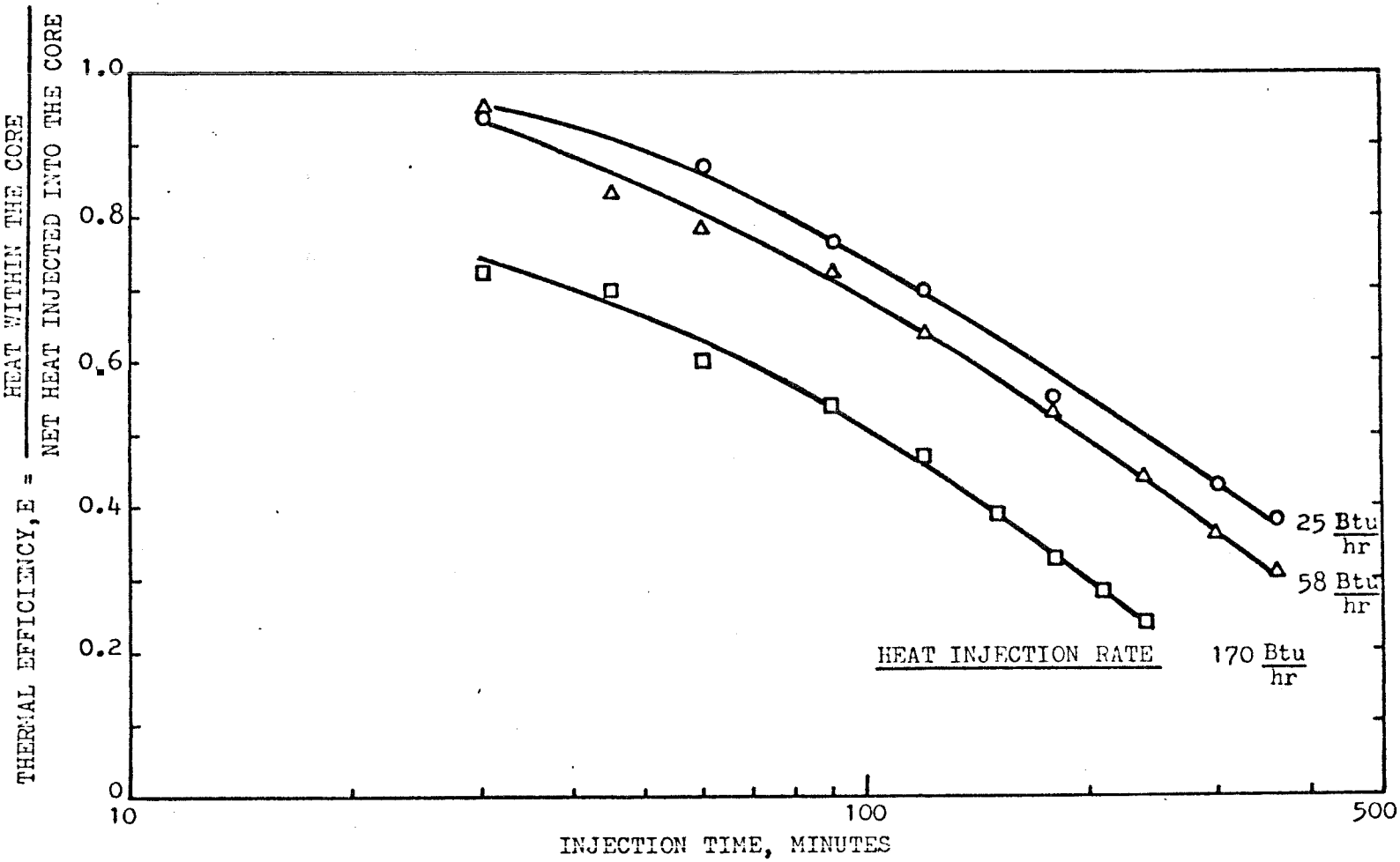

FIGURE 21. THERMAL EFFICIENCY AS A FUNCTION OF INJECTION TIME IN HOT WATER INJECTION, SYNTHETIC SANDSTONE

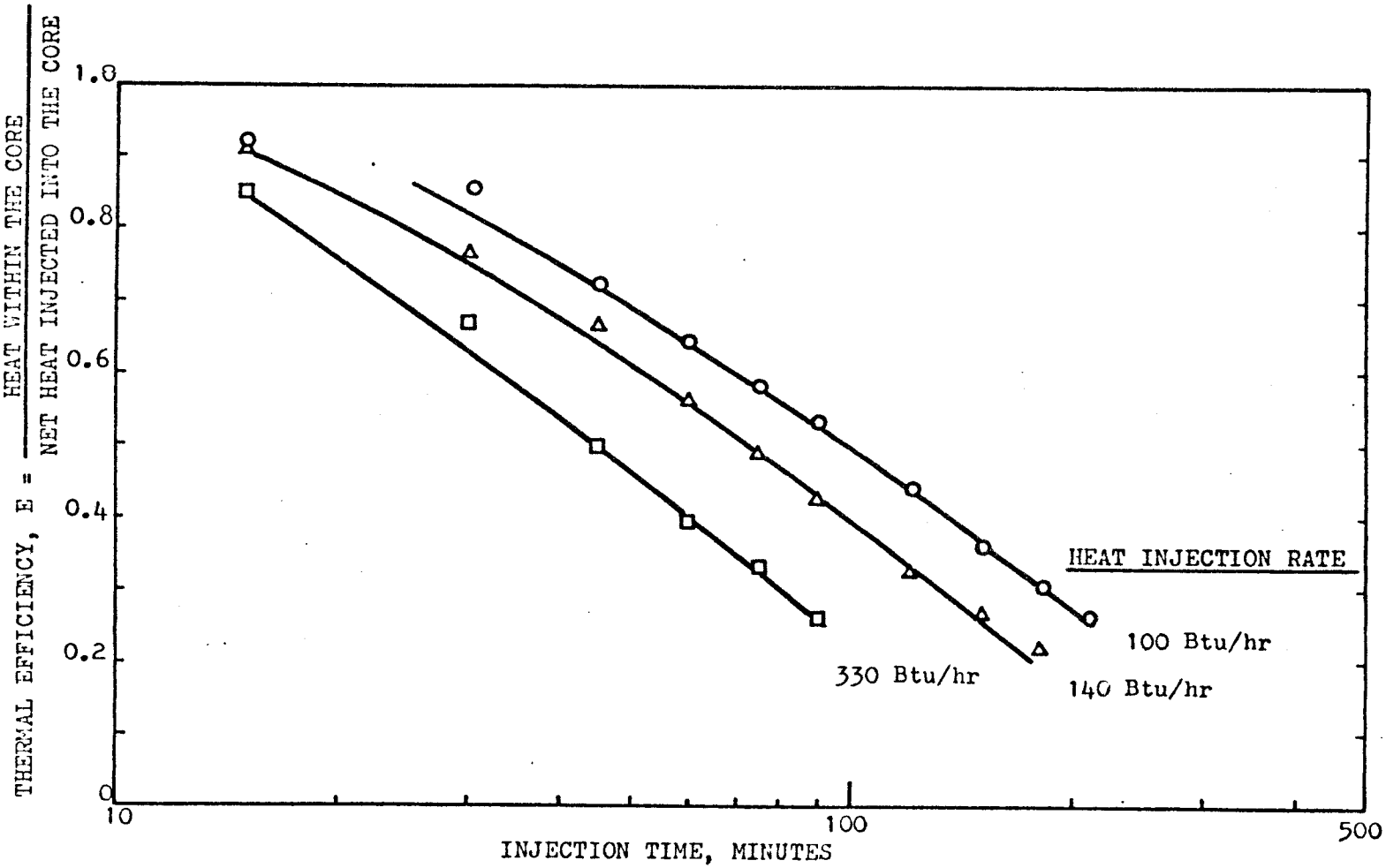

FIGURE 22. THERMAL EFFICIENCY AS A FUNCTION OF INJECTION TIME IN HOT WATER INJECTION, BEREA SANDSTONE

Overall Heat Transfer Coefficient for Core Holder

As can be seen in Figs. 8-15, the temperature profiles become nearly linear at long injection times, indicating that the heat loss per unit length is almost constant:. Thus, the total heat loss can be averaged and a simple determination of the overall heat transfer coefficient made. The following formula was used for computation:

$$U = \frac{\dot{m}C_w\ (T_{in} - T_{out})}{2\pi r_o \int_o^L (\frac{dT}{dX}i\ X + T_i - T_\infty)\ dX} \qquad (48)$$

The results are shown in Fig. 23 and Table 1. Fig. 23 shows that the higher mass injection rate is, the greater the overall heat transfer coefficient, and that the data for the hot water injection appears to follow a power law, i.e., $U = 0.94(\dot{m})^{0.328}$

As described by Willhite[32] and Ramey[33], the overall heat transfer coefficient can be estimated by evaluating the size of each heat transfer component. Fig. 24 shows the core holder model which will be used to derive U. The end effect is assumed to be negligible, First, U is defined by the following equation:

$$Q = 2\pi r_o U\ (T_f - T_\infty)\ AL \qquad (49)$$

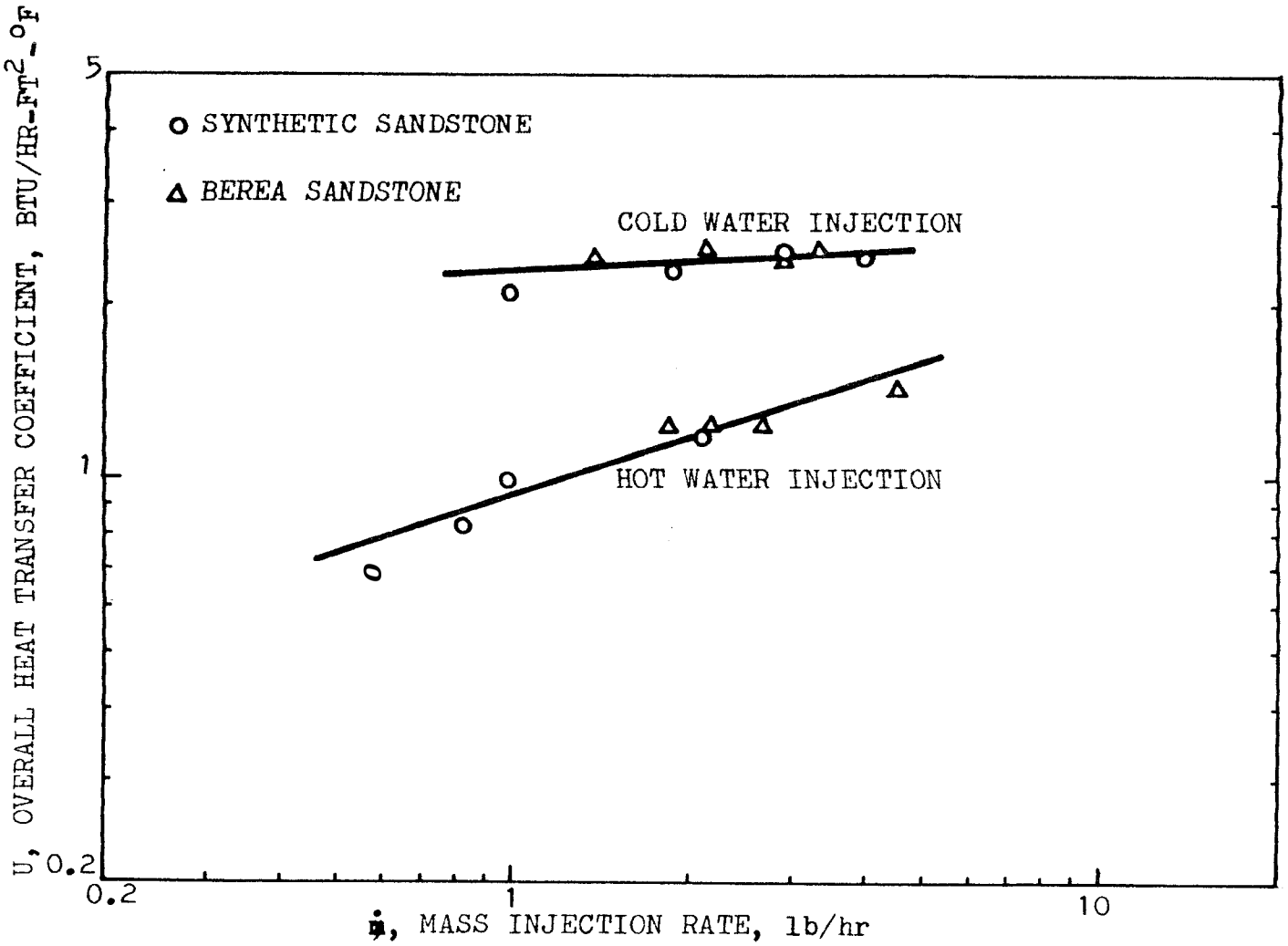

FIGURE 23. OVERALL HEAT TRANSFER COEFFICIENT VS. MASS INJECTION RATE

TABLE 1 Calculation of Overall Heat Transfer Coefficient of the Core Holder For Hot Water and Cold Water Injection Runs.

Run No.	$\dot{E}$ (lb-hr)	T_{in} (^{o}F)	T_{out} (^{o}F)	T_{∞} (^{o}F)	$\frac{dT_1}{dx}$ ($^{o}F/ft$)	U (Btu/hr-ft^2-^{o}F
HWI-S-1	0.575	126	92.5	82	-17.11	0.689
2	0.817	149	102	80	-24.50	0.831
3	0.968	152	102.5	80	-26.00	1.002
4	2.105	162	124	76	-20.00	1.173
HWI-B-1	1.846	130.5	105	80	-14.00	1.246
2	2.654	129.5	109	76	-11.00	1.245
3	2.180	174.5	131	79	-22.00	1.249
4	4.535	150	130	79	-10.00	1.443
CWI-S-1	0.971	131	149	148	9.00	2.080
2	1.865	116.5	140	147	12.00	2.277
3	2.886	158	211.5	247	28.00	2.441
4	3.929	135	183	235	24.00	2.401
CWI-B-1	1.380	157.5	177	177	[illegible].00	2.452
2	2.122	177	211	221	[illegible].00	2.480
3	2.918	153	186	208	[illegible].00	2.384
4	3.307	159	193	220	[illegible].30	2.442

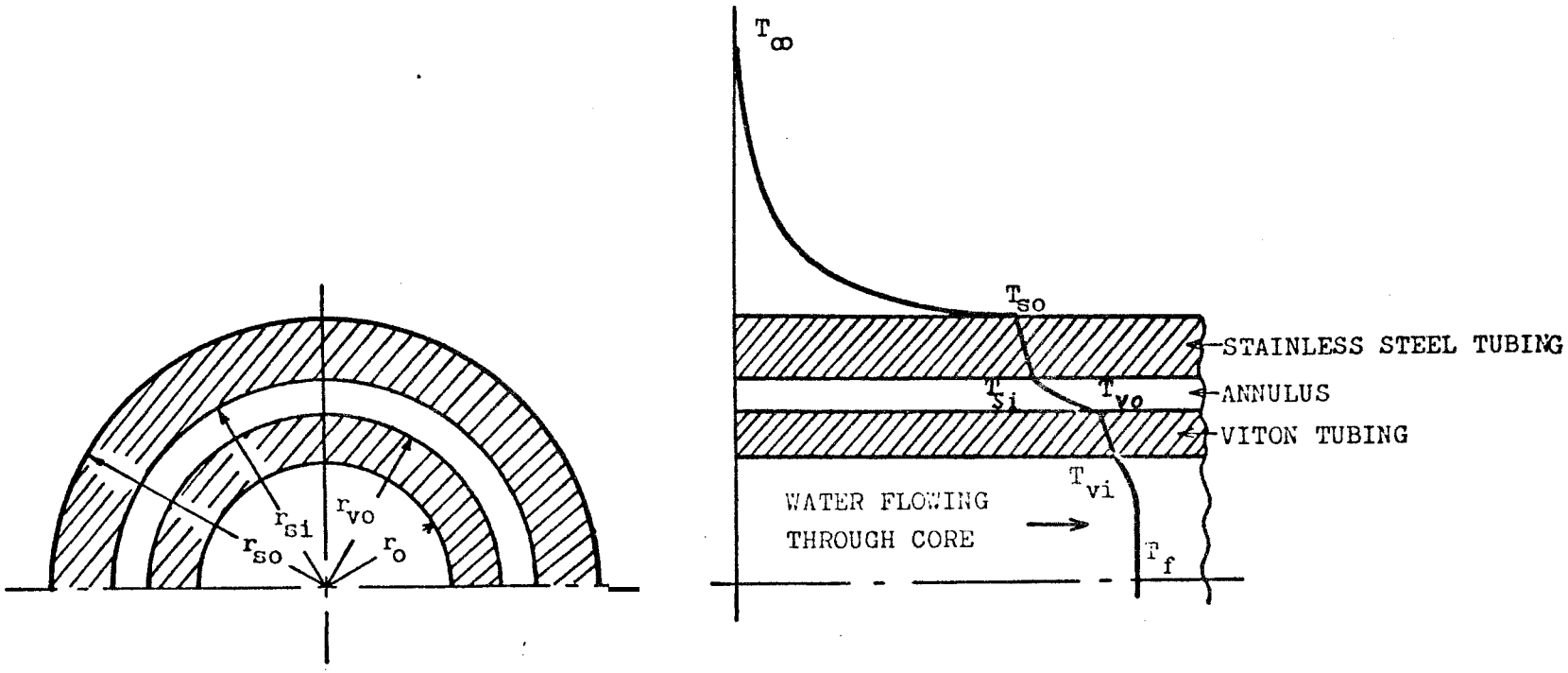

FIGURE 24. RADIAL TEMPERATURE DISTRIBUTION IN HOT WATER INJECTION

Eq. 49 means that U is based on a characteristic area $2\pi r_o \Delta L$, which is the outside surface area of an incremental length of the core, and on a characteristic temperature difference $\Delta T = T_f - T_\infty$ which is the difference between the temperature of the flowing fluid, T_f, and the ambient temperature, T_∞.

At the core-Viton sleeve interface, the rate of heat transfer is given by:

$$Q = 2\pi r_o h_f (T_f - T_{vi}) \Delta L \qquad (50)$$

h_f in Eq. 50 is the film coefficient for heat transfer based on the inside surface area of the Viton tubing, and the temperature difference between the flowing fluid and the inside Viton tubing wall. The interface area between the flowing fluid and the Viton tubing is assumed to be $2\pi r_o \phi \Delta L$, because a model as shown in Fig. 25 can be considered, in which sand grains (shown as hatched part) have a tight contact with the Viton tubing. Thus an infinite conductivity at the contact can be reasonably assumed. Now, hot water flows through the the Viton tubing, whose inner radius is $r_o \phi$. According to Holman[34], h_f

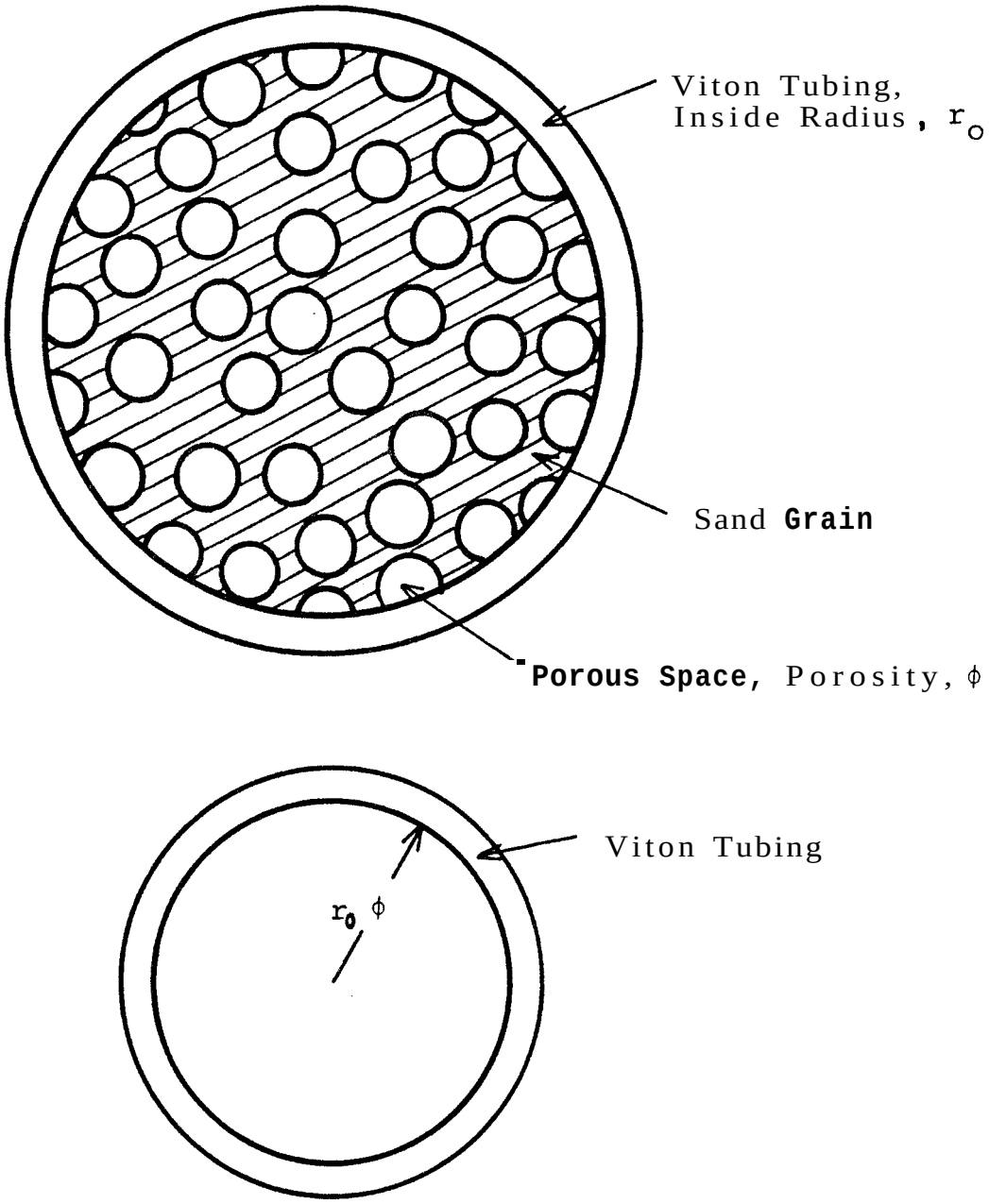

FIGURE 25. MODEL CONSIDERED TO ESTIMATE FILM COEFFICIENT AT INSIDE SURFACE OF VITON TUBING

is given by:

$$h_f = \frac{\lambda}{d} Nu_d$$

and $$Nu_d = 1.75 \left[Gz_d + 0.012 \left(Gz_d Gr_d^{1/3}\right)^{4/3}\right]^{1/3} \qquad (51)$$

where: Graetz number $$Gz_d = Re_d \, Pr \frac{d}{L}$$

Grashof number $$Gr_d = \frac{\rho^2 g\beta \, (T_{vi} - \overline{T}_b) \, d^3}{\mu^2}$$

Reynolds number $$Re_d = \frac{Gd}{\mu}$$

Prandtl number $$Pr = \frac{Cp\mu}{\lambda}$$

$\beta = \frac{1}{V} \left(\frac{\partial V}{\partial T}\right)_p$ volume coefficient of expansion

$\overline{T}_b = \frac{1}{L} \int_0^L T_f dz$ mean hulk temperature

$G = {}^{m}/_{A}$ mass velocity

The applicable range of Eq. 51 is for $10^{-2} < Pr(\frac{d}{L}) < 1$.

Heat flow through the Viton tubing wall occurs by conduction.

From Fourier's law:

$$Q = 2\pi r \lambda_v \frac{dT}{dr} \Delta L$$

Integrating:

$$Q = \frac{2\pi\lambda_v \, (T_{vi} - T_{vo}) \, \Delta L}{\ln \frac{r_{vo}}{r_o}} \qquad (52)$$

Three modes of heat transfer may be considered in the annulus between the Viton tubing and the outer shell. See Willhite[32] for an analogous problem in a wellbore. Heat is conducted through the atmosphere of confining pressure contained in the annulus. Radiation and natural convection also occur independently. At very low Grashof numbers, there are minute free-convection currents, and the heat transfer occurs mainly by conduction across the fluid layer. If the effect of curvature is assumed to be negligible, heat transfer in horizontal enclosed spaces can be applied to the subject case with reasonable error. Let δ be the separation distance between two horizontal plates. Then,

according to Holman for values of Gr_δ below about 1700, pure conduction is observed and:

$$Nu_\delta \equiv \frac{A_e}{\lambda} = 1.0 \tag{53}$$

where λ_e is apparent thermal conductivity.

Thus, neglecting radient heat transfer, heat flux in the annulus is:

$$Q = \frac{2\pi\lambda_e (T_{vo} - T_{si}) AL}{\ln \frac{r_{si}}{r_{vo}}} \tag{54}$$

Heat :flow through the outer shell wall is given by:

$$Q = \frac{2\pi\lambda_{ss} (T_{si} - T_{so}) \Delta L}{\ln \frac{r_{so}}{r_{si}}} \tag{55}$$

Finally, at the outside surface of the shell, free convection occurs from the surface of the horizontal cylinder to the air at atmospheric pressure. A simplified equation for estimation of the average heat transfer coefficient was given by McAdams[35] as follows:

$$h_\infty = 0.27 \left(\frac{\Delta T}{d}\right)^{1/4} \tag{56}$$

where $\Delta T = T_{so} - T_\infty$

The heat flux is:

$$Q = 2\pi r_{so} h_\infty (T_{so} - T_\infty) \Delta L$$

Because radial heat transfer is assumed to be at steady state, the heat flux through all components are equal, and the overall heat transfer coefficient U in Eq. 49 is given by the following:

$$U = \frac{1}{r_o}\left(\frac{1}{r_o h_f} + \frac{\ln \frac{r_{vo}}{r_o}}{\lambda_v} + \frac{\ln \frac{r_{si}}{r_{vo}}}{\lambda_e} + \frac{\ln \frac{r_{so}}{r_{si}}}{\lambda_{ss}} + \frac{1}{r_{so} h_\infty}\right)^{-1} \tag{57}$$

As indicated by Ramey[33], because λ_v and λ_{ss} are of high value, the second and fourth terms can be dropped. Thus,

$$U = \frac{1}{r_o}\left(\frac{1}{r_o h_f} + \frac{\ln \frac{r_{so}}{r_{si}}}{\lambda_e} + \frac{1}{r_{so} h_\infty}\right)^{-1} \tag{58}$$

The computed results are shown in Table 2. Among h_f, λ_e, and h_∞, the film coefficient at the outer surface of the stainless steel tubing, h_∞, is the dominant factor. h_∞ as well as λ_e is an increasing function of temperature. Although the film coefficient at the boundary between the core and Viton tubing, h_f, is a function of the mass rate of flow, it is a small contribution to the overall heat transfer coefficient. In Table 2 the values of U calculated with the assumption of infinite h_f are also listed. There are only small differences between the values of U calculated by assuming finite and infinite h_f. The theoretical results are in good agreement with the results from Eq. 48, which are shown in Fig. 23.

TABLE 2. Summary of Computed and Experimental Overall Heat Transfer Coefficient of the Core Holder for Hot Water Injection (Computed values from Eq. 58).

Run No.	h_f (Btu/hr-ft^2-^{o}F)	λe (Btu/hr-ft-^{o}F)	h_∞ Btu/hr-ft^2-^{o}F)	U (Btu/hr-ft^2-^{o}F)	Calc.(1) U	Measured(2) U
HWI-S-1	9.898	0.0158	0.787	0.890	1.019	0.689
2	12.322	0.0162	0.957	1.041	1.182	0.881
3	15.356	0.0163	0.977	1.066	1.201	1.002
4	19.778	0.0166	1.083	1.174	1.281	1.173
HWI-B-1	20.434	0.0161	0.933	1.059	1.159	1.246
2	23.857	0.0161	0.952	1.087	1.175	1.245
3	24.609	0.0168	1.095	1.206	1.312	1.249
4	32.000	0.0165	1.039	1.182	1.259	1.443

(1) Calculated with the assumption of infinite h_f

(2) given by Eq. 48 from experimental data, also presented in Table 1

Cold Water Injection

Four runs of cold water injection were carried out for each core at varying rates and ambient temperatures. Figs. 26-29 show temperature vs. distance for the synthetic core, and Figs. 30-33 present results for the Berea sandstone core. Because cold water injection is the reverse procedure to hot water injection, the same analysis as is made for hot injection can be performed. Fig. 34 presents the calculated temperature distributions for various times. For this computation, an overall heat transfer coefficient for steady state was used for all injection times, which caused lower temperature distributions before the radial heat transfer became steady.

The following constants were used for the calculation of Eq. 46:

ρ_s = 165.4 lb/ft^3

C_s = 0.21 Btu/lb - ^oF

ρ_w = 62.0 lb/ft^3

C_w = 1.0 Btu/lb - ^oF

ϕ = 22%

U = 2.384 Btu/hr - ft^2 - ^0F

The value of U was calculated with Eq. 48 from experimental data.

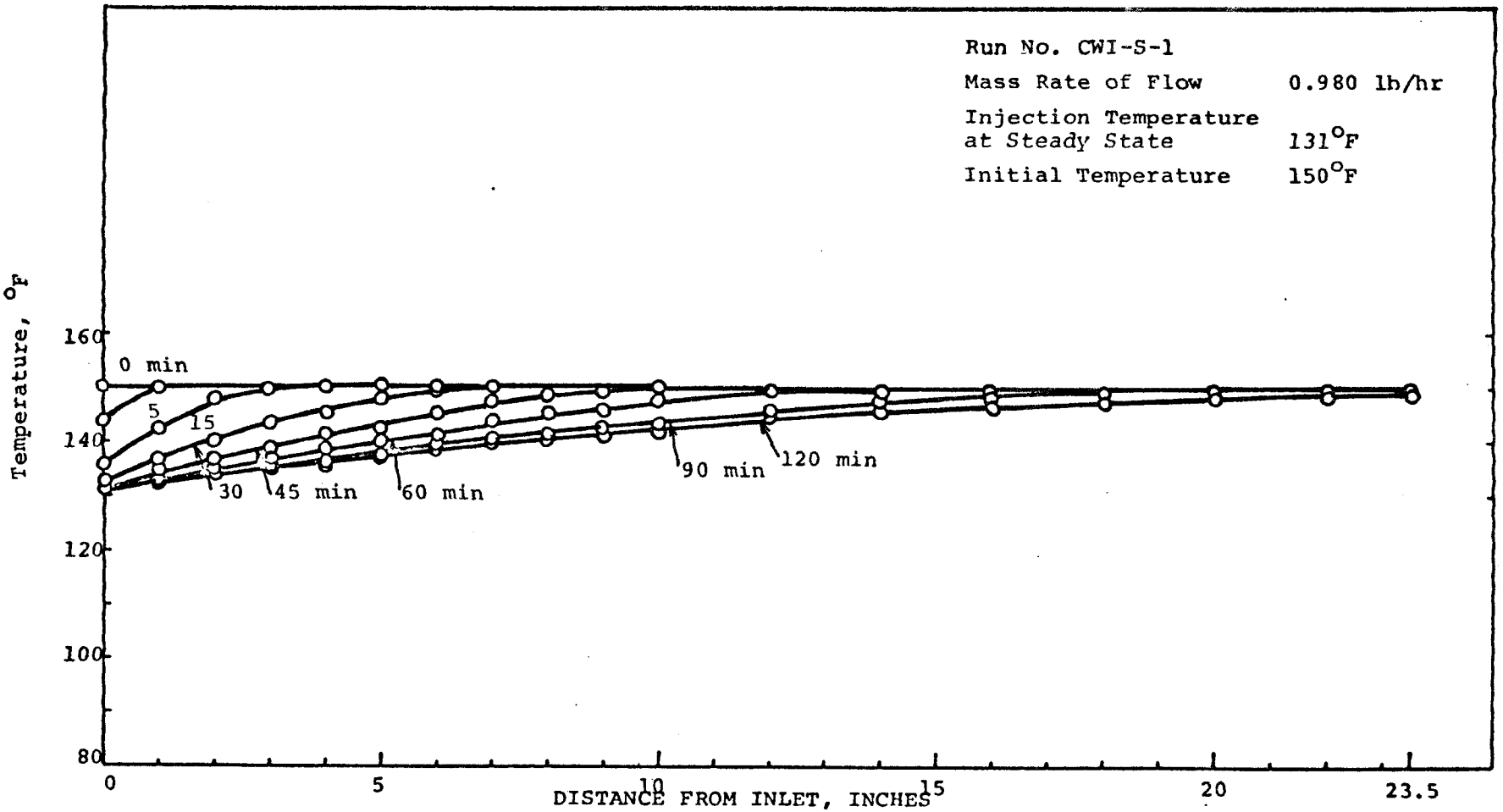

FIGURE 26. TEMPERATURE VS. DISTANCE FOR COLD WATER INJECTION, SYNTHETIC SANDSTONE; RATE = 0.980 lb/hr, TEMP. = 131°F

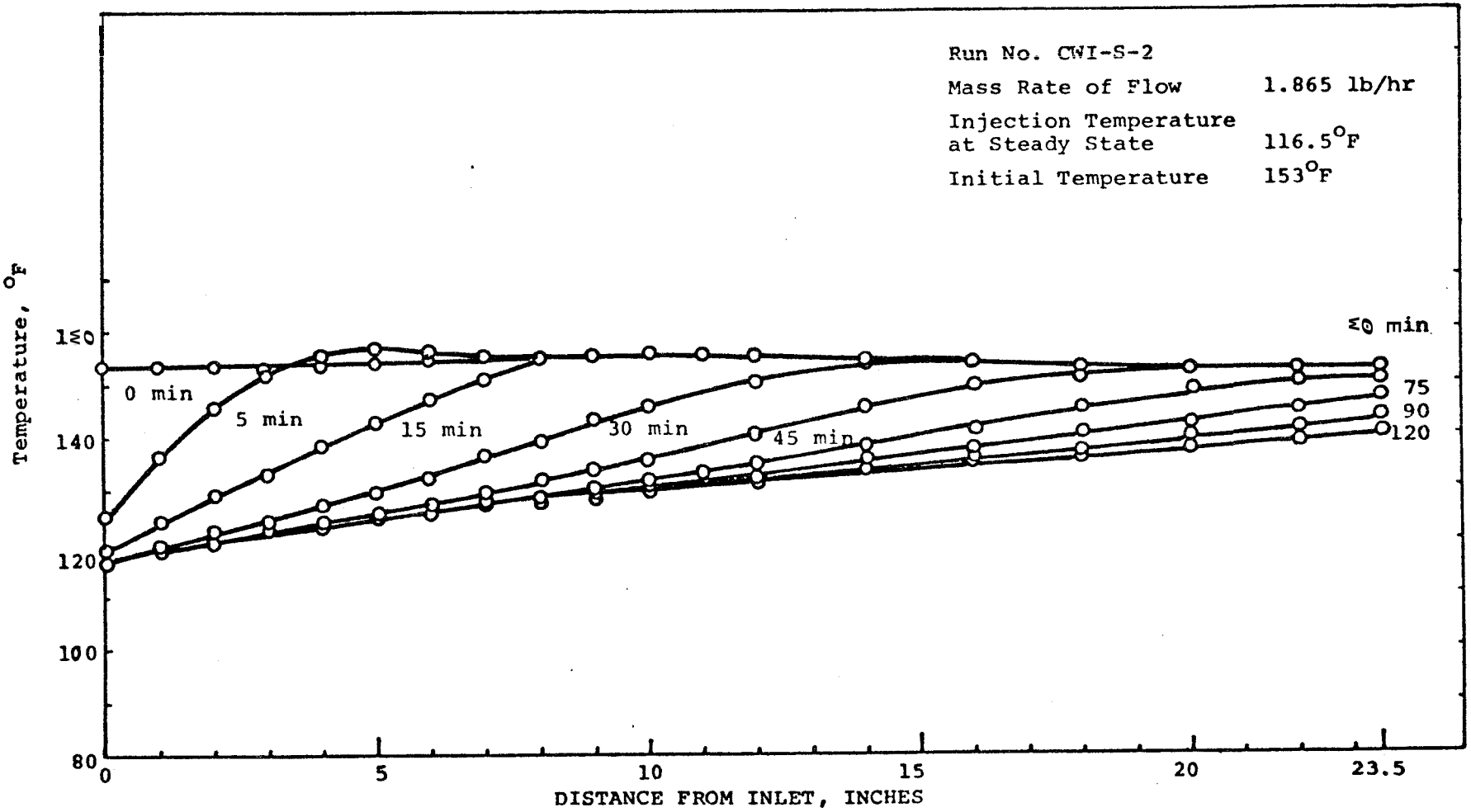

FIGURE 27. TEMPERATURE VS. DISTANCE FOR COLD WATER INJECTION, SYNTHETIC SANDSTONE; RATE = 1.865 lb/hr, TEMP. = 116.5°F

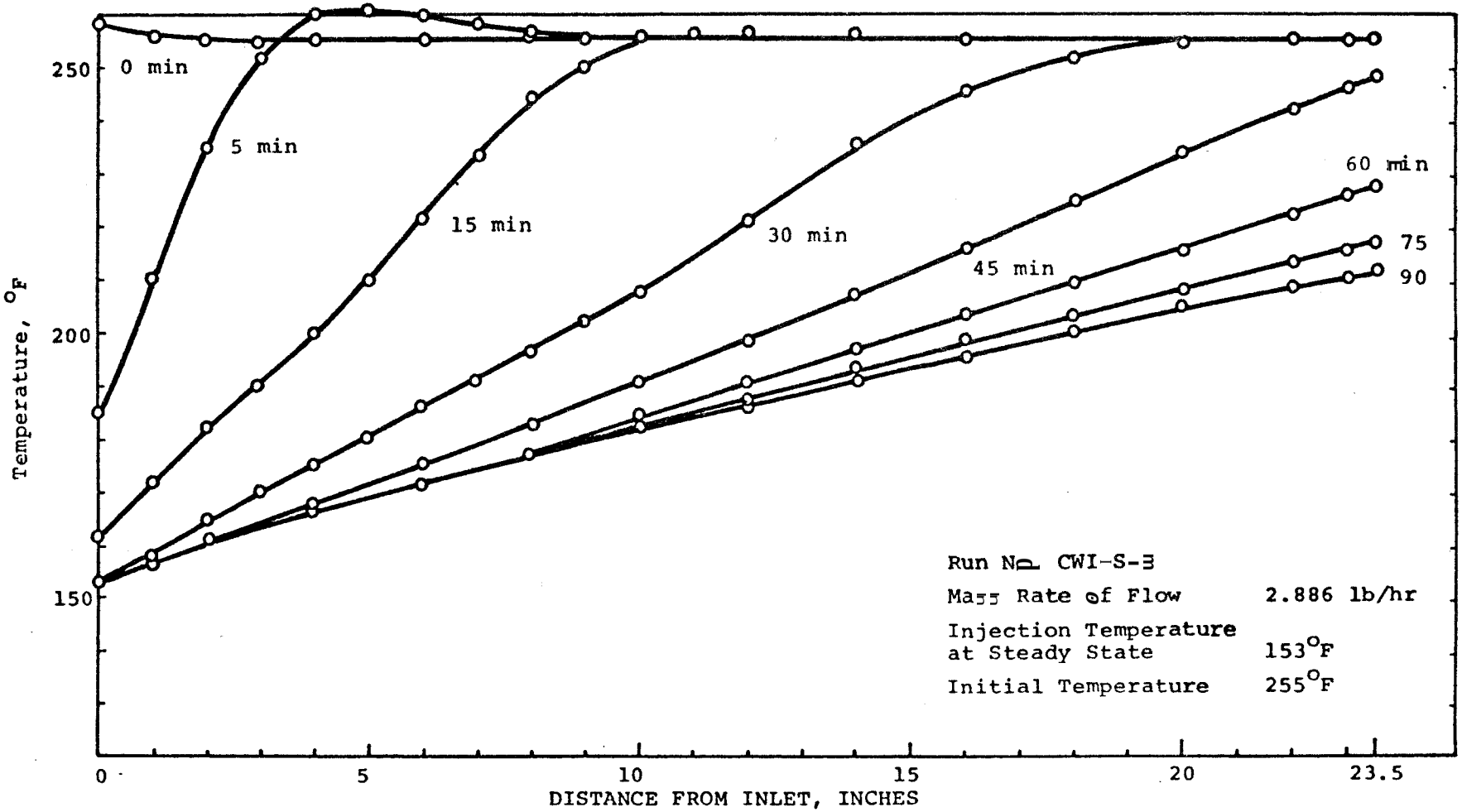

FIGURE 28. TEMPERATURE VS. DISTANCE FOR COLD WATER INJECTION, SYNTHETIC SANDSTONE; RATE = 2.886 lb/hr, TEMP. = 153°F

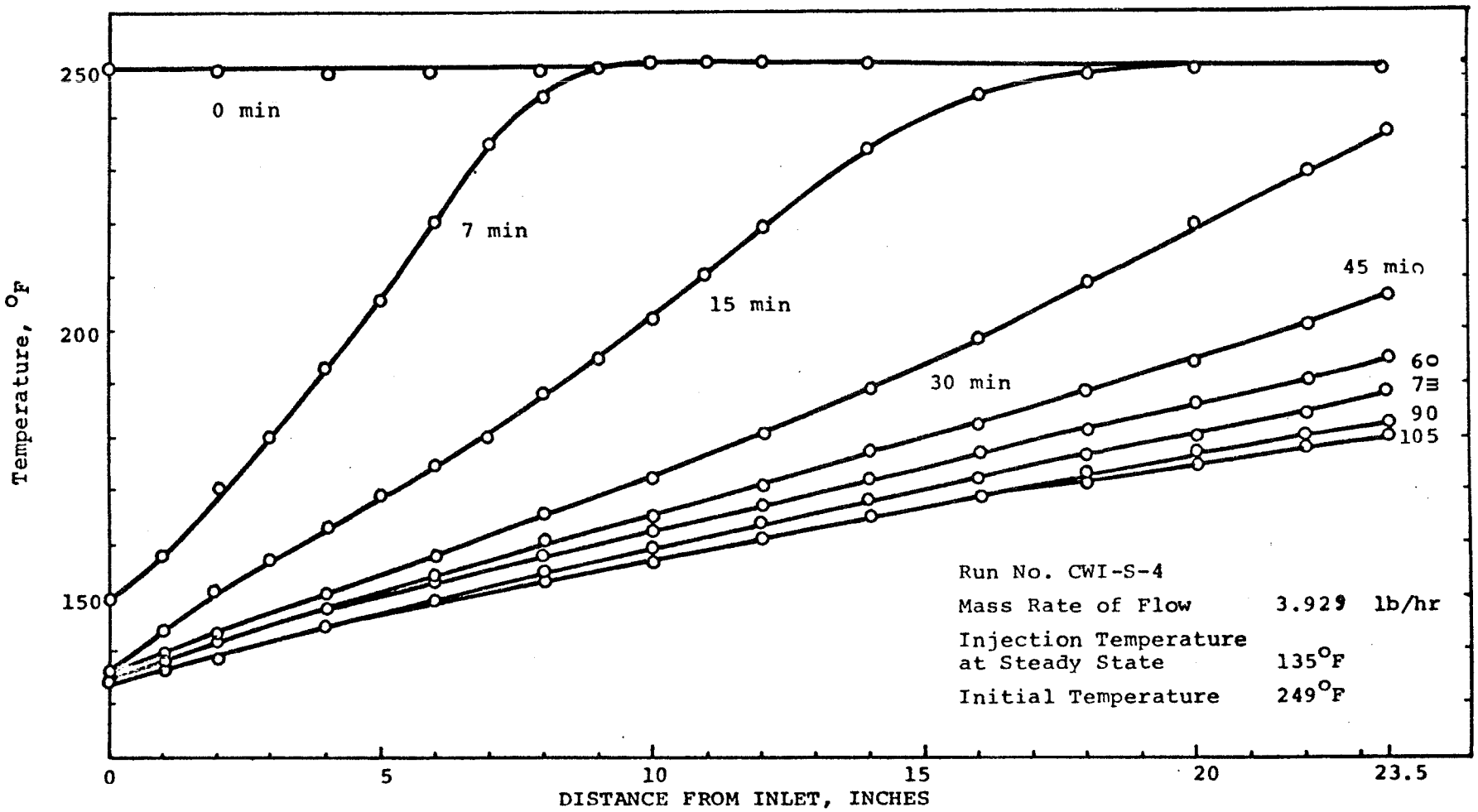

FIGURE 29. TEMPERATURE VS. DISTANCE FOR COLD WATER INJECTION SYNTHETIC SANDSTONE; RATE = 3.929 lb/hr, TEMP. = 135°F

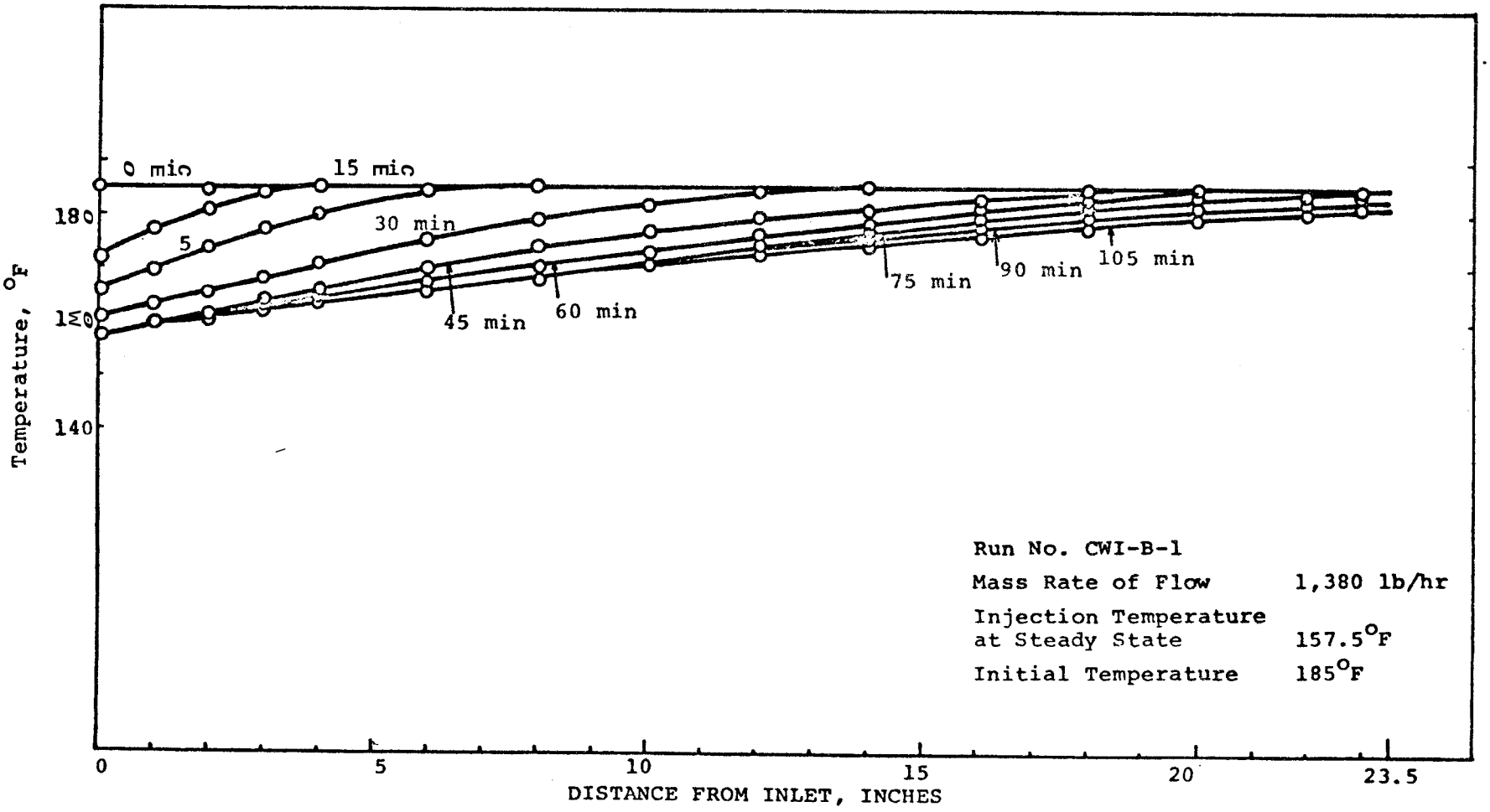

FIGURE 30 TEMPERATURE VS. DISTANCE FOR COLD WATER INJECTION, BEREA SANDSTONE; RATE = 1.380 lb/hr, TEMP. = 157.5°F

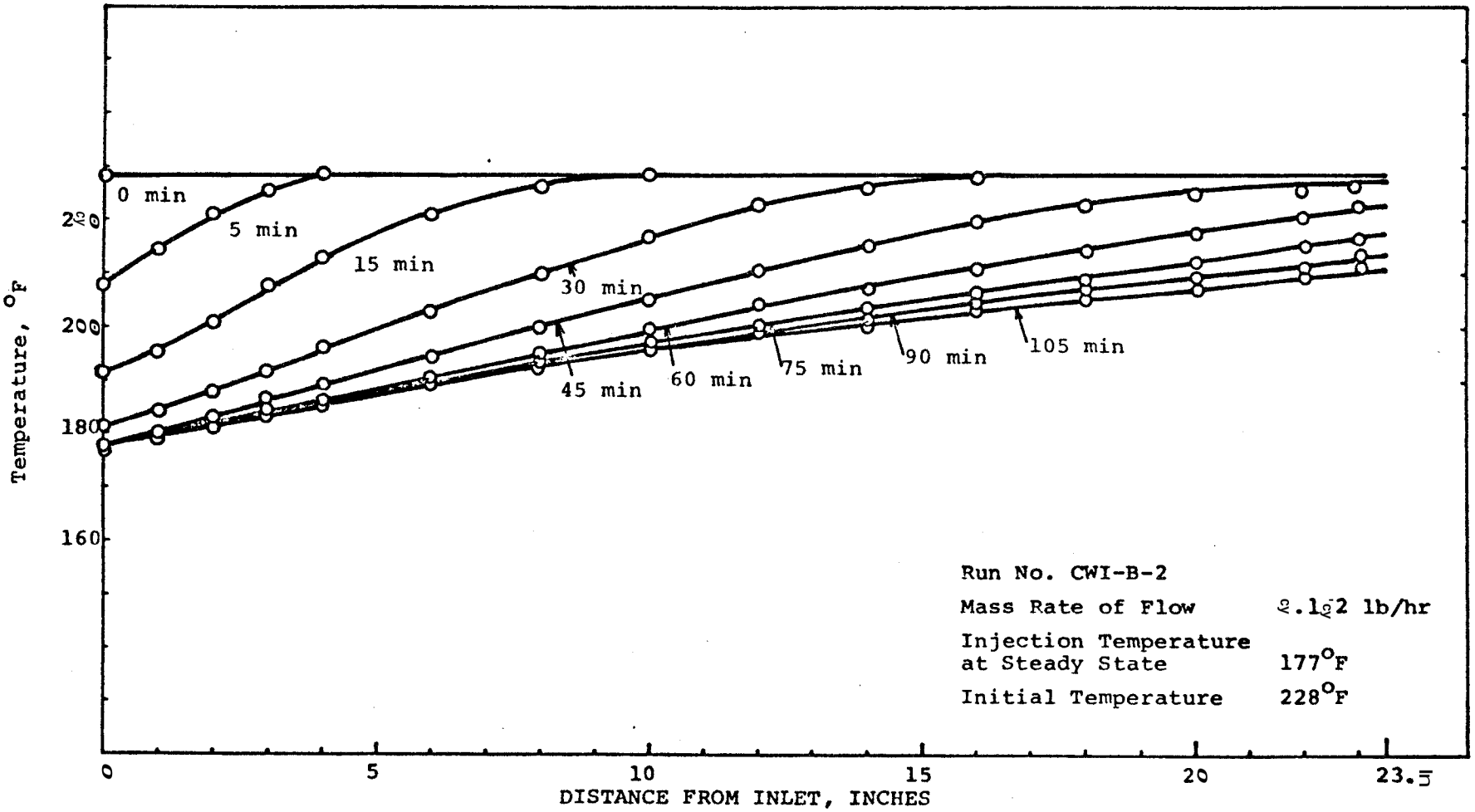

FIGURE 31. TEMPERATURE VS. DISTANCE FOR COLD WATER INJECTION BEREA SANDSTONE; RATE = 2.122 lb/hr, TEMP. = 177°F

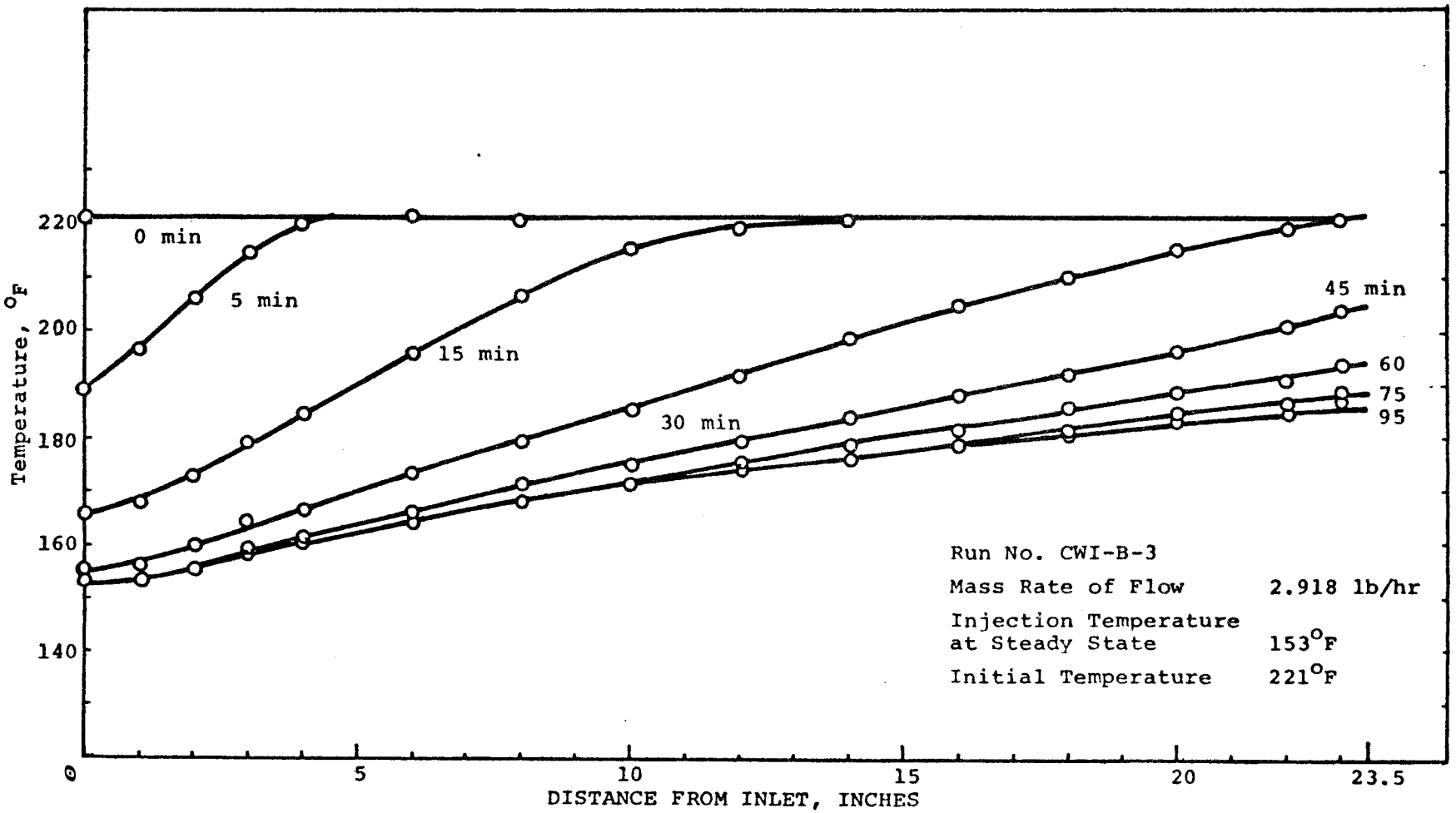

FIGURE 32. TEMPERATURE VS. DISTANCE FOR COLD WATER INJECTION, BEREA SANDSTONE: RATE = 2.918 lb/hr, TEMP. = 153°F

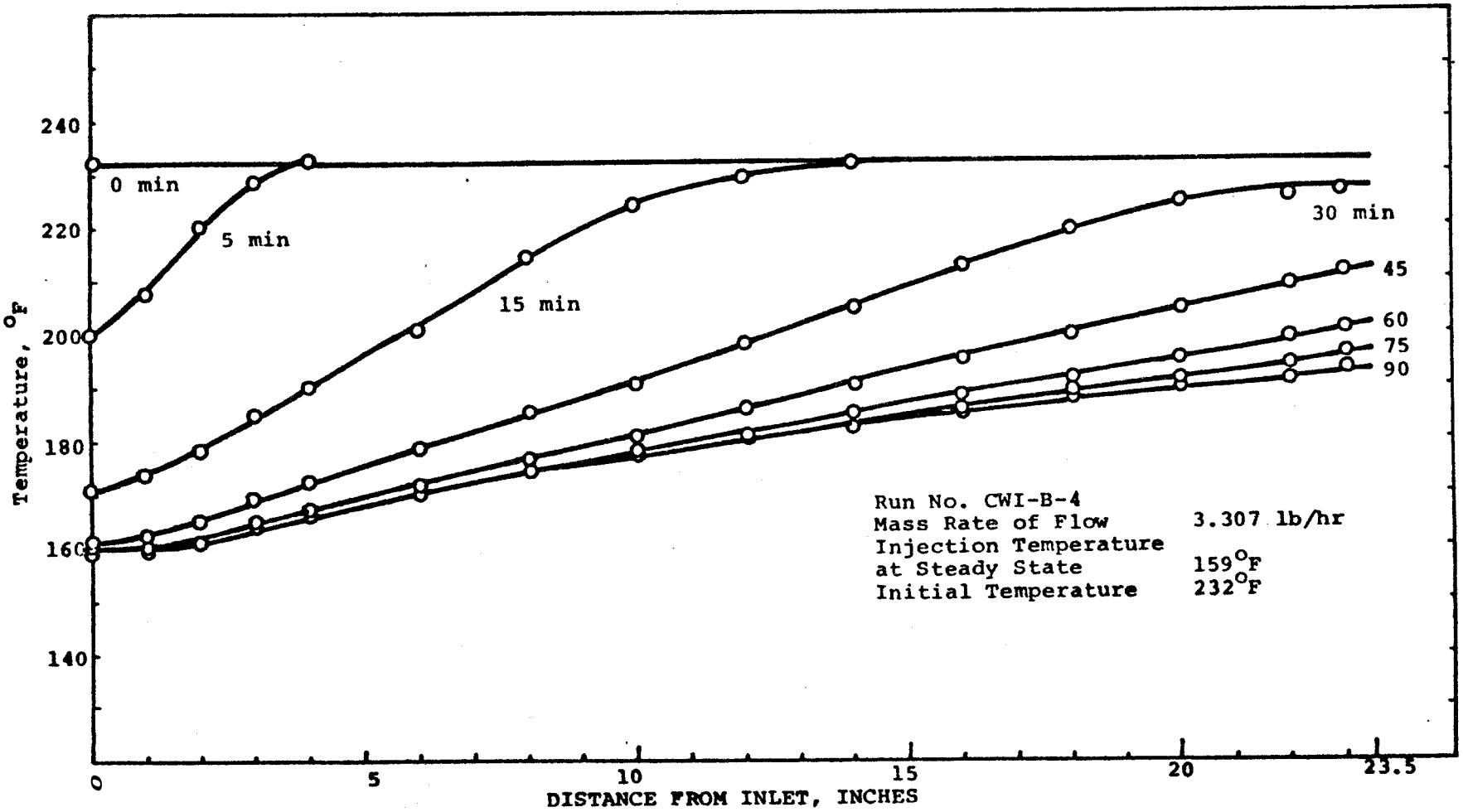

FIGURE 33. TEMPERATURE VS. DISTANCE FOR COLD WATER INJECTION, BEREA SANDSTONE; RATE = 3.307 lb/hr, TEMP. = 159°F

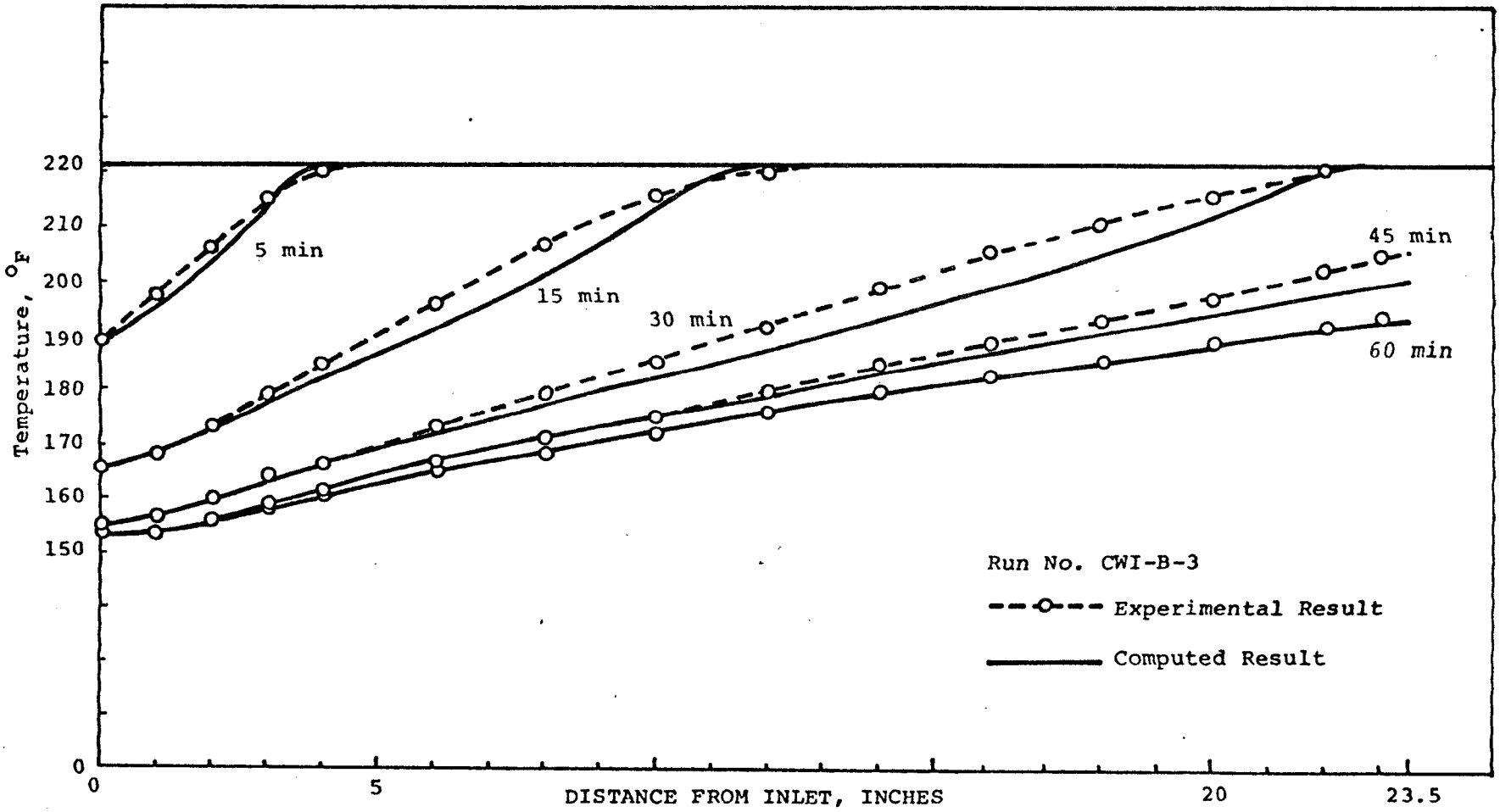

FIGURE 34. COMPARISON OF THEORETICAL AND EXPERIMENTAL TEMPERATURES FOR COLD WATER INJECTION, BEREA SANDSTONE

The thermal efficiencies in cold water injection are shown in Figs. 35 and 36 for the synthetic core and Berea sandstone core, respectively. In this case, thermal efficiency is defined as:

$$E \triangleq \frac{\text{Cumulative Rtu Cooling in the Core}}{\text{Cumulative Btu Cooling Injected}}$$

$$= \frac{\text{Cumulative Btu Cooling 'Injected - 'Heat from Surroundings}}{\text{Cumulative Rtu Cooling Injected}}$$

Thermal efficiency in cold water injection is also heat injection rate dependent, which means that the core is cooled more efficiently (less heat comes in from the surroundings) when the injection rate, $\dot{m}C_w\Delta T$, is higher. ΔT in this case is equal to the initial uniform temperature of the core minus the injection temperature, i.e., $\Delta T = T_o - T_i$.

This heat rate dependency in cold water injection is more obvious than in the hot water injection runs because of a difference in the overall heat transfer coefficient. In the case of cold water injection, the heat gained from the surroundings is of interest. This would be analogous to a cold water injection for heat scavenging in a geothermal energy production operation. It may be concluded, from Figs. 35 and 36, that the lower the heat injection rate, the more efficiently heat is extracted from the surroundings. Figs. 37 and 38 are different presentations in which thermal efficiency is graphed against injection time.

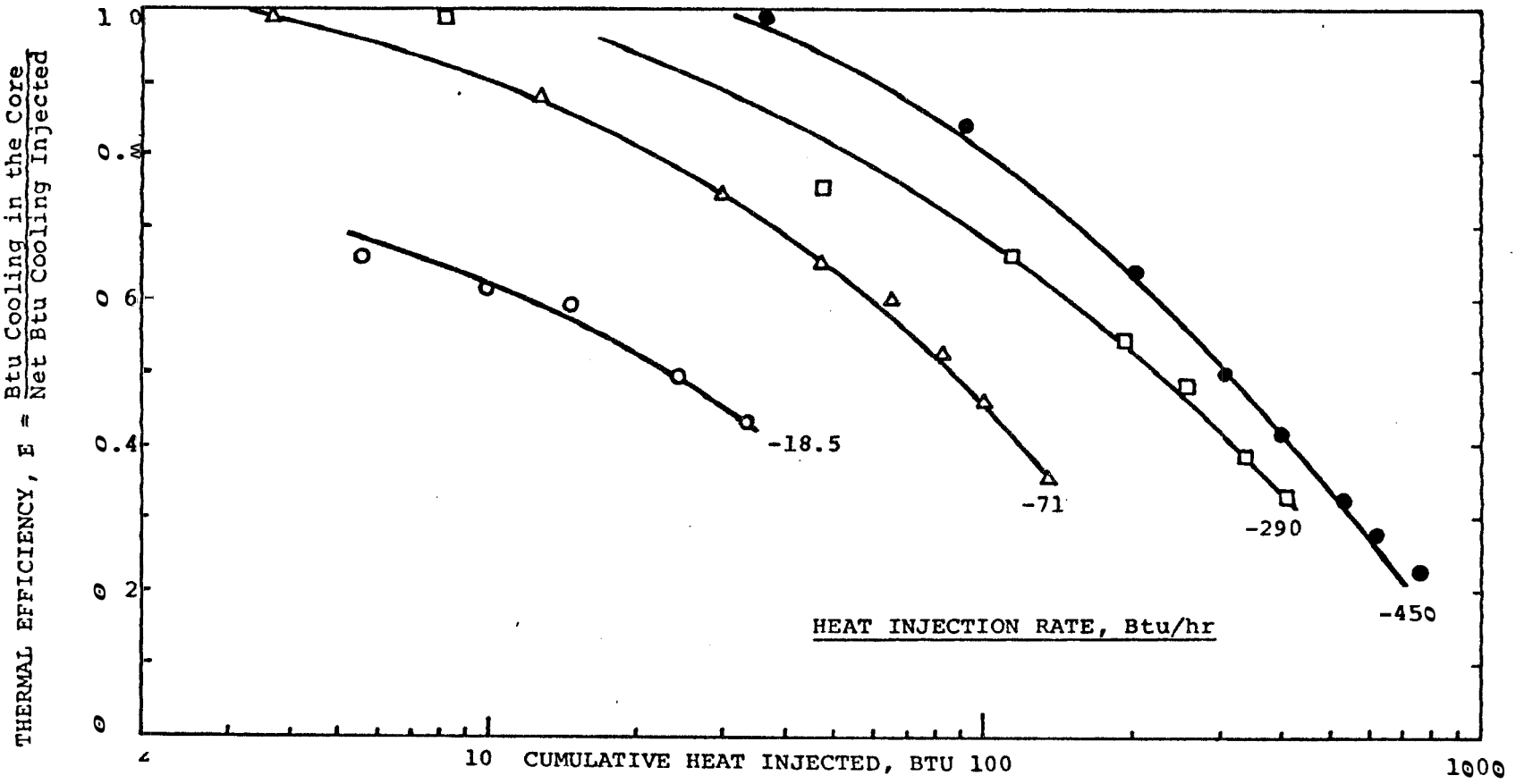

FIGURE 35. THERMAL EFFICIENCY AS A FUNCTION OF CUMULATIVE HEAT INJECTED IN COLD WATER INJECTION, SYNTHETIC SANDSTONE

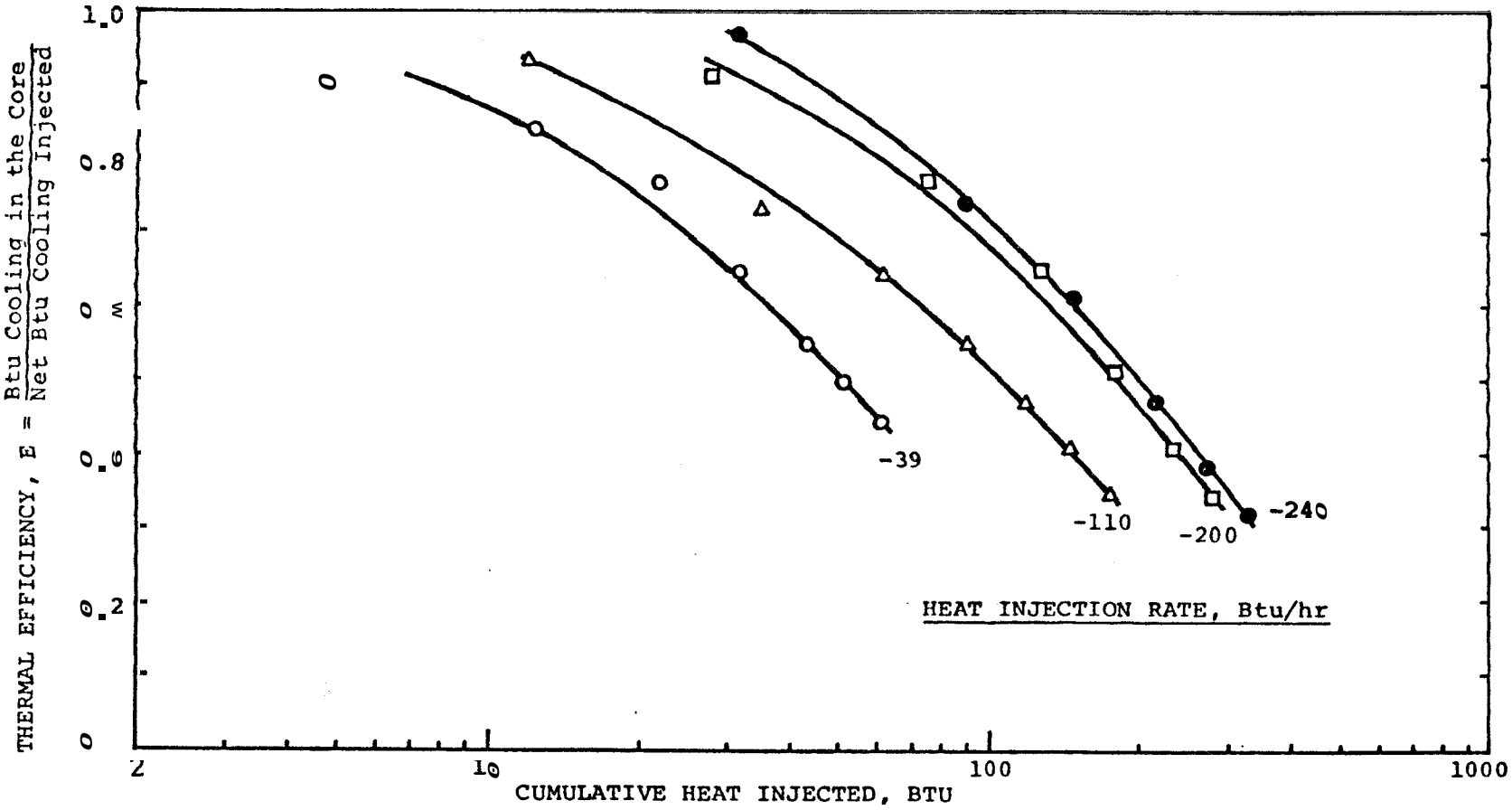

FIGURE 36. THERMAL EFFICIENCY AS A FUNCTION OF CUMULATIVE HEAT INJECTED IN COLD WATER INJECTION, BEREA SANDSTONE

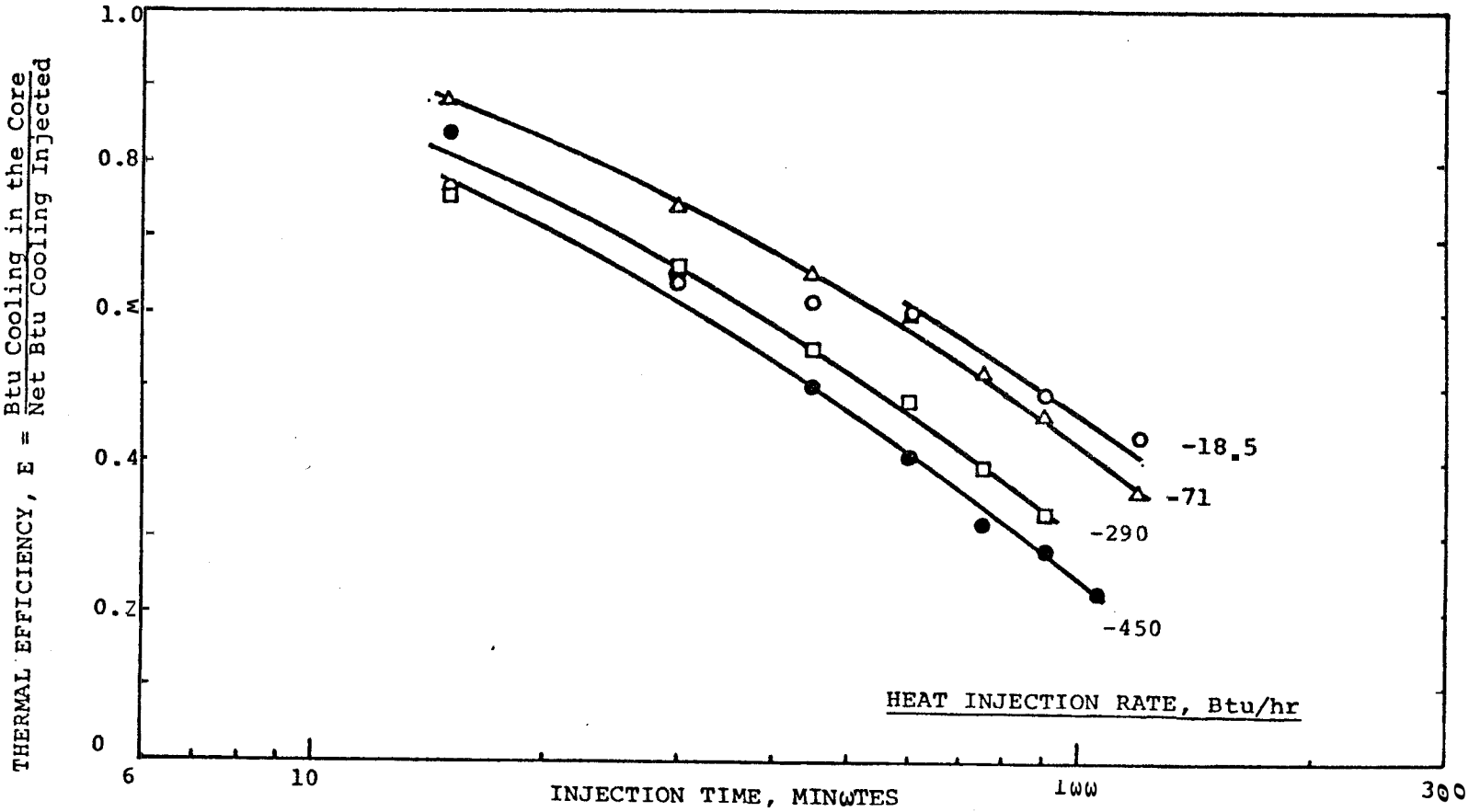

FIGURE 37. THERMAL EFFICIENCY AS A FUNCTION OF INJECTION TIME IN COLD WATER INJECTION, SYNTHETIC SANDSTONE

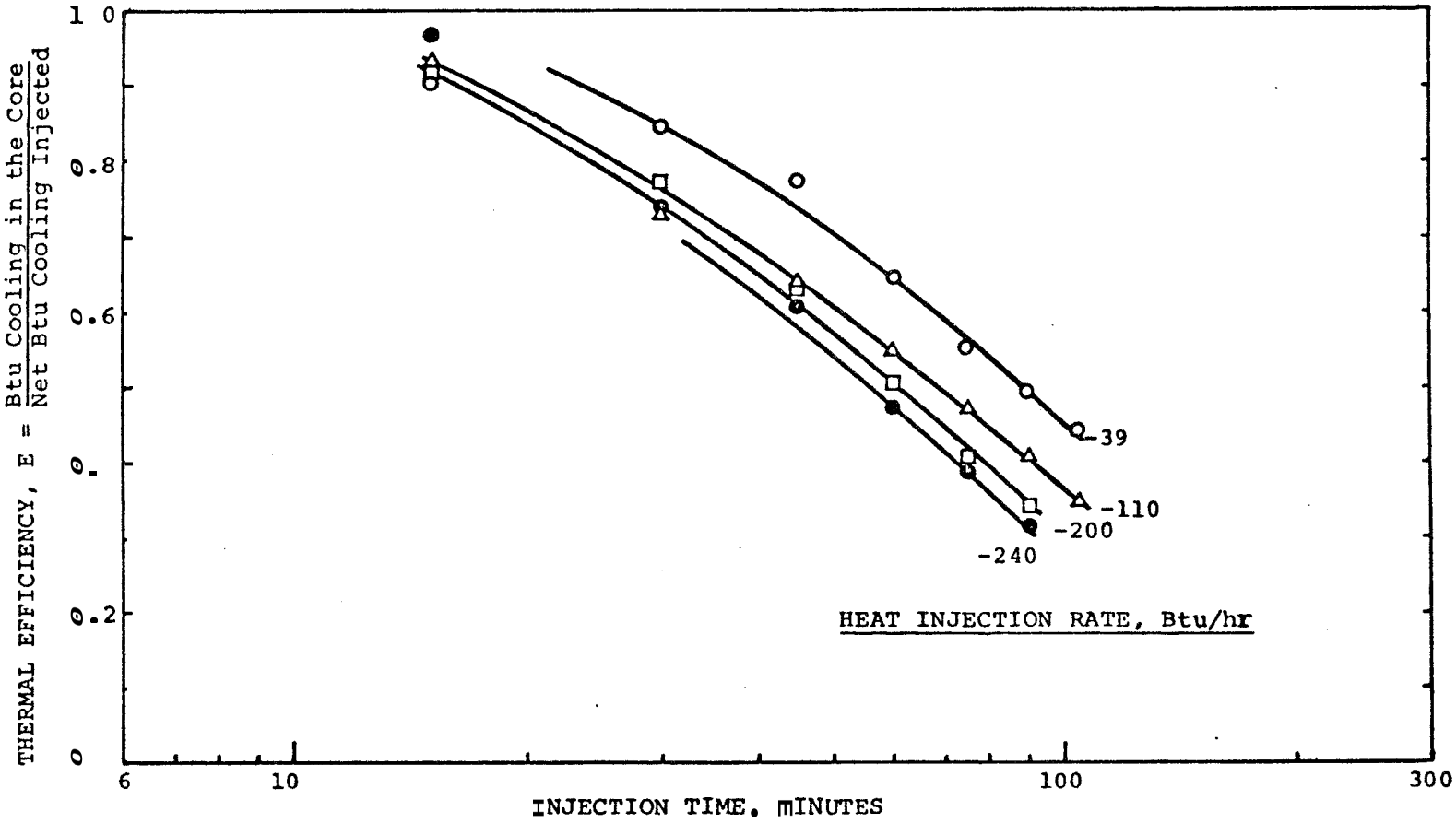

FIGURE 38. THERMAL EFFICIENCY AS A FUNCTION OF INJECTION TIME IN COLD WATER INJECTION, BEREA SANDSTONE

These are of interest because the apparent heat rate dependency is reversed. The core is cooled down more efficiently when the injection rate $\dot{m}C_w\Delta T$ is lower. Thus, for a specified injection period, higher values of $\dot{m}C_w\Delta T$ result in more effective heat extraction from the surroundings. When water is injected with a constant mass rate, the lower the injection temperature is than the surroundings temperature, the more effectively heat is extracted from the surroundings within a certain period of time.

The overall heat transfer coefficients at steady state can be also estimated by using Eq. 48. The calculated results are presented in Fig. 23 and Table 1. As clearly seen in Fig. 23, the overall coefficient for cold water injection is about twice as large as that for hot water injection runs. The reason appears to be related to the film coefficient outside the core holder.

In the cold water injection experiments, the ambient air was stirred by a fan, and at constant temperatures ranging from about 150°F to 250°F depending on the run. The radial heat transfer mechanism was the same except for forced convection at the outer surface of the core holder, rather than the free convection which existed for the hot water injection experiments. This forced convection caused high film coefficients outside the core and thus overall heat transfer coefficients for cold water injection that were much higher than those for hot water injection.

This fact can be substantiated by evaluating the average heat transfer coefficient at the outer surface of the shell. Holman[34] presented a correlation for the heat transfer coefficient of a cylinder placed in a transverse airstream, h_∞, as follows:

$$\frac{h_\infty d}{\lambda_f} = C \left(\frac{u_\infty d}{\nu}\right)^n Pr_f^{1/3} \qquad (59)$$

The properties of air are evaluated at the film temperature, as indicated by the subscript f.

For $4{,}000 < Re_{df} < 40{,}000$, $C = 0.193$ and $n = 0.618$

Table 3 presents the calculated results. It can be seen in Table 3 that apparent thermal conductivity of the atmosphere of confining pressure, λ_e, and the film coefficient at the outer :surface of the stainless steel tubing, h_∞, contribute importantly to the overall heat transfer coefficient, U. In Table 3, the values of U calculated with the assumption of infinite film coefficient at the boundary between the core and Viton tubing, h_f, are also listed. Contrary to the rate sensitivity of h_f, h_∞ has nearly constant values. The overall heat transfer coefficient has only a weak rate sensitivity in the cold water injection runs, because h_∞ masks the rate sensitive h_f.

Finally, some observations concerning pressure drop during cold and hot water flooding have been made. Weinstein, et al.[18], applied a numerical model to cold water flooding a warm reservoir. Their study showed that:

TABLE 3. Summary of Computed and Experimental Overall Heat Transfer Coefficient of the Core Holder for Cold Water Injection. (Computed values were given by Eqs. 58 and 59.)

Run No.	h_f (Btu/hr-ft^2-^{o}F)	λ_e (Btu/hr-ft-^{o}F)	h_∞ (Btu/hr-ft^2-^{o}F)	Calc. U (Btu/hr-ft^2-^{o}F)	Calc.[1] U	Measured[2] U
CWI-S-1	14.217	0.0166	3.605	2.000	2.491	2.080
2	17.909	0.0163	3.591	2.061	2.459	2.277
3	24.625	0.0177	3.475	2.225	2.549	2.441
4	27.848	0.0170	3.501	2.217	2.497	2.401
CWI-B-1	21.341	0.0173	3.578	2.125	2.545	2.452
2	27.157	0.0181	3.508	2.238	2.592	2.480
3	29.825	0.0174	3.541	2.228	2.543	2.384
4	32.045	0.0175	3.511	2.247	2.543	2.442

(1) calculated with the assumption of infinite h_f

(2) given by Eq. 48 from experimental data, also presented in Table 1

(1) cold water quickly cools the reservoir in the region surrounding the wellbore, and accounts for the major part of the pressure drop across the reservoir, and (2) that heating the injected water has a marked effect in decreasing the pressure drop. This phenomenon has also been observed in the present study, and can be explained with Darcy's law:

$$m = A\frac{\rho_w k_w}{\mu_w}\frac{\Delta p}{\Delta L}, \text{ or } \Delta p = \frac{m\mu_w \Delta L}{A\rho_w k_w}$$

The pressure drop across a certain length AL is proportional to (μ_w/ρ_w) in water flow with a constant mass rate $\dot{m}$. Both viscosity and density decrease as temperature increases, as shown in Appendix B, but viscosity drops rapidly from about 1 cp at 70°F to 0.18 cp at 300°F, while density decreases more slowly from 62.4 lb/ft3 to 57.3 lb/ft^3 for the same temperature increase. As a result of the behavior of the factor (μ_w/ρ_w), the pressure drop at 70°F is about five times as large as at 300°F.

Steam Injection

Figs. 39, 49, and 41 are the temperature profiles measured during steam injection into a core containing water at room temperature. The linear portion of the temperature profiles from the inlet of the core is the condensing steam region. All radial heat loss would have to be supplied by latent heat of condensation. The sharp break downwards indicates that all steam has been condensed and may be considered the leading edge of the steam bank. In all cases, tlhe injection rates are low such that the injected steam loses all latent heat and the steam front stagnates within the length of the core. After the steam front stagnates, the system beyond the steam front is heated only by the flow of hot water. Using Figs. 39-41, the overall heat transfer coefficient, U, can be obtained. Assuming a constant U, and that saturated steam is injected, the heat loss from the inlet of the core to the steam front stagnating is given by the following,

$$\dot{m}\, h_{fg} = U\, 2\pi r_o \int_o^{X_s} (T_1 - T_\infty)\, dX$$

where X_s is the distance of the stagnation point from the inlet.

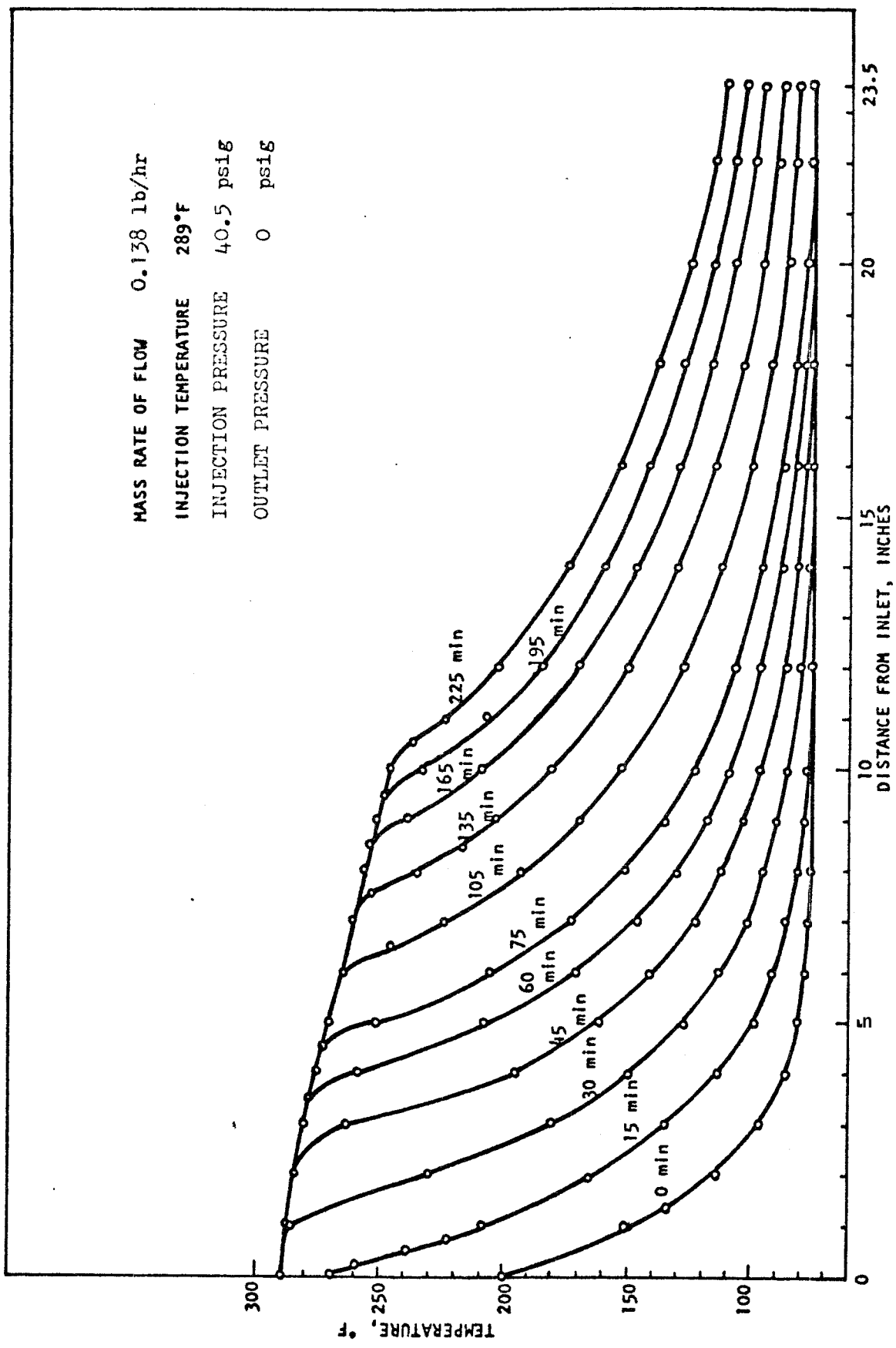

FIGURE 39. TEMPERATURE VS. DISTANCE FOR STEAM INJECTION

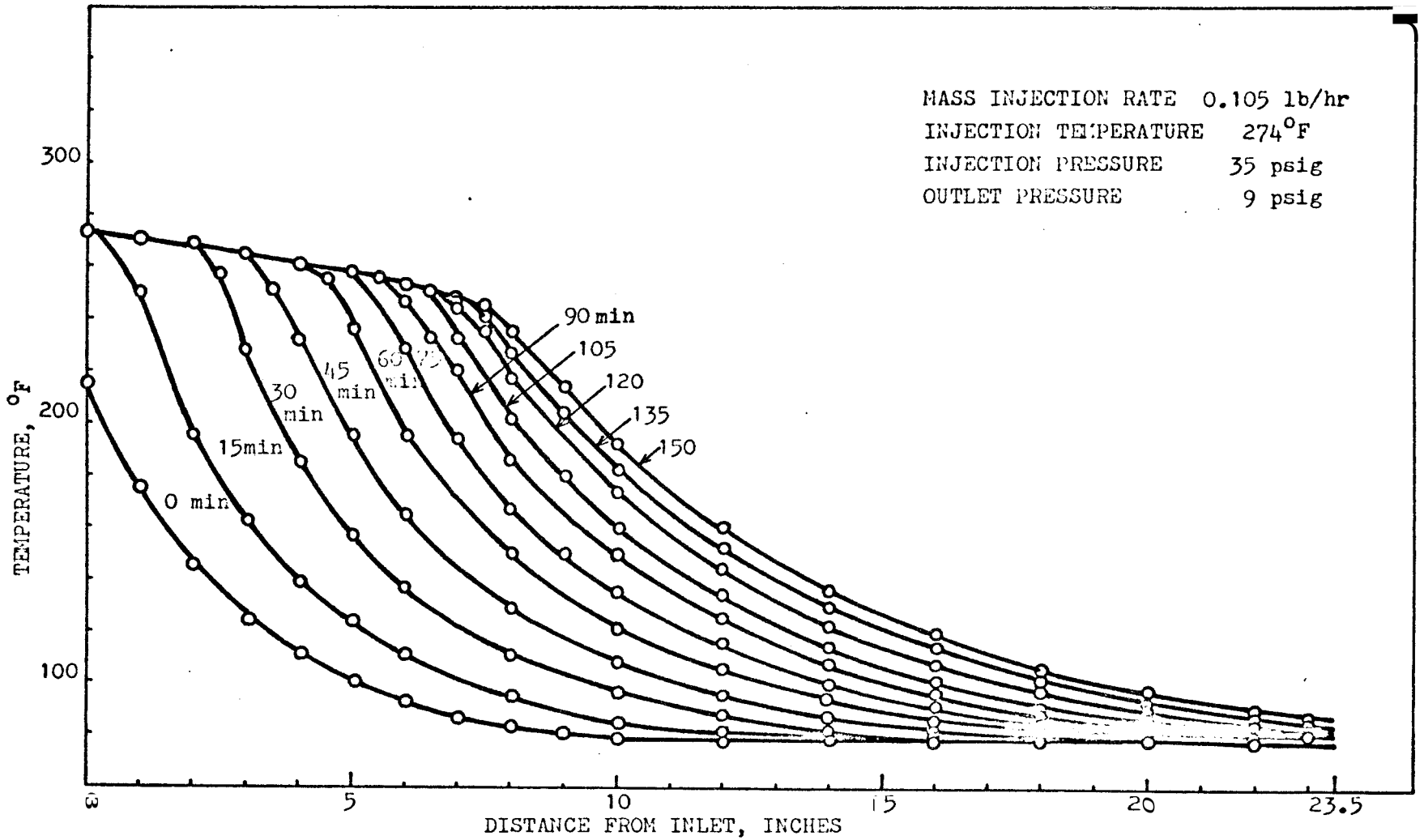

FIGURE 40. TEMPERATURE VS. DISTANCE FOR STEAM INJECTION; BEREA SANDSTONE

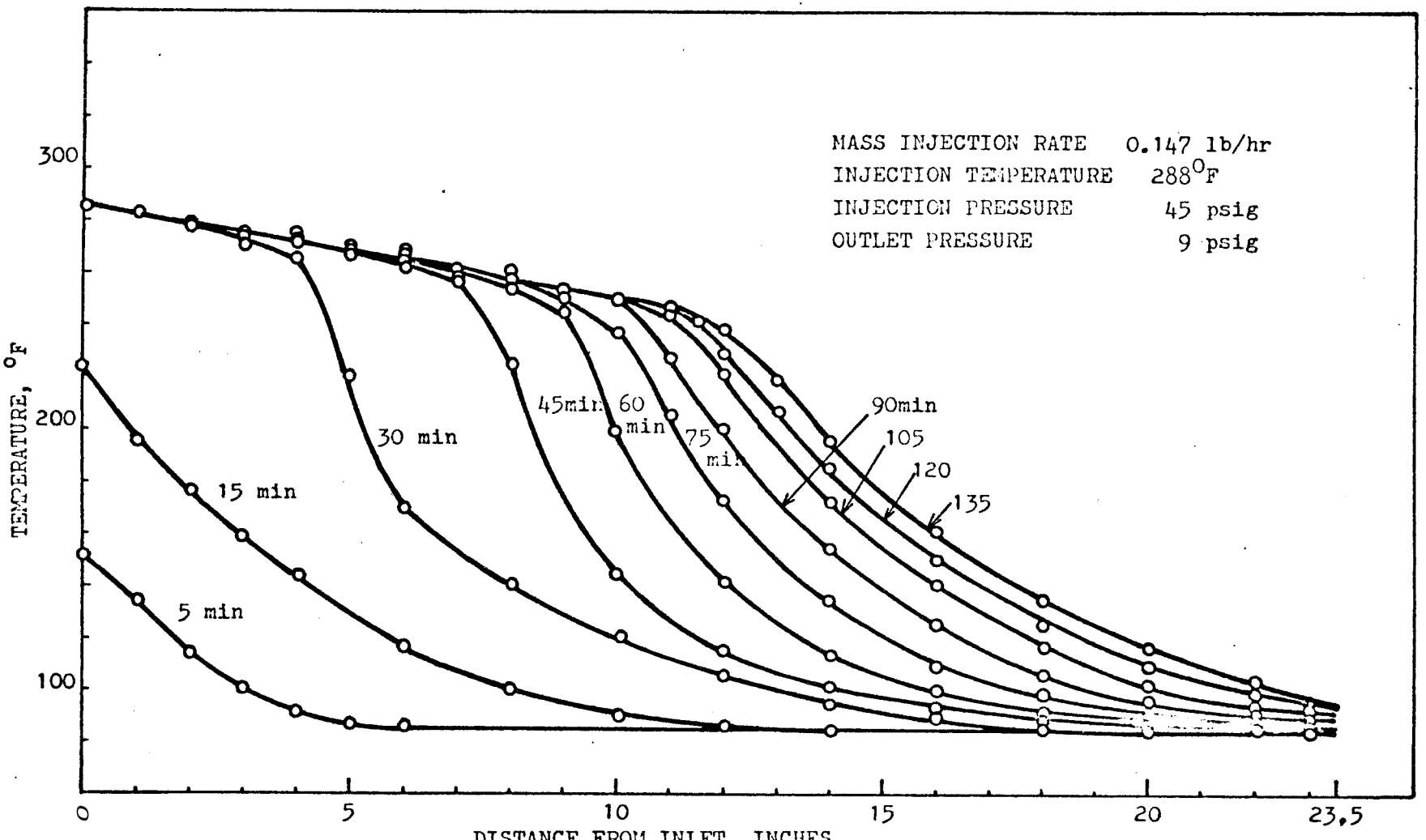

FIGURE 41. TEMPERATURE VS. DISTANCE FOR STEAM INJECTION, BEREA SANDSTONE

Then,

$$U = \frac{\dot{m}\, h_{fg}}{\pi r_o \left(\frac{dT_l}{dX} X_s^2 + 2 (T_i - T_\infty) X_s \right)}$$

The calculated results are shown in Table 4.

TABLE 4. Calculation of Overall Heat Transfer Coefficient for the Core Holder during Steam Injection

Run No.	$\dot{m}$ lb/hr	h_{fg} Btu/lb	X_s ft	T_i °F	T_∞	dT_l/dX °F/ft	U Btu/hr-ft^2-°F
SI-S-1	0.138	920	0.833	389	81	-50	1.553
SI-B-1	0.105	929	0.625	274	80	-40	1.637
SI-B-2	0.147	919	1.0	288	81	-40	1.383

The values of U in Table 4 are slightly higher than the ones in the hot water injection. This may be a result of selecting stagnation locations that were too small. Because this was not a major objective of the study, this point was not pursued. However, it now appears interesting (particularly in regard to Baker's[10] observations on steam injection) and it is recommended that future steam injection studies be made in an attempt to achieve stagnation of the steam front and steady state in the hot water zone. (See the Crichlow[12] figures 17 and 18, for example.)

Depletion Experiment

In depletion experiments, the inlet end of the core was closed and two-phase fluid was produced from the closed inlet system containing compressed hot water initially. The producing rate was controlled high enough to cause large gradients in pressure, temperature and liquid saturation distributions along the axis of the core. The same kind of experiment was done by Cady[36], Bilhartz[47] and Strobel[37], but in their cases, fluid was produced at low rates such that the pressure drop across the system was negligible. Transient mass and heat transfer during depletion can be described by Eqs. 29 and 30, or Eqs. 39 and 40. A numerical model developed by Paul Atkinson has been described in detail by Kruger and Ramey.[16] The present fluid depletion experiment was accomplished in order to supply physical data for comparison with the numerical model. The experimental results are presented in Appendix E.

Two-Phase Flow Experiments

The main experiment considered under the category of "Two-Phase Flow Experiments" was steady injection of hot, compressed liquid water into one end of a core at a rate such that a boiling front would form somewhere within the core length leading to an obvious two-phase, declining temperature and pressure flow region.

Fig. 42 presents temperature vs. distance along the synthetic core for injection of cold water into a core initially containing hot water. The ambient temperature was maintained at 385°F. As can be seen in Fig. 42, cold water is heated by the core on flowing through it, then starts boiling at about 16 inches from the inlet. Because of high enthalpy in the two-phase region, the temperature distribution in the two-phase flow region retains the same profile.

Figs. 43-46 show temperature and pressure vs. distance along the synthetic core at steady state for a range of flow rates. These figures show that it is experimentally possible to produce significant changes in both temperature and pressure within the two-phase boiling flow region. Figs. 47 and 48 show the same kind of results with a Berea sandstone core. In these runs the temperature of the injected water was the same as the ambient temperature. Therefore, before developing two-phase flow by increasing the pressure drop across the core, flow of single phase (liquid) was isothermal. The transient period from single-phase flow to two-phase flow occurred very rapidly, then the two-phase flow developed essentially a steady-state phase.

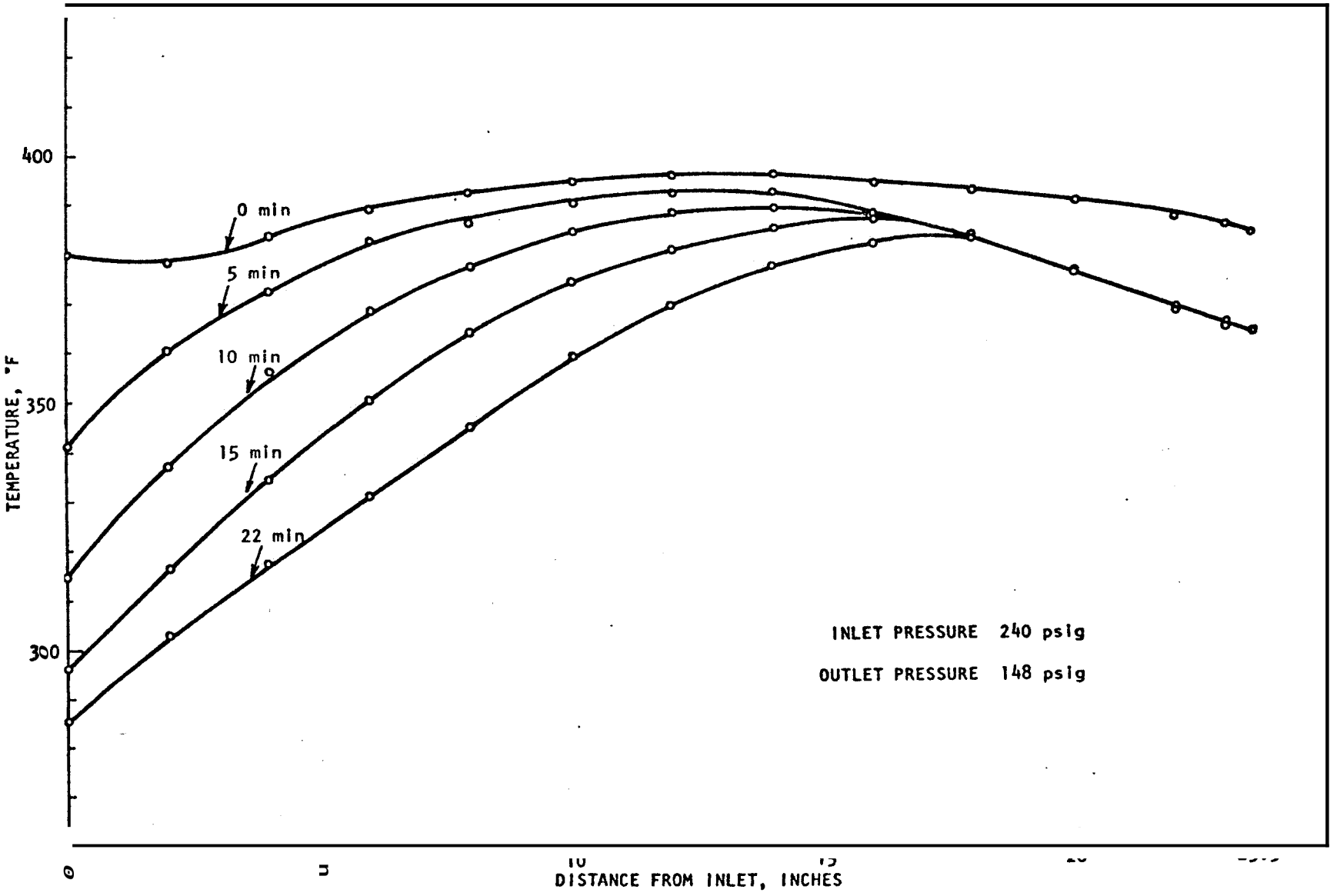

FIGURE 42. TEMPERATURE VS. DISTANCE FOR TWO-PHASE FLOW, SYNTHETIC SANDSTONE.

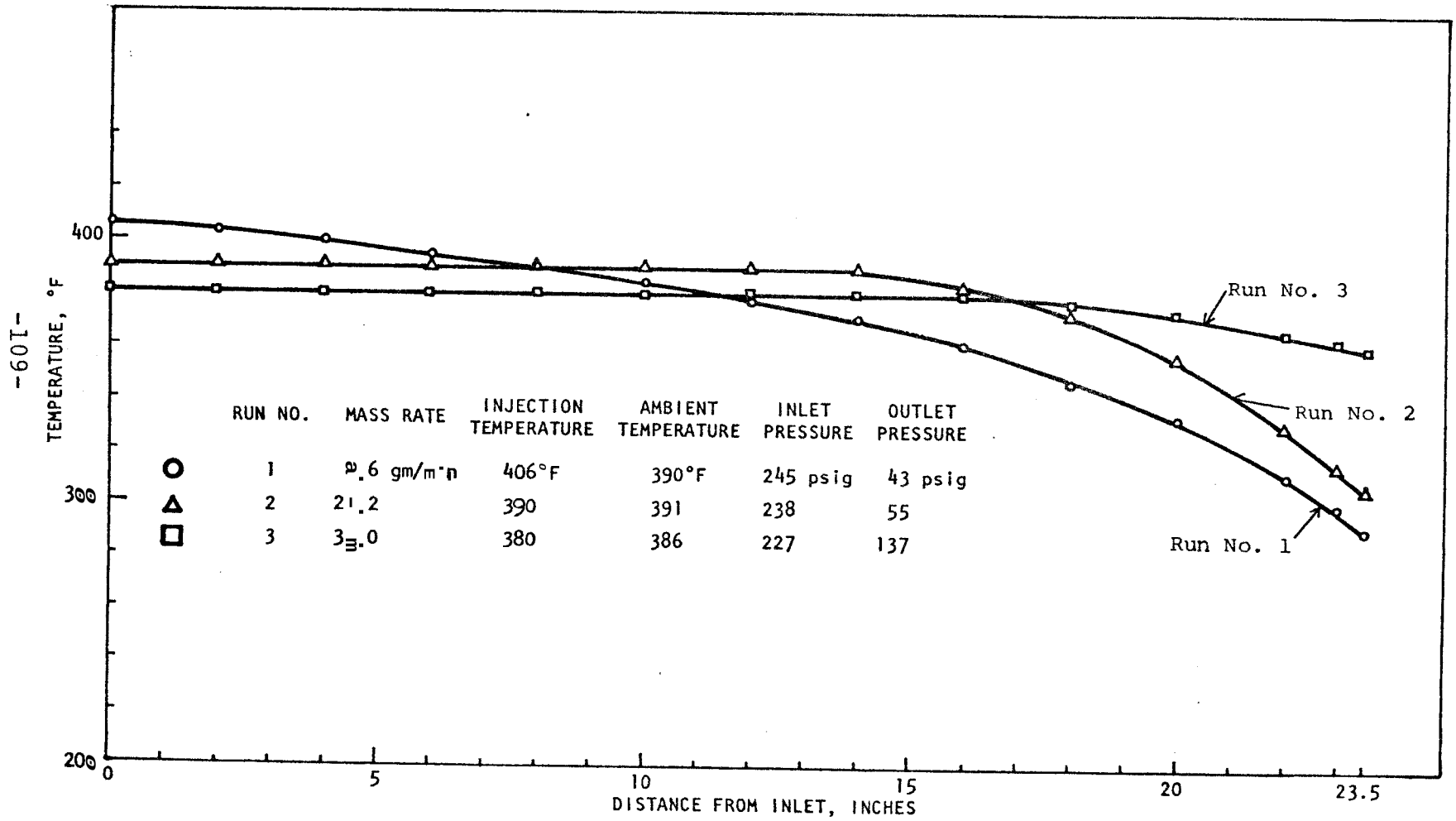

FIGURE 43. TEMPERATURE VS. DISTANCE FOR TWO-PHASE STEADY FLOW, SYNTHETIC SANDSTONE

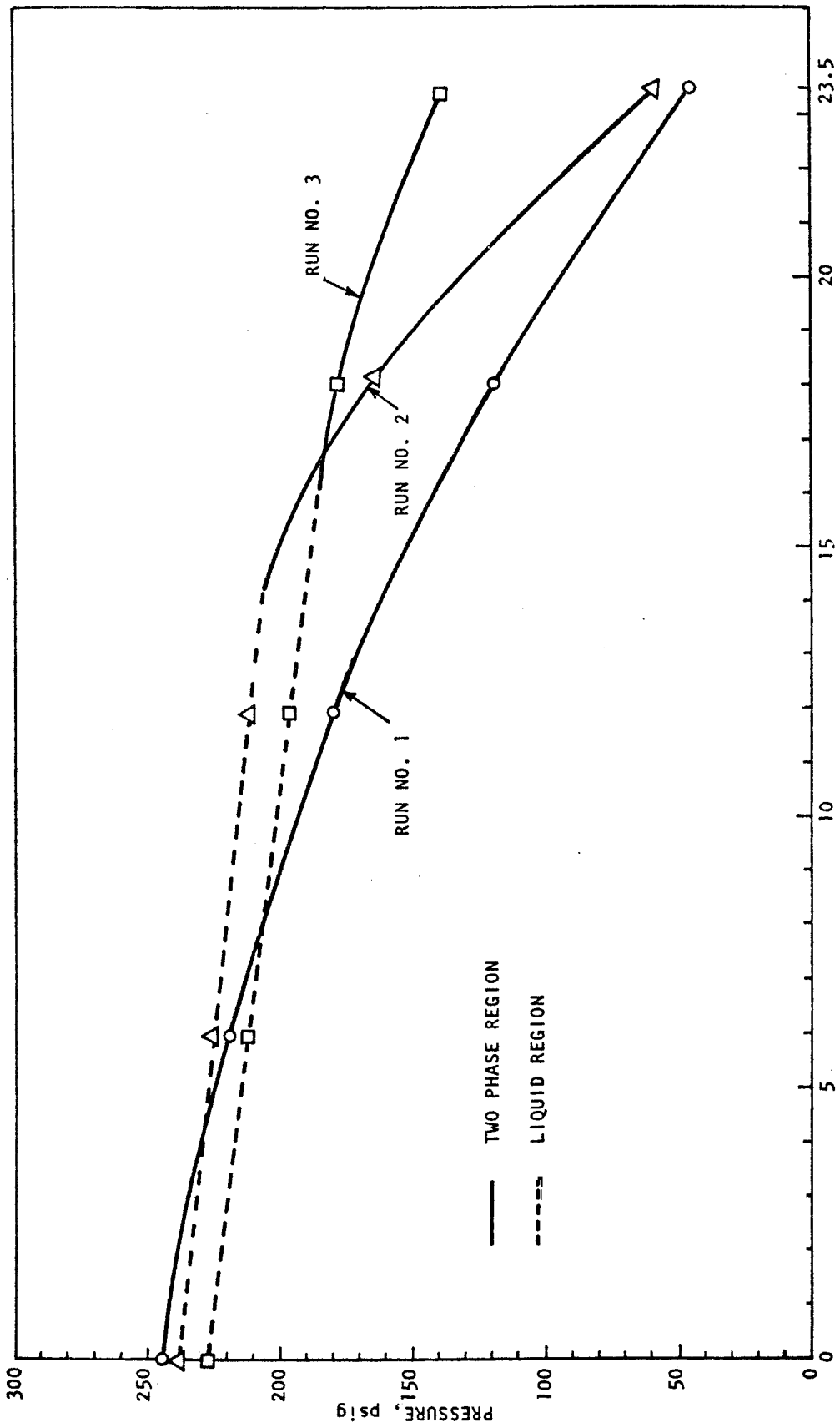

FIGURE 44. PRESSURE VS. DISTANCE FOR TWO-PHASE STEADY FLOW, SYNTHETIC SANDSTONE

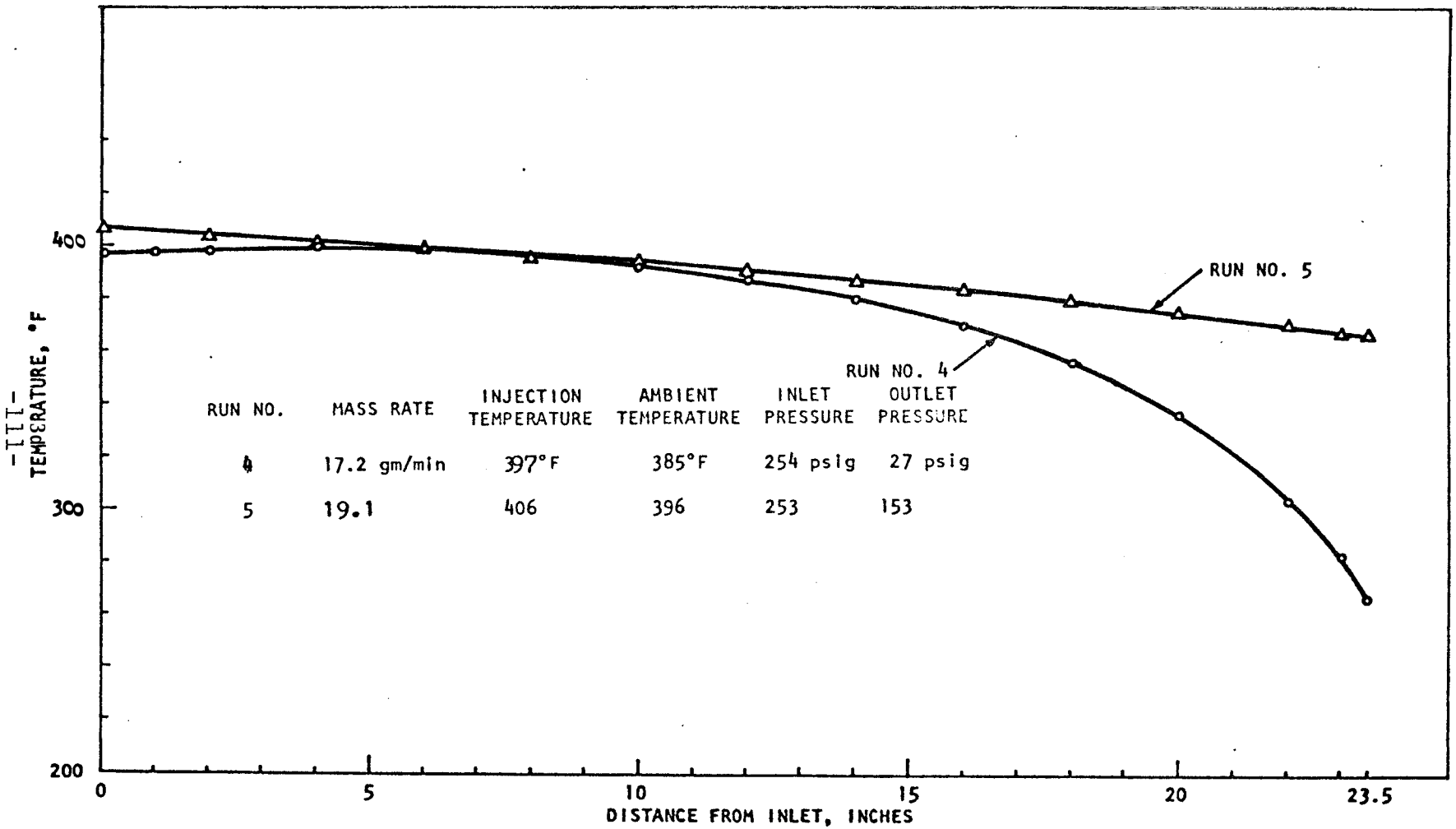

FIGURE 45. TEMPERATURE VS. DISTANCE FOR TWO-PHASE STEADY FLOW, SYNTHETIC SANDSTONE

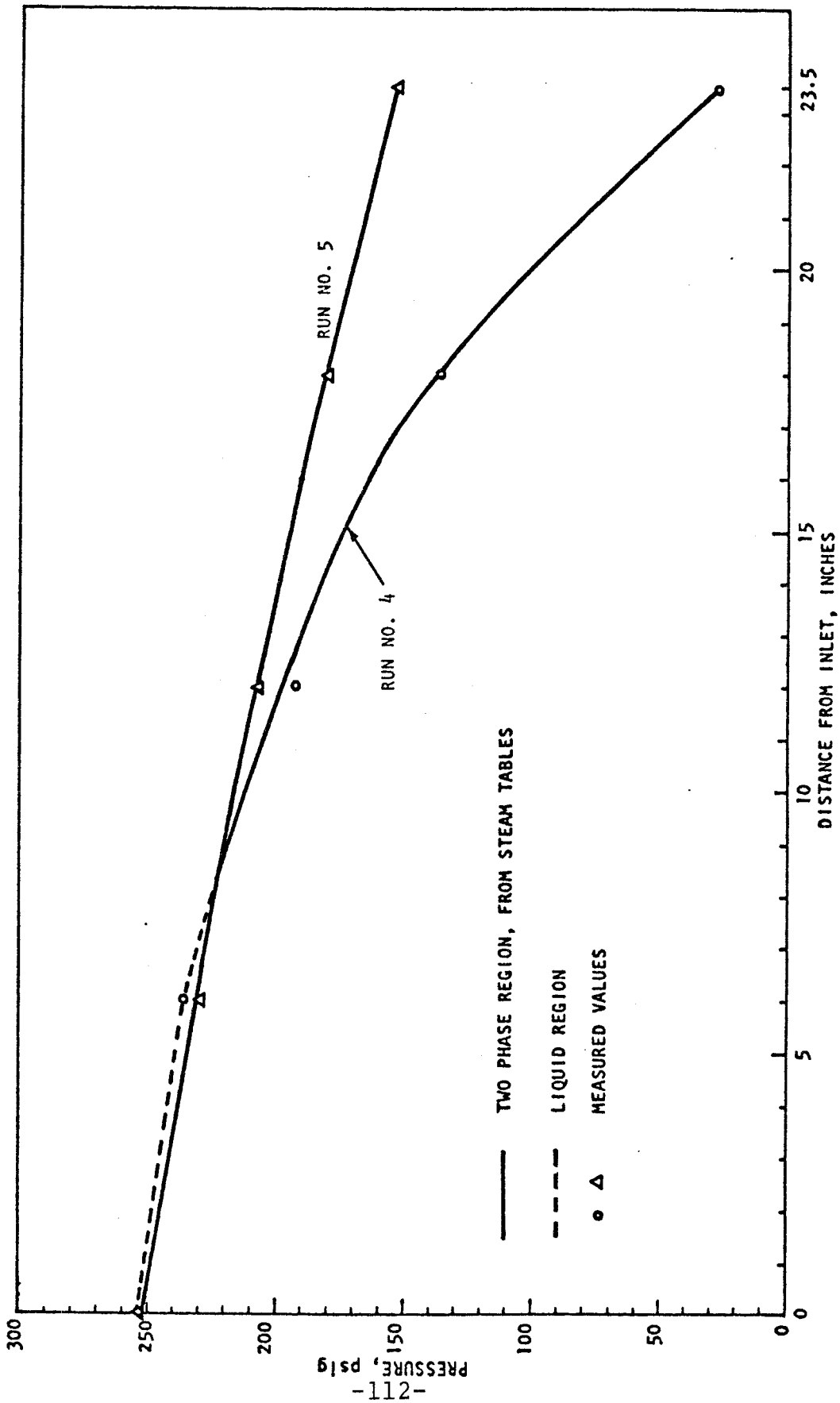

FIGURE 46. PRESSURE VS. DISTANCE FOR TWO-PHASE STEADY FLOW, SYNTHETIC SANDSTONE

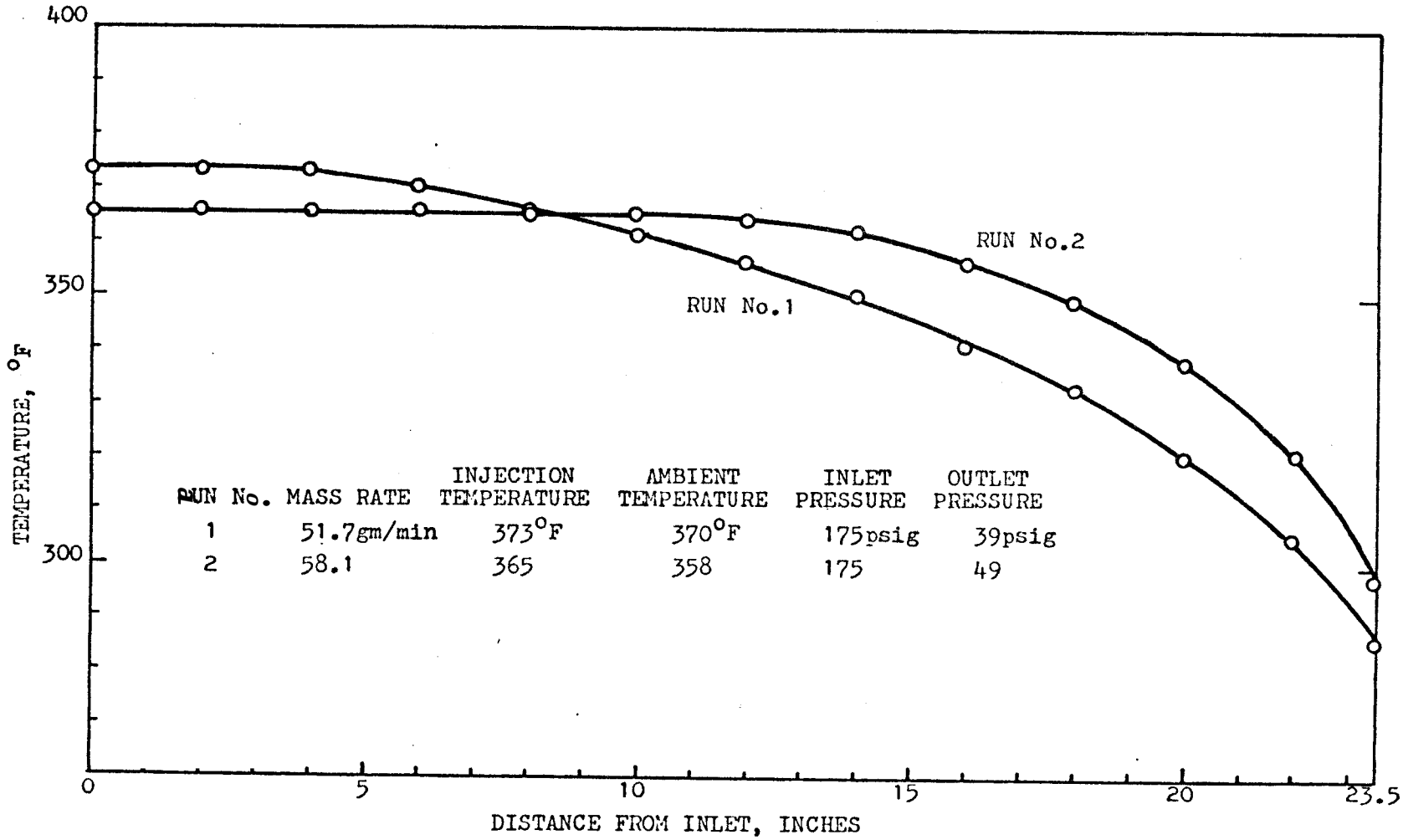

RUN No.	MASS RATE	INJECTION TEMPERATURE	AMBIENT TEMPERATURE	INLET PRESSURE	OUTLET PRESSURE
1	51.7gm/min	373°F	370°F	175psig	39psig
2	58.1	365	358	175	49

FIGURE 47. TEMPERATURE VS. DISTANCE FOR TWO-PHASE STEADY FLOW, BEREA SANDSTONE

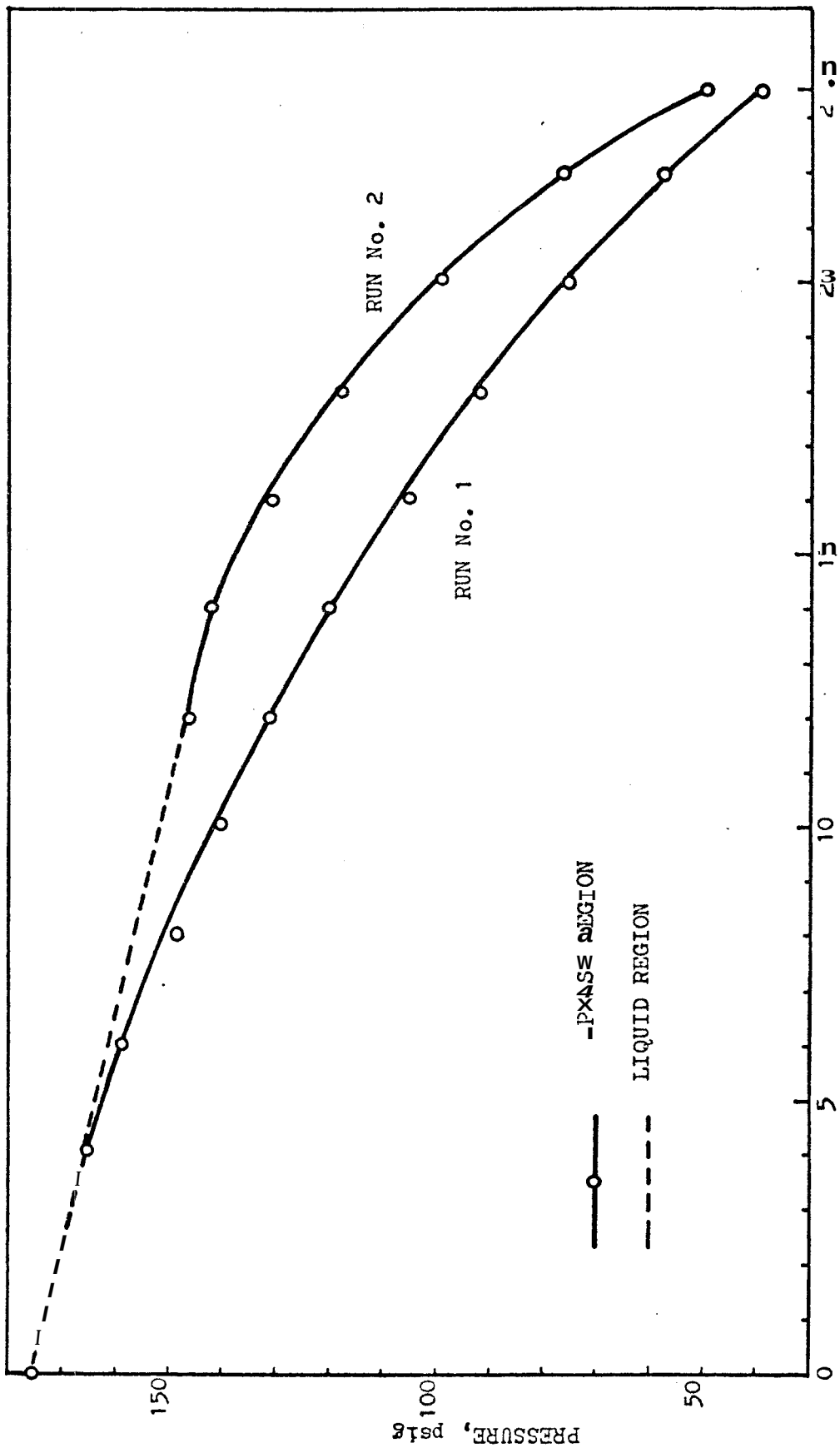

FIGURE 48. PRESSURE VS. DISTANCE FOR TWO-PHASE STEADY FLOW, BEREA SANDSTONE

It was noticed that mass flow rate decreased with increasing pressure drop across the core in two-phase flow. This resulted because larger pressure drops caused greater vaporization, thus more steam and a reduction in the total permeability to both phases.

The experimental results shown in Figs. 43-48 are useful to study the thermodynamic and fluid mechanic behavior of two-phase boiling flow.

Referring to Luikov, mass and heat transfer in two-phase flow can be described by the following differential equations by assuming that flow is steady state, and that ambient temperature, T_∞, is equal to the temperature of the water injected.

$$\frac{d}{dx}\left[\left(\frac{\rho_g k_g}{\mu_g} + \frac{\rho_\ell k_\ell}{\mu_\ell}\right)\frac{dP}{dx}\right] = 0 \tag{60}$$

$$\frac{d}{dx}\left(\lambda\frac{dT}{dx}\right) - h_{fg}\frac{d}{dx}\left(\rho_\ell \frac{k_\ell}{\mu_\ell}\frac{dP}{dx}\right) + \left[\left(C_g\rho_g\frac{k_g}{\mu_g} + C_\ell\rho_\ell\frac{k_\ell}{\mu_\ell}\right)\frac{dP}{dx}\right]\frac{dT}{dx} \tag{61}$$

$$+ \frac{P}{A}\,U(T_\infty - T) = 0$$

where $T = T_s(P)$, which means that temperature is saturation temperature, and a single-valued function of the pressure. Eq. 60 means that the total mass rate is conserved. In Eq. 61, the first term is the gradient of conductive heat flux in the direction of flow, the second term is the gradient of latent heat for vaporization of water, the third term is the gradient of

convective heat transfer, and the last term is the heat gain in the radial direction. Because all the terms but the first are positive in value, Eq. 61 means that with respect to the infinitesimal increment in the direction of flow, the convective heat in flowing fluid and the radial heat gain are balanced by conductive heat flux and latent heat for vaporization. In order to evaluate the effect of heat transfer by conduction in the flow direction and convection from the surroundings, the first and fourth terms in Eq. 61 were calculated for the case of Run No. 4 shown in Fig. 45. The net heat flux coming into the core by the conduction and convection can be obtained by computing the following:

$$q(x) = \int_0^t \left[\frac{d}{dx}\left(\lambda \frac{dT}{dx} \right) + \frac{P}{A} U(T_\infty - T) \right] dx. \qquad (62)$$

The results were graphed against distance along the length of the core in Fig. 49. In Fig. 49 the heat flux carried by the flowing fluid calculated with the assumption of the adiabatic conditions and no conduction, were also graphed. In this calculation, the overall heat transfer coefficient of the core holder U was assumed to be 2.4 Btu/hr - ft^2 - °F , and the conductivity was predicted by the correlations derived by Anand, et al.,[38] and Gomaa and Somerton[39,40], as shown in Appendix B.

Fig. 49 shows that convective heat flux of flowing fluid is constant: throughout the entire length of the core, and that the heat flux due to conduction and the radial convection is comparatively of minor values. From this result it can be deduced

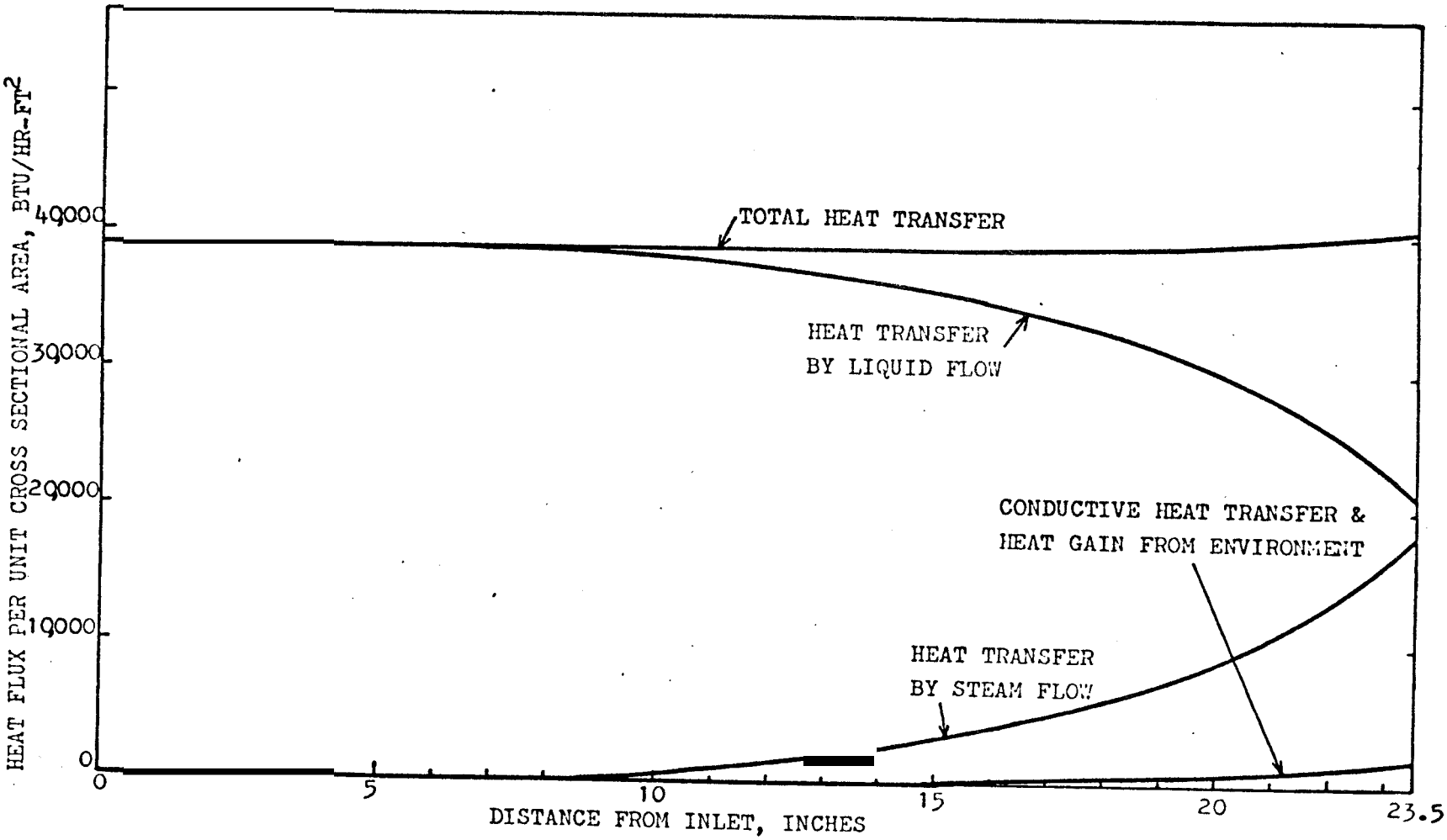

FIGURE 49. HEAT FLUX VS. DISTANCE

that the flow is isenthalpic. This means that the total enthalpy of the fluid is constant at every section, although heat flow in the liquid and steam phases changes in an exponential way as seen in Fig. 49.

Fig. 50 presents the computed distribution of the second term of Eq. **61,** $h_{fg} \frac{d}{dx}(\rho_\ell \frac{k_\ell}{\mu_\ell} \frac{dP}{dx})$. This term expresses the latent heat needed for vaporization of liquid water. It increases exponentially. Heat supply for this latent heat of vaporization causes an exponential decrease in the system temperature.

Isenthalpic flow is illustrated by a vertical line in Fig. 51[41], a pressure-enthalpy diagram for pure water. Constant temperature lines in the liquid region are nearly vertical, thus the isenthalpic process nearly coincides with an isothermal process in the liquid region. It can be also noticed that an isenthalpic flow starting in the liquid phase cannot attain a dry steam phase.

The temperature and pressure distributions shown in Figs. 43-48 were also employed in order to determine the relative permeabilities to liquid and steam phases. With the assumption of isenthalpic, steady-state two-phase flow, the relative permeability ratio is expressed as follows (see Eqs. 18-23):

$$\frac{k_\ell}{k_g} = \frac{\mu_\ell}{\mu_g} \frac{\bar{v}_\ell}{\bar{v}_g} \frac{1 - f}{f} \tag{63}$$

where

$$f = \frac{h - h_\ell}{h_g - h_\ell}$$

The enthalpy h can be computed and thus k_ℓ/k_g can be obtained for every section **x** from the known temperature and pressure distri-

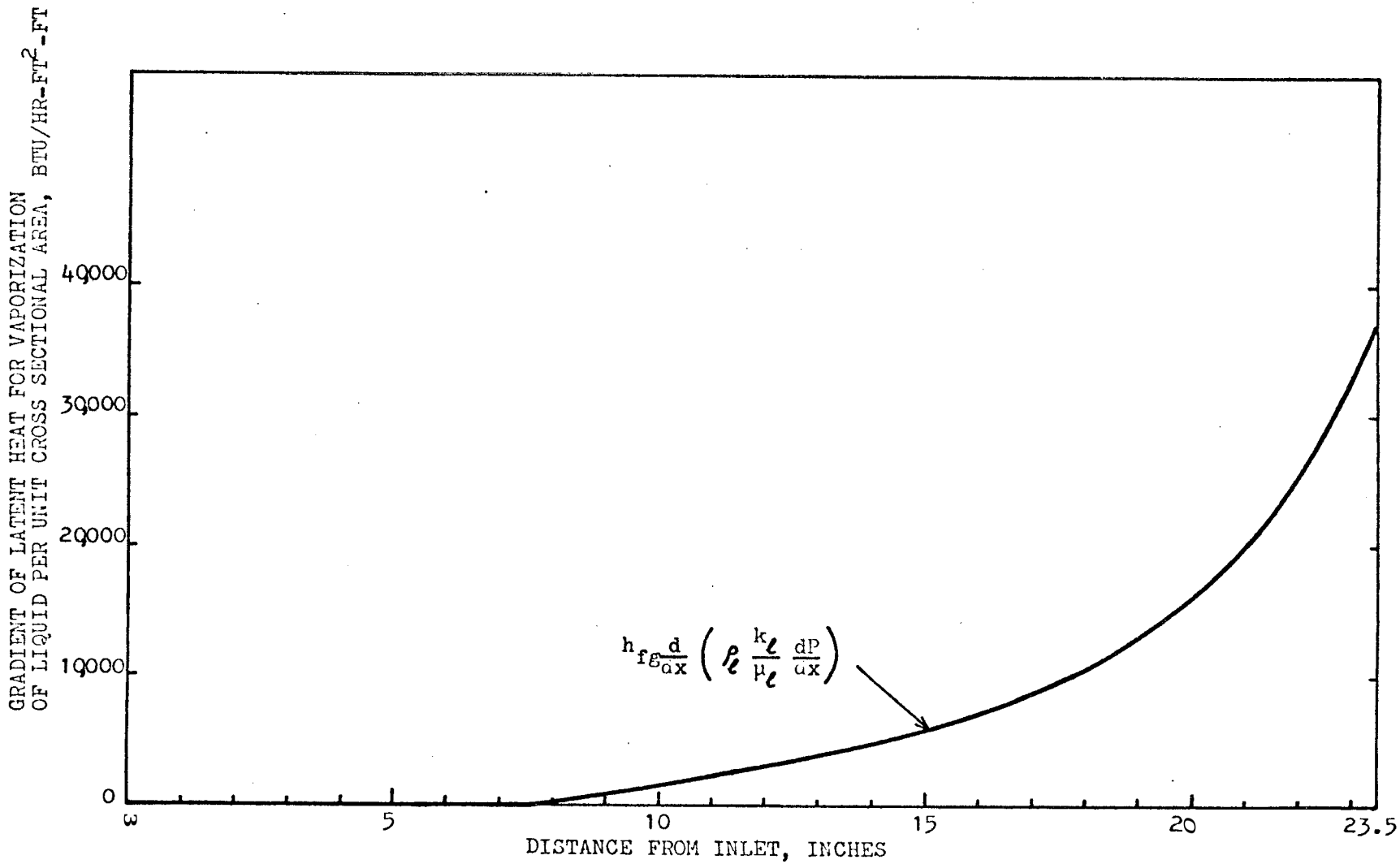

FIGURE 50. GRADIENT OF LATENT HEAT FOR VAPORIZATION OF LIQUID PER UNIT CROSS SECTIONAL AREA VS. DISTANCE

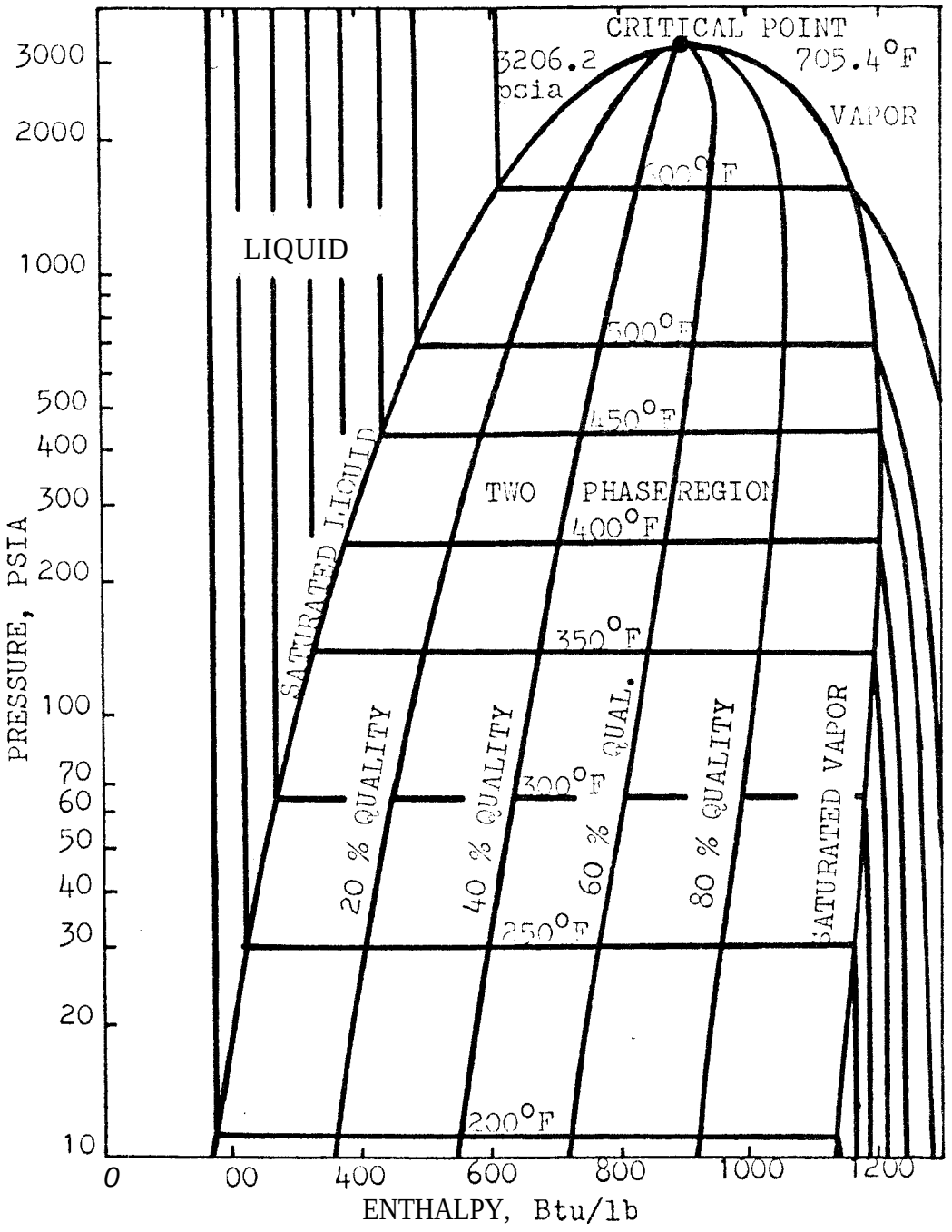

FIGURE 51 . PRESSURE–ENTHALPY DIAGRAM
FOR WATER (FROM REFERENCE 41)

bution. Now, if the k_ℓ/k_g vs. liquid saturation shown in Fig. 5242 can be assumed to be applicable to the synthetic core in the present study, the liquid saturation along the core can be calculated. Fig. 53 presents the computed liquid saturation vs. distance along the core for two different flow rates.

In addition to Eq. 63, the following equation is also valid in the two-phase flow region:

$$\frac{k_\ell/k}{\mu_\ell v_\ell} + \frac{k_g/k}{\mu_g v_g} = -\frac{\dot{m}}{Ak\frac{dP}{dx}} \qquad (64)$$

Because all the factors in the right-hand sides of Eqs. 63 and 64 are known, the relative permeabilities k_ℓ/k and k_g/k can be obtained with the aid of Fig. 52 presented by Weinbrandt. Fig. 54 presents the calculated steam-water relative permeabilities, and Table 5 presents the calculation results for Run No. 4 with the synthetic sandstone.

Determination of relative permeability-liquid saturation data was outside the main objective of this study. It is a main objective of continuing work on this project, however. In the planned extension, liquid saturations will be measured with the capacitance probe described in Appendix C. The results presented in Figs. 53 and 54 are shown as a matter of interest only. It is hoped they will aid planning for this continuing program of study. No similar experimental measurements have yet been made in consolidated sandstones to our knowledge.

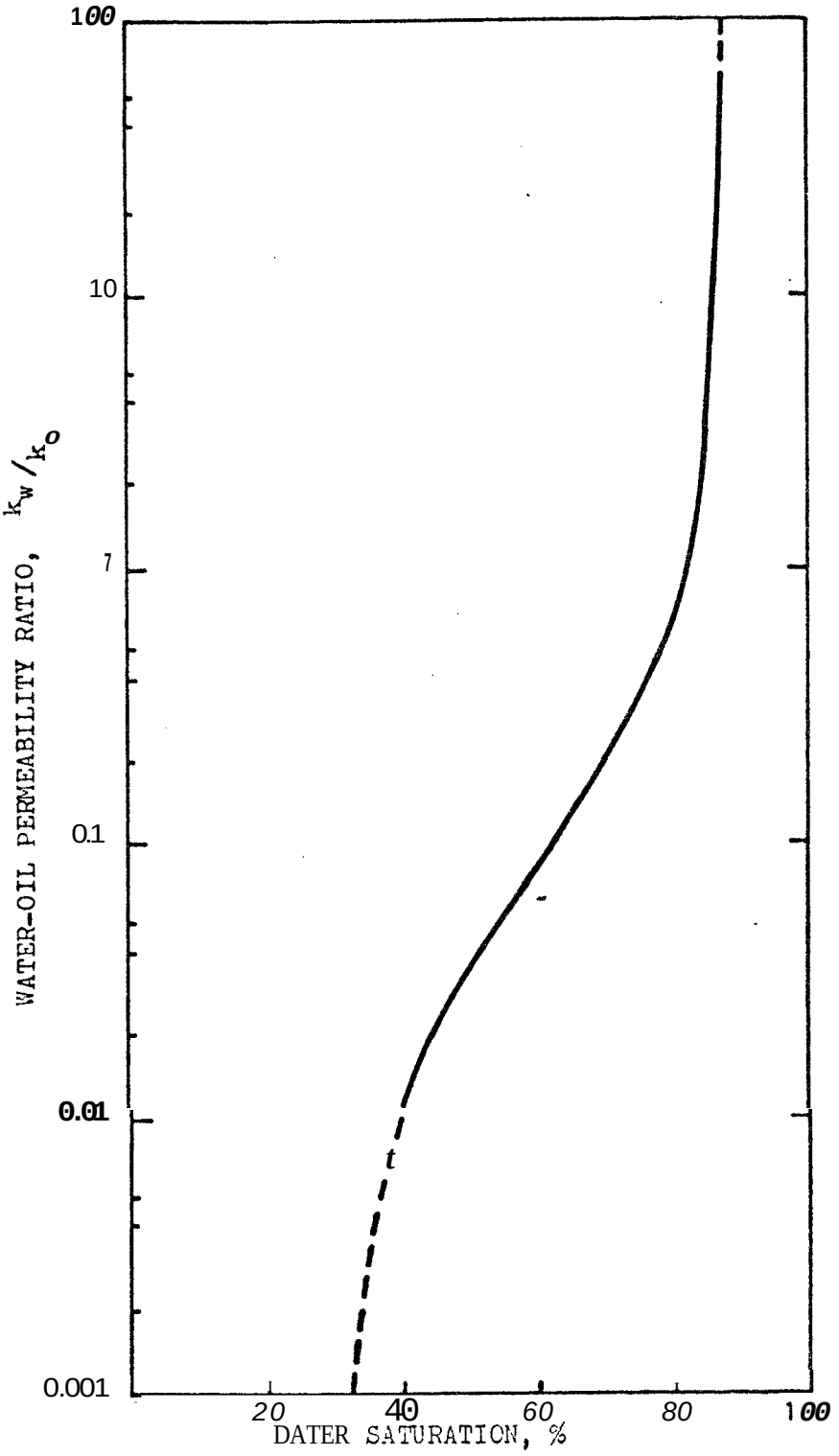

FIGURE 52. RELATIVE PERMEABILITY RATIO VS. WATER SATURATION AT 175°F, BOISE SANDSTOIJE (FROM REFERENCE 42)

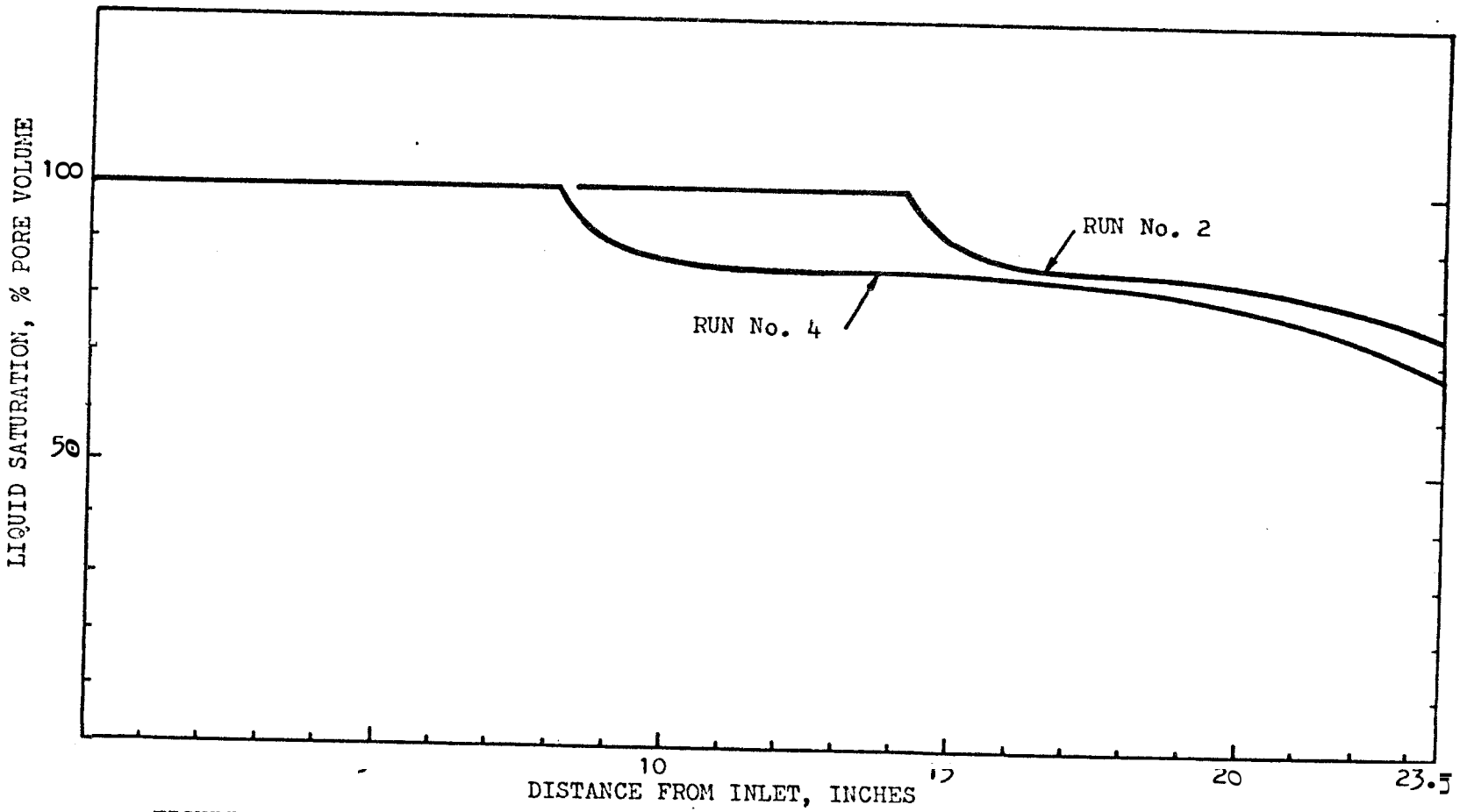

FIGURE 53. CALCULATED LIQUID SATURATION VS. DISTANCE FOR TWO-PHASE FLOW, SYNTHETIC SANDSTONE

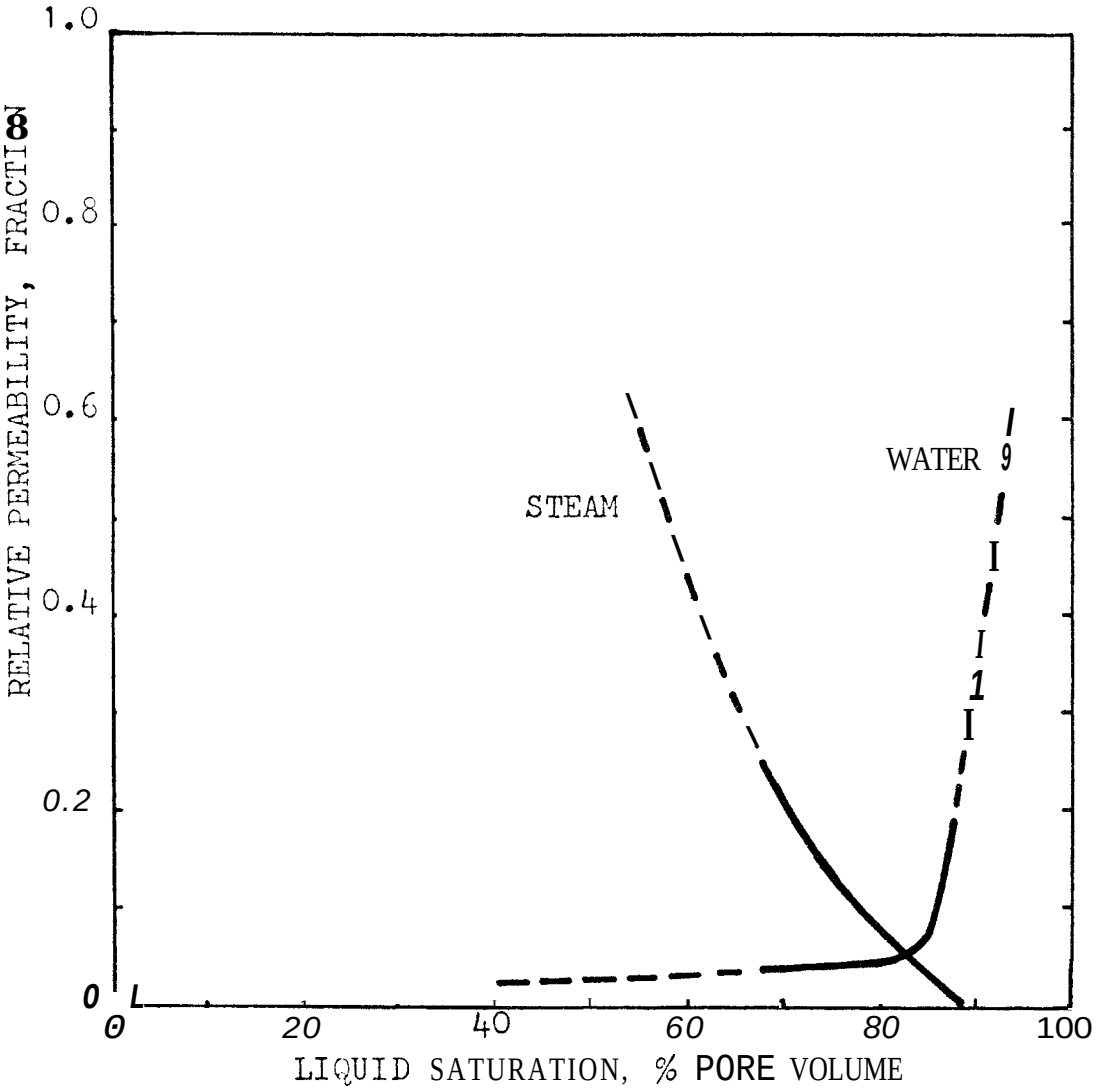

FIGURE 54. WATER-STEAM RELATIVE PERMEABILITY FOR RUN No. 4, SYNTHETIC SANDSTONE

TABLE 5

CALCULATION OF STEAM-WATER RELATIVE PERMEABILITY
(a) Synthetic Sandstone, Run No. 4

P psia	T °F	Y^1 inches	f	k_ℓ/k_g [2]	S_ℓ %	$F(p)^3$ ft^{-1} $\cdot sec^{-1}$ $\times 10^{-6}$	k_g/k	k_ℓ/k
268.7	397	23.5						
260	397	20.94						
250	397	18.22						
240	397	15.50						
238.9	397	15.35		∞		4.50		
235	395.6	14.65	0.0019	41.58	87.5	3.70	0.005	0.189
230	393.7	13.80	0.0043	18.23	87.0	3.00	0.008	0.153
220	389.9	12.40	0.0092	8.27	86.3	2.40	0.015	0.123
210	385.9	11.50	0.0143	5.15	86.0	2.00	0.020	0.103
200	381.8	9.80	0.0195	3.64	85.7	1.72	0.025	0.089
190	377.5	8.50	0.0248	2.75	85.3	1.50	0.029	0.078
180	373.1	7.35	0.0302	2.17	84.5	1.32	0.032	0.069
170	368.4	6.60	0.0359	1.74	84.3	1.18	0.036	0.063
160	363.6	5.90	0.0417	1.44	83.7	1.08	0.040	0.057
150	358.4	5.40	0.0478	1.19	83.3	1.00	0.045	0.054
140	353.0	4.80	0.0540	1.00	82.5	0.938	0.051	0.051
130	347.3	4.25	0.0606	0.843	81.5	0.857	0.055	0.047
120	341.3	3.75	0.0676	0.712	81.0	0.816	0.063	0.045
110	334.8	3.25	0.0749	0.602	80.0	0.775	0.071	0.043
100	327.8	2.80	0.0826	0.508	79.0	0.751	0.083	0.042
90	320.3	2.33	0.0908	0.431	77.5	0.734	0.097	0,042
80	312.0	1.90	0.0997	0.389	77.0	0.710	0.106	0.041
70	302.9	1.43	0.1093	0.302	74.5	0.690	0.135	0.041
60	292.7	0.90	0.1198	0.247	72.5	0.668	0.164	0.041
50	281.0	0.40	0.1317	0.197	70.0	0.643	0.202	0.040
41.7	267.0	0.0	0.1450	0.161	68.0	0.620	0.246	0.040

Note: 1. $y = 23.5 - x$

2. $k_\ell/k_g = \frac{\mu_\ell \bar{v}_\ell}{\mu_g \bar{v}_g} \cdot \frac{1 - f}{f}$

3. $F(p) = \frac{k_\ell/k}{\mu_\ell \bar{v}_\ell} + \frac{k_g/k}{\mu_g \bar{v}_g}$

(b) Synthetic **Sandstone,** Run No. 2

P psia	Y inches	f	k_ℓ/k_g	S_ℓ %	F(p) ft^{-1} sec^{-1} $\times 10^{-6}$	k_g/k	k_ℓ/k
252.7	23.5						
250	22.00						
240	17.65						
230	13.20						
220.3	9.40	*0.0*	m		8.75		
220	9.30						
210	7.90	0.0052	14.36	86.7	2.42	0.009	0.126
200	6.90	0.0104	6.91	86.1	1.77	0.013	0.093
190	6.15	0.0157	4.39	85.8	1.46	0.018	0.077
180	5.45	0.0212	3.11	85.3	1.36	0.023	0.072
170	4.80	0.0269	2.35	85.0	1.21	0.028	0.065
160	4.25	0.0328	1.85	84.3	1.16	0.034	0.062
150	3.65	0.0389	1.48	83.8	1.11	0.041	0.060
140	3.15	0.0452	1.21	83.0	1.01	0.045	0.055
130	2.65	0.0519	0.995	82.5	0.958	0.053	0.053
120	2.20	0.0588	0.826	81.5	0.910	0.061	0.050
110	1.75	0.0662	0.687	80.6	0.890	0.072	0.050
100	1.30	0.0739	0.573	79.5	0.860	0.085	0.049
90	0.85	0.0823	0.480	78.3	0.830	0.099	0.048
80	0.40	0.0913	0.398	77.0	0.800	0.117	0.047
69.7	0.0	0.1009	0.330	75.3	0.770	0.139	0.046

CONCLUSIONS

On the basis of the observations and calculations made in this study, it may be concluded that:

1. The overall heat transfer coefficient of the core holder was of very minor dependence on mass flow rate in both hot water and cold water injection experiments.

2. As observed by Baker and Crichlow, the thermal efficiency of hot water injection increases with increasing rate of heat injection.

3. A rate sensitivity of the thermal efficiency also exists in cold water injection into a system containing hot water initally. Unlike the case of hot water injection wherein high thermal efficiency is desirable, the main objective in cold water injection is apt to be extraction of heat from the over-burden and underburden. Thus a low thermal efficiency would be desirable. In this case, it was concluded that lower injection rate of cold water, or a smaller temperature difference between the surroundings and the injected water was more effective in extraction of heat from the surroundings.

4. The dependence of thermal efficiency on heat injection rate is amplified, if the overall heat transfer coefficient of the core holder increases.

5. It is experimentally possible to develope in-place boiling two-phase flow with wide ranges of temperature and

pressure drops, and total mass flow rate. The total mass rate of flow decreases with increasing temperature and pressure drops across the interval of the two-phase boiling flow.

6. The in-place boiling flow can be steady state even when heat transfer exists in the direction perpendicular to flow.

7. It appears that reasonably large ranges in liquid saturation result during steady boiling flow in consolidated porous media.

NOMENCLATURE

English

A	=	area, ft^2
b	=	half of the formation thickness, ft
C	=	specific heat, Btu/lb - ^oF
D	=	$\frac{\lambda}{\rho C}$, thermal diffusivity, ft^2/hr
d	=	diameter, ft
E	=	thermal efficiency, fraction
Gr	=	Grashof number, dimensionless
Gz	=	Graetz number, dimensionless
H	=	heat injection rate, Btu/hr
h	=	enthalpy, Btu/lb
h_f, h_∞	=	film coefficient for convective heat transfer, Btu/hr - ft^2 - ^oF
k	=	permeability, millidarcies
L	=	length of the formation or core, ft
m	=	mass rate of flow, lb/hr
Nu	=	$\frac{h_f d}{\lambda}$ Nusselt number, dimensionless
P	=	perimeter, ft
Pr	=	$\frac{C_p \mu}{\lambda}$ Prandtl number, dimensionless
P	=	pressure, psi
Q	=	heat flux, Btu/hr
q	=	volumetric fluid flow rate, ft^3/hr

NOMENCLATURE, CONTINUED

English

Re = $\frac{u\rho d}{\mu}$, Reynolds number, dimensionless

r = radius, ft

S = saturation, fraction

T = temperature, ^{o}F

t = time, hr

U = overall heat transfer coefficient, Btu/hr - ft^2 - ^{o}F

V = flow velocity, ft/hr

$\bar{v}$ = specific volume, ft^3/lb

x = distance in the direction of flow, ft

Y = distance in the perpendicular direction to the flow, ft

Greek

ρ = density, lb/ft^3

μ = viscosity, cp

λ = thermal conductivity, Btu/hr - ft - ^{o}F

ϕ = porosity, fraction

Δ = increment

∇ = gradient, ∇^2 is Laplacian operator

Subscripts

g = steam

ℓ = liquid water

Subscripts, continued

s	=	sand
w	=	water
1	=	properties of the liquid-filled part of the pay zone
2	=	properties of the formations adjacent to the pay zone (overburden or underburden)

Functions

$\rho_1 C_1 = (1 - \phi)\ \rho_s C_s + \phi \rho_w C_w$

$\operatorname{erfc} z = \frac{2}{\sqrt{\pi}} \int_z^\infty e^{-\beta^2}\, d\beta$

REFERENCES

1. Lauwerier, H.A.: "The Transport of Heat in an Oil Layer Caused by the Injection of Hot Fluid," Appl. Sci. Res., Sec. A (1955) 5, 145.

2. Marx, J.W. and Langenheim, R.H.: "Reservoir Heating by Hot Fluid Injection," Trans. AIME (1959) 216, 312.

3. Carter, R.D.: Appendix to "Optimum Fluid Characteristics for Fracture Extension," by G.C. Howard and C.R. Fast, Drill. and Prod. Prac., API (1957) 267.

4. Ramey, H.J., Jr.: "Reservoir Heating by Hot Fluid Injection, Discussion," Trans. AIME (1959) 216, 364.

5. Churchill, R.V. : Operational Mathematics, 2nd Ed., McGraw-Hill Book Co., New York (1958)

6. Ramey, H.J., Jr. : "How to Calculate Heat Transmission in Hot Fluid Injection," Pet. Engr. (Nov. 1964) 110.

7. Rubinshtein, L.I. : "The Total Heat Losses in Injection of a Hot Fluid into a Stratum," Neft I Gaz, 2, No. 9 (1959) 41.

8. Spillette, A.G. : "Heat Transfer During Hot Fluid Injection into an Oil Reservoir," Jour. Canadian Pet. Tech. (Oct.-Dec. 1965) 213.

9. Baker, P.E.: "Heat Wave Propagation and Losses in Thermal Oil Recovery Process," Proc., 7th World Petroleum Congress, Mexico City, (1968).

10. Baker, P.E. : "An Experimental Study of Heat Flow in Steam Flooding," Soc. Pet. Engr. J. (March 1969) 89.

11 Baker, P.E.: "Effect of Pressure and Rate on Steam Zone Development in Steam Flooding," Soc. Pet. Engr. J. (Oct. 1973) 274.

12. Crichlow, H.B.: "Heat Transfer in Hot Fluid Injection in Porous Media," Ph.D. Dissertation, Stanford University, (May 1972).

13. Prats, M.: "The Heat Efficiency of Thermal Recovery Process," J. Pet. Tech. (March 1969) 323.

14. Miller, F.G.: "Steady Flow of Two-Phase Single-Component Fluids Through Porous Media," Trans. AIME (1951) 192, 205.

15. Luikov, A.V.: Heat and Mass Transfer in Capillary-Porous Bodies, Pergamon Press, Oxford, (1966).

16. Kruger, P. and Ramey, H.J., Jr.: Stimulation and Reservoir Engineering of Geothermal Resources, Progress Report No. 3, to Advanced Technology Dept., RANN, National Science Foundation, Grant No. GI-34925 (June 1974).

17. Coats, K.H., George, W.D., Chu, C. and Marcum, B.E.: "Three-Dimensional Simulation of Steam Flooding," Paper No. SPE 4500, presented at 48th Annual Fall Meeting of SPE of AIME, Sept. 30-Oct. 3, 1973, Las Vegas, Nevada.

18. Weinstein, H.G., Wheeler, J.A. and Woods, E.G.: "Numerical Model for Steam stimulation," Paper No. SPE 4759

19. Wygal, R.J.: "Construction of Models that Simulate Oil Reservoirs," Soc. Pet. Engr. J. (Dec. 1963) 281.

20. Heath, L.J.: "Variations in Perveability and Porosity of Synthetic Oil Reservoir Rock - Method of Control," Soc. Pet. Engr. J. (Dec. 1965) 329.

21. Evers, J.F., Preston, F.W., Sadiq, S. and Swift, G.W.: "Preparation and Testing of Low Permeability Porous Media to Meet Sealing Requirements for Gas Reservoir Modeling," Soc. Pet. Engr. J. (June 1967) 189.

22. Muskat, M., Wyckoff, R.D., Botset, H.G. and Meres, M.W.: "Plow of Gas-Liquid Mixtures through Sands," Trans. AIME (1337) 123, 69.

23. Botset, H.G.: "Flow of Gas-Liquid Mixtures through Consolidated Sand," Trans. AIME (1940) 136, 91

24. Brunner, E. and Mardock, E.S.: "A Neutron Method for Measuring Saturation in Laboratory Flow Experiments," Trans. AIME (1946) 165, 33.

25. Finnemore, R.J. and Schaaf, J.R.: A Gamma-Ray Attenuation System for Laboratory Measurement of Soil Moisture Content, Technical Report No. 127 (Dec. 1972) Dept. of Civil Engineering, Stanford University.

26. Schaaf, J.R.: Unsteady, Unsaturated Flow from a Horizontal, Buried Cylindrical Source into a Porous Medium, Technical Report No. 165 (April 1973) Dept. of Civil Engineering, Stanford University.

27. Morgan, F., McDowell, J.M., and Doty, F.C.: "Improvements in the X-Ray Saturation Technique of Studying Fluid Flow," Trans. AIME (1950) 189, 183.

28. Jones, S.C., Senior Res. Engr. Marathon Oil Co., Denver Res. Center, Personal Communication.

29. Klinkenberq, L.J.: "The Permeability of Porous Media to Liquids and Gases," Drill. and Prod. Prac, API (1941) 200.

30. Weinbrandt, R.M., Ramey, H.J., Jr. and Cassé, F.: "The Effect of Temperature on Relative Permeability of Consolidated Rocks," Paper No. SPE 4142, presented at the 47th Annual SPE Fall Meeting, San Antonio, Texas, Oct. 8-11, 1972.

31. Cassé, F., Graduate Student, Dept. of Pet. Engr., Stanford University, Personal Communication.

32. Willhite, G.P. : "Overall Heat Transfer Coefficients in Steam and Hot Water Injection Wells," J. of Pet. Tech. (May 1967) 607.

33. Ramey, H.J., Jr.: "Wellbore Heat Transmission," J. Pet. Tech. (April 1962) 427.

34. Holman, J.P.: Heat Transfer, 3rd Edition, McGraw-Hill Book Co., New York, N.Y., 1972.

35. McAdams, W.H.: Heat Transmission, 3rd Edition, McGraw-Hill Book Co., New York, N.Y., 1954.

36. Cady, G.V.: "Model Studies of Geothermal Fluid Production," Ph.D. Dissertation, Stanford University (Nov. 1969).

37. Strobel, C.J.: "Model Studies of Geothermal Fluids Production from Consolidated Porous Media," Engineers Thesis, Stanford University (July 1973).

38. Anand, J., Somerton, W.H. and Gomaa, E.: "Prediction of Thermal Properties of Formations From Other Known Properties," Paper No. SPE 4171, 43rd Annual California Regional Meeting, SPE of AIME, Bakersfield, Calif., Nov. 8-10, 1972.

39. Gomaa, E.E. and Somerton, W.H.: "Thermal Behavior of Multifluid-Saturated Formations, Part I: Effect of Wettahility, Saturation, and Grain Structure," Paper No. SPE 4896-A, 44th California Regional Meeting, SPE of AIME, San Francisco, Calif., April 4-5, 1974.

40. Gomaa, E.E. and Somerton, W.H.: "Thermal Behavior of Multifluid-Saturated Formations, Part II: Effect of Vapor Saturation - Heat Pipe Concept and Apparent Thermal Conductivity," Paper No. SPE 4896-B, 44th California Regional Meeting, SPE of AIME, San Francisco, Calif., April 4-5, 1974.

41. Whiting, R.L., and Ramey, H.J., Jr.: "Application of Material and Energy Balances to Geothermal Steam Production," J. Pet. Tech. (July 1969) 893.

42. Weinbrandt, R.M.: "The Effect of Temperature on Relative Permeability," Ph.D. Dissertation, Stanford University, (May 1972).

43. Ramey, H.J., Jr., Brigham, W.E., Chen, H.K., Atkinson, P.G., and Arihara, N.: "Thermodynamic and Hydrodynamic Properties of Hydrothermal Systems," The Utilizatian of Volcano Energy, edited by Colp, J.L. and Furumoto, A.S., Proceedings of a Conference held at Hilo, Hawaii on Feb. 4-8, 1974.

44. Mandl, G. and Volek, C.W.: "Heat and Mass Transport in Steam-Drive Processes," Soc. Pet. Engr. J. (March 1969) 59.

45. Hearn, C.L.: "Effect of Latent Heat Content of Injected Steam in a Steam Drive," (Forum) J. Pet. Tech. (April 1969) 374.

46. Ersoy, D.: "Temperature Distribution and Heating Efficiency of Oil Recovery by Hot Water Injection," Ph.D. Dissertation, Stanford University, August (1969).

47. Bilhartz, H.L., Jr.: "Fluid Production From Geothermal Steam Reservoirs," MS Report, Stanford University, June (1971).

APPENDICES

A. Physical Data for the Cores

B. Thermal Property Data

C. Saturation Probe Design

D. List of Equipment Manufacturers & Suppliers

E. Experimental Data

(1) Permeability Measurements

(2) Hot Water and Cold Water Injection

(3) Depletion Tests

APPENDIX A

PHYSICAL DATA FOR THE CORES

APPENDIX A

PHYSICAL DATA FOR THE CORES

1. Synthetic Core

	Core No. 1	2*	3
Length, in.	23.5	23.5	23.5
Diameter, in.	2.0	2.0	2.0
Sand (100 mesh Ottawa), weight %	80.0	80.0	80.0
Cement ($CaO \cdot Al_2O_3$), weight %	20.0	20.0	20.0
Porosity, % bulk volume	36.2	35.9	36.1
Permeability, millidarcies	95.2	98.5	90.0

2. Berea Sandstone Core

Length	- 23.5 in.
Diameter	- 2.0 in.
Porosity	- 22.2%
Permeability	- 401 millidarcies

*Core No. 2 was used throughout the present study.

APPENDIX B

THERMAL PROPERTY DATA

APPENDIX B

THERMAL PROPERTY DATA

1. Density

Fig. B-1 shows the density of water vs. temperature. Because of the low compressibility of water in the liquid phase, Fig. B-1 can be applied for pressures ranging from saturation pressure to about 500 psia. The curve can be approximated as follows:

$$\rho_w = 62.4 - \frac{1}{70} (T-70) \text{ for } 70^\circ < T < 150^\circ F$$

$$\rho_w = 61.013 - \frac{1.91}{80} (T-160) \text{ for } 150^\circ < T < 250^\circ F$$

The density of a sand grain is assumed to be a constant value, 165.36 lb/ft^3.

2. Viscosity

Fig. B-2 shows the viscosity of water and saturated steam vs. temperature. The viscosity of water given in Fig. **B-2** can be used for a wide range of pressure.

The viscosity of nitrogen gas is given by the Sutherland formula:

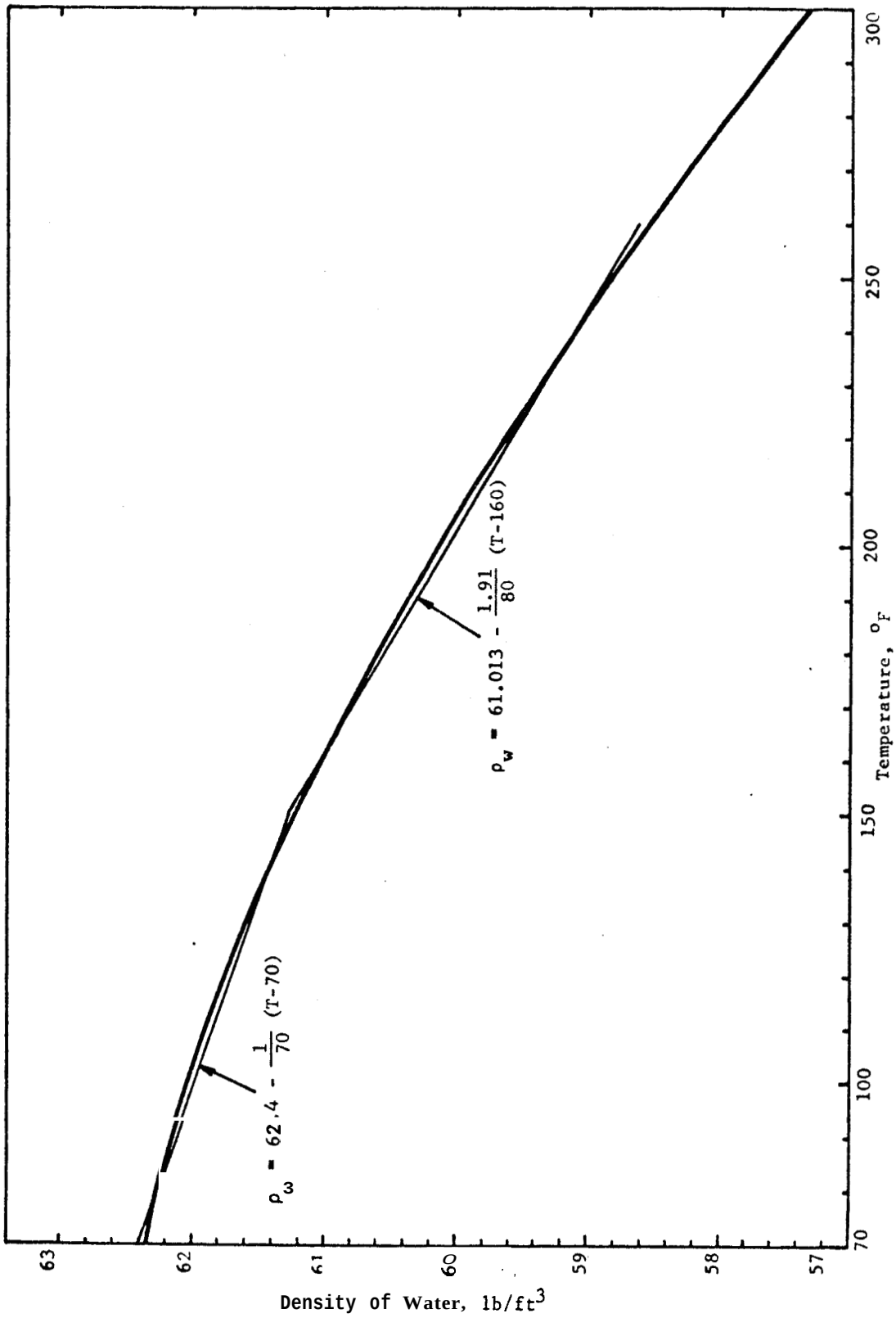

FIGURE B-1. DENSITY OF WATER VS. TEMPERATURE

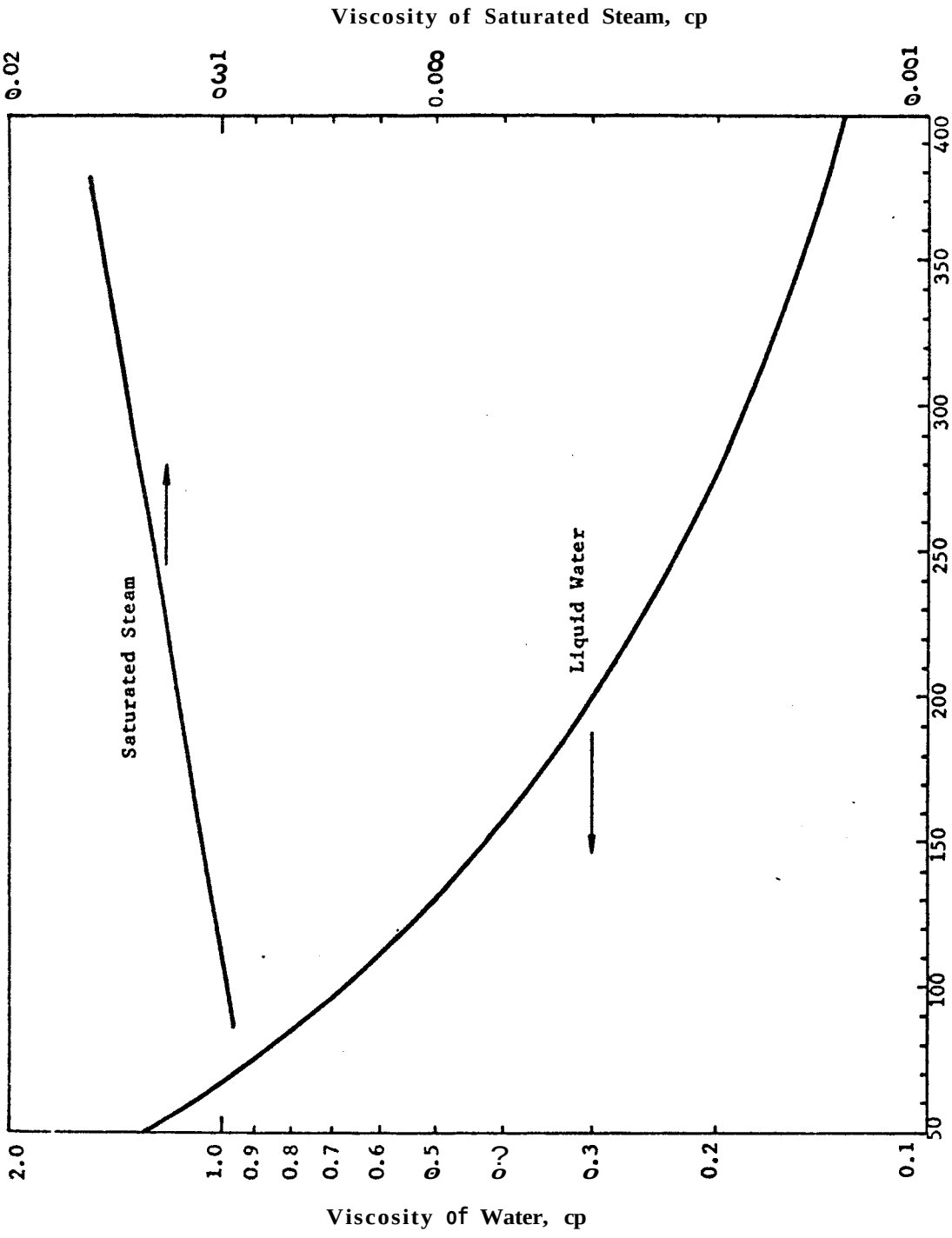

FIGURE B-2. VISCOSITY OF WATER VS. TEMPERATURE

$$\frac{\mu}{\mu_o} = \frac{273 + C}{T + C}\left(\frac{T}{273}\right)^{3/2}, \text{ for } -76^oC < T < 250^oC$$

where μ_o = 0.0166 cp

C = 102.7

T = temperature, ^oK

3. Specific Heat

Fig. B-3 shows the specific heat at constant pressure of saturated steam and of water vs. temperature. The specific heat of water in Fig. B-3 can be used for pressures ranging from saturation pressure to about 1000 psia.

For the specific heat of sand, the following linear function of temperature was used:

$$C_s = 0.2 + 10^{-4} T$$

where T is given in ^oF.

4. Thermal Conductivity

Fig. B-4 shows the thermal conductivity of saturated steam and water vs. temperature.

Anand, et al.[38], presented correlations for the thermal conductivity of sandstone. The thermal conductivity of dry sandstone (containing air) was correlated as follows:

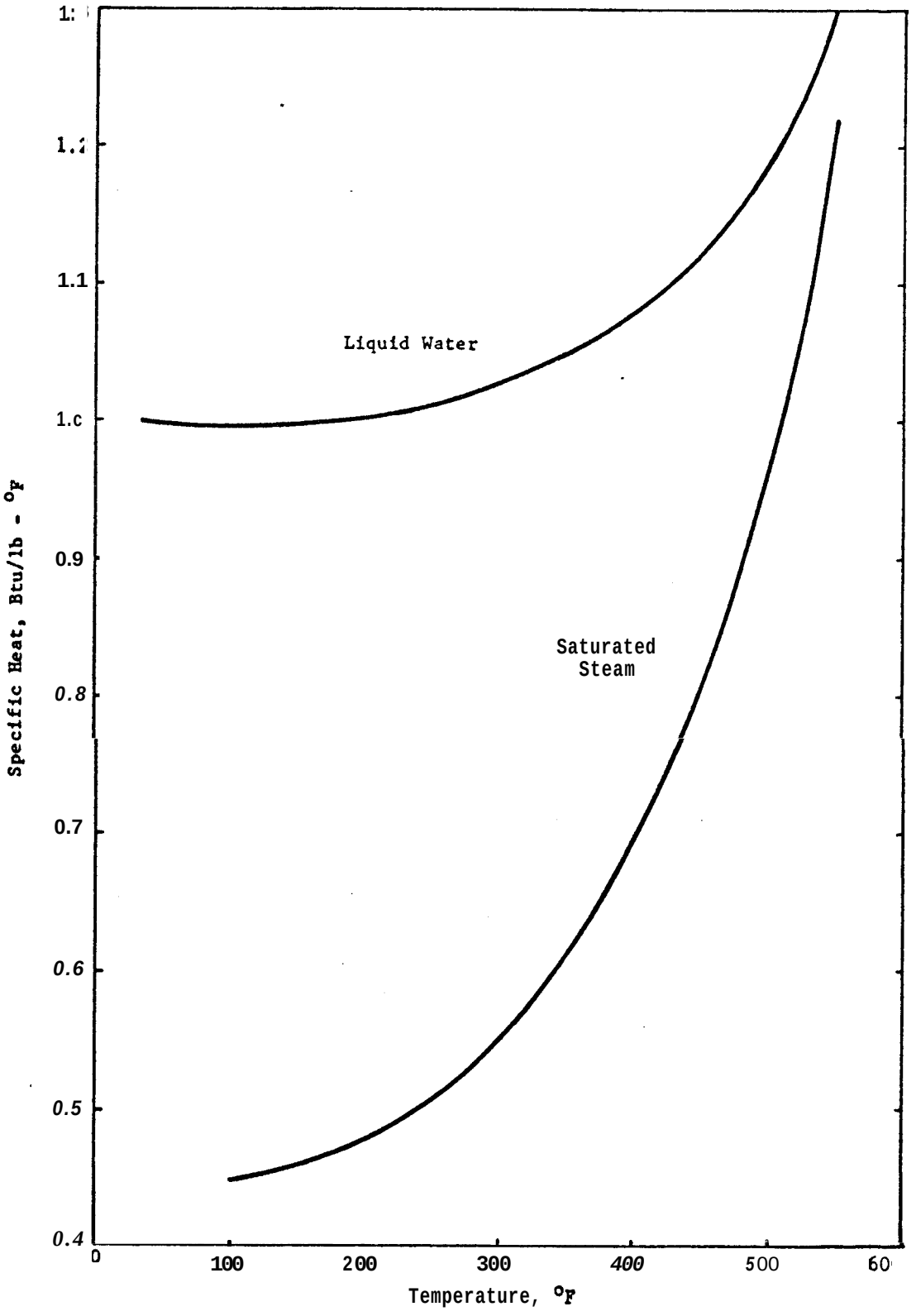

FIGURE B-3. SPECIFIC HEAT OF WATER VS. TEMPERATURE

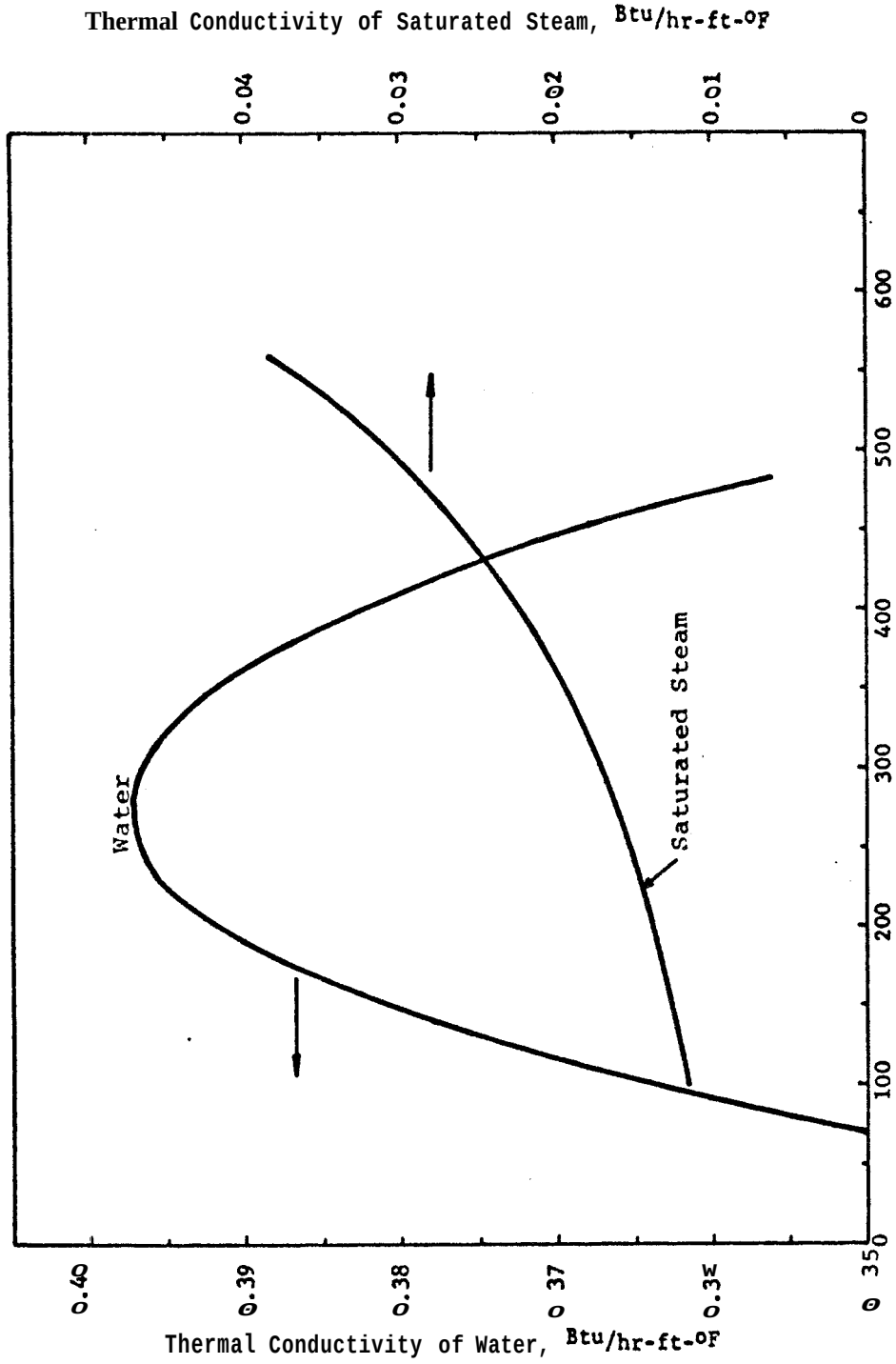

FIGURE B-4. THERMAL CONDUCTIVITY VS TEMPERATURE

$$\lambda_d = 0.339\rho^{1.03} - 3.194 + 0.53k^{0.10} + 0.013F - 0.031$$

where λ_d = thermal conductivity of dry sandstone, Btu/hr-ft-^oF

ρ = bulk density, gm/cc

ϕ = fractional porosity

k = permeability, millidarcies

F = formation resistivity factor

For the thermal conductivity of fluid saturated sandstone, the following empirical equation was obtained by Anand, et al[38]

$$\frac{\lambda_{sf}}{\lambda_d} = 1 + 0.3\left[\left(\frac{\lambda_f}{\lambda_{air}}\right)^{0.33} - 1\right] + 4.57\left(\frac{\rho_{sat}}{\rho_d}\right)^{4.3} \cdot \left(\frac{\phi}{1-\phi}\,\frac{\lambda_f}{\lambda_d}\right)^{0.482m}$$

where λ_{sf}, λ_f, λ_{air} = thermal conductivities of fluid saturated rock, of fluid, and of air, respectively,

ρ_{sat}, ρ_d = bulk density of fluid saturated and dry rock, respectively.

Gomaa and Somerton[40] showed a correlation of the thermal conductivity of sandstone containing liquid and vapor as follows:

$$\lambda = \lambda_g + (\lambda_\ell - \lambda_g)\sqrt{S_\ell} + \lambda_{HP}$$

where λ = thermal conductivity of rock containing liquid water and steam

λ_g, λ_ℓ = thermal conductivity of rock saturated with steam and with liquid, respectively

S_e = volumetric liquid water saturation

λ_{HP} = increase in thermal conductivity due to the heat pipe effect

The correlation for the heat pipe effect is as follows:

$$\lambda_{HP} = 0.003\phi^{0.357} k^{0.424}\left(\frac{h_f \gamma_v}{\sqrt{\nu_\ell \nu_g}}\right)(1 + 0.107 \sin\psi)F(S)$$

$$\text{and } F(S) = \sin\left[\pi\left(\frac{1-S_\ell}{1-S_{\ell c}}\right)\right] \sin\left[\pi\left(\frac{1-S_g}{1-S_{gc}}\right)\right]$$

$$\cdot (0.74 + 0.61 S_g + 1.56 S_g^2 + 2.85 S_g^3)]$$

$$S_{\ell c} = 0.098 k^{-0.236}$$

$$S_{gc} = 0.060 k^{-0.236}$$

where S_ℓ, S_g = the fraction of pore space filled with liquid water and steam, respectively

k = permeability, darcies

h_{fg} = latent heat of vaporization, Btu/lb

γ_{vp} = vapor pressure - temperature derivative, psi/^{o}F

ν_{ℓ}, ν_{g} = kinematic viscosity of liquid and steam, respectively, ft2/day

ψ = angle of heat flow direction, positive upward

APPENDIX C

CAPACITANCE PROBE DESIGN

APPENDIX C

CAPACITANCE PROBE DESIGN

A schematic diagram of the capacitance probe in operating position is shown in Fig. 1 in the main text. A detailed diagram of the probe is shown in Fig. C-1. The glass tube used for both the guide and the probe is Corning Glass 7740. The dielectric constant of this glass, as well as 7720, does not change much with temperature below 200°C. Figs. C-2 and C-3 are two circuits used with the probe. The design of the probe and the detection circuits were furnished by Dr. Paul Baker through the courtesy of the Chevron Oil Field Research Company, La Habra, California.

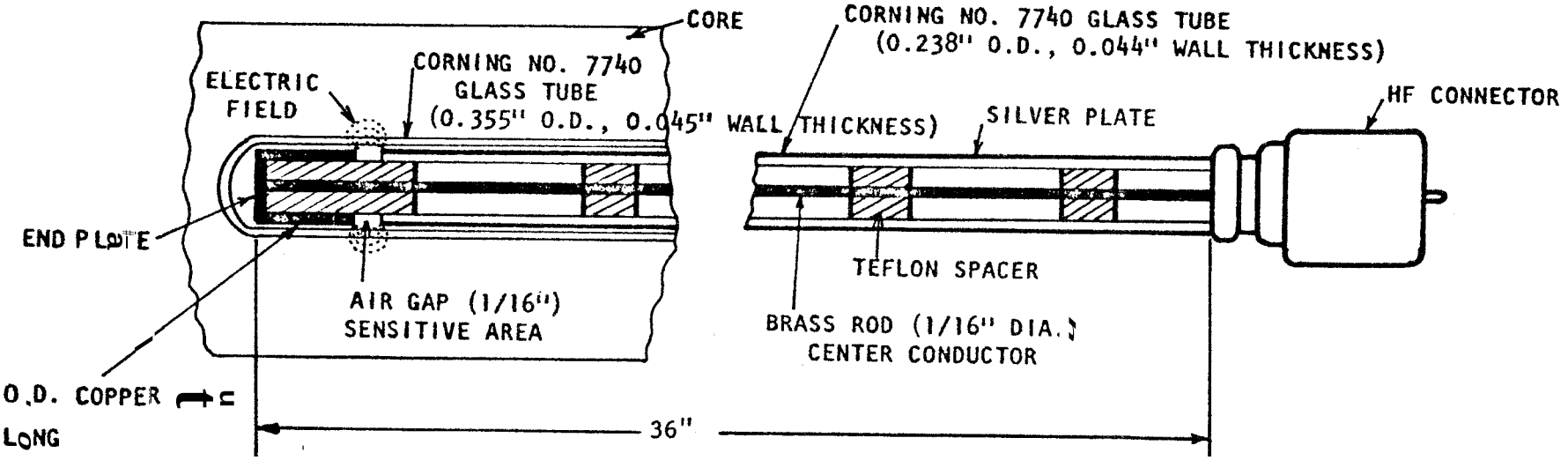

FIGURE C-1. SATURATION PROBE

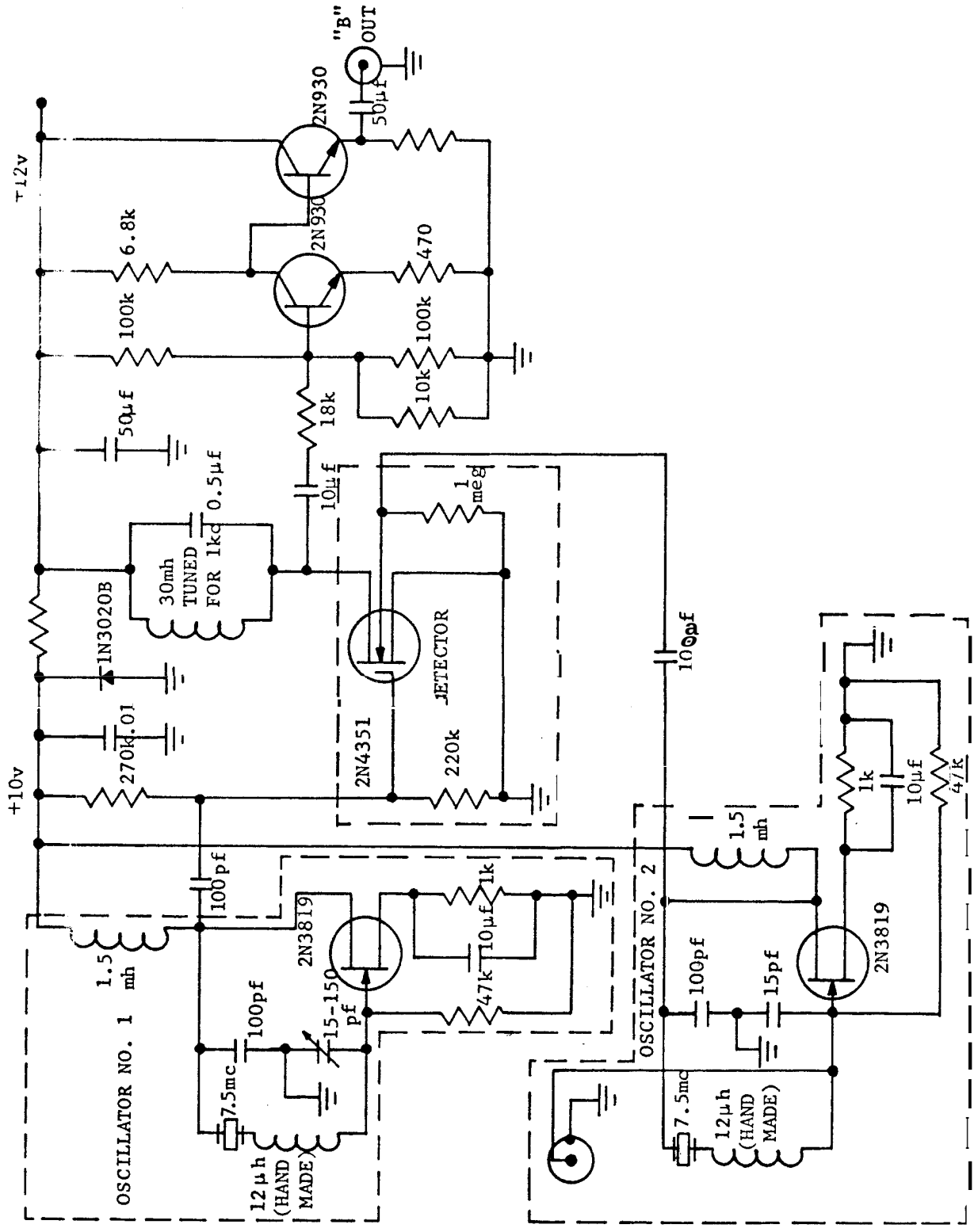

FIGURE C-2. CAPACITANCE PROBE CIRCUIT

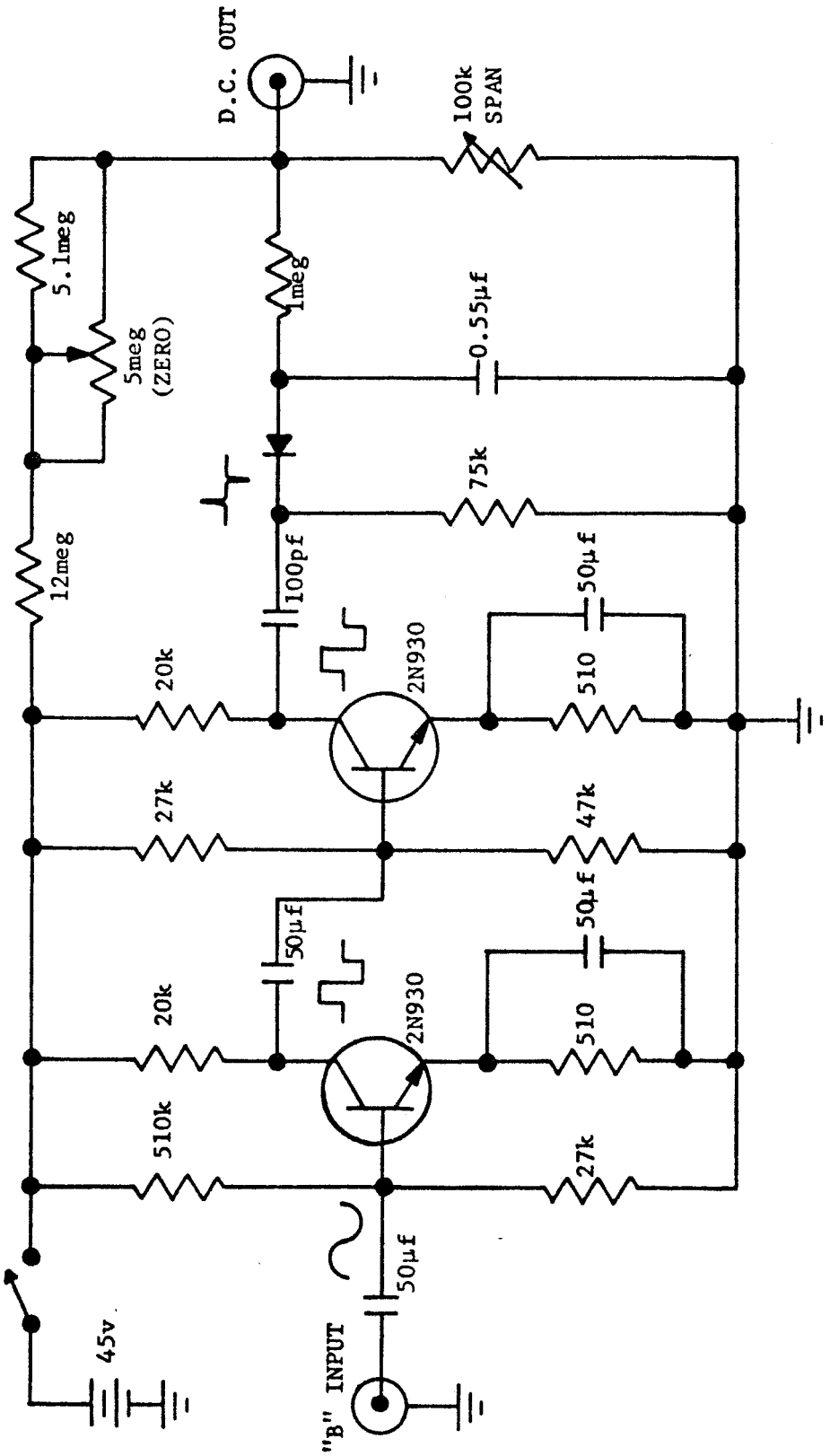

FIGURE C-3. DIGITAL TO ANALOG CONVERTER CIRUIT USED TO RECORD FREQUENCY SHIFT

APPENDIX D

LIST OF EQUIPMENT MANUFACTURERS & SUPPLIERS

APPENDIX D

LIST OF EQUIPMENT MANUFACTURERS & SUPPLIERS

Oven - NAPCO, Model 430, Van Waters & Rogers
Redwood City, Calif. (369-5561)

Tubular Furnace - Varian, Model 1027
Palo Alto, Calif. (493-4000)

Pump - Milton Roy, Model R121A,
San Mateo, Calif. (341-8796)

4. Accumulator - Hydraulic Controls Inc., Greerolator
Model 20-15TMR-S-½WS,
Emeryville, Calif. (658-8300)

5. Temperature Recorder - Leed & Northrup Co., Model Speedo-
max W Multi-Point Recorder,
San Mateo, Calif. (349-6656)

6. Pressure Recorder - Heathkit Electronic, Model EU-20W,
Redwood City, Calif. (365-8155)

7. Flowrator - Fischer & Porter Co., Model 10A3565A,
Walnut Creek, Calif. (933-8880)

8. Temperature Controller - Van Water & Rogers, Model
61329-054,
Redwood City, Calif. (369-5561)

9. Pressure Transducer - Celesco Industries, Model KP15,
GADO Instrument Sales,
Mountain View, Calif. (961-2222)

10. Pressure Indicator - Celesco Industries, Model CD25

11. Pressure Gage: AMETEK, Model P1536, Jensen Instrument
CO.,
South San Francisco, Calif. (589-9720)

Helicoid, Model KMonel 460

12. Pressure Regulator - Matheson Gas Products, Model 2-580,
Newark, Calif. (793-2559)

13. **Sheathed** Thermocouple, Thermocouple Wire - Claud S. Gordon Co., San Carlos, Calif. (591-7070)

14. **Valve,** Fitting, Filter: Swagelok, NUPRO, WHITEY, Van **Dyke** Valve & Fitting, Sunnyvale, Calif. (734-3145)

    Conax, Instrument Laboratory Palo **Alto,** Calif. (328-1040)

15. Pipe, Tubing - Tubesales, San Francisco, Calif. (922-2240 or Ent. 11919)

16. 0-Ring - McDowell & Co., Hayward, Calif. (785-7744)

17. Core Sleeve - Viton A Tubing, West American Rubber Co., Orange, Calif. (714 - 532-3355)

18. Core - Berea Sandstone Core, The Cleveland Quarries Co., Amherst, Ohio (216 - 986-4501)

APPENDIX E

EXPERIMENTAL **DATA**

.APPENDIX E

EXPERIMENTAL DATA

(1) Permeability Measurements

The experimental data of the permeabilities to water and nitrogen gas are tabulated as follows. The cores used for the thorough study are the Berea sandstone core and the synthetic sandstone core No. 2, as shown in Appendix A.

PERMEABILITY TO WATER, BEREA SANDSTONE

Core Temp. T_c, °F	Room Temp. T_r, °F	Room Press. P_r, psig	Press. Drop Δp, psi	Rate at T_r q, cc/sec	Viscosity at T_c μ, cp	Sp. Vol. at T_c ν, ft^3/lb	Sp. Vol. at T_r ν_r, ft^3/lb	Perm. at T_c k, md*
79.0	79.0	14.9	17.0	0.178	0.87	0.01607	0.01607	400.0
79.0	79.0	14.8	22.3	0.2381	0.87	0.01607	0.01607	405.6
76.0	76.0	15.0	15.0	0.1509	0.91	0.01610	0.01610	400.4
170.0	80.0	15.0	10.0	0.2447	0.335	0.01644	0.01607	399.9
175.0	80.0	13.0	15.0	0.3798	0.353	0.01647	0.01607	400.9
175.0	80.0	15.0	15.3	0.3996	0.335	0.0167	0.01607	405.2
252.0	80.0	15.0	7.8	0.300	0.272	0.01702	0.01607	402.8
275.0	80.0	15.0	10.7	0.4271	0.273	0.01704	0.01607	412.2
320.0	80.0	15.0	10.3	0.5085	0.219	0.01725	0.01607	401.1

*$k = 5786.6 \frac{q\mu L}{A\Delta p} \frac{\nu}{\nu_r}$, L = 23.5 in, and A = 3.14 in^2

P ERMEABILITY TO WATER, SYNTHETIC SANDSTONES, CORE NO 2

Core Temp. T_c °F	Room Temp T_r, °F	Room Press. p_r, psia	Press Drop Δp, psi	Rate at T_r q, cc/sec	Viscosity at T_c μ, cpc	Sp. Vol. at T_c ν, ft^3/lb	Sp. Vol. at T_r ν_r, ft^3/lb	Perm. at T_c k, md*
80 0	80 0	14 8	31.5	0 082T	0 860	0.1507	0.1507	98 8
80 0	80 0	14.8	49.0	0 1300	0 850	0 01507	0 01507	99.8
80.0	80 0	14 8	82.0	0.2153	0 850	0 1507	0 1507	98 8
155 0	78 0	14.8	32.0	0 1735	0 380	0 01641	0.01509T	92 1
155 0	78.0	14.8	58.0	0.3195	0 380	0 01641	0 01607	93 5
245.0	78 0	14 8	31.5	0.2T78	0.234	0 01595	0.01507	95 3
243.0	78.0	14.8	43 0	0.4087	0 234	0.01595	0.01507	98 1
340.0	78 0	14 8	23.0	0 2892	0 157	0 01786	0 01607	95 5
340.0	78.0	14.8	40.0	0 5010	0 157	0 01785	0.01509T	95 5

$$*k = 5786.6 \frac{q\mu L}{A\Delta p} \frac{\omega}{\omega_=}, \quad \text{@} = 23.5 \text{ in and } A = 3\ 14\ in^2$$

PERMEABILITY TO NITROGEN GAS, SYNTHETIC SANDSTONE, CORE NO. 2

Core Temp. T_c, °F	Room Temp. T_r, °F	R om Press. p_r, psia	Inlet Press. p_1, psig	Press. Drop Δp, psi	Mean Press. p_m, psia	p_r/p_m atm^{-1}	Rate at T_r q, cc/sec	Viscosity at T_c μ, cp	Perm. at T_c k, md*
77.0	81.0	14.78	98.8	2.18	112.49	0.131	2.262	0.178	105.4
77.0	81.0	14.78	66.0	2.93	79.32	0.186	2.146	0.178	105.5
77.0	81.0	14.78	36.0	2.63	49.47	0.299	1.253	0.178	110.0
77.0	81.0	14.78	24.5	2.43	37.57	0.393	1.263	0.178	112.0
77.0	81.0	14.78	12.0	2.88	25.34	0.583	0.739	0.178	115.7
76.0	82.0	14.76	64.7	2.80	78.06	0.189	2.058	0.178	107.0
76.0	82.0	14.76	64.5	4.00	77.26	0.191	2.890	0.178	106.3
76.0	82.0	14.76	35.3	3.80	48.16	0.306	1.779	0.178	110.6
76.0	82.0	14.76	24.0	3.80	36.86	0.400	1.385	0.178	112.4
76.0	82.0	14.76	11.3	2.95	24.56	0.601	0.465	0.178	116.0
76.0	76.0	14.72	65.5	2.52	78.96	0.186	1.845	0.0178	106.3
76.0	76.0	14.72	32.7	3.63	45.61	0.323	1.577	0.0178	109.3
76.0	76.0	14.72	21.3	3.23	34.41	0.428	1.101	0.0178	113.6
76.0	76.0	14.72	11.5	3.05	24.70	0.596	0.761	0.0178	115.8
145.0	82.5	14.70	98.5	2.23	112.37	0.132	1.887	0.0195	105.9
145.0	82.0	14.70	65.5	3.28	78.56	0.187	1.961	0.0195	106.9
145.0	81.0	14.70	34.0	3.12	47.14	0.312	1.174	0.0195	112.0
145.0	79.0	14.70	22.0	3.73	34.84	0.422	1.046	0.0195	113.1
145.0	78.0	14.70	10.7	3.05	23.88	0.616	0.606	0.0195	117.4
232.5	78.0	14.79	99.3	3.20	112.49	0.131	2.110	0.0215	104.8
232.5	78.0	14.79	65.0	3.82	77.88	0.190	1.799	0.0215	108.5
232.5	78.0	14.79	34.5	4.38	47.10	0.314	1.292	0.0215	112.3
232.5	78 0	14.79	21.8	3.87	34.64	0.427	0.856	0 0215	113.3
232.5	78 0	14.79	8.8	3.12	22.23	0.665	0.456	0 0215	119.0

Cont.

$$*k = 5786 \frac{L\mu q}{A\Delta p} \frac{p_r}{p_m} \frac{T_c}{T_r}, \quad L = 23.5 \text{ in and } A = 3.14 \text{ in}^2$$

PERMEABILITY TO NITROGEN GAS, SYNTHETIC SANDSTONE, CORE NO 2, CONT.

Core Temp. T_c, °F	Room Temp. T_r, °F	Room Press. p_r, psia	Inlet Press. p_1, psig	Press. Drop Δp, psi	Mean Press. p_m, psia	p_r/p_m atm^{-1}	Rate at T_r q, cc/sec	Viscosity at T_c μ, cp	Perm. at T_c k, md*
231.0	77.5	14.78	99.8	3.25	112.95	0.131	2.165	0.0214	103.0
231.0	77.5	14.78	66.0	2.90	79.33	0.186	1.385	0.0214	105.2
231.0	77.5	14.78	35.0	3.25	48.15	0.307	0.984	0.0214	109.9
231.0	77.5	14.78	23.3	3.76	36.19	0.408	0.873	0.0214	111.5
231.0	77.5	14.78	12.5	3.75	25.40	0.582	0.635	0.0214	116.5
342.0	77.0	14.80	98.3	2.92	111.64	0.133	1.458	0.0238	102.8
342.0	77.0	14.80	64.8	2.92	78.14	0.189	1.068	0.0238	107.6
342.0	77.0	14.80	33.0	3.57	46.02	0.322	0.800	0.0238	111.9
342.0	77.0	14.80	23.0	4.26	35.67	0.415	0.741	0.0238	112.1
342.0	77.0	14.80	12.0	4.53	24.54	0.603	0.552	0.0238	114.3

$$*k = 5786 \frac{L\mu q}{A\Delta p} \frac{p_r}{p_m} \frac{T_c}{T_r}\ ;\ L = 23.5 \text{ in and } A = 3.14 \text{ in}^2$$

(2) Hot Water and Cold Water Injection

In the following tables, the axial temperature distributions at various injection times are shown for each run of the hot water and cold water injection experiments. The following numbering system for the runs was used: the first three letters designate Hot Water Injection (HWI) or Cold Water Injection (CWI), a letter after a dash means Synthetic sandstone (S) or Berea sandstone (B), and the last digit indicates the run number. The necessary data for calculation of thermal efficiency are also tabulated for each run.

AXIAL TEMPERATWRE DISTRIBUTION IN THE CORE, RUN NO HWI-S-1

Location, in.	Time, min. 30	60	90	120	180	300	360
0	100	106.5	113	117	121	126	126
1	95	101.5	107.5	112.5	118	123.5	123.5
2	90	98	104	108.5	114	121	121
3	87.5	95	100	105	111	118.5	118.5
4	85	92	97.5	102.5	109	117	117
5	84.5	90	95	100	107.5	114	115.5
6	84	87.5	92.5	97.5	105	111	114.5
7	83.5	85	90	95	102	108.5	112
8	83	85	88	94	100	107	110.5
9		84.5	87.5	91	98	105	109
10		84	86	89.5	96	103	107
11		83 5	85	88	93	101.5	106
12		83	84	86.5	91	99	104
13							
14			83	85	86.5	97	100.5
15				84	85	96	100
16				84	84	95	99
17				83	83.5	93	97
18					83	92.5	96.5
19						91.5	95.5
20						91	95
21						90.5	93.5
22						90	93
23						89.5	92
24						89	92
Inlet Press. (psig)	23 0	22.0	24 2	24 0	23.5	24.5	24 0
Press. Drop Across Core psi	23.0	22 0	24.2	24.0	23.5	24.5	24 0

CALCULATION OF THERMAL EFFICIENCY

Run No. HWI-S 1 (T_∞ = 83°F)

Time min.	Injection Temp., °F	Injection Rate, lb/hr	Cumulative Heat Injected Btu	Heat Within Core Btu	E
0	85	0. ≤	0	0	-
30	100	0.4≤	2 175	2.988	0.9437
60	107	0 4≤	7 783	6.801	0.8738
90	113	0 50	14.307	17.048	0.7722
120	117	0 52	22.644	15.877	0.7012
180	121	0 52	41.547	22.682	0.5459
300	128	0 58	87.995	37.875	0.4304
360	128	0.58	114,389	43.653	0.3816

AXIAL TEMPERATURE DISTRIBUTION IN THE CORE, RUN NO. HWI-S-2

Location, in	Time, min. 15	30	45	60	90	120	180	240	300	360
0	100	114.5	122	128	138	142	146	148	149	149
1	90.5	102.5	113.5	121	131	137.5	144	145.5	148	148
2	86	96	106	115	126	134.5	140.5	143	146	146
3	82	91	100.5	109.5	122.5	129.5	139	141.5	143.5	145
4	80	86.5	95.5	104.5	117	125.5	135.5	138.5	140.5	142
5	79	83.5	90.5	99.5	112.5	121.5	132.5	136.5	139	140
6	78.5	81.5	87	95	108.5	117	129.5	134	135.5	137
7	77.5	80	84	90	104.5	114	125.5	131	133.5	135
8		79	83	87	100	109.5	122.5	128	130.5	132.5
9		78	81	84.5	96	107	119.5	125	129	130
10		77.5	79	83	93	103.5	115.5	122.5	126	128
11			78	81						
12			77.5	80	88	97 5	110	11[illegible] 5	121 5	123 5
13				79						
14				78	[illegible]4	90.5	105 5	111 5	11[illegible].5	119
15				77.5						
16					80.5	86 5	100	107.5	113	1[illegible]4 5
17										
18					79 5	84	95	102 5	108	110.5
19										
20					78.5	81	91	99	104.5	107.5
21										
22					[illegible]8.5	80	8[illegible]	95	100	104 5
23										
24					78.5	80	85	92	97	101
Inlet Pres[illegible] (psig)	260	260	260	260	260	260	260	260	260	260
Press. Drop Across Co[illegible]e psi	44	4[illegible]	42	41	38.5	[illegible]6 5	33.5	31 0	[illegible]1 0	[illegible]0 0

CALCULATION OF THERMAL EFFICIENCY

Run No. HWI-S-2 (T_∞ = 77.5°F)

Time Min.	Injection Temp., °F	Injection Rate, lb/hr	Cumulative Heat Injected Btu	Heat Within Core Btu	E
0	80	0.77	0	0	-
30	114.5	0.77	8.303	7.893	0.9506
45	122	0.77	16.126	13.492	0.8367
60	128	0.79	25.419	19.920	0.7837
90	138	0.79	47.497	34.144	0.7189
120	142	0.81	73.048	46.989	0.6433
180	146	0.81	127.454	67.825	0.5321
240	148	0.82	181.092	79.203	0.4374
300	149	0.82	239.124	86.743	0.3628
360	149	0.82	297.448	90.865	0.3055

AXIAL TEMPERATURE DISTRIBUTION IN THE CORE, RUN NO. HWI-S-3

Location, in.	Time, min 15	30	45	60	75	105	165	225	315
0	100	112.5	120.5	129	134.5	141	149	151.5	152
1	90	102.5	112	121	128	136.5	145	150	151
2	84	96	106	115	122.5	132	141.5	148	149
3	81	91	100	110	117.5	128	139	145	148
4	78	86	95.5	105	113	125	136	143	146
5	77	84	90.5	100	108	121	132	140	143.5
6	76	80	87	95	104	116	129	137	141
7		78.5	84	90.5	100	112	126	135	138
8		77	81.5	87	96	109	123	132	136
9		76.5	79	85	92.5	105	120	129.5	134
10		76	77.5	82	90	101.5	117	127	131
11			77	80	86.5	98	114	123.5	129
12			76	79	84	95	110	120.5	126.5
13				78	82	92.5	107.5	117.5	124.5
14				77.5	80	88.5	105.5	115	122
15				77	78	87	103	112	120
16				76	77.5	85	100	110	118
17					77	83	97	107.5	115.5
18					76	81.5	95	105	113
19						80	93	103.5	111
20						79	90	101	112
21						78	89	99	108
22						77.5	88	97	106
23						76	86	95	103
24							85	93	101
Inlet Press. (psig)	260	260	260	260	260	260	270	270	270
Press. Drop Across Core psi	48 0	49 0	48 0	49 0	49 0	44.0	37.0	34.5	33 0

CALCULATION OF THERMAL EFFICIENCY

Run No. HWI-S-3 (T_∞ = 76°F)

Time min.	Injection Temp., °F	Injection Rate, lb/hr	Cumulative Heat Injected Btu	Heat Within Core Btu	E
0	88	0.90	0	0	-
15	100	0.90	4.046	3.337	0.8248
30	112.5	0.94	10.939	8.525	0.7793
45	121	1.02	20.938	14.258	0.6805
60	130	0.99	33.572	21.631	0.6443
75	136	1.03	48.589	30.304	0.6237
105	143	0.95	80.780	46.173	0.5716
165	151	0.84	143.427	71.341	0.4811
225	155	0.96	222.491	88.563	0.3981
315	156.5	0.97	336.950	99.445	0.2951

AXIAL TEMPERATURE DISTRIBUTION IN THE CORE, RUN NO. HWI-S-4

Time, min.

Location in.	15	30	45	60	75	90	120	150	180	210	240
0	114.5	131	143	148	152	154	159	160.5	161.5	161.5	161.5
1	99.5	119	134	141	147	150	156	158	160	160	160
2	89.5	110 5	127	136	142.5	146.5	153	155.5	157	157	157 5
3	83	105	122	132	139	144.5	150	154.5	155.5	156	157
4	78	98	116	127.5	136	140	148	152.5	154	154.5	155.5
5	76	92	111 5	124	131.5	137.5	145	150.5	152.5	153.5	154.5
6	75	86	105	119.5	128	134.5	143.5	148	150.5	151.5	152.5
7	74.5	82	100.5	114.5	124.5	130	140.5	146	149	150	150.5
8	74	79	95	109.5	120	126	137	144	148	148	149
9		76 5	90.5	105.5	116	124	136	141 5	145.5	147	147 5
10		76	86	101	112	120	130 5	139 5	143	145	14≤
11		74	84	97	108 5						
12			80	92.5	105	112.5	125.5	134.5	138.5	141	143
13			78	89	101						
14			77	86	97 5	105.5	119.5	129	134	137.5	139 5
15			76	84							
16			74.5	80.5	91	100	114	124 5	130 5	134	135 5
17			74	79							
18				77.5	8≤	94	108 5	119	125 5	130	132
19				76.5							
20				75	81	₽₽	103.5	114	121 5	126	128 5
21				74							
22					77.5	83.5	98	110	118	122.5	126
23											
24					74 5	79	93	105	114	119	123
Inlet Pr₽33 (psig)	250	250	250	250	250	250	250	250	250	250	250
Press. Drop Across Core psi	84	80	80	76	69	6≤	≤5	3Z	61	≤0	≤5

CALCULATION OF THERMAL EFFICIENCY

Run No. HWI-S-4 (T_∞ = 74°F)

Time min.	Injection Temp., °F	Injection Rate, lb/hr	Cumulative Heat Injected Btu	Heat Within Core Btu	E
0	90	1.52	0	0	-
15	114.5	1.52	7.667	6.182	0.8063
30	131	1.52	23.647	17.100	0.7231
45	143	1.61	46.658	32.614	0.6990
60	148	1.62	80.429	48.843	0.6073
90	154	1.68	143.785	77.752	0.5408
120	159	1.82	215.600	100.426	0.4671
150	160.5	1.88	296.163	116.105	0.3920
180	161.5	1.93	377.677	125.028	0.3310
210	161.5	1.92	463.541	129.874	0.2802
240	161.5	2.11	548.024	133.143	0.2430

AXIAL TEMPERATURE DISTRIBUTION IN THE CORE, RUN NO. HWI-B-1

Time, min.

Location in.	0	5	15	30	45	60	75	90	120	150	180	210
0	82.5	95	106.5	114	118.5	112.5	125	128	130.5	130.5	130.5	132
1	80	90.5	104	112	118	120.5	124	127	180	130	130	131.5
2	78.5	86	99	110	115	119	122.5	125.5	128	129.5	129.5	130.5
3	77.5	81.5	95	106.5	112.5	116	120.5	122.5	126.5	128	128	130
4		80	91	104	109.5	114	118	121.5	125	127	127	129
5		78.5										
6		77.5	85	98	105	110	114.5	117.5	122	124.5	125	126.5
7												
8			80	92.5	99.5	105	108	113	118	120.5	122.5	124
9												
10			78	87	95	100.5	105	109	115	117.5	119	120.5
11												
12			77.5	83	90.5	95.5	100.5	105	111.5	115	116	118.5
13												
14				81	87	93	97	102	108	112	114	115.5
15												
16				79	84	89	95	99	105	109	112	114
17												
18				78	81	86	91	96	101.5	106.5	110	112
19												
20				77.5	79.5	84	88	93	99	104	107	110
21												
22					78	81	85.5	90	96	101	105	107
23												
24					77.5	79	83	86	93	99	102	105
Inlet Press. (psig)	247	248	248	250	250	250	250	252	252	252	252	252
Press. Drop psi	22.0	20.5	20.0	18.5	17.2	16.0	15.2	14.2	13.8	13.3	13.3	13.3

CALCULATION OF THERMAL EFFICIENCY

Run No. HWI-9-1 (T_∞ = 77 5°F)

Time min.	Injection Temp., °F	Injection Rate, lb/hr	Cumulative Heat Injected Btu	Heat Within Core Btu	E
0	82.5	1.83	0	0	-
5	95	1 85	1.729	2.5750	1.4893
15	106.5	1 89	8 973	9.1574	1.0205
30	114	1.85	24.580	21 050	0.8555
45	118.5	1 80	42.092	30 575	0.7264
60	122.5	1.79	61 500	39.673	0.6451
75	125	1 81	82 160	48 129	0.5858
90	128	1 77	104.261	58 025	0.5374
120	130.5	1.80	148 475	66 068	0.4450
150	130 5	1 82	198 508	72.854	0.3661
180	130.5	1 85	247.928	78.304	1.3078
210	132	1 85	309.024	79.804	0.2582

AXIAL TEMPERATURE DISTRIBUTION IN THE CORE, RUN NO. HWI-B-2

Time, min

Location in.	0	5	15	30	45	60	75	90	120	150	180
0	90	102.5	110.5	115	120	123	126	127.5	129	129	129
1	85	99	108.5	114	119	123	125.5	127.5	128.5	128.5	128.5
2	80.5	95	106.5	113	117.5	121 5	124	126.5	126.5	128	128
3	76.5	89	104	110	115	120	123	125.5	126	127	127
4	76	85	100	108 5	113.5	118	121	124	125	126	126.5
5	75.5										
6		79	95	104.5	110	114	118	121	123 5	125	125
7											
8		75 5	87 5	100	10[illegible]	110.5	115	118	121	123.5	124
9											
10			81	9[illegible]	103	107	111 5	115	119	121 5	122
11											
12			77.5	[illegible]1 5	99	104	108	113	117	119 5	120
13											
14			7[illegible]	87	96	100.5	10[illegible]	110	114 5	117	118
15											
16			75.5	84	92.5	98	103.5	107.5	111.5	115	116
17											
18				80	89	95	100	105	110	113 5	115
19											
20				78.5	86	93	98	102	108	112.5	114
21											
22				7[illegible] 5	84	89 5	95	100	10[illegible] 5	110	11[illegible]
23											
24				76	81	87	92	98	105	108	111
Inlet Press. (psig)	246	246	248	248	248	248	248	247	248	248	248
Press. Drop Across Core psi	28 3	29 0	2[illegible] 7	23 1	21 0	20.2	19 7	20.2	18.2	18.0	18 0

CALCULATION OF THERMAL EFFICIENCY

Run No. HWI-B-2 (T_∞ = 75.5°F)

Time min.	Injection Temp., °F	Injection Rate, lb/hr	Cumulative Heat Injected Btu	Heat Within Core Btu	E
0	90	2.48	0	0	-
5	102.5	2.65	4 446	5 519	2358
15	110.5	2.61	18 006	16.301	9053
30	115	2.52	40.980	31.833	7768
45	120	2.51	68 008	45.382	6673
60	123	2.59	92.622	54.680	5904
75	126	2.61	129 118	63.338	4905
90	127.5	2.81	166 577	70 787	4327
120	129	2.61	234 116	78.076	.3335
150	129	2.61	305 951	83 014	2713
180	129	2.65	374.365	84.696	.2262

AXIAL TEMPERATURE DISTRIBUTION IN TH RUN NO. HWI-B-3

Time, min.

Location in.	0	5	15	30	45	≤0		120	150	180	210	240
0	86	97.5	113	129	141	149		1≤8	173	174.5	174.5	174.5
1	82.5	92	108.5	125	137	146.5		1≤6	172	174	174	174
2	78	86	102	120	134	142		1≤4	170	172	172	172
3	74	81	97.5	115	129	138		1≤0 5	166.5	169	170	170
4	73	78	91	110	124	134		137	164	167	168	168
5	72	75										
6		73.5	80	100 5	115	12≤		150 5	159	162.5	163	1≤0
7		72.5										
8		72	77	93	106	118	132.5	10ɔ	153	157.5	158.5	1ɔ9
9												
10			74	8≤	99	111	12≤	138.ɔ	147 ɔ	152.5	153 5	1ɔ0 ɔ
11												
12			73	80.5	9z.5	104	119 ɔ	132	141	107 ɔ	1ɔ0	151
13												
14			72	76	86	97	113	126	137	143	146	148
15												
16				70	81.5	91	10ɔ 5	120.ɔ	130 ɔ	138 ɔ	141 5	144
17												
18				72	78	8≤	103	11≤	127	13ɔ	137 5	100
19												
20					75.ɔ	82.ɔ	98	111	122.ɔ	130	135	137 5
21												
22					73 5	79 ɔ	94	107	119	12≤ 5	130 5	133 5
23												
24					7z	77 ɔ	90	103	115	122 ɔ	127	130
Inlet Pressure (psig)	208	208	208	249	249	249	249	249	209	250	250	250
Press. Drop Across Core psi	23 0	22 0	20 3	19 2	10 0	1ɔ 3	13 0	12 ɔ	1z.0	10 ≤	11 ɔ	11 0

CALCULATION OF THERMAL EFFICIENCY

Run No. HWI-B-3 (T_∞ = 72°F)

Time min.	Injection Temp., °F	Injection Rate, lb/hr	Cumulative Heat Injected Btu	Wi	Heat in Core Btu	E
0	8[illegible]	1.91	0		0	-
5	97 5	6.87	3 098		[illegible].242	1.0463
15	113	1.86	1[illegible] 420		12 [illegible]	0.9111
30	1[illegible]9	1.96	[illegible] 287		28 803	0.7725
45	141	1.95	68.174		[illegible].[illegible]20	0 [illegible]985
60	149	1.95	103 [illegible]84		[illegible]5.887	0.[illegible]355
90	1[illegible]0	2.01	185.[illegible]0		92.6[illegible]	0 5000
120	168	2.11	279.853		1[illegible] 921	0 4214
150	17[illegible]	2.11	[illegible]87 2[illegible]7		1[illegible] 319	0 [illegible]520
180	174 5	2.07	501 0[illegible]4		147 000	0 [illegible]934
210	[illegible]4.5	2.18	[illegible]04 612		151.008	0.2498
240	174.5	2.18	72[illegible].822		153.954	0 2118

AXIAL TEMPERATURE DISTRIBUTION IN THE CORE, RUN NO. HWI-B-4

Location, in.	Time, min. 0	5	15	30	45	60	75	90
0	102	110	127	140	145	148	149	150
1	94	108.5	125	139	144	147.5	148.5	150
2	85	106	122.5	137.5	142.5	146	148	149
3	78	101.5	119	135	140	145	147	148
4	74	97.5	116	132.5	139	143.5	146	146.5
5		94	114	130				
6		88.5	110.5	127	135.5	140	145	145
7		84	107	125				
8		80.5	105	123	132	136.5	142.5	142.5
9		78	102.5	120.5				
10		76	99	119	128.5	134	140	140
11								
12		74	94.5	114.5	125	131	138	138
13								
14			89	110	122.5	128.5	135	137
15								
16			84	107	118	125.5	134	135
17								
18			78.5	102	115	122.5	131	134
17								
20			76	97.5	111	120	128	132
21								
22			74	94	108.5	117	126	130.5
23								
24			74	89	106	113	124	129
Inlet Press. (psig)	242	242	242	241	241	241	241	240
Press. Drop psi	43.5	43.5	40.0	31.0	27.0	26.0	25.5	24.0

CALCULATION THERMAL EFFICIENCY

Run No. HWI -4 (T_∞ = 74°F)

Time min.	Injection Temp., °F	Injection Rate, lb/hr	Cumulative Heat Injected Btu	Heat Within Core Btu	E
0	102	4.54	0	0	-
5	110	4.38	11.844	11.750	0.9920
15	127	4.36	44.894	38.302	0.8532
30	140	4.54	112.339	75.631	0.6732
45	145	4.47	190.091	95.949	0.5048
60	148	4.54	270.752	107.681	0.3977
75	149	4.54	361.147	119.883	0.3320
90	150	4.54	459.339	123.098	0.2680

AXIAL TEMPERATURE DISTRIBUTION IN THE CORE, RUN NO. CWI-S-1

Location, in.	Time, min. 5	15	30	45	60	90	120
0	144	136	133	132	131	131	131
1	150	142.5	137	134.5	133	132	132
2		148	140.5	136.5	134.5	134	134
3		149.5	143.5	138.5	136.5	135.5	134.5
4		150	145	141.5	138.5	136.5	135.5
5			147.5	142.5	140	137.5	136.5
6			149	145	141	139	138.5
7			150	147.5	143.5	140.5	139.5
8				148.5	145	141	140
9				149	146	142.5	141
10				150	147.5	143.5	141.5
11							
12					149	145.5	144
13							
14					150	147.5	145
15							
16						148.5	146
17							
18						150	147.5
19							
20							148.5
21							
22							149
23							
24							150
Inlet Press. (psig)	260	260	260	260	263	265	268
Press. Drop Across Core psi	27.0	27.5	28.0	28.5	28.5	28.5	29.0

CALCULATION OF THERMAL EFFICIENCY

Run No. CSI-S-1 (T_{∞} = 150°F)

Time min.	Injection Temp., °F	Injection Rate, lb/hr	Cumulative Heat Injected Btu	Heat Within Core Btu	E
0	150	0.95	0	0	-
5	144	0 97	0 202	0.163	0.6717
15	136	0 97	1.780	1.354	0.7605
30	133	0 98	5.559	3.683	0.6626
45	132	0 98	9.922	6.065	0.6113
60	131	0.98	14.727	8.772	0.5958
90	131	0 98	24.011	11.913	0.4961
120	131	0 97	33.261	14.567	0.4380

AXIAL TEMPERATURE DISTRIBUTION IN THE CORE, RUN NO. CWI-S2

Location, in.	Time, min. 5	15	30	45	60	75	90	120
0	125	119	116.5	116.5	116.5	116.5	116.5	116.5
1	136	124	119.5	118.5	118.5	118.5	118.5	118.5
2	145	129	122.5	120	120	120	120	120
3	152	133	124	122	122	1221	122	122
4	155	138	127	124	123	123	123	123
5		142.5	129	125.5	124	124	124	124
6		147	132	127	125	125	125	125
7		150.5	136	129	127.5	126.5	126.5	126.5
8		154.5	139	131.5	128.5	127	127	127
9		155	143	133.5	130	129	128	128
10			145.5	135.5	131.5	130	129	129
11								
12			150	140.5	134.5	132	131	131
13								
14			153	145	138	135	133	133
15								
16			155	149	141	137.5	135.5	134.5
17								
18				150.5	145	140	137	135.5
19								
20				153	148	142	139	137.5
21								
22				155	149.5	144.5	141	138.5
23								
24					151	147.5	143.5	140
Inlet Press. (psig)	255	255	255	255	260	260	260	265
Press. Drop Across Core psi	56.0	56.0	57.0	58.0	59.0	61.5	62.0	61.5

CALCULATION OF THERMAL EFFICIENCY

Run No. CWI-S-2 (T_∞ = 155°F)

Time min.	Injection Temp., °F	Injection Rate, lb/hr	Cumulative Heat Injected Btu	Heat Within Core Btu	E
0	155	1 [illegible]	0	0	-
5	125	1 [illegible]7	2.327	3 735	1 6052
15	119	1 9[illegible]	12 922	11.335	0.8772
30	116.5	1.80	29 [illegible]37	21 [illegible]80	0 7408
45	116.5	2 14	4[illegible] 11[illegible]	31.39[illegible]	0 652[illegible]
60	116.5	1 80	65.674	39 296	0.[illegible]984
75	116.5	1 91	83.377	44.082	0 5287
90	116.5	1 78	101.556	47 001	0.462[illegible]
120	116.5	1 87	134.701	48.[illegible]2[illegible]	0 [illegible][illegible]8

AXIAL TEMPERATURE DISTRIBUTION IN THE CORE, RUN NO. CWI-S-3

Location, in.	Time, min. 5	15	30	45	60	75	90	120
0	185	162	153	153	153	153	153	
1	210	171.5	158					
2	235	182.5	165	161	161	161	161	
3	252	190	170					
4	255	200	175.5	168	167	167	167	
5		210	181					
6		221.5	186	175.5	172	172	172	
7		233	191					
8		244	197	183	177	177	177	
9		250	202.5					
10		255	208	191	184.5	182.5	182.5	
11								
12			221.5	199	191	188	187	
13								
14			235	207	197	193.5	191	
15								
16			24[illegible]	216	203.[illegible]	198.5	195.5	
17								
18			2[illegible]2	22[illegible]	209	203.5	200	
19								
20			2[illegible][illegible]	234	215.5	208	205	
21								
22				242	222.5	213.[illegible]	208.[illegible]	
23								
24				251	230	218	212	
Inlet Press (psig)	253	253	255	255	255	255	257	
Press. Drop Across Core psi	36.5	40.0	45.0	48.0	49.5	50.[illegible]	51.0	

CALCULATION OF THERMAL EFFICIENCY

Run No. CWI-S-3 (T_∞ = 255°F)

Time min.	Injection Temp., °F	Injection Rate, lb/hr	Cumulative Heat Injected Btu	Heat Within Core Btu	E
0	255	2.96	0	0	-
5	185	2.96	8.620	8.210	0.9524
15	162	2.84	47.862	35.829	0.7486
30	153	2.98	113.317	74.844	0.6605
45	153	2.88	195.498	106.992	0.5473
60	153	2.82	260.160	125.176	0.4811
75	153	2.87	340.033	131.849	0.3878
90	153	2.89	405.822	135 320	0 3334

AXIAL TEMPERATURE DISTRIBUTION IN THE CORE, RUN NO. CWI-S-4

Location, in.	Time, min. 7	15	30	45	60	75	90	105
0	136	136	135 5	135	135	133	133	133
1	158	144						
2	170	151	144	142	142	139	139	139
3	180	157						
4	192.5	163	151	140	1Φ8	144	144	144
5	206	169		o				
6	220	175	158	15≤	1≡2 5	149	148.5	148.5
7	235	180						
8	244	188	165 5	160	157 5	1≡4	15≡	153
9	249	195						
10	250	202	172	165	162	159	156 5	156.5
11								
12		219	181	170.5	167	164	161	161
13								
14		234	189	177	172	168	165	165
15								
16		244	198 5	[illegible]2	[illegible]77	172	160.5	168.5
17				[illegible]o	[illegible]			
18		248	209	[illegible]9	[illegible]81 5	176.5	17[illegible]	171
19							cam	
20		250	220	194	186	180	177	175
21								
22			230	201	190.5	184	180	175.5
23								
24			240	208	195	190	184	181
Inlet Press. (psig)	Z50	Z50	250	250	253	250	253	253
Press. Drop Across Core psi	[illegible]0.0	[illegible]4.0	70.0	73.5	75.3	86.5	85.5	86.0

CALCULAΠΞ OF ΠHERMAL EFFICIENCY

Run No. -S-4 (T_∞ = 250°F)

Time min.	Injection Temp., °F	Injection Rate, lb/hr	Cumulative Heat Injected Btu	Heat Within Core Btu	E
0	250	3 97	0	0	-
7	150	3.99	36.618	3≤.≤18	1 0000
15	136	Ξ 97	93.251	78.487	0.8417
30	135.5	Ξ 71	202.659	129 400	0 6385
45	135	3.5≤	Ξ0≤.17≤	153 8≤9	0 5026
60	135	3.93	394 855	162.586	0 4118
75	133	3 95	528.945	170 68≤	0 3Z27
90	133	Ξ.9Ξ	624.347	175.066	0 2804
105	133	4 02	759.391	176.851	0 2329

AXIAL TEMPERATURE DISTRIBUTION IN THE CORE, RUN NO. CWI-B-1

Location, in.	Time, min. 5	15	30	45	60	75	90	105
0	173	166	161	157.5	157.5	157.5	157.5	157.5
1	177.5	169	162.5	159	159	159	159	159
2	181.5	173.5	165	161	160	160	160	160
3	184.5	177	168	164	163	162	162	162
4	185	180	170.5	166	164	163.5	163.5	163.5
5								
6		184	175.5	170	167	166	165	165
7								
8		185	179	174	170	168	167.5	167.5
9								
10			182	177	173	171.5	170	170
11								
12			184	179	176	174.5	173	172
13								
14			185	181	178	177	175	174
15								
16				183	181	179	177	176
17								
18				185	183	181	179	177
19								
20					185	183	181	179
21								
22						184	182	180
23								
24						185	183	182
Inlet Press. (psig)	251	251	252	251	252	253	253	253
Press. Drop Across Core psi	7.0	7.3	7.5	7.7	7.8	7.8	7.8	7.8

CALCULATION OF THERMAL EFFICIENCY

Run No. CWI-B-1 (T_{∞} = 185°F)

Time min	Injection Temp., °F	Injection Rate, lb/hr	Cumulative Heat Injected Btu	Heat Within Core Btu	E
0	180	1.39	0	0	-
5	173	1.44	1.010	1 384	1.3709
15	166	1.44	4.730	4.288	0 9065
30	161	1.47	12 ≤33	10.≤92	0 8463
45	157.5	1.44	22 045	17 122	0.7767
60	157.5	1.44	32.068	20 702	0.6456
75	157.5	1.42	41.ᚻ99	22.982	0.5498
90	157.5	1.38	51.ᚼ37	2ᚼ ᚼ87	0.4965
105	157.5	1.38	≤0.836	27.161	0 4465

AXIAL TEMPERATURE DISTRIBUTION IN THE CORE, RUN NO. CWI-B-2

Location in.	Time, min. 5	15	30	45	60	75	90	105
0	208	192	182	178	177	177	177	177
1	214.5	195.5	184.5	180	178.5	178.5	178.5	178.5
2	221	201	188	183	181	181	181	181
3	225.5	208	192	186.5	184	183	183	183
4	228	213	196	189.5	186	185	185	185
5								
6		221	203	19 .5	190 5	189	189	189
7								
8		226	210	200	195 5	193 5	192 5	192 5
9								
10		228	217	205	199 5	19[illegible]	19[illegible]	196
11								
12			223	210 5	204	200	199	199
13								
14			22[illegible]	215	207	203 5	201	201
15								
16			228	2 9	211 5	20[illegible] 5	204	203
17								
18				222	214 5	209	207	205
19								
20				225	217 5	212	209	20[illegible]
21								
22				226	220	215	211	209
23								
24				227	224	218	214	211
Inlet Press. (psig)	251	250	250	250	250	250	251	252
Press. Drop psi	7.9	8.3	9.0	9.3	9.8	9.8	9.8	9.8

CALCULATION OF THERMAL EFFICIENCY

Run No. CWI-B-2 (T_∞ = 228°F)

Time min.	Injection Temp., °F	Injection Rate, lb/hr	Cumulative Heat Injected Btu	Heat Within Core Btu	E
0	225	2.08	0	0	-
5	208	2.08	1.987	2.665	1.3412
15	192	2.19	12.007	11.197	0.9326
30	182	2.25	34.792	25.431	0.7310
45	178	2.23	61.636	39.828	0.6462
60	177	2.25	90.671	50.422	0.5561
75	177	2.23	119.815	56.560	0.4721
90	177	2.09	146.916	59.655	0.4061
105	177	2.12	173.705	61.013	0.3512

AXIAL TEMPERATURE DISTRIBUTION IN THE CORE, RUN NO. CWI-B-3

Location, in.	Time, min. 5	15	30	45	60	75	90	105
0	189	165.5	155 5	153	153	153	153	
1	196.5	168	156	153.5	153.5	153.5	153.5	
2	206.5	173	170	155.5	155.5	155.5	155.5	
3	215	179	164	169	158.5	158.5	158.5	
4	220	184.5	166.5	161	160	160	160	
5	221							
6		19≤	173 5	1≤6	1≤4	1≤4	1≤4	
7								
8		207	179	171	1≤7 5	167 5	1≤7.5	
9								
10		215	185	175	171.5	171	171	
11								
12		219	191	179	175	174	174	
13								
14		221	198.5	184	178.5	175.5	175.5	
15								
16			205	188	181	179	179	
17								
18			210	192	185.5	181 5	181	
19								
20			215	196	188.5	184.5	182.5	
21								
22			Z19	201	191	18≤.5	184.5	
23								
24			Z21	Z05	194	189	186	
Inlet Pressure (psig)	Z47	247	Z4≤	24≤	Z47	247	247	
Press. Drop Across Core psi	13 0	13.5	15 0	15.5	15.5	15 5	15.5	

CALCULATION OF THERMAL EFFICIENCY

Run No. CWI-B-3 (T_∞ = 221°F)

Time min.	Injection Temp., °F	Injection Rate, lb/hr	Cumulative Heat Injected Btu	Heat Within Core Btu	E
0	221	3.17	0	0	-
5	189	3 39	4.513	5.027	1.1139
15	165.5	3.20	28.311	25.876	0.9140
30	155.5	3.17	76.379	58.769	0.7694
45	153	3 08	129.653	82.181	0.6339
60	153	3 14	181.000	91.237	0.5041
75	153	2 89	234.333	94.870	0.4049
90	153	2.92	280.527	95.792	0.3415

AXIAL TEMPERATURE DISTRIBUTION IN THE CORE, RUN NO CWI-B-4

Location, in.	Time, min 5	15	30	45	60	75	90
0	200	171	161	159	159	159	159
1	207.5	174	162.5	160	159	159	159
2	220	178	165	161.5	161	161	161
3	228.5	185	169.5	165	164	1641	164
4	232	190	172.5	167.5	166	166	166
5							
6		201	178.5	171.5	170	170	170
7							
8		214	185	176.5	174.5	174.5	174.5
9							
10		224	191	181	178	177	177
11							
12		229	198.5	186	181	180	180
13							
14		232	205	190	185	182.5	182.5
15							
16			212.5	195	188.5	185.5	184.5
17							
18			219.5	200	192	189	187.5
19							
20			225	204	195	191	189
21							
22			228	209	198.5	194	191
23							
24			230	214	203	198	193
Inlet Press (psig)	247	248	248	248	247	247	247
Press. Drop Across Core psi	12.5	18.5	15.0	15.5	15.7	15.8	15.7

CALCULATION OF THERMAL EFFICIENCY

Run No. CWI-B-4 (T_∞ = 232°F)

Time min.	Injection Temp., °F	Injection Rate, lb/hr	Cumulative Heat Injected Btu	Heat Within Core Btu	Σ
0	232	3.45	0	0	-
5	200	3.45	4.591	4.567	0.9946
15	171	3.45	31.280	30.365	0.9707
30	161	3.36	89.880	66.579	0.7408
45	159	3.36	148.633	90.622	0.6097
60	159	3.31	211.482	100.005	0.4729
75	159	3.31	269.185	103.529	0.3846
90	159	3.31	330.950	105.102	0.3176

(3) Depletion Tests

Fig. E-1 is a recorded pressure history at the outlet end of the core for Run No. 3 with Berea sandstone. The outlet pressure behaved very similarly whether the core was synthetic or Berea sandstone. Total mass rate of production corresponding to Fig. E-1 is shown in Fig. E-2. The pressure and temperature distribution along the core were observed at various depletion times as shown in Figs. E-3 through E-10.

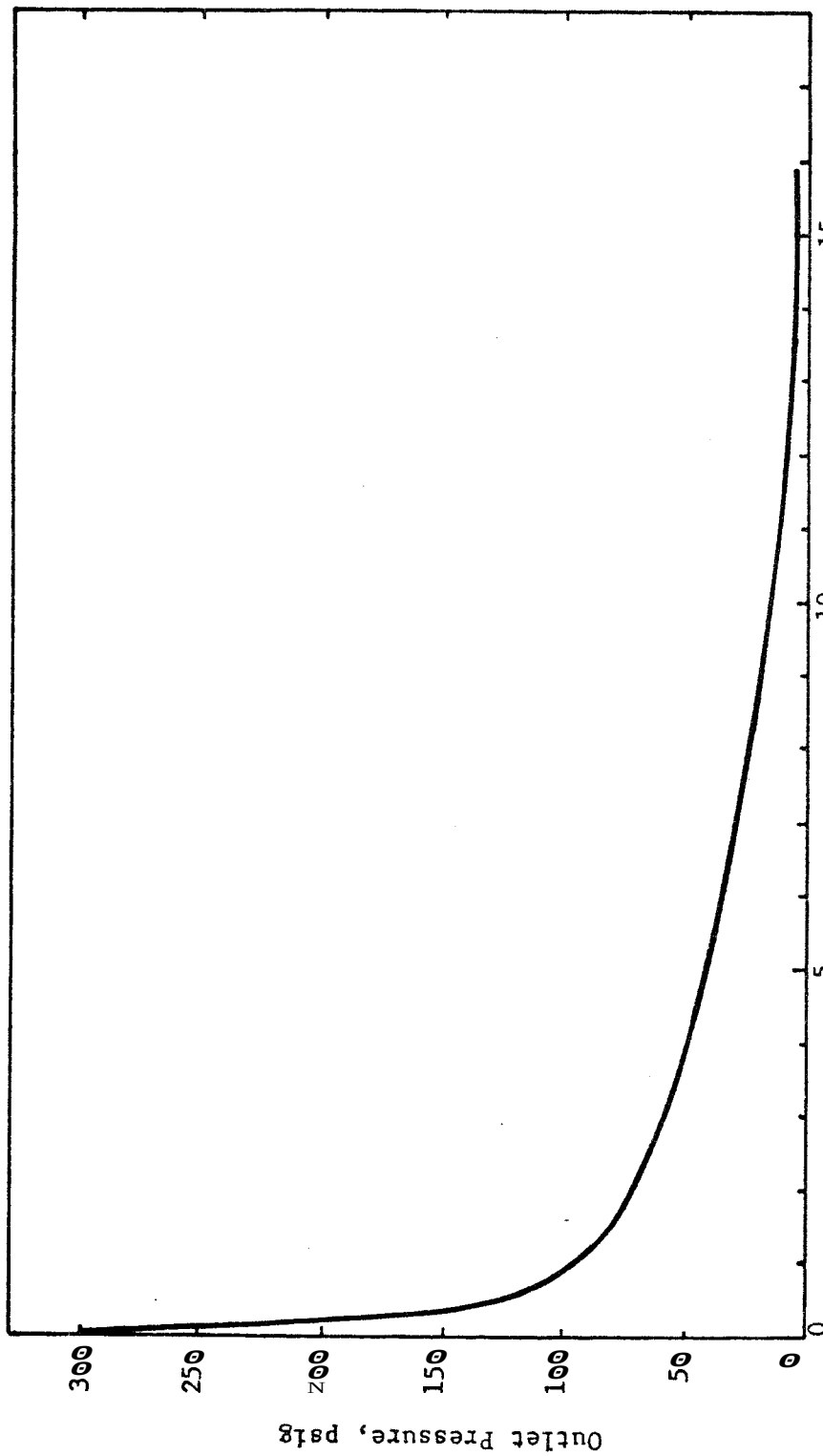

FIGURE E-1. OUTLET PRESSURE AS FUNCTION OF DEPLETION TIME FOR BEREA SANDSTONE CORE, RUN NO. 3.

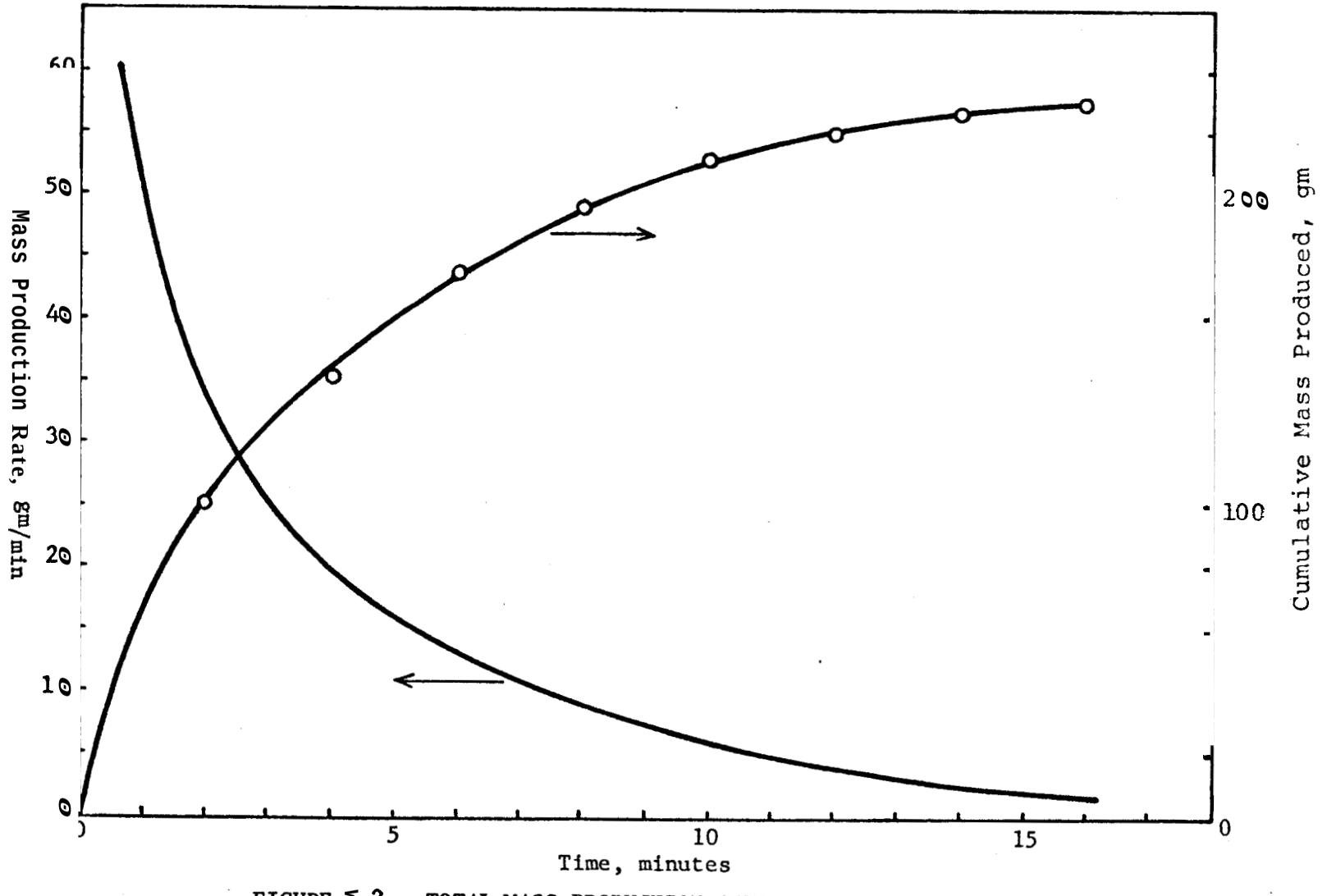

FIGURE 8-2 TOTAL MASS PRODUCTION RATE VS. DEPLETION TIME FOR BEREA SANDSTONE CORE, RUN NO. 3.

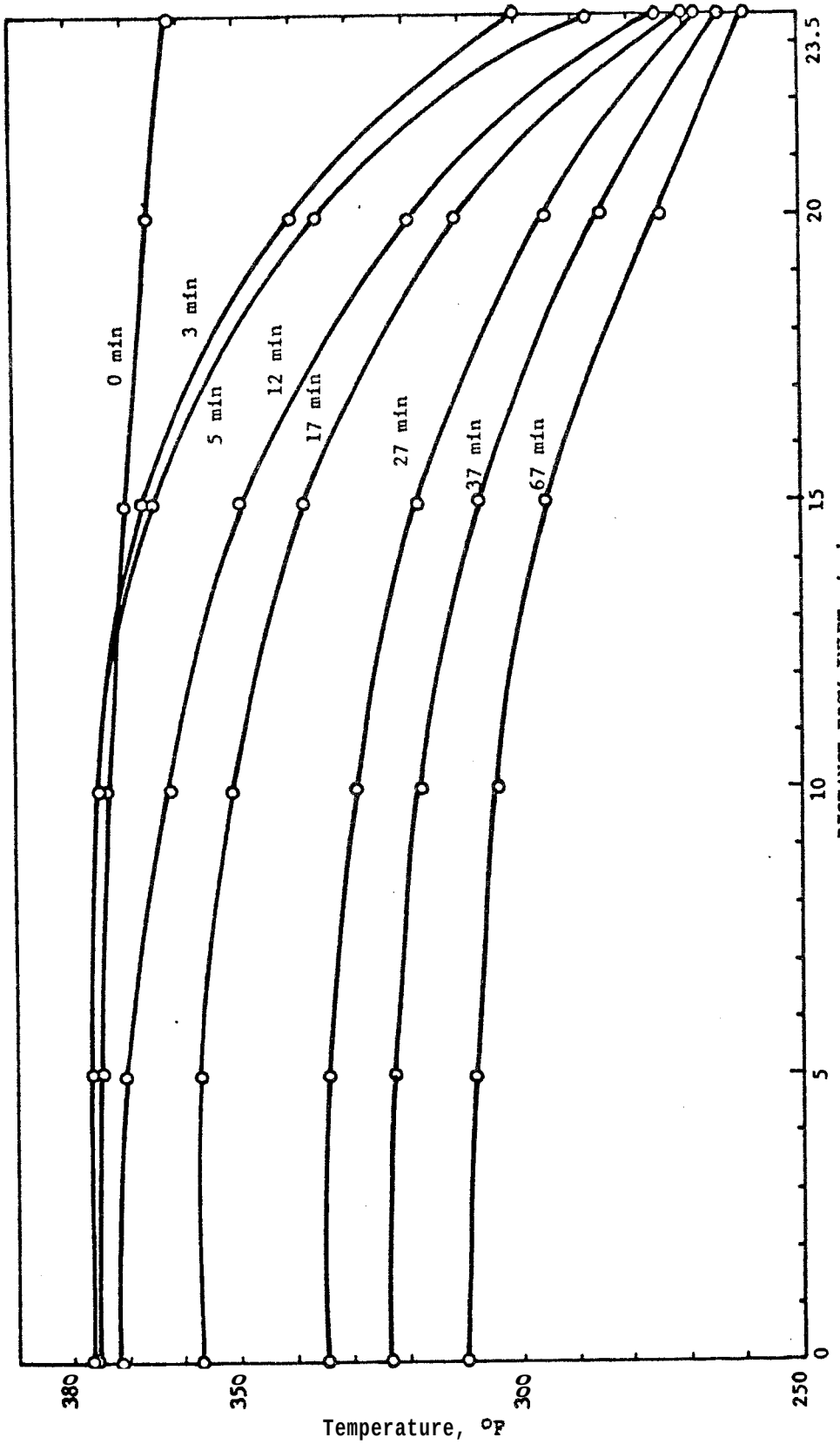

FIGURE E-3. TEMPERATURE DISTRIBUTION AT DIFFERENT DEPLETION TIMES, SYNTHETIC SANDSTONE.

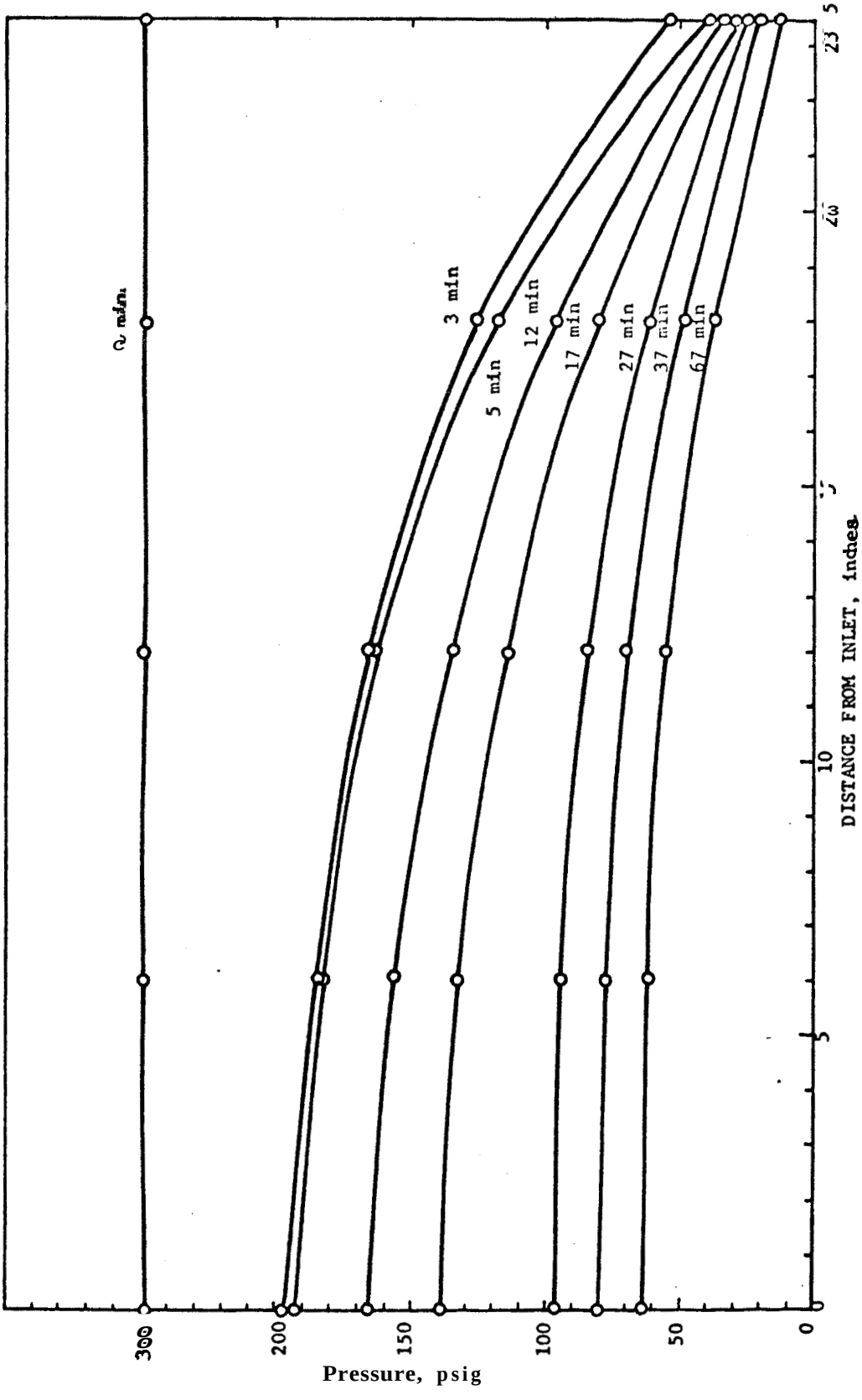

FIGURE E-4. PRESSURE DISTRIBUTION AT DIFFERENT DEPLETION TIMES, SYNTHETIC SANDSTONE

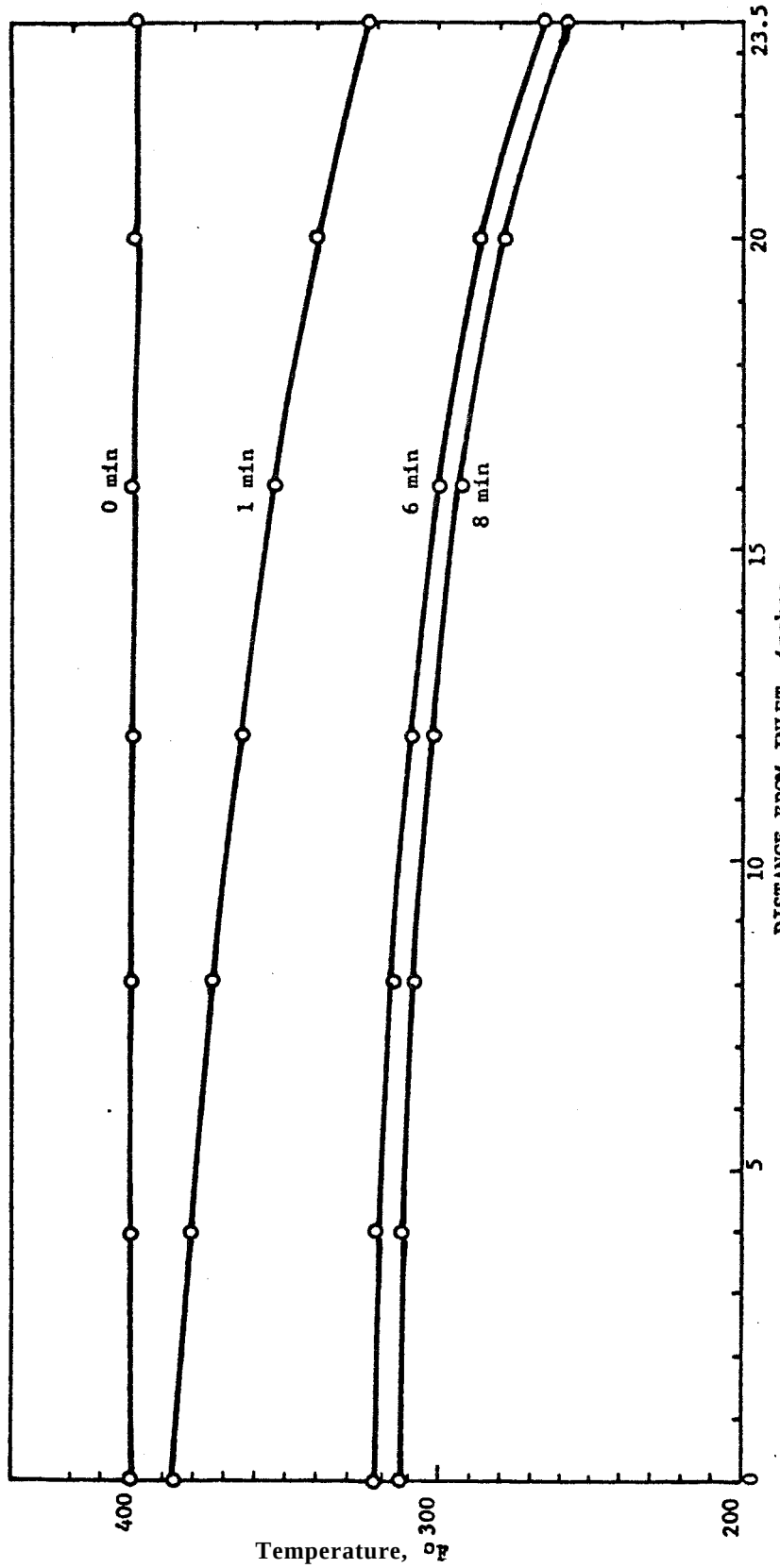

FIGURE E-5. TEMPERATURE HISTORY IN DEPLETION TEST, BEREA SANDSTONE, RUN NO. 1

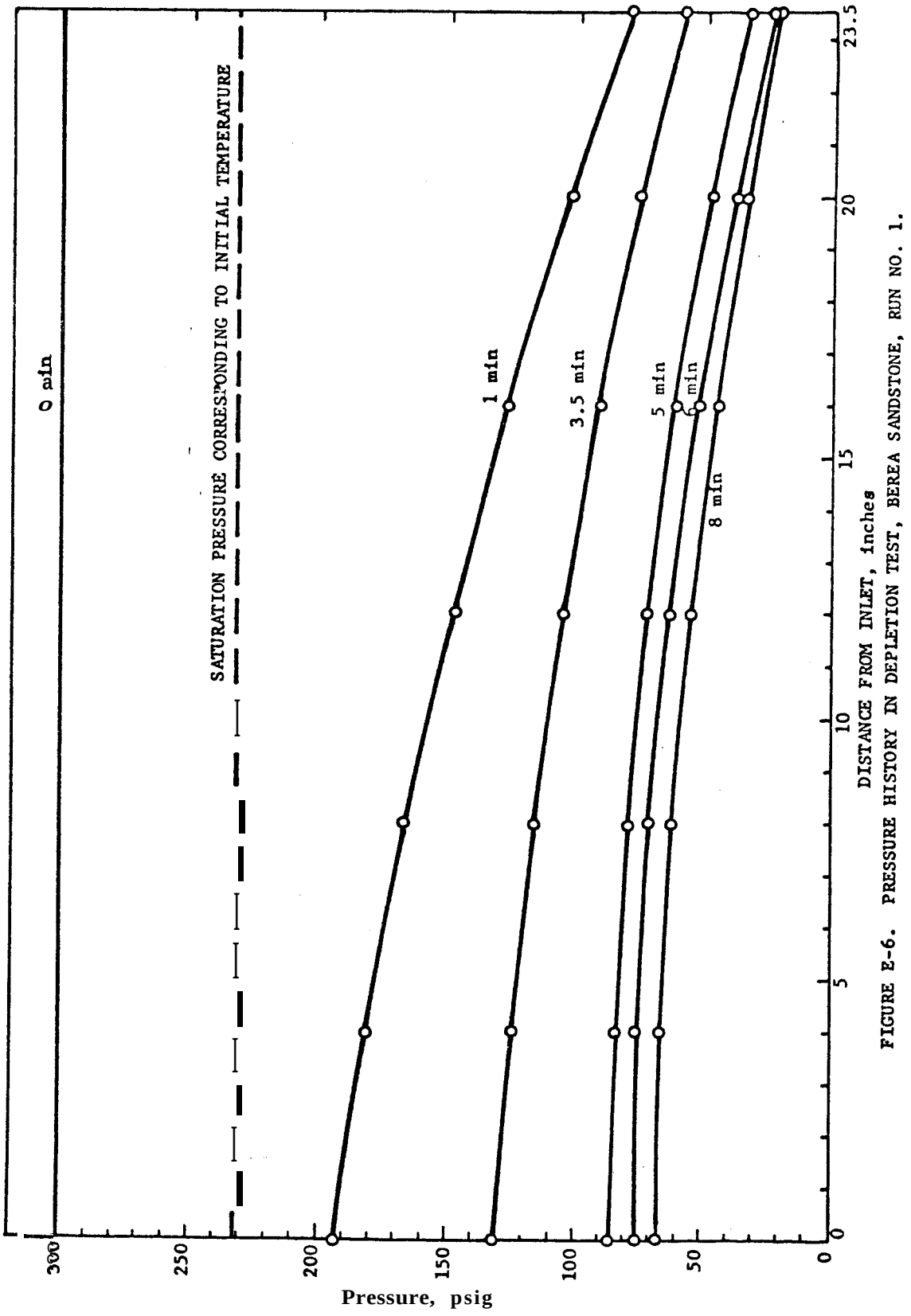

FIGURE E-6. PRESSURE HISTORY IN DEPLETION TEST, BEREA SANDSTONE, RUN NO. 1.

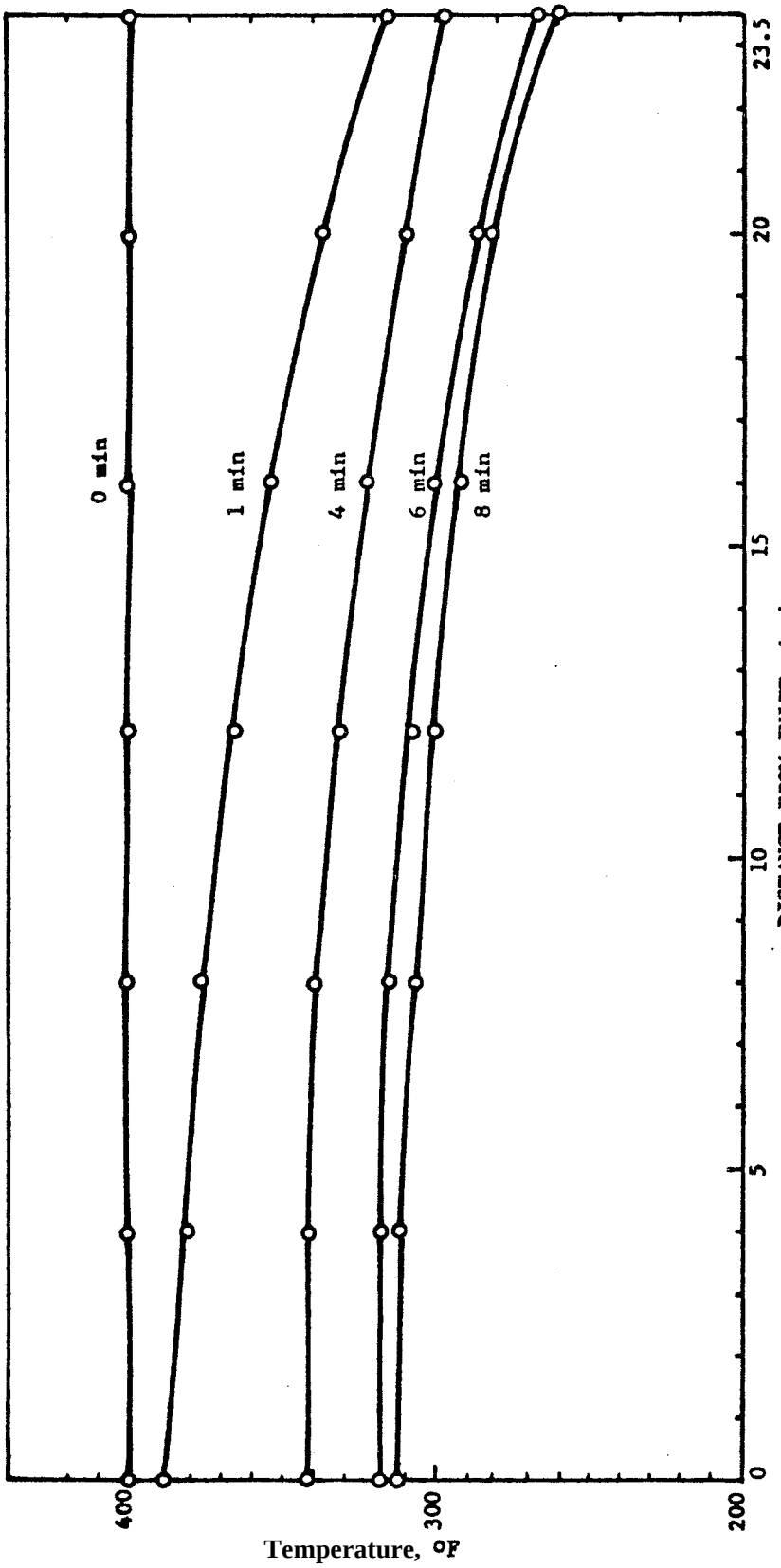

FIGURE E-7. TEMPERATURE HISTORY IN DEPLETION TEST, BEREA SANDSTONE, RUN NO. 2.

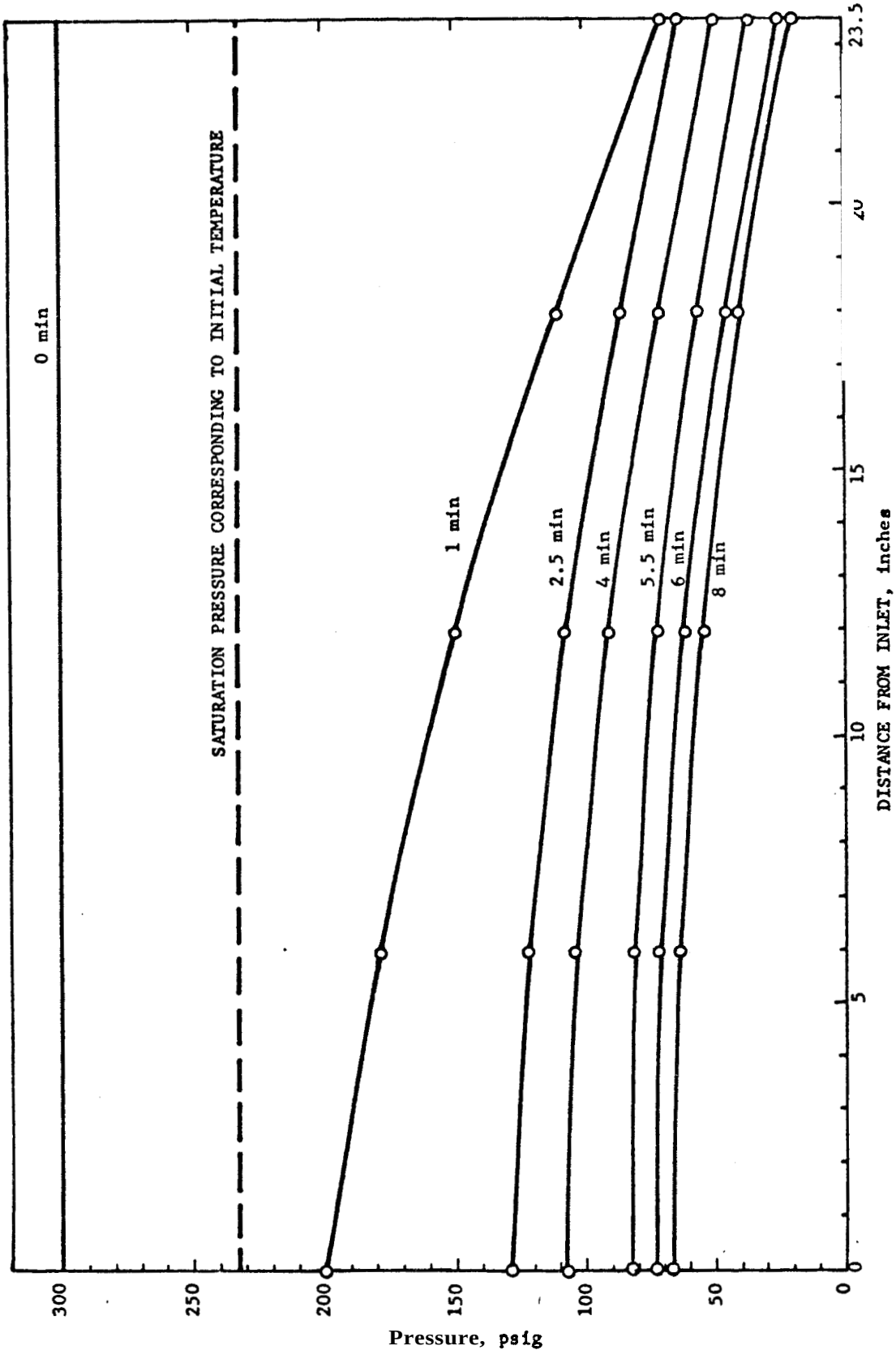

FIGURE E-8. PRESSURE HISTORY IN DEPLETION TEST, BEREA SANDSTONE, RUN NO. 2.

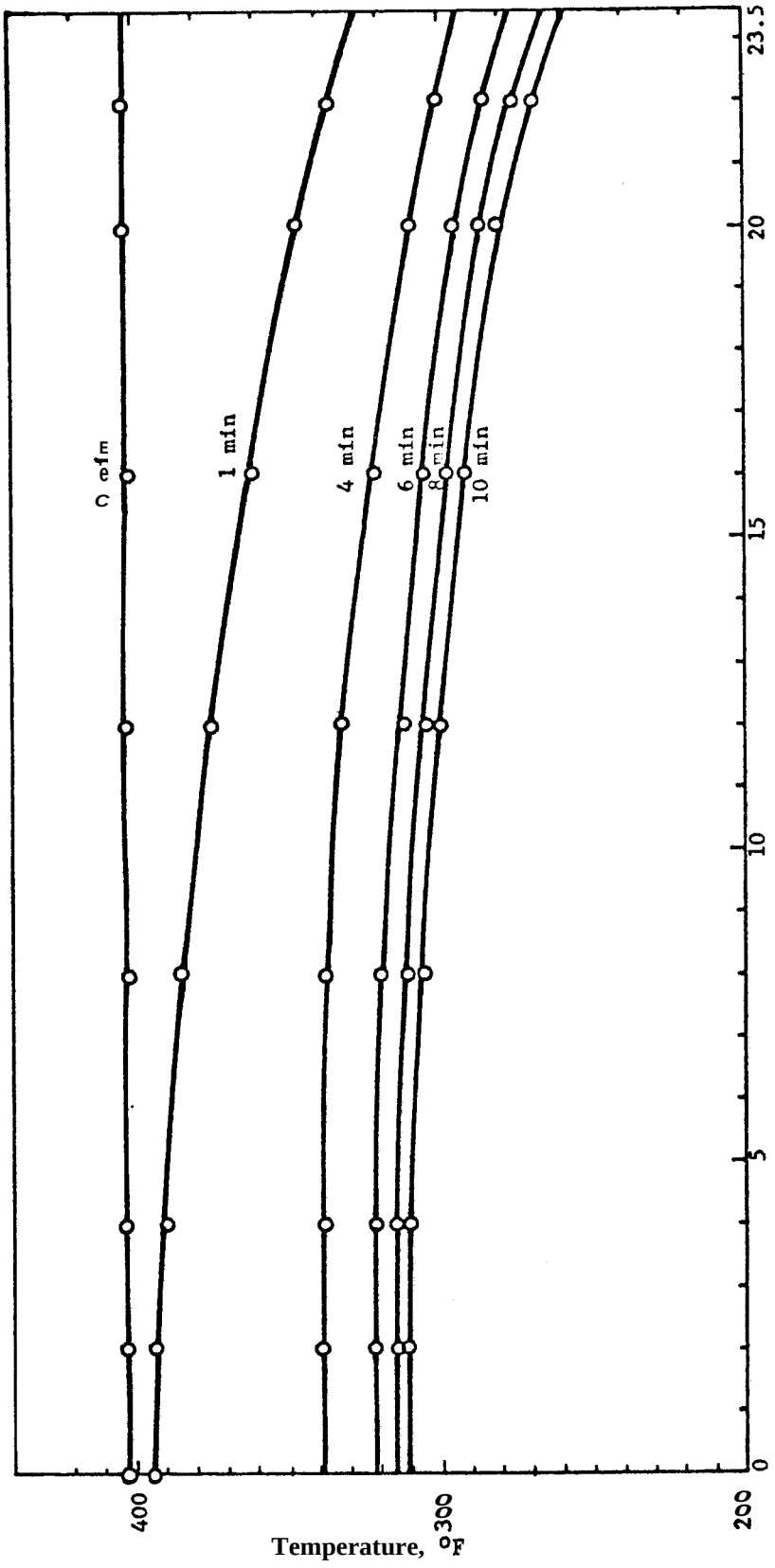

FIGURE E-9. TEMPERATURE HISTORY IN DEPLETION TEST, BEREA SANDSTONE, RUN NO. 3

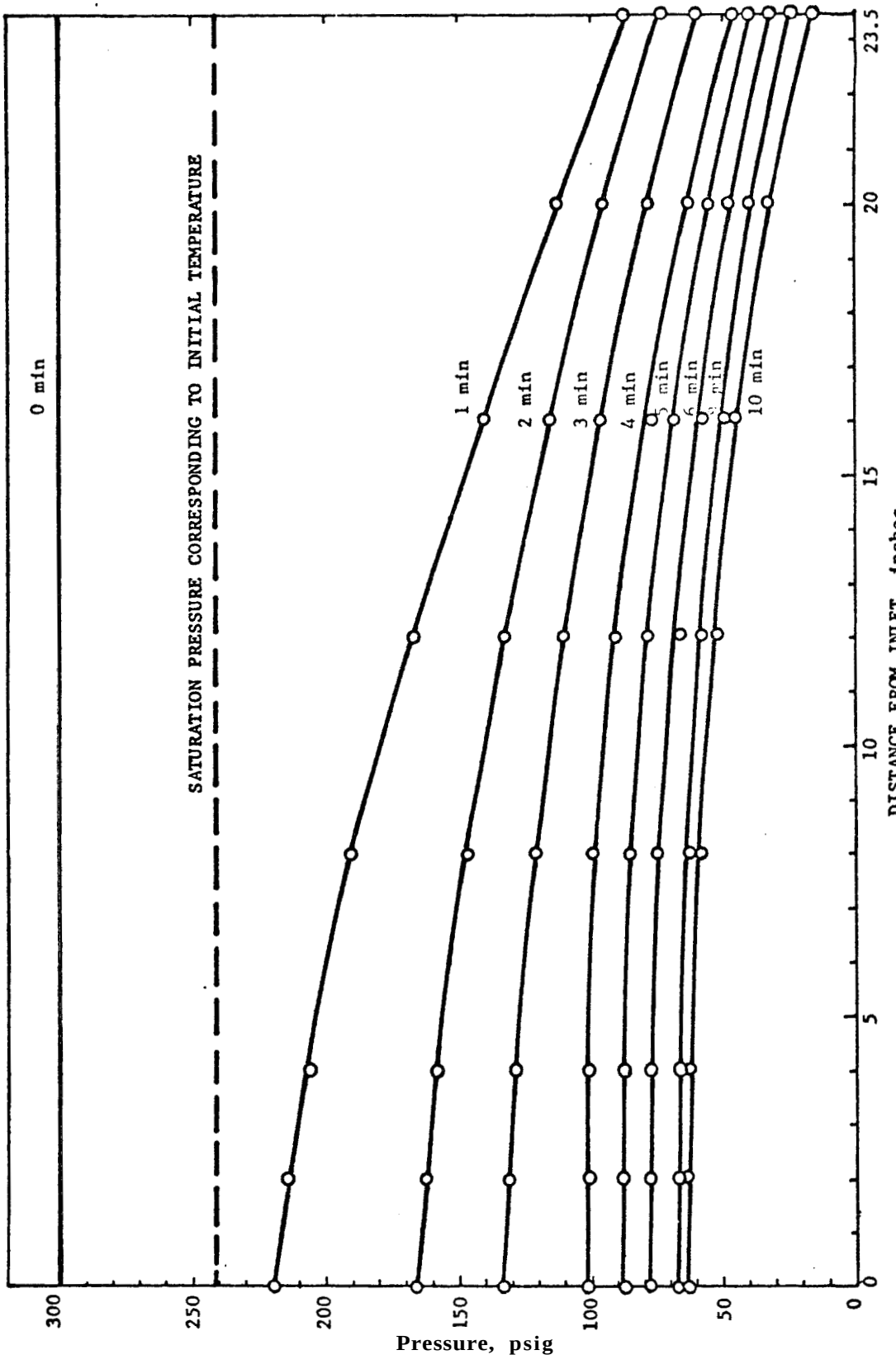

FIGURE E-10. PRESSURE HISTORY IN DEPLETION TEST, BEREA SANDSTONE, RUN NO. 3.